NASA CONTRACTOR REPORT

NASA CR-2063

NASA CR-2063

DISTRIBUTION STATEMENT A
Approved for public release;
Distribution Unlimited

HOLOGRAPHIC MEASUREMENT OF WAVE PROPAGATION IN AXI-SYMMETRIC SHELLS

by David A. Evensen, Robert Aprahamian, and Jerold L. Jacoby

19960426 026

Prepared by
TRW SYSTEMS GROUP
Redondo Beach, Calif.
for Langley Research Center

NATIONAL AERONAUTICS AND SPACE ADMINISTRATION • WASHINGTON, D. C. • JUNE 1972

DTIC QUALITY INSPECTED 1
18257

DISCLAIMER NOTICE

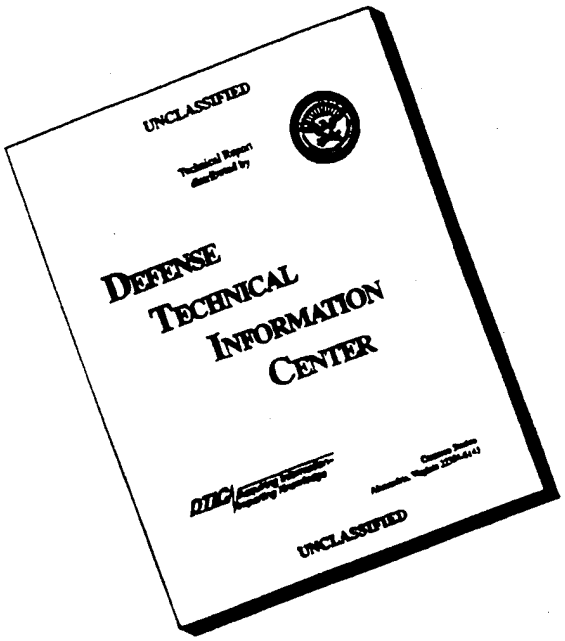

THIS DOCUMENT IS BEST QUALITY AVAILABLE. THE COPY FURNISHED TO DTIC CONTAINED A SIGNIFICANT NUMBER OF PAGES WHICH DO NOT REPRODUCE LEGIBLY.

1. Report No.	2. Government Accession No.	3. Recipient's Catalog No.
NASA CR-2063		

4. Title and Subtitle	5. Report Date
HOLOGRAPHIC MEASUREMENT OF WAVE PROPAGATION IN AXI-SYMMETRIC SHELLS	June 1972
	6. Performing Organization Code
7. Author(s)	8. Performing Organization Report No.
David A. Evensen, Robert Aprahamian, Jerold L. Jacoby	AM 71-8
9. Performing Organization Name and Address	10. Work Unit No.
TRW Systems Group One Space Park Redondo Beach, Calif.	124-08-14-08-00
	11. Contract or Grant No.
	NAS 1-9876
12. Sponsoring Agency Name and Address	13. Type of Report and Period Covered
National Aeronautics and Space Administration Washington, D.C. 20546	Contract Report
	14. Sponsoring Agency Code

15. Supplementary Notes

16. Abstract

Holography is a lensless imaging technique which allows the reconstruction of three dimensional images. A related technique, called holographic interferometry, allows one to measure static or dynamic displacement on the order of a wavelength of light. The present report deals with the use of pulsed, double-exposure holographic interferometry to record the propagation of transverse waves in thin-walled axi-symmetric shells.

The report is subdivided into sections dealing with

(i) Wave propagation in circular cylindrical shells

(ii) Wave propagation past cut-outs and stiffeners

and

(iii) Wave propagation in conical shells

Several interferograms are presented herein which show the waves reflecting from the shell boundaries, from cut-outs, and from stiffening rings. The initial response of the shell was nearly axi-symmetric in all cases, but non-symmetric modes soon appeared in the radial response (i.e., $w \sim w_o + w_n \cos n\theta$). This result suggests that the axi-symmetric response of the shell may be dynamically unstable, and thus may preferentially excite certain circumferential harmonics through parametric excitation.

Attempts were made throughout this study to correlate the experimental data with analysis. For the most part, good agreement between theory and experiment was obtained. Occasional differences were attributed primarily to simplifying assumptions used in the analysis. As faster and more economical computer analyses of wave propagation become available, it is hoped that the experimental data given herein will serve to verify computer solutions.

From the standpoint of engineering applications, it is clear that pulsed laser holography can be used to obtain quantitative engineering data. Areas of dynamic stress concentration, stress concentration factors, local anomalies, etc., can be readily determined by holography.

17. Key Words (Suggested by Author(s))	18. Distribution Statement
Wave Propagation in Axi-Symmetric Shells Pulsed Laser Holography	Unclassified - Unlimited

19. Security Classif. (of this report)	20. Security Classif. (of this page)	21. No. of Pages	22. Price*
Unclassified	Unclassified	203	$3.00

*For sale by the National Technical Information Service, Springfield, Virginia 22151

FOREWORD

This contract resulted from a desire to provide experimental data for comparison with analytical results on wave propagation in shells. Valuable advice and discussions on this problem were held with several colleagues at NASA/Langley, Lockheed (Palo Alto), and at TRW Systems.

A special note of thanks is due R. N. Schreiner, who helped reduce the fringe data, and J. E. Wright, who solved many of the design problems which arose during this study.

CONTENTS

		Page
	FOREWORD	iii
	SUMMARY	1
1.0	INTRODUCTION	2
2.0	DOUBLE-EXPOSURE HOLOGRAPHIC INTERFEROMETRY	4
3.0	TRANSVERSE WAVES IN CIRCULAR CYLINDRICAL SHELLS	7
	Introduction and Description of the Problem	7
	Some Analytical Considerations	8
	Experimental Set-Up and Test Procedure	14
	Test Specimens	14
	The Applied Loading	16
	Optical Arrangement for Recording Holograms	17
	Timing of the Laser Pulse(s)	17
	Test Procedure	17
	Typical Results for the Thin-Walled Cylinder	20
	Demonstration of Repeatability	20
	Determination of Radial Displacements from the Interferograms	20
	Non-Symmetric Behavior	29
	Initial Response	29
	Additional Results and a Computed Fringe Pattern	30
	Displacement Curves	31
	Dynamic Stability of the Axi-Symmetric Response	34
	Waves Reflecting from the Ends of the Shell	37
	Background	37
	Reflection from a Clamped Boundary	37
	Reflections from a Free Edge	38
	Reflections from a Simply-Supported Boundary	41
	Comparison with Computer Analysis	44
	Input Data for the Analysis	44
	Ratio Between Experimental/Theoretical Responses	48
4.0	WAVE PROPAGATION PAST CUT-OUTS AND STIFFENERS	50
	Background and Summary	50
	Tests on a Thick-Walled Cylinder	51
	Background	51
	Shell Specimen and Test Procedure	51
	Response Without Cut-Outs	51
	Response with Cut-Outs	57
	Comparison with the STAR Code	69
	Input Data for the Analysis	69

Ratio Between Experimental/Theoretical Responses. . . 70
Analytical Results and Comparison with Experiment . . 72
Some Simple Wave Propagation Problems in Thick and Thin-Walled Shells. 76
Additional Experimental Results for the Thick-Walled Shell 79
Results from Elasticity Theory 83
Test Results for the Thin-Walled Cylinder. 85
Wave Propagation Past a Circular Cut-Out. 85
Wave Propagation Past a Square Cut-Out. 85
Wave Interaction with a Stiffening Ring 98

5.0 WAVE PROPAGATION IN CONICAL SHELLS. 104

Introduction and Background. 104
Tests on the Cone-Cylinder Specimen. 104
Tests on the Large Conical Shell 104

6.0 CONCLUDING REMARKS. 118

7.0 REFERENCES. 119

APPENDIX A - THE EXPERIMENTAL LOADING TECHNIQUE 122

APPENDIX B - WAVES IN THE THIN-WALLED CYLINDER (ADDITIONAL INTERFEROGRAMS) 135

APPENDIX C - WAVES REFLECTING FROM THE ENDS OF THE SHELL (ADDITIONAL INTERFEROGRAMS) 143

APPENDIX D - WAVE PROPAGATION IN THE THICK-WALLED SHELL (ADDITIONAL INTERFEROGRAMS) 160

APPENDIX E - WAVES PAST CUT-OUTS AND STIFFENERS (ADDITONAL INTERFEROGRAMS) 172

APPENDIX F - WAVES IN CONICAL SHELLS (ADDITIONAL INTERFEROGRAMS). 186

HOLOGRAPHIC MEASUREMENT OF WAVE PROPAGATION IN AXI-SYMMETRIC SHELLS

David A. Evensen
Robert Aprahamian
Jerold L. Jacoby

TRW Systems Group

SUMMARY

Holography is a lensless imaging technique which allows the reconstruction of three dimensional images. A related technique, called holographic interferometry, allows one to measure static or dynamic displacement on the order of a wavelength of light. The present report deals with the use of pulsed, double-exposure holographic interferometry to record the propagation of transverse waves in thin-walled axi-symmetric shells.

The report is subdivided into sections dealing with

(i) Wave propagation in circular cylindrical shells

(ii) Wave propagation past cut-outs and stiffeners

and

(iii) Wave propagation in conical shells

Several interferograms are presented herein which show the waves reflecting from the shell boundaries, from cut-outs, and from stiffening rings. The initial response of the shell was nearly axi-symmetric in all cases, but non-symmetric modes soon appeared in the radial response (i.e., $w \sim w_o + w_n \cos n\theta$). This result suggests that the axi-symmetric response of the shell may be dynamically unstable, and thus may preferentially excite certain circumferential harmonics through parametric excitation.

Attempts were made throughout this study to correlate the experimental data with analysis. For the most part, good agreement between theory and experiment was obtained. Occasional differences were attributed primarily to simplifying assumptions used in the analysis. As faster and more economical computer analyses of wave propagation become available, it is hoped that the experimental data given herein will serve to verify computer solutions.

From the standpoint of engineering applications, it is clear that pulsed laser holography can be used to obtain quantitative engineering data. Areas of dynamic stress concentration, stress concentration factors, local anomalies, etc., can be readily determined by holography.

1.0 INTRODUCTION

Wave-propagation in thin walled shells is of interest in many areas of applied mechanics. For example, pyrotechnic shock loading in launch vehicles causes waves to propagate along the length of the structure. Other practical areas of application include waves interacting with cut-outs and stiffeners in re-entry vehicles, spacecraft, etc.

From an analytical standpoint, the problem of calculating the shell response is very difficult (unless simplifying assumptions are made). For example, one common approximation is to assume the response is axi-symmetric. This assumption can then be verified by experiment, if necessary. Another common assumption is to neglect rotary inertia and transverse shear effects in the analysis. Again, this approximation can be checked (by using an improved theory) or by experiments.

The primary objective of the present study is to provide experimental data for comparison with analysis. Since the experiments involve the use of holography (Refs. 1 - 8), the reader who is unfamiliar with the method may wish to look up either the texts or reports referenced herein. It is safe to say that by now holography is a widely-accepted measuring technique. Pulsed laser holography has been used in previous studies of wave propagation (Refs. 7, 8) in structures, as well as measuring shock waves in gases and solids.

Regarding wave propagation in shells, it is worth noting that most of the analyses are (1) linear and (2) restricted to shells of revolution. A further simplification that is ordinarily introduced in the calculations is to ignore all variations in θ, the circumferential co-ordinate. Only recently have non-axisymmetric computer analyses become available. Thus, one objective of this study was to provide non-symmetric data (showing waves passing a cut-out, etc.) to compare with computer simulations.

The tests were done on two aluminum cylinders, with a nominal radius $a = 5"$, and the thickness of $h = .106$, and $h = .25$ inches, respectively. The experimental results suggest, that the axi-symmetric response may not be stable. That is, if you have an axi-symmetric wave propagating longitudinally along the shell, will it then cause the non-symmetric modes ($\cos n\theta$) to become unstable. The experimental results suggest that the axi-symmetric response is indeed unstable, since certain harmonics ($\cos 12\theta$, for example) are predominant in the non-symmetric response.

Another point of interest involves the response of the thick-walled shell ($h = .25$ inches). In this case, the loading of $T = 10$ μsec duration excited an elasticity type response which could not be predicted using shell theory.

Results given herein include the holograms (photos) and in many cases the corresponding radial displacement, w. For the most part, the theory and experiment are in agreement, with the lack of agreement thought to be attributed to simplifying assumptions of the analysis.

Tests were also conducted on two conical shell specimens as well, and these results are included herein.

From the standpoint of practical engineering applications, it is clear that pulsed laser holography can be used to obtain quantitative engineering data. Areas of dynamic stress concentration, stress concentration factors, local anomalies, etc., can be readily determined and evaluated by holography.

2.0 DOUBLE-EXPOSURE HOLOGRAPHIC INTERFEROMETRY

Holographic interferometry is an optical technique which allows measurement of displacements on the order of a wavelength of light. Textbooks are available which discuss holography and its applications (Refs. 1, 2, and 3). A brief summary of holography which is oriented toward structures and dynamics applications is given in Ref. 4. Detailed descriptions of holographic interferometry are thus readily available to the uninitiated reader.

The present study deals exclusively with the application of double-exposure holography, using a pulsed ruby laser. First a hologram is made of the undeformed, stationary object (in this case a shell). Then the object is deformed (by an applied load) and the hologram is exposed for a second time. When this "double-exposed hologram" is developed and then illuminated, two images are produced: one is from the undeformed object and the other from the deformed object. The light waves (which form the two images) interact with one another and create visible interference fringe patterns. By analyzing these fringe patterns, one can determine the surface deformations of the object (see Ref. 5).

Each exposure of the hologram by the pulsed ruby laser involves a light pulse which has a duration of about 50 nanoseconds (50×10^{-9} sec.). This exposure time is sufficiently short to effectively "freeze" the deformation of the structure at a particular instant in time. Thus the double-exposure hologram gives a record of the deformation on the surface of the object, at a particular time, say t_i. This spatial recording can be used to complement conventional strain gages or accelerometers which yield time-histories of the deformation, at a fixed location, say $\vec{x}_i$.

Double-exposure holographic interferometry has been used to measure wave propagation in rods (Ref. 6), beams (Ref. 7), plates (Ref. 8), as well as surface waves, and shock waves in solids. Aerodynamic waves have also been studied using holography (Refs. 9, 10). Thus it is clear that holographic interferometry is now a well-established experimental technique which has been successfully applied to many problems in engineering mechanics.

Typical double-exposure holographic results are given in Figure 1, which shows wave propagation in a flat plate.

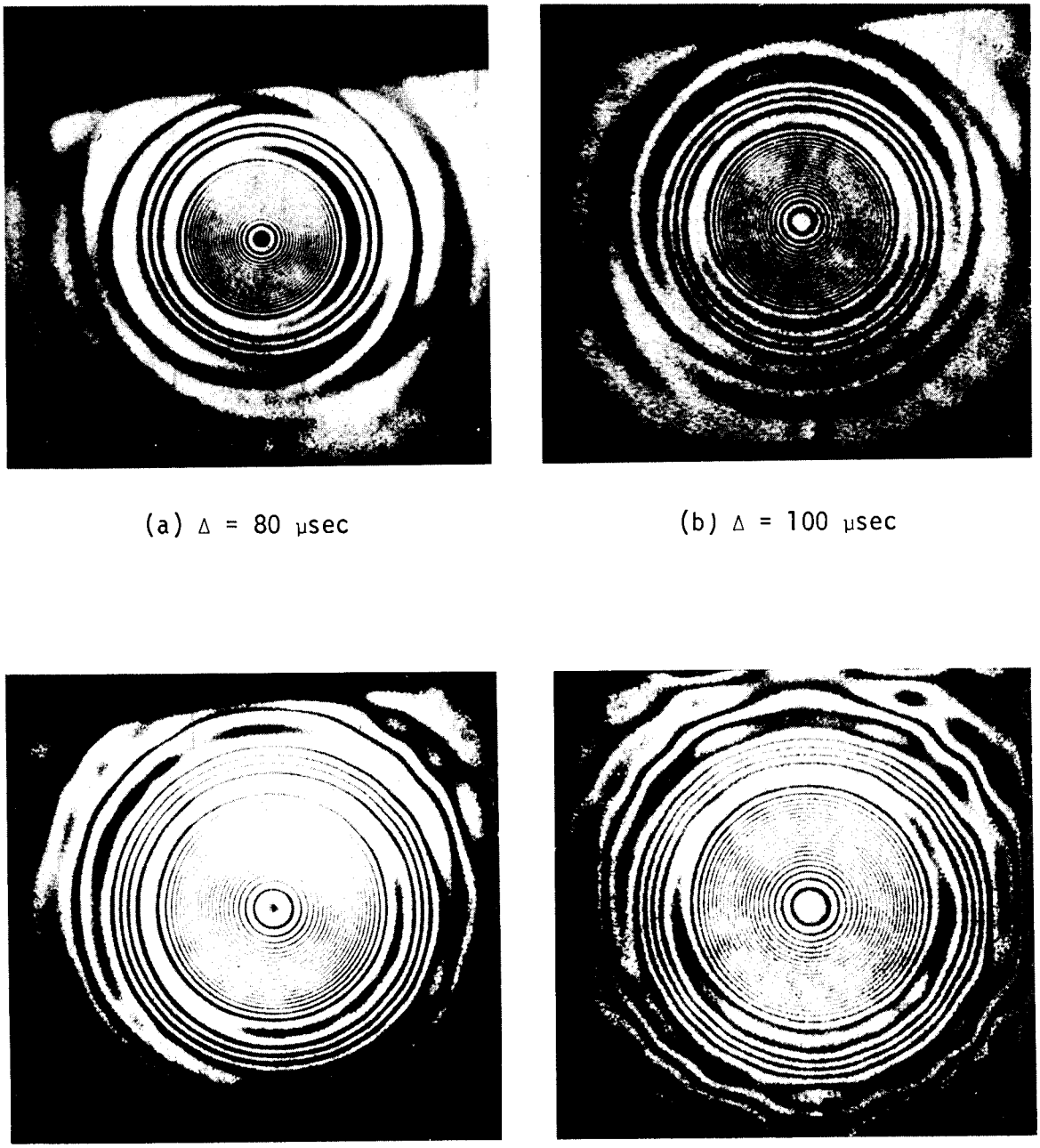

(a) Δ = 80 μsec

(b) Δ = 100 μsec

(c) Δ = 130 μsec

(d) Δ = 150 μsec

Figure 1(a): Flexural waves in an elastic plate, recorded holographically (see Ref. 8).

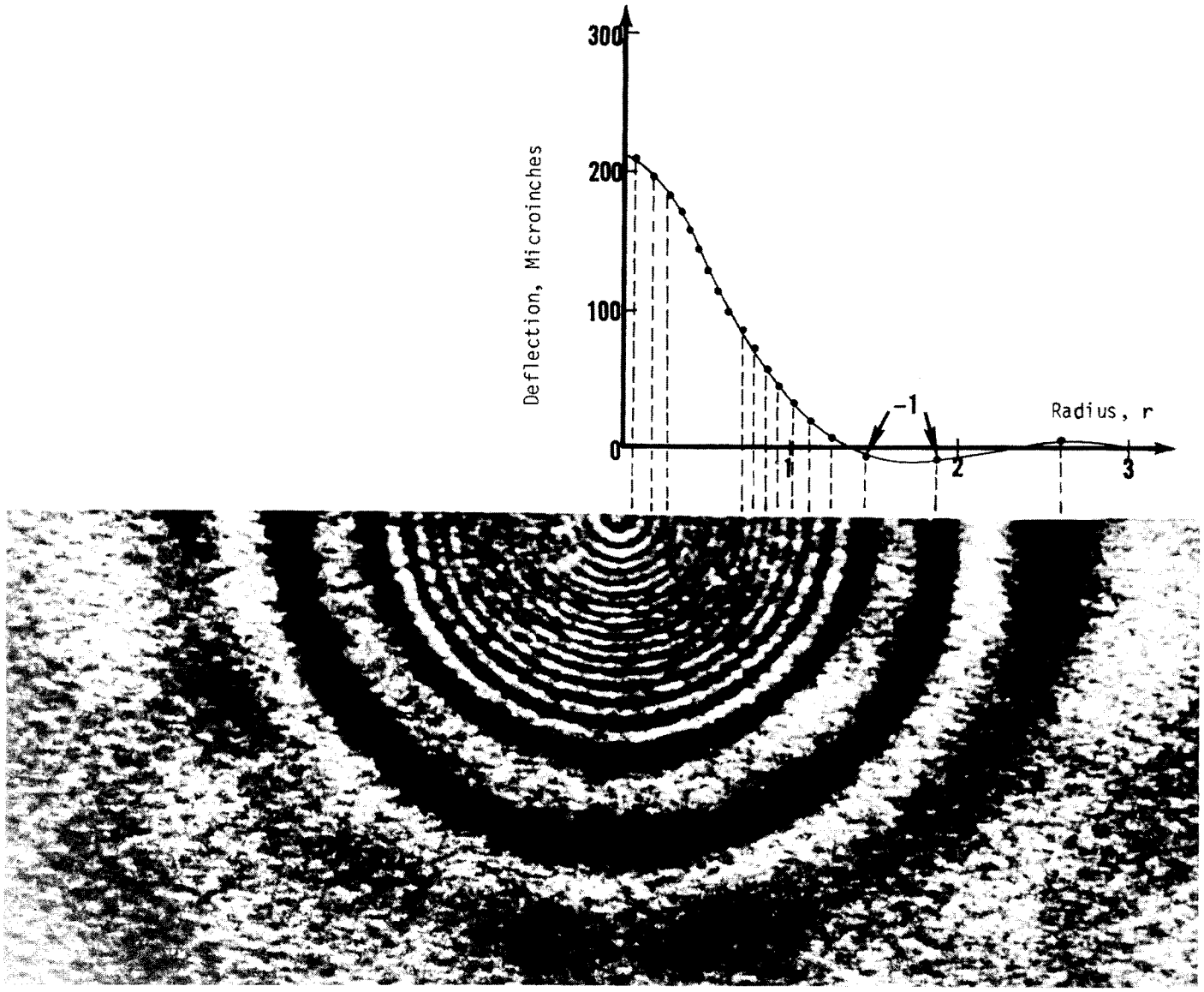

Figure 1(b): Deflection data obtained from the interferogram (see Ref. 8).

3.0 TRANSVERSE WAVES IN CIRCULAR CYLINDRICAL SHELLS

Introduction and Description of the Problem

Consider a thin-walled circular cylindrical shell, which is subjected to an axi-symmetric impulse loading in the radial direction (see Fig. 2).

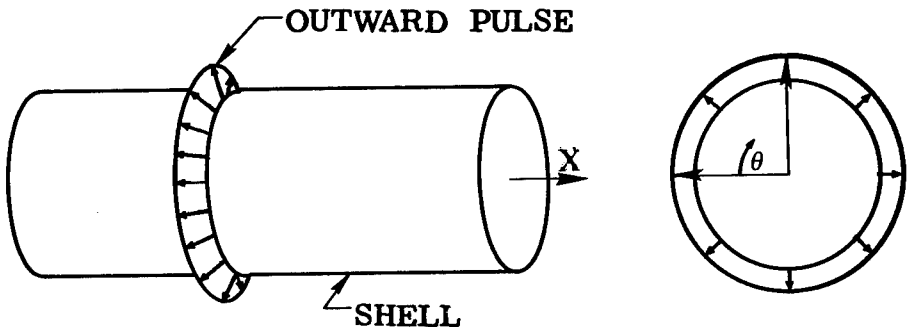

Figure 2: Radial pulse loading on shell
(r, θ, x, cylindrical polar co-ordinate)

The shell is described in terms of cylindrical co-ordinates (r, θ, x) in the radial, circumferential and longitudinal directions, respectively. The corresponding elastic displacements of the shell are w (radial), v (circumferential), and u (longitudinal). The axi-symmetric impulsive load causes waves to propagate longitudinally, and the experiments described herein give results for the radial displacement (w) as a function of position (x) along the shell.

The following sections discuss some analytical considerations relating to this problem, and experimental holographic results involving both symmetric and non-symmetric responses, reflections from the ends of the shell, and comparisons between theory and experiment.

Some Analytical Considerations

For dynamic problems (such as wave propagation) in thin-walled shells, the mathematical modeling of the structure usually involves one of the following levels of sophistication:

(I) - Love's First Approximation (Ref. 11) which is a shell theory analogous to Bernoulli-Euler Beam Theory.

(II) - "Timoshenko" Theory, which is a shell theory that includes rotary inertia and transverse shear effects (See Ref. 12)

(III) - Three-Dimensional Elasticity Theory (Ref. 13), which the shell theories approximate.

The main differences between these three mathematical approaches to shell dynamics can be described in terms of the vibration frequencies and structural wavelengths which are excited by the applied loading.

For example, reference 14 indicates that conventional, thin shell theory (I) applies when

$$0 \leq \omega_f \leq .1\ \omega_s \tag{3-1}$$

where ω_f designates the flexural vibration frequencies and

$$\omega_s = \frac{\pi c_s}{h} = \frac{\pi}{h}\left[\frac{E/\rho}{2(1+\nu)}\right]^{1/2} \tag{3-2}$$

is the frequency of the first "thickness-shear" mode in an infinite flat plate (Ref. 15).

When rotary inertia and shear are included in the analysis, the corresponding inequality is (Ref. 14)

$$0 \leq \omega_{II} \leq \omega_s \tag{3-3}$$

where ω_{II} denotes the vibration frequencies computed using this "improved" shell theory.

Elasticity theory (III) is valid for

$$0 \leq \omega \leq \omega_E \tag{3-4}$$

where ω_E is a cut-off frequency significantly greater than ω_s. For example, ω_E may be associated with lattice vibrations or other effects in which the equations of continuum mechanics no longer apply.

In the experiments reported herein, the forcing function applied to the shell has a time-history given approximately by

$$f(t) = \sin^2 \frac{\pi t}{T} \qquad 0 \leq t \leq T$$

which is shown in Figure 3. The corresponding Fourier transform,

$$F(\omega) = \int_{-\infty}^{\infty} e^{-i\omega t} \sin^2 \frac{\pi t}{T} \, dt$$

(tabulated in Ref. 16) is readily evaluated and has a spectrum $|F(\omega)|$ as indicated in Figure 4. This spectrum (of the input forcing function) has a well-defined cutoff frequency given by

$$\omega_c = \frac{4\pi}{T} \tag{3-5}$$

where T is the duration of the input pulse.

The experimental loading device (described in Appendix A) gave a pulse duration on the order of 10 μsec. From Equation (3-5), the corresponding cutoff frequency is

$$\omega_c = 4\pi \times 10^5 = 1.256 \times 10^6 \text{ rad/sec} \tag{3-6}$$

That is, the input forcing function contains frequencies primarily within the range

$$0 \leq \omega \leq 1.256 \times 10^6 \text{ rad/sec}$$

For comparison purposes, the thickness-shear frequency of the thin-walled cylinder used in our experiments is given by

$$\omega_s = \frac{\pi c_s}{h} = 3.83 \times 10^6 \text{ rad/sec} \tag{3-7}$$

(i.e., an aluminum shell with a thickness h = .1 inch). Equations (3-6) and (3-7) show that in our thin-shell experiments, we have frequencies in the range

$$0 \leq \omega \leq .3 \, \omega_s \tag{3-8}$$

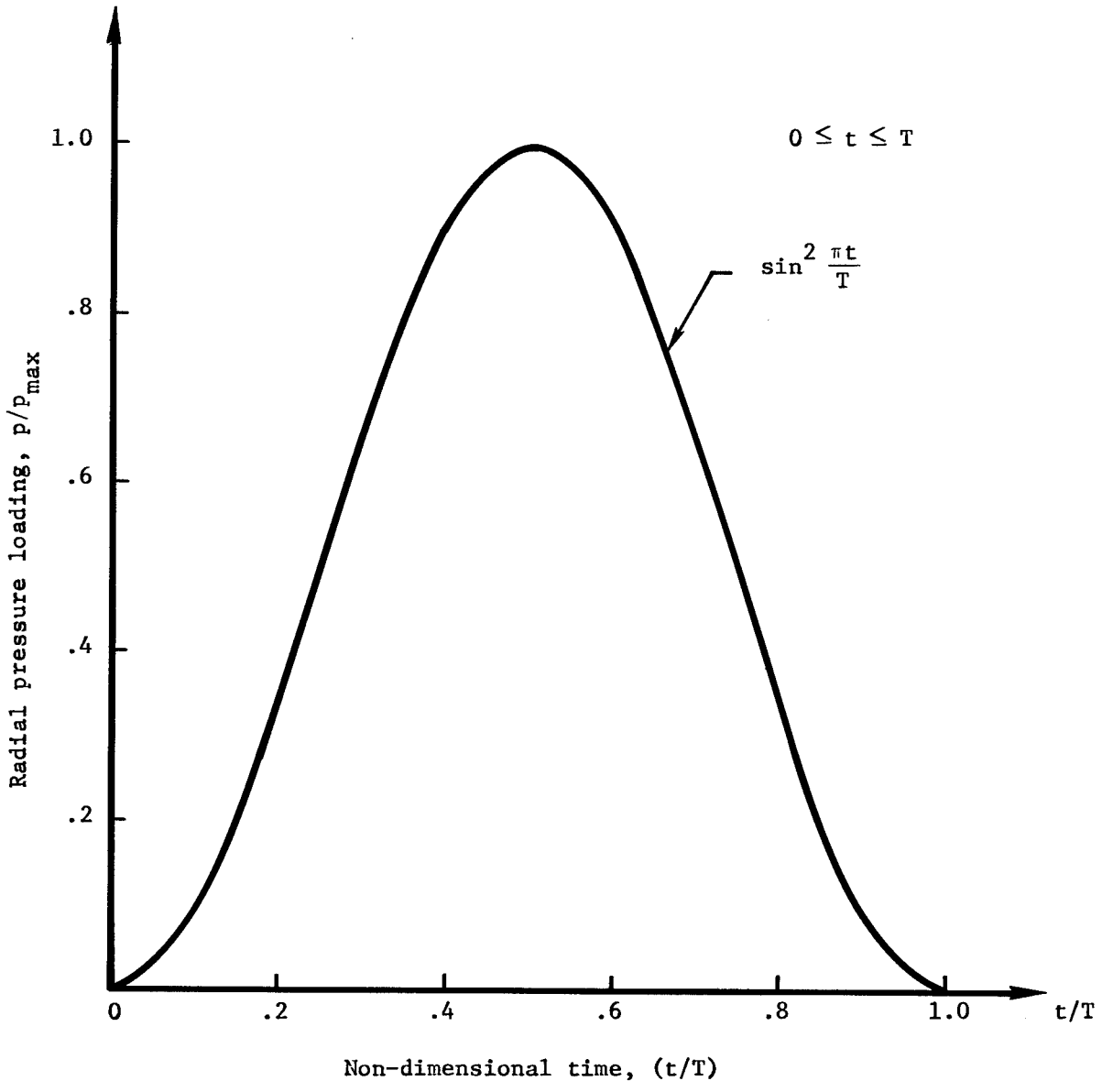

Figure 3: Time-history of the applied load (schematic)

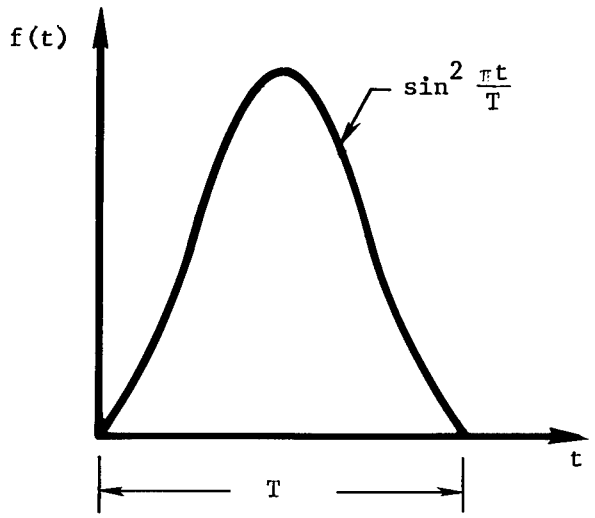

(a) Pressure-time history

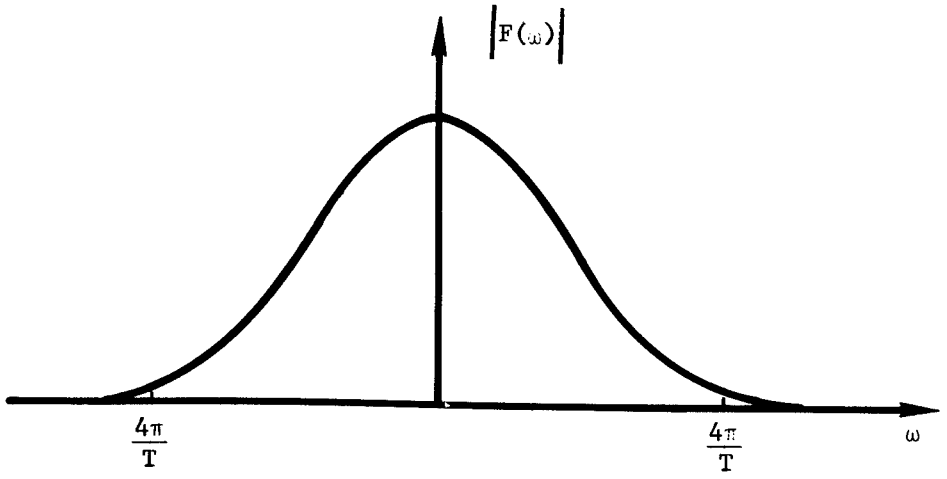

(b) Spectrum of the pulse

Figure 4: Input pulse and its Fourier transform

which suggests that conventional shell theory (I) may not apply, in view of the inequality (3-1).

A similar calculation for the thick-walled aluminum test cylinder (h = .25 inches) gives

$$\omega_s = 1.53 \times 10^6 \text{ rad/sec}$$

and

$$0 \leq \omega \leq .8\ \omega_s \tag{3-9}$$

which clearly exceeds the bounds of the inequality (3-1) given by Ref. 14 for conventional shell theory (I).

However, it appears that the frequency bounds (3-1) and (3-3) given by Reference 14 are somewhat conservative. For example, it is possible to exceed these bounds (for transient loadings) and still obtain adequate solutions for the radial displacement, w(x,t). In such cases, conventional theory (I) may correctly predict the displacements but not the accelerations (and/or strains), which involve derivatives of the displacement. A thorough discussion of this point and the limitations of shell theory (I and II) is given in Ref. 17.

It should be noted that the thickness-shear frequency (ω_s) given in Equation (3-2) is directly related to the time required for a shear wave to propagate through the thickness of the shell. That is,

$$T_s = \frac{2\pi}{\omega_s} = \frac{2h}{c_s} \tag{3-10}$$

is the travel time for a wave (having speed c_s) to propagate a distance 2h (round trip). For the cylindrical shells which were tested, Equation (3-10) gives

$$T_s = 1.65\ \mu\text{sec} \qquad \text{(for h = .1 inch)}$$

and

$$T_s = 4.1\ \mu\text{sec} \qquad \text{(for h = .25 inch)}$$

These travel times are significantly less than the duration of the input force pulse ($T \approx 10$ μsec) and indicate that wave propagation through the thickness of the shell is much less important than wave propagation along the length of the shell. This gives additional evidence to support the conclusion that shell theory will adequately describe the observed experimental response, and that it is not necessary to use elasticity theory (III) in the analysis.

With this preliminary discussion as a background, the next section describes the tests on a thin-walled aluminum shell and the corresponding holographic measurements.

Experimental Set-Up and Test Procedure

Test Specimens - The shell specimens used in these experiments were sections of seamless aluminum tubing, which is available commercially. The tubing was cut to the nominal length of 24 inches and was of approximately 10 inches in diameter. Two wall thicknesses were used, namely

$h \cong .1$ inch (referred to as the "thin" shell)

and

$h \cong .25$ inch (referred to as the "thick" shell)

The wall thickness and the inside diameter of the thin shell were carefully measured at several locations around the circumference. These measurements are summarized in Table I.

TABLE I

Geometry of Thin-Walled Cylinder

Average wall thickness,	$h = 0.1060$ inches
Maximum deviation in wall thickness,	$\Delta h = 0.0053$ inches
Per cent deviation in wall thickness,	$\frac{\Delta h}{h} = 5\%$
Average inside diameter,	$D_i = 9.807$ inches
Maximum variation in diameter	$\Delta D = 0.080$ inches
Per cent variation in diameter	$\frac{\Delta D}{D_i} = 0.82\%$
Average radius to the mid-surface	$R = \frac{D_i}{2} + \frac{h}{2} = 4.957$ in
Radius/thickness ratio	$R/h = 46.8$

The shell specimen was supported by a heavy steel ring which was pressed into the left end of the shell. (A photograph of the thin shell specimen is given in Figure 5). The steel end rings were used to simulate a clamped boundary condition ($w = 0$, $\frac{\partial w}{\partial x} = 0$, $u = 0$) at the ends of the shell. For some tests, the right-hand ring was

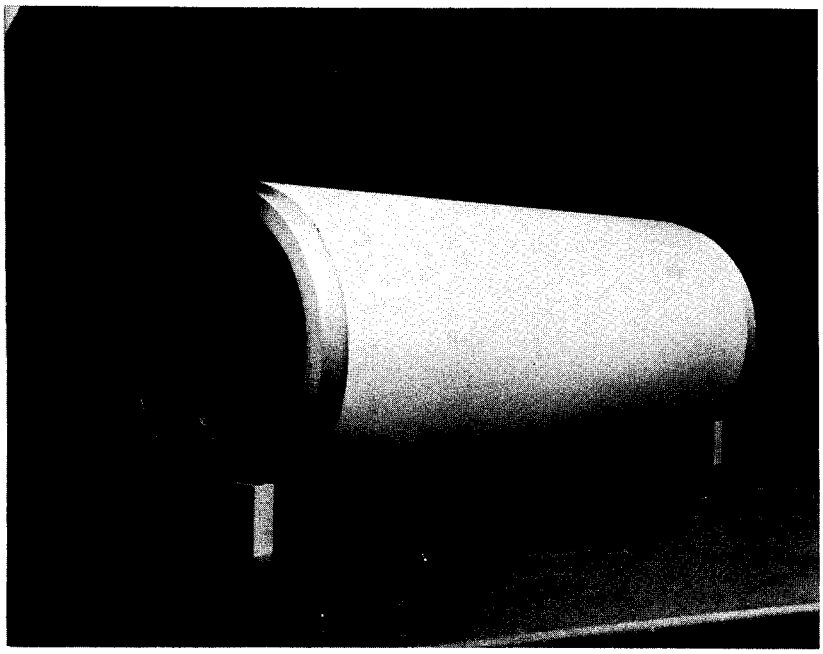

(a) Actual Specimen

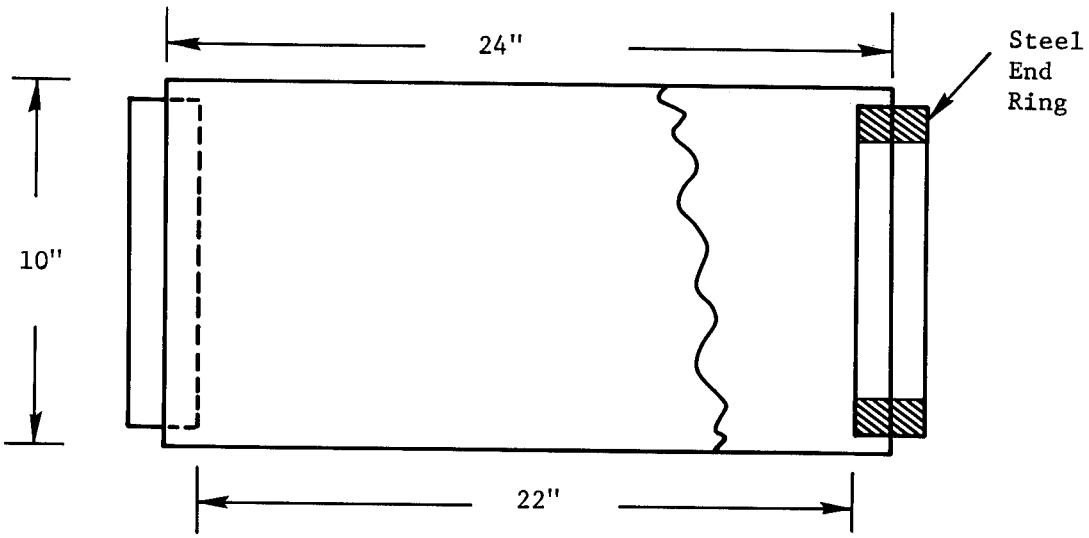

(b) Schematic Diagram

Figure 5: Aluminum Shell Specimen

removed to provide a stress-free boundary. The impulsive load was applied midway along the length of the shell (see Figure 2). A discussion of the applied load is given in the section which follows.

The Applied Loading - The load applied to the shell was subject to the following design constraints:

(1) The load had to be repeatable, so that the same forcing function could be applied several times.

(2) The timing had to be precise (i.e., to within a micro-second) so that the laser firing could be properly controlled.

(3) The load had to be concentrated in space and of short duration in time.

(4) The load should excite axi-symmetric waves, for comparison with available analyses.

The method selected to meet these criteria involved using a repelling wire technique, which is described in detail in Appendix A.

The technique relies on the fact that two parallel wires which carry current exert an electromagnetic force on each other. By sending a large surge of current through two concentric loops of wire, the outer wire was driven radially outward to exert a force pulse on the inside of the cylindrical shell.

The force on the shell can be described (approximately) by a band of pressure that is

- uniform in the axial direction (x) with a length of $\frac{1}{4}$ inch
- nearly uniform around the circumference (θ),
- of short duration in time, on the order of 10 μsec

Mathematically, the band of pressure $p(x,\theta,t)$ is approximated by

$$p(x,\theta,t) = A \sin^2 \frac{\pi t}{T}$$

within the domain

$$-\varepsilon \leq x \leq \varepsilon$$

$$0 \leq \theta \leq 2\pi$$

$$0 \leq t \leq T$$

and zero elsewhere. The value of the constant ε is 1/8 of an inch, and the load duration T is approximately 10 μs. A more detailed discussion of the applied loading is given in Appendix A.

Optical Arrangement for Recording Holograms - The optical arrangement (shown schematically in Figure 6) was used to record the double-exposure holograms. The actual equipment used in the experiments is shown in Figure 7. The equipment and optical set-up are standard for pulsed-laser holography (e.g., see Ref. 7).

Timing of the Laser Pulse(s) - The holograms were made by first firing the laser to record the static, underformed position of the shell and then firing the laser a second time to record the wave propagation event. The initial, first pulse of the laser (first exposure) presented no problems and was readily accomplished. The second laser pulse (second exposure) had to be synchronized with respect to the loading of the shell. The timing was accomplished electronically, using well-established techniques (Refs. 7, 8).

An inductive loop near the capacitor bank provided the timing signal to mark the beginning of the repelling-wire loading pulse. This timing signal was used as the input to the adjustable time-delay circuit of an oscilloscope. The output signal from the oscilloscope was used to control the laser pulse, by means of the Pockels cell within the laser cavity. This arrangement allowed the experimenter to initiate the waves in the shell (by firing the repelling-wire circuit) and then to record the deformation at a desired time later (i.e., at time t = 5 μs, 10 μs, 50 μs, etc.) by means of the laser pulse. The separation in time was obtained by adjusting a potentiometer on the oscilloscope. Since the pot settings provide only a nominal estimate of the time-delay, the timing signal (from the repelling-wire circuit) and the light pulse (which was sensed by a fast photodiode) were recorded simultaneously on an oscilloscope trace. This trace provided an accurate measurement of the timing.

Test Procedure - Once the experiment was arranged and the electronic timing established, the test procedure was straightforward, as follows:

(1) The hologram was placed in position and the laser fired to give the first exposure.

(2) The capacitors for the repelling-wire circuit were charged to the desired voltage.

(3) The oscilloscope time-delay was set to the desired value (e.g., 50 μs)

(4) The repelling-wire circuit was fired, which initiated the timing sequence and resulted in the second exposure of the hologram.

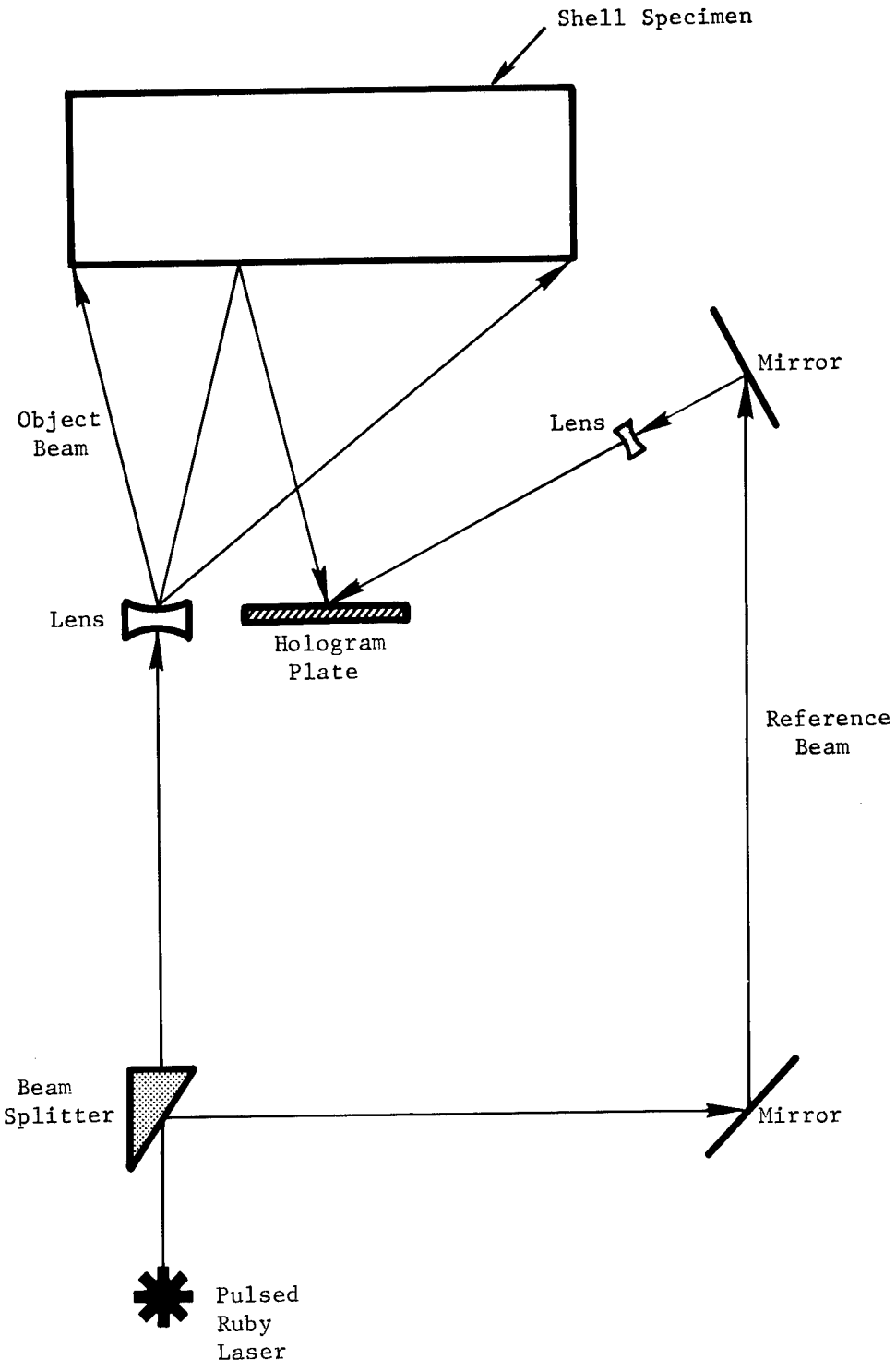

Figure 6: Schematic diagram of the holographic set-up

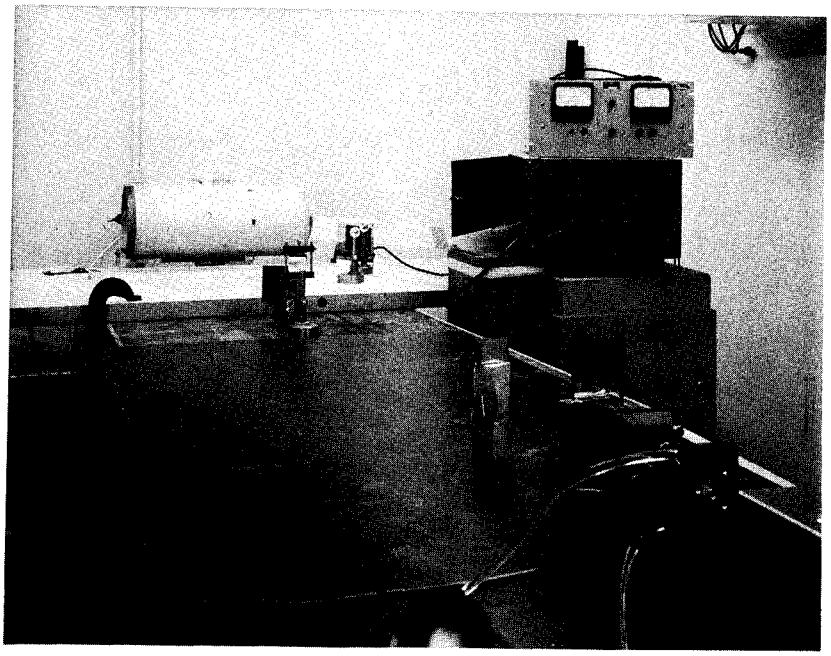

Figure 7: Experimental Set-up and Optical Arrangement

Typical holograms and results obtained in this fashion are discussed in the pages which follow.

Typical Results for the Thin-Walled Cylinder

Demonstration of Repeatability - Holograms were recorded at several different time-delays, which showed the waves at various distances along the shell. To record the waves at times t = 5μs, 10 μs, etc. required a separate experiment for each time. That is, the shell was loaded once and a hologram recorded at t = 5 μs; then the shell was loaded again and another hologram made at t = 10 μs, and so forth.

For purposes of understanding the wave propagation phenomena, it is desirable to relate the results obtained from several experiments (at individual times t_i, where i = 1,2,3,...N) to a single experiment (in which data is obtained at various times t_i).

In particular, the assumption is made that the holograms obtained from several separate experiments are equivalent to making several holograms in rapid succession on a single experiment. This assumption is akin to the "ergodic hypothesis" in random process theory (See Ref. 18, for example) in which statistics obtained from a single record (in time) are related to several similar records (the ensemble).

If the experiment is completely deterministic, and contains no random behavior, then holograms obtained from separate tests but at the same time-delay (say t = 50 μs) will show identical fringe patterns. Such behavior is indicated in Figure 8, which shows the results of three tests, all run for the same loading input and the same time-delay. The fact that these fringe patterns (Figure 8) are virtually identical demonstrates the repeatability of the experiment and serves to justify the equivalence assumption just discussed.

Determination of Radial Displacements from the Interferograms - Figures 9 through 11 show interferograms obtained at the times t = 5 μs, 10 μs, and 20 μs after initiation of the impulse. The corresponding curves of radial displacement (w) versus x (the distance along the shell length, measured from the plane of loading) are given in Figure 12. In order to understand how the data points in Figure 12 were obtained from the photographs, it is first necessary to discuss the equations relating the shell displacements and the interference fringes.

The general relationship between a displacement field and the corresponding holographic fringe pattern has been examined by several authors (e.g., Refs. 5 and 19). In particular, Reference 19 shows that the reconstructed image of a hologram exposed twice to a body which has deformed between exposures will exhibit dark fringes on parts of the body wherever the condition

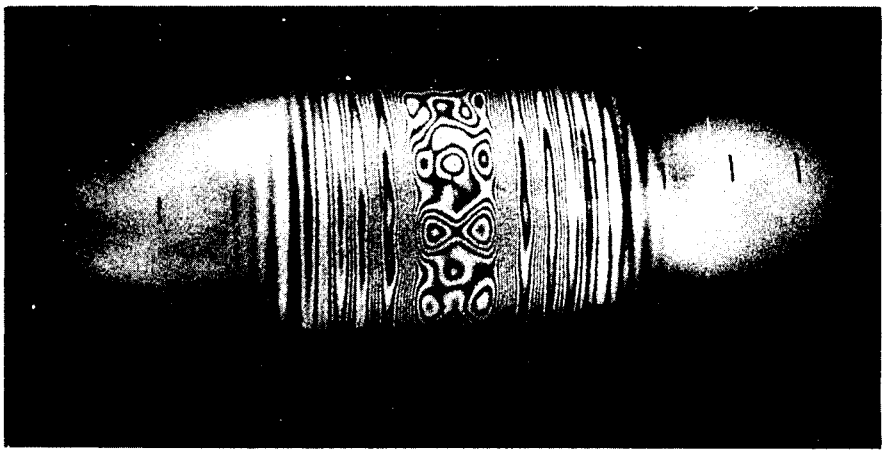

Figure 8(a): Interferogram Showing Waves at 5 = 50.5 μsec (Shot Number 2)

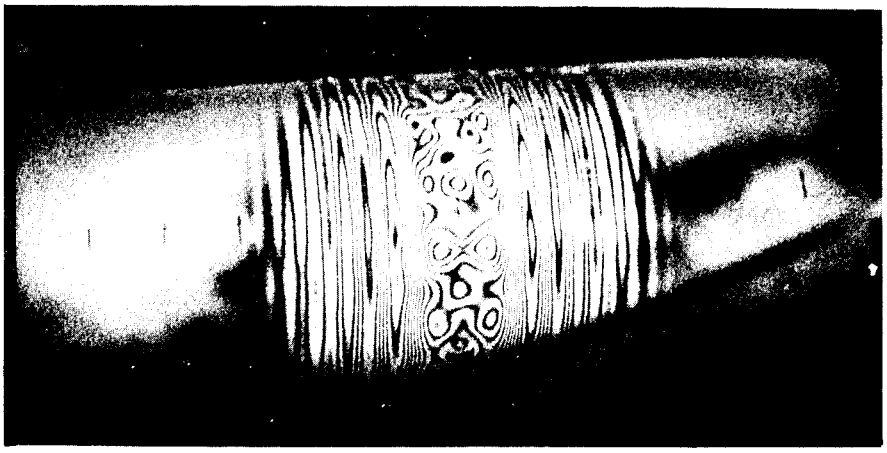

Figure 8(b): Interferogram Showing Waves at t = 50 μsec (Shot Number 3)

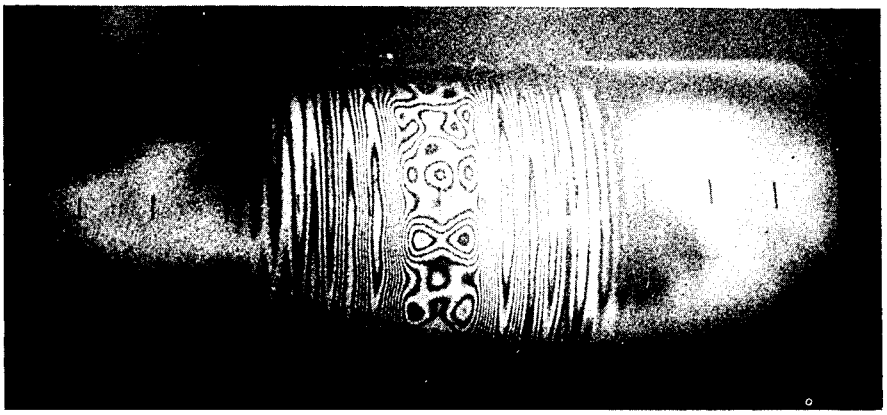

Figure 8(c): Interferogram Showing Waves at t = 50 μsec (Shot Number 8)

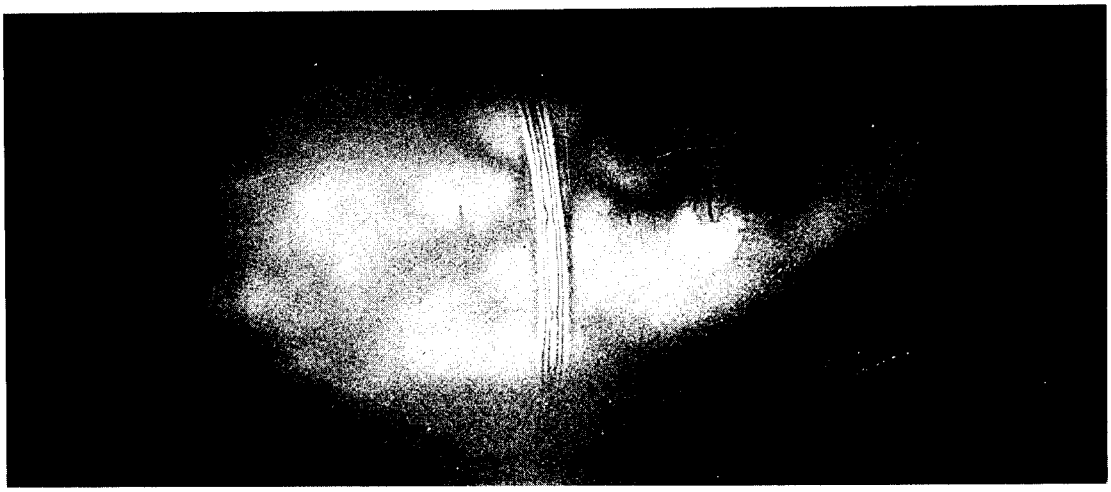

Figure 9: Interferogram Showing Waves in Thin Shells at t = 5 μsec

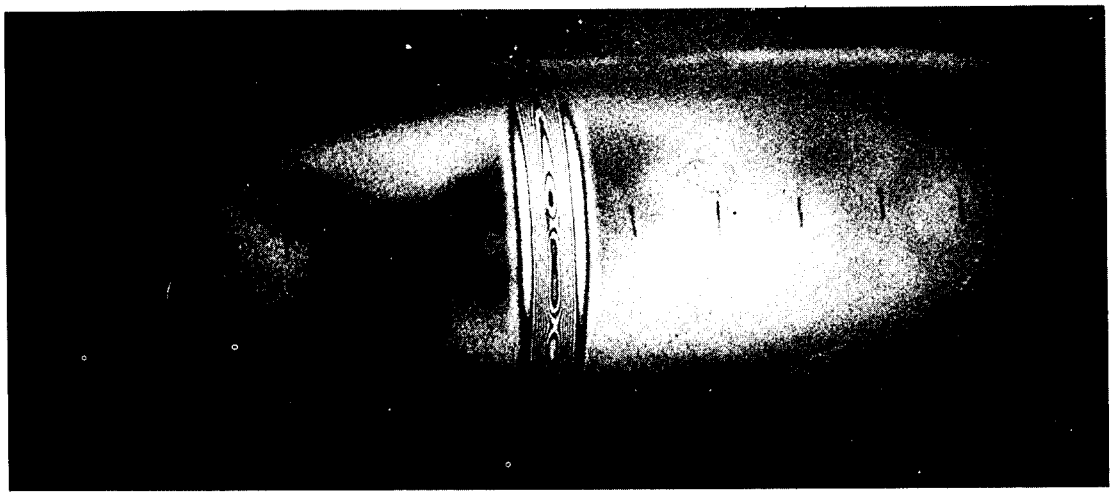

Figure 10: Interferogram Showing Waves in Thin Shell at t = 10 μsec

Figure 11: Interferogram Showing Waves in Thin Shell at t = 20 μsec

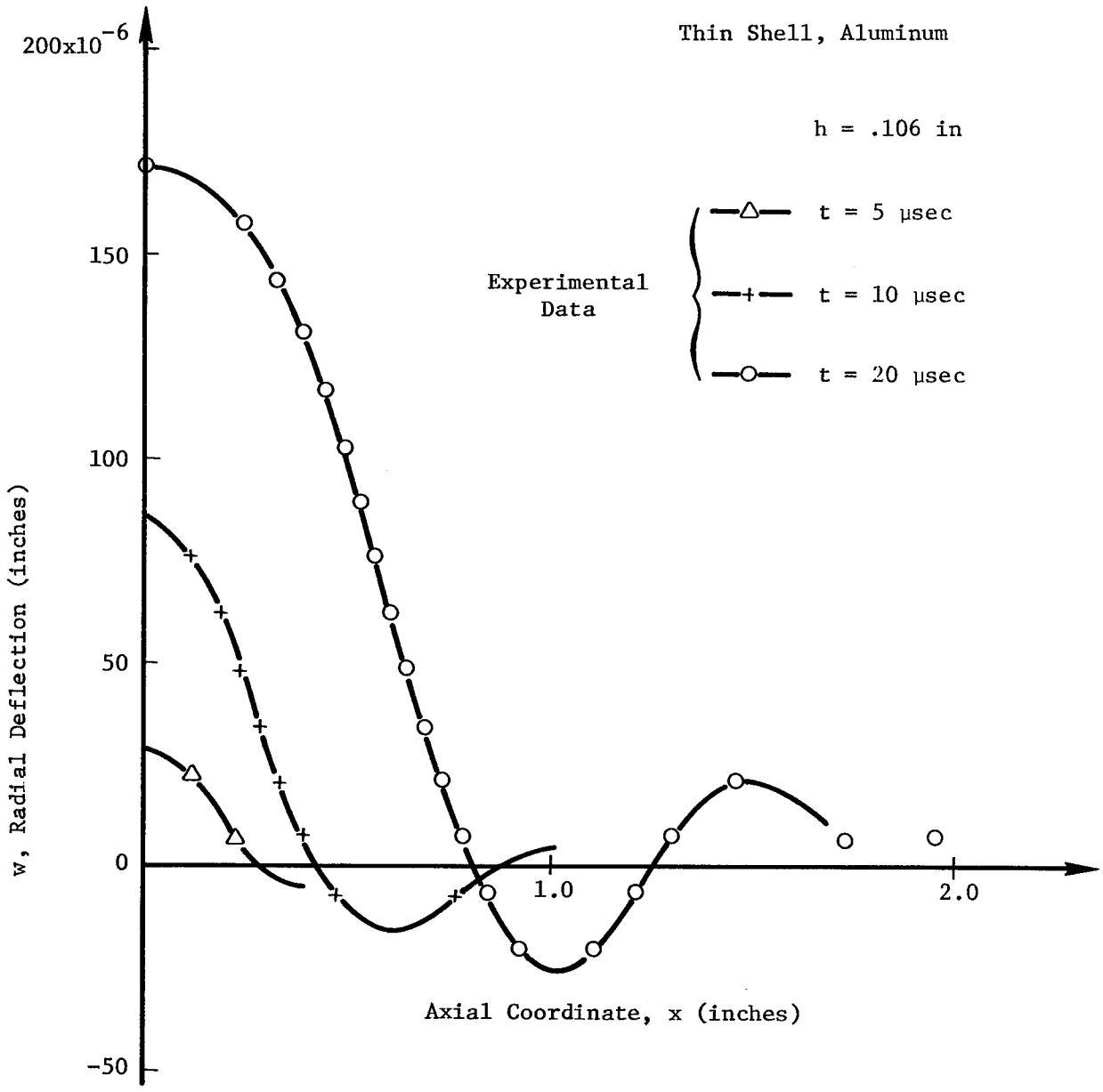

Figure 12: Radial Deflection Along the Shell

$$\vec{\delta} \cdot (\vec{n}_i + \vec{n}_v) = \frac{(2n \pm 1)\lambda}{2} \qquad (3\text{-}11)$$

is satisfied; where

$\vec{\delta}$ = the displacement vector

λ = wavelength of the light from the laser used to make and reconstruct the holographic images

$\vec{n}_i$ = unit vector in the direction from the object to the illuminating source

$\vec{n}_v$ = unit vector in the direction of view, from the object through the hologram to the observer

n = integer, the fringe order, ± 1, ± 2, ± 3, etc.

The term $\vec{\delta} \cdot (\vec{n}_i + \vec{n}_v)$ is illustrated by the vector diagram shown in Figure 13. The term $(\vec{n}_i + \vec{n}_v)$ is a vector sum, and it is represented by a vector which lies in the plane containing $\vec{n}_i$ and $\vec{n}_v$ and bisects the angle between them. The magnitude of this vector sum is $2 \cos \frac{1}{2}(\vec{n}_i, \vec{n}_v)$, where $(\vec{n}_i, \vec{n}_v)$ is the angle which is bisected. Finally, the dot product $\vec{\delta} \cdot (\vec{n}_i + \vec{n}_v)$ is the projection of the displacement vector $\vec{\delta}$ in the direction of $(\vec{n}_i + \vec{n}_v)$, as shown in Figure 13.

A particular case of Equation (3-11) which often occurs in transverse wave propagation problems is illustrated in Figure 14. Referring to Figure 14, the structure of interest (in our case, the circular shell) lies with its axis in the horizontal plane. The angle θ is measured positive clockwise from the horizontal plane as shown in Figure 14. A general displacement, $\vec{\delta}$, of the shell surface is represented by

$$\vec{\delta} = u\,\vec{e}_x + v\,\vec{e}_\theta + w\,\vec{e}_r$$

where $\vec{e}_x$, $\vec{e}_\theta$, and $\vec{e}_r$ represent unit base vectors, and u, v, w are the corresponding displacements, in the (x, θ, r) directions, respectively. The illumination and viewing vectors are given (in Cartesian co-ordinates) by

$$\vec{n}_i = n_{ix}\,\vec{e}_x + n_{iy}\,\vec{e}_y$$

$$\vec{n}_v = n_{vx}\,\vec{e}_x + n_{vy}\,\vec{e}_y$$

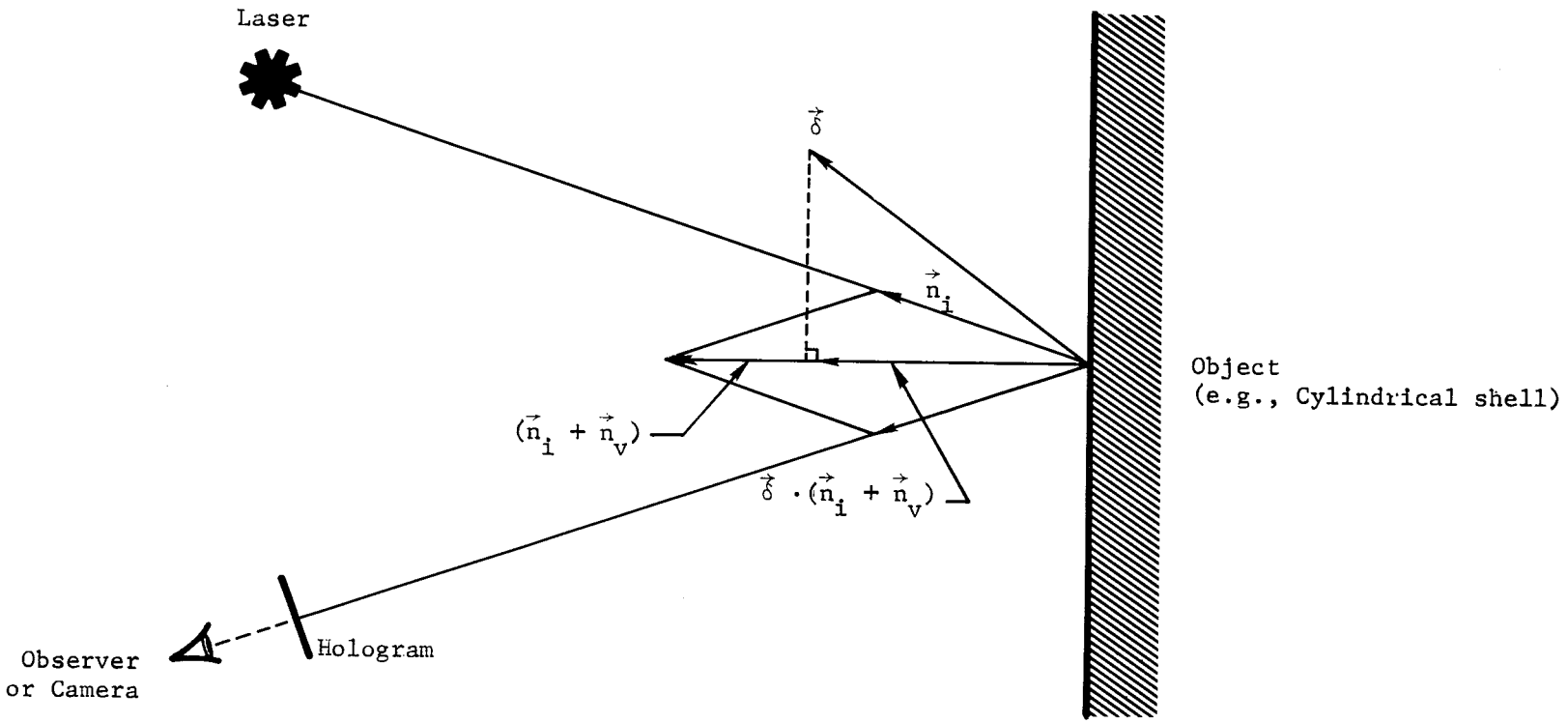

Figure 13: Vector diagram showing the illuminating and viewing directions, with the displacement $\vec{\delta}$ between exposures.

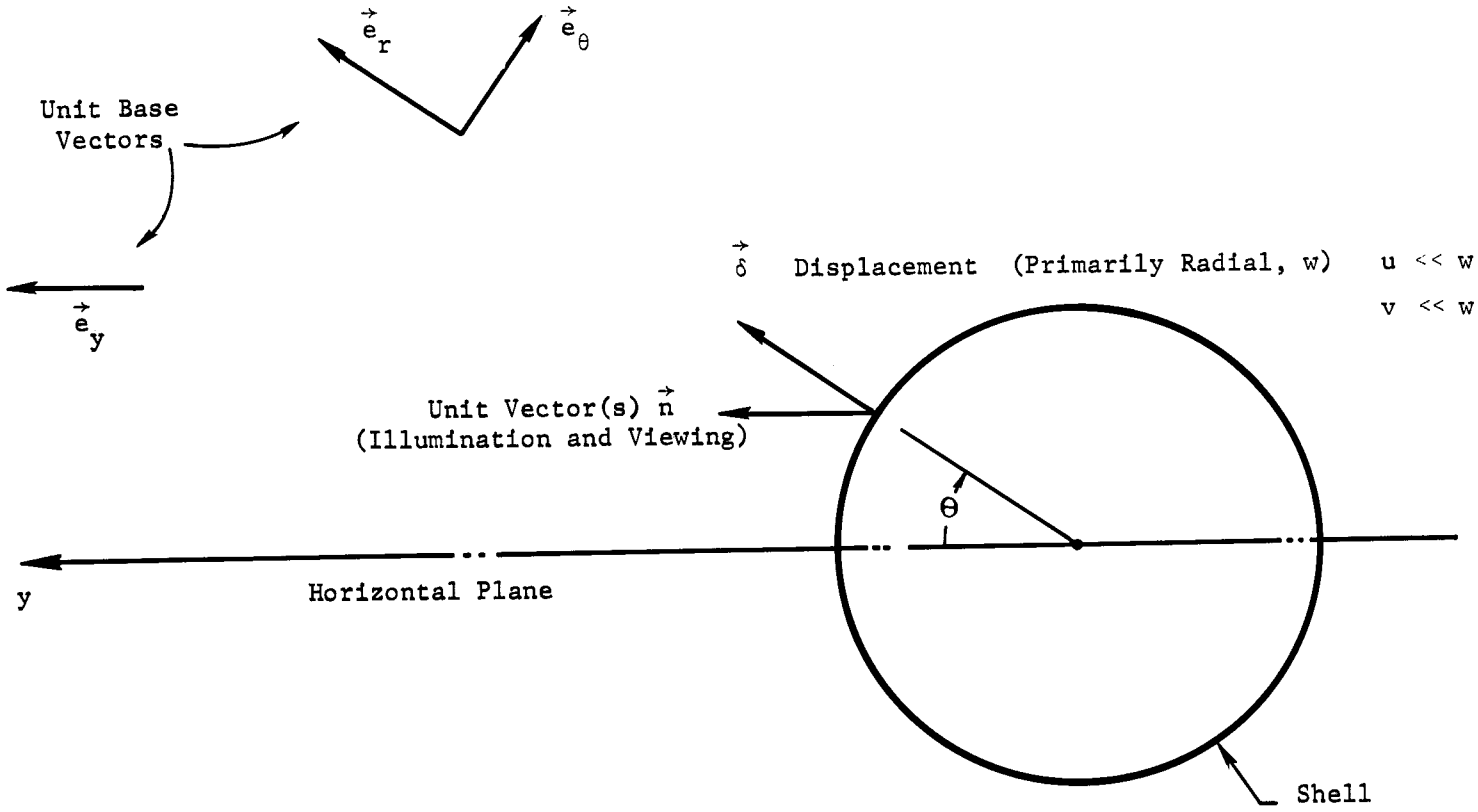

Figure 14: Horizontal plane, radial displacement, and unit vector(s) for analyzing the interferograms.

where $\vec{e}_x$ is the same unit vector (along the axis of the shell) and $\vec{e}_y$ is a unit vector in the (horizontal) x-y plane. The relationship between $\vec{e}_y$ and $\vec{e}_r$, $\vec{e}_\theta$ is

$$\vec{e}_y = \vec{e}_r \cos\theta - \vec{e}_\theta \sin\theta$$

Forming the dot product $\vec{\delta} \cdot (\vec{n}_i + \vec{n}_v)$ gives

$$\begin{aligned}\vec{\delta} \cdot (\vec{n}_i + \vec{n}_v) = u(n_{ix} + n_{vx}) \\ - v \sin\theta(n_{iy} + n_{vy}) \\ + w \cos\theta(n_{iy} + n_{vy})\end{aligned} \qquad (3\text{-}12)$$

At this point, it is convenient to introduce two engineering approximations:

(i) For transverse wave propagation, involving primarily flexural motions, calculations (as well as previous experiments) show that the radial deformation is predominant:

That is,

$$u << w$$

$$v << w$$

(ii) In setting up the holographic experiment, it is often possible to locate the illumination and viewing points such that the vectors $\vec{n}_i$ and $\vec{n}_v$ are nearly perpendicular to the x-axis: That is

$$n_{ix} << n_{iy}$$

$$n_{vx} << n_{vy}$$

the vectors $\vec{n}_i$ and $\vec{n}_v$ are nearly parallel to $\vec{e}_y$.

Under these conditions, Equation (3-12) is well-approximated by

$$\vec{\delta} \cdot (\vec{n}_i + \vec{n}_v) \cong w \cos\theta (n_{iy} + n_{vy})$$

or

$$\vec{\delta} \cdot (\vec{n}_i + \vec{n}_v) \cong 2\, w \cos\theta$$

Since the components n_{iy} and n_{vy} are approximately unity. Thus, we have (from Equations 3-11 and 3-12)

$$\vec{\delta} \cdot (\vec{n}_i + \vec{n}_v) = \frac{(2n \pm 1)\lambda}{2} \cong 2\, w \cos\theta$$

or

$$w \cong \frac{(2n \pm 1)\lambda}{4 \cos\theta} \qquad (3\text{-}13)$$

The most direct approach to reducing the holographic fringe data is to apply Equation (3-13) along the horizontal plane (i.e., centerline) through the shell (where $\theta = 0$). Then Equation (3-13) gives

$$w \cong \frac{(2n \pm 1)\lambda}{4} \qquad (3\text{-}14)$$

for the radial deflection, w.

In order to apply the preceding equations and obtain quantitative data, it is necessary to determine the fringe order, n, corresponding to each fringe seen in the reconstructed interferograms (Figures 8 through 11). The assignment of fringe order requires some engineering judgment and was influenced by the following considerations:

(a) In response to the applied loading (which acts radially outward) the portion of the shell directly over the load will initially move outward, in the radial direction. It is expected that the maximum radial deflection will occur at the plane of loading at least for the first few holograms (which record the initial response).

(b) Ahead of the wavefront, where no fringes appear, the deflection of the shell is known to be "zero", which provides a reference level. (More precisely, the absence of a fringe in the "undisturbed" region ahead of the wave indicates that the deflection there is less than one-quarter of a wavelength of the laser light.)

(c) From previous experience with wave propagation phenomena (e.g., waves in beams, plates, etc.), it is expected that the deflections will describe a series of ripples or undulations which are alternately up and down. That is, the shell surface will be a series of hills and valleys (as a function of the longitudinal coordinate, x) much like a damped sine wave.

As an example of the data reduction process, consider Figure 10, ($t = 10$ μs). Starting at the center of the fringe pattern (i.e., at $x = 0$) and proceeding toward the right half of the photo, the interference fringes indicate a central "hill" and then a slope downward to the right. (The interference fringes may be regarded as contour lines on a topographic map. The closely-spaced fringes for $x > 0$ indicate that the deflection surface slopes downward to the right in that region.) Continuing to the right, the photograph shows a wide white area followed by a heavy, dark fringe. Close examination of the dark fringe (on the right) shows that it merges with the adjacent fringe (on the left) near the top and bottom of the shell (i.e., near $\theta = \pm 90°$). The merging of adjacent fringes at the extremes of the shell is due to the "$\cos\theta$ effect" described mathematically in equation (3-13).

The fact that the two fringes coincide near $\theta = 90°$ indicates that these fringes have the same fringe order, n. The wide spacing between the two fringes at $\theta = 0$ suggests that they represent opposite sides of a "valley" in the deflection curve. To the right of this valley, no additional fringes are evident, which indicates a lack of deformation in this region. If we now retrace our steps and move from right to left across the fringe pattern, we conclude that the heavy dark fringe (on the right) has a fringe order $n = -1$, which corresponds to a radial displacement $w = -\lambda/4$ (inward) at that point on the shell. Proceeding to the left (across the valley) we come to the "companion" fringe, which also has order $n = -1$ and deflection $w = -\lambda/4$ (inward). Continuing to the left, the fringe order increases monotonically ($n = 1,2,3,...$etc.) as we climb the hill in the deflection surface up to the crest.

Having thus identified the fringe order, the radial displacement can be computed at each fringe location using equation (3-14). In order to plot the displacement (as a function of x) the location of each fringe was determined by mechanical measurement on the photograph using a traveling microscope. The curves of radial displacement vs position shown in Figure 12 were obtained in this fashion.

Non-Symmetric Behavior

Initial Response - From a qualitative standpoint, the interferograms shown in Figures 9 through 11 exhibit two major trends:

(i) At the front of the wave, the interference fringes show only slight variation in the circumferential direction. Slight variations with θ are indicated by the "$\cos\theta$ effect" in equation (3-13) and indicate that the shell deformation is very nearly axisymmetric in the vicinity of the wavefront.

(ii) At the loading plane (i.e., x = 0) significant circumferential variation is indicated by the closed elliptical fringe contours. This non-symmetric response is evident even at the very early times (e.g., t = 5 μs), including the times when the loading occurs ($0 \leq t \leq 10$ μs).

Since the applied load (due to the repelling wire) did not extend fully around the circumference, it was expected that non-symmetric behavior would eventually occur. However, the "gap" in the loading would cause waves to propagate circumferentially and they are required to travel half way around the shell to reach the front side (at θ = 0). The travel time of these circumferential waves is given approximately by

$$t_1 = \frac{\pi R}{c_p} = \frac{\pi(5 \text{ in})}{.2 \text{ in}/\mu s} \approx 75 \ \mu\text{sec}$$

The fact that non-symmetric behavior occurs much sooner than this (e.g., at t = 10 μs) points out that the applied loading must contain slight local non-uniformities (in addition to the "gap" region just discussed).

Additional Results and a Computed Fringe Pattern - Additional results which exhibit significant non-symmetric behavior are the interferograms shown in Figures 15 and 16. Referring to Figure 15, (which was recorded at time t = 75 μs) the appearance of the closed, nearly-circular fringes and their repeated nature (around the circumference) suggest a radial deflection on the form

$$w(x,\theta) = A_o f_o(x) + A_k f_k(x) \cos k\theta \qquad (3\text{-}15)$$

Equation (3-15) represents an axisymmetric response combined with a non-symmetric mode. The value of the harmonic k and the relative amplitudes A_k and A_o are of interest. As a rough estimate, the functional form

$$w(x,\theta) = [A_o + A_k \cos k\theta] \cos\frac{2\pi x}{L} \qquad (3\text{-}16)$$

was used to approximate the response near the loading plane (x = 0).

Using the approximations discussed previously, we have (see Equation (3-13)

$$w = \frac{(2n-1)\lambda}{4 \cos\theta} \qquad (3\text{-}17)$$

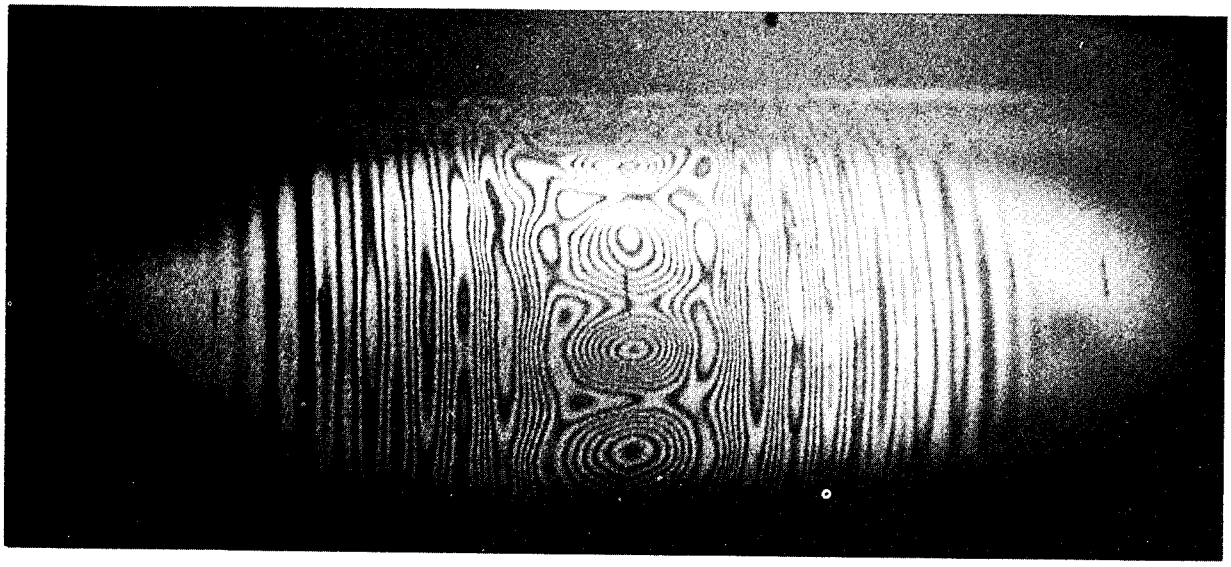

Figure 15: Interferogram Showing Waves in the Thin Shell at t = 75 μsec. (Note: Non-symmetric response, which involves cos k θ)

where θ is the circumferential coordinate. Combining equations (3-16) and (3-17) gives

$$A_o[1 + r\ \cos k\theta]\ \cos\frac{2\pi x}{L} = \frac{(2n-1)\lambda}{4\ \cos\theta} \qquad (3\text{-}18)$$

where $r = A_k/A_o$ is the ratio of amplitudes.

Equation (3-18) was solved numerically to give the fringe contours $x = x(\theta)$ for various values of n, the fringe order. The results are shown in Figure 17, where x/L is plotted vertically (for the range $0 \leq x/L \leq 1/4$) and θ is the abscissa ($0 \leq \theta \leq \pi/2$). The contour lines of Figure 17 vary from n = 1 (the outermost contour) to n = 10 (a single point at x = 0, θ = 0). Figure 17 was calculated for k = 12, $A_o = 12(\lambda/4)$, and $A_k = 7(\lambda/4)$ and was meant to correspond with the interferogram of Figure 15. Thus, the closed, circular contours of this interferogram suggest the presence of cos(12θ) in the shell response.

Displacement Curves - Figure 16 (recorded at t = 99 μs) shows non-symmetric behavior, which is also thought to involve cos(12θ). The shell response at these later times is clearly two-dimensional, involving variations in both the longitudinal (x) and circumferential (θ) directions. A complete description of the experimental data would involve longitudinal

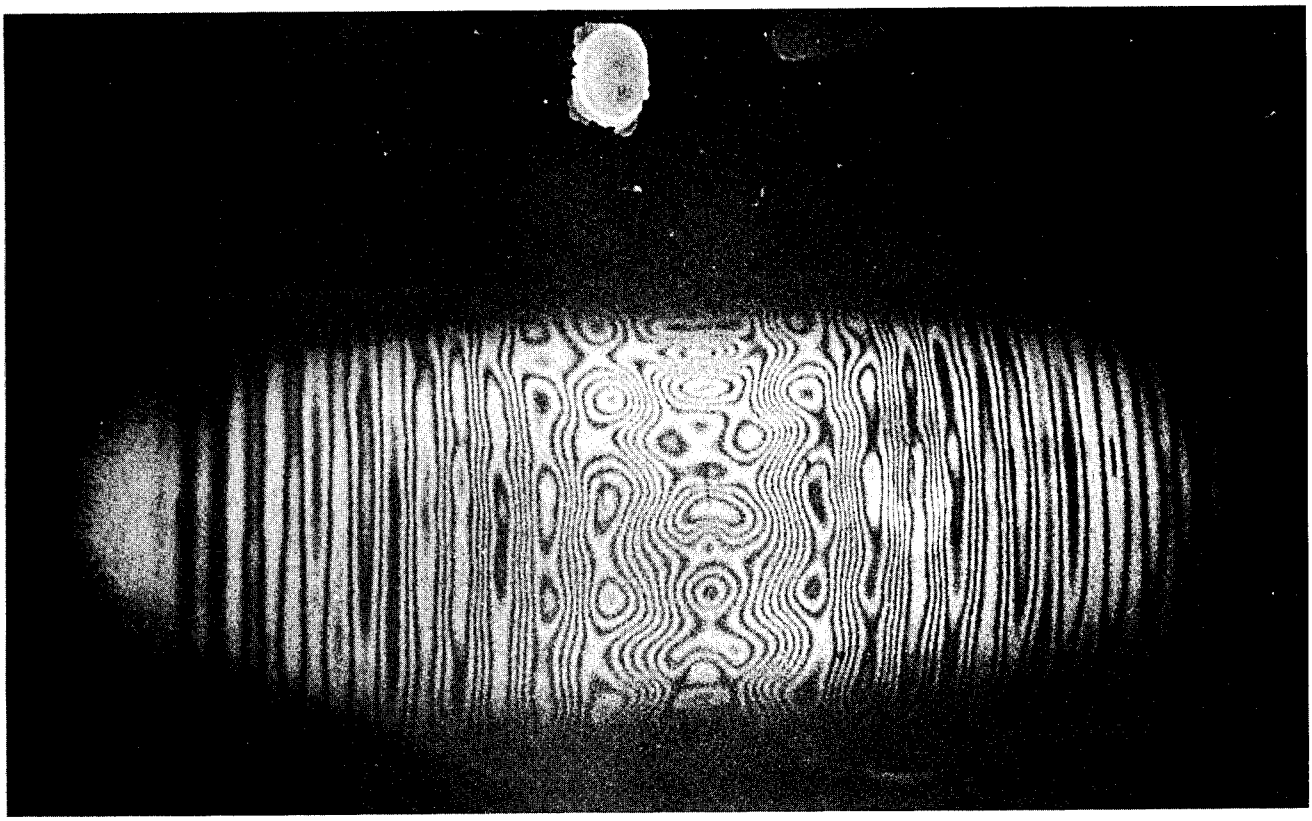

Figure 16: Interferogram showing waves in the thin shell at t = 99 μsec. (Note: non-symmetric response, which involves cos k θ.)

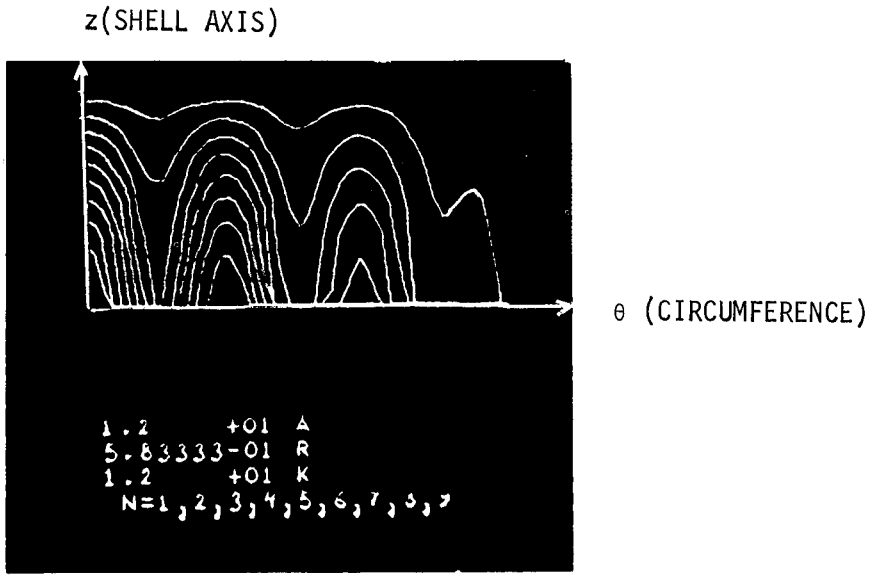

Figure 17: Computer-Generated Fringe Pattern
(See Equation 3-18)

traverses ("cuts" at constant θ) as well as circumferential (cuts at constant x). This detailed description of non-symmetric responses is a formidable task in data reduction and was not attempted. Representative plots of the radial displacement vs. x are shown in Figures 18 and 19, which were obtained by interpreting the fringes along the centerline ($\theta = 0$). The experimental data shown in these figures is typical of flexural waves propagating along the shell in the x-direction. (See Appendix B.)

The reader will note that the data points (see Figure 18) give a good definition of the shell behavior near $x = 0$, where several fringes occur within one structural wavelength of the deformation. Near the front of the wave, however, the wave amplitude is reduced, and only one or two fringes occur to characterize the deformation. Thus, for these later times, the oscillations near the front of the wave are not well-defined by the experimental data. This lack of definition at the wavefront can be overcome by increasing the impulse to the shell, i.e., causing an increase in the structural response. Increasing the shell response will lead to other problems, however, such as very high fringe density and possible lack of resolution near the plane of the loading ($x = 0$). The repelling wire loading device was designed using preliminary estimates for the shell behavior, and consequently it was not capable of producing large-amplitude response near the wavefront.

Dynamic Stability of the Axi-symmetric Response - Despite attempts to produce a nearly axisymmetric response of the shell, the experimental results show that the initial axisymmetric behavior is followed by waves propagating in non-symmetric modes (i.e., $\cos k\theta$). The fact that one of these circumferential harmonics predominates suggests that the axisymmetric response may be dynamically unstable. In other words, an axisymmetric response may (through non-linear coupling terms) excite non-symmetric waves in the shell. In this case, small non-symmetric perturbations will initially increase with time, as they extract energy from the symmetric response.

Structural behavior of this type (where a symmetric response becomes unstable and excites $\cos n\theta$ modes) is well-documented in many problems involving shells (see Ref. 20 , for example). A simple example of dynamic instability of this type was studied by McIvor (Ref. 21) with reference to circular rings. McIvor showed that a uniform radial impulse excites the axisymmetric, "ring mode," response and that the symmetric response in turn causes certain flexural modes (involving $\cos n\theta$) to participate in the motion. Stability studies such as Ref. 21 involve using non-linear equations for the shell, whereas virtually all analyses to date for wave propagation in shells use linear theory (e.g. Refs. 17 , 22, and 23).

From a practical standpoint, the observation of significant non-symmetric behavior indicates that

(a) Calculations of axisymmetric wave propagation behavior in shells are rather idealized,

(b) Considerable care must be exercised in such wave propagation experiments to eliminate circumferential variations in the structure and its loading, and

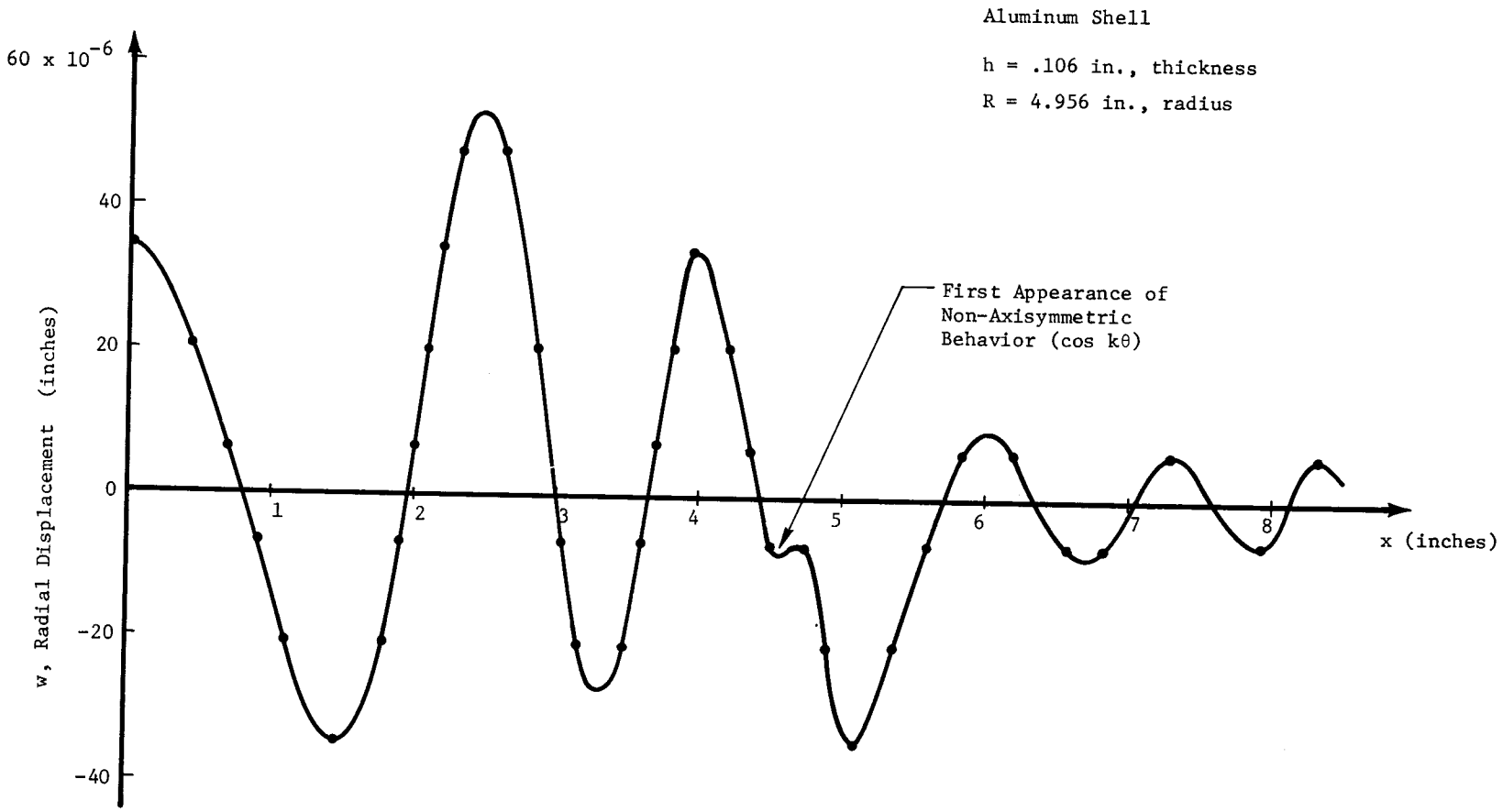

Figure 18: Radial Displacement, w, vs. Axial Position, x (time, t = 75 μsec)

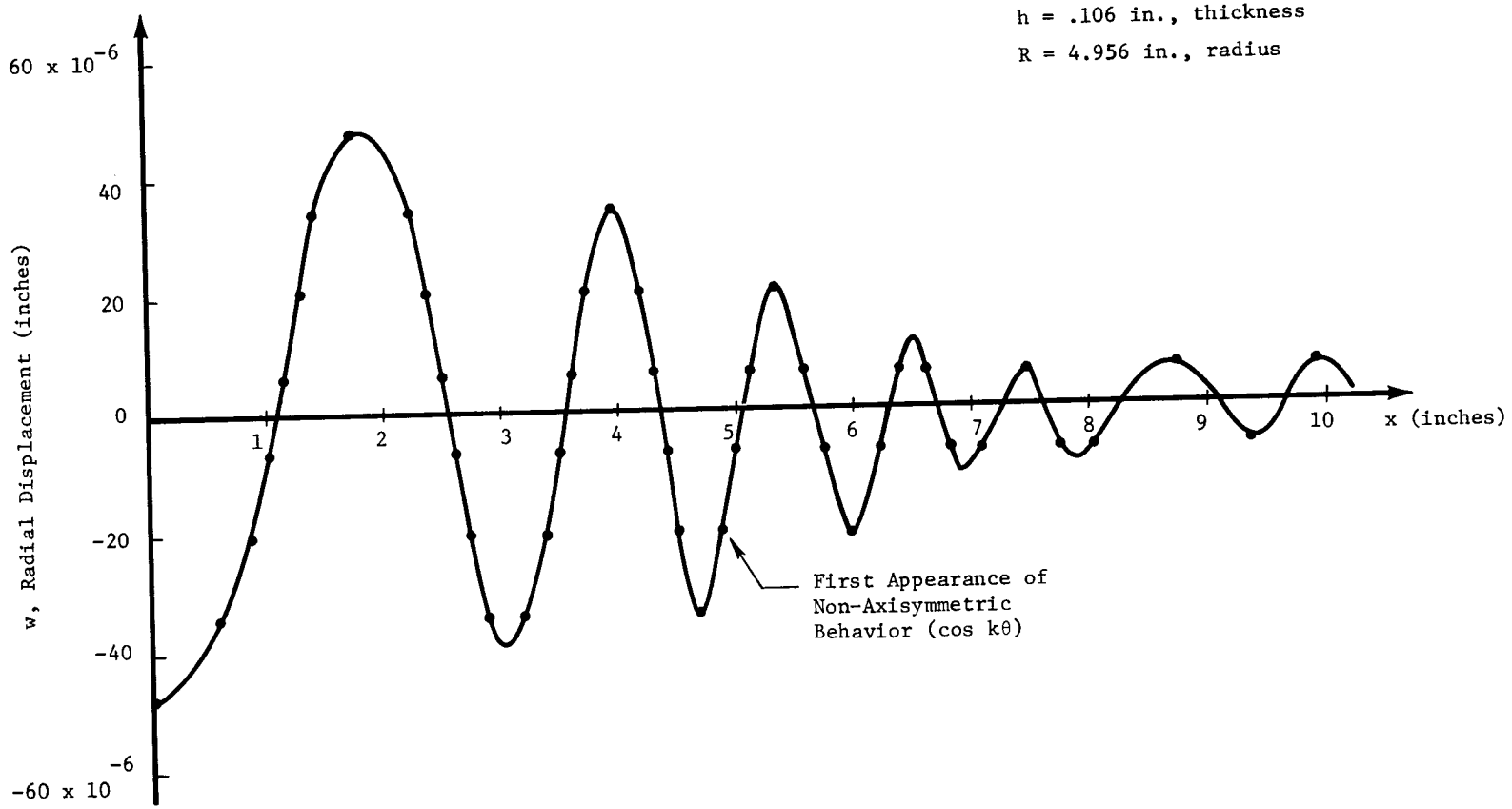

Figure 19: Radial Displacement, w, vs. Axial Position, x (time, t = 99 μsec)

(c) Analytical studies concerning the dynamic stability of an axisymmetric wave might be a fruitful topic for further research.

Waves Reflecting from the Ends of the Shell

Background - This section deals with the propagation of transverse waves toward the ends of the shell, and the subsequent reflection of the wave(s) from the shell boundaries. The characteristics of the reflected wave depend upon the boundary conditions at the ends of the shell. Three different boundary conditions were used, which will be referred to as (i) "clamped", (ii) "free" , and (iii) "simply-supported." These generic terms correspond to three distinct, idealized boundary conditions commonly applied in theoretical studies of shell dynamics.

The problem of an axi-symmetric wave reflecting from an axi-symmetric boundary is more readily analyzed than wave reflections which have a general, non-symmetric character. Thus, it was desired to generate an axi-symmetric wave experimentally for comparisons with analysis. However, the previous test results (c.f., Figure 15) had shown that axi-symmetric behavior occurred primarily near the front of the wave, followed by pronounced non-symmetric response. In order to keep the reflections "as axi-symmetric as possible," the loading device was moved to a location near the boundary being studied.

This re-adjustment of the plane of load application had another beneficial effect, in that the propagating wave reached the boundary in a shorter time. For purposes of analysis, it is more convenient to have the loading plane near the shell boundary, thereby reducing the time necessary to compute the wave reflection (i.e., shorter computer "run times" are required). Despite this attempt to facilitate the analysis, it was not practical to compute the wave reflections. The reflection data presented in the next few paragraphs is typical of the experimental results for the three boundary conditions. It is anticipated that this data may eventually be compared with analysis when faster computer programs become available.

Reflection from a Clamped Boundary - The idealized, "clamped" boundary (used in analysis) is specified by the conditions

$$u = 0 \quad \text{(zero axial displacement)}$$

$$w = 0 \quad \text{(zero radial displacement)}$$

and

$$\frac{\partial w}{\partial x} = 0 \quad \text{(zero slope)}$$

which are applied at the end of the shell that is "clamped". These conditions of zero slope and displacement were simulated experimentally by inserting a large steel ring in the end of the aluminum shell (c.f., Figure 5).

The steel ring had a rectangular cross-section 1 inch deep and 2 inches wide, whereas the aluminum shell wall was approximately .1 inches thick. The outer diameter of the steel ring was a few thousandths of an inch greater than the inside diameter of the shell, and the ring was pressed into the shell (e.g., a force fit) to provide a well-restrained boundary.

The test procedure used was similar to that described previously, but the loading device was located at a distance of nine (9) inches from the left edge of the aluminum shell. The steel end ring was inserted approximately one (1) inch into the end of the shell, which resulted in a distance L = 8 inches from the plane of the loading to the "clamped" boundary.

A typical interferogram (taken at time t = 90 μsec) is shown in Figure 20. The corresponding radial deflection curve (along the line $\theta = 0$) is shown in Figure 21. Aluminum has a shear wave speed $c_s \approx .1$ inch/μsec, and at a time t = 90 μsec the transverse wavefront has propagated from the loading plane, to the "clamped" boundary, and is starting back toward the center of the shell. Several additional interferograms, which show the wave at various other times (before and after reflection) are given in Appendix C.

Reflections from a Free Edge - A series of interferograms were made to determine the reflection of a transverse wave from a free edge. The idealized boundary conditions that the edge be "stress-free" were well-satisfied in the experiments. Thin shell theory requires that

$$M_x = 0 \qquad \text{(moment - free)}$$

$$N_x = 0 \qquad \text{(zero axial stress)}$$

and

$$Q_x = 0 \qquad \text{(zero transverse shear)}$$

which can be related to the (more exact) boundary conditions of elasticity theory, namely that the surface tractions vanish:

$$T_i^{\nu} = \sigma_{ij}\,\nu_j = 0 \qquad \begin{matrix} i = 1,2,3 \\ j = 1,2,3 \end{matrix}$$

(see Ref. 24). The shell was cantilevered from its left end, and the right end was indeed "stress-free" in the experiment.

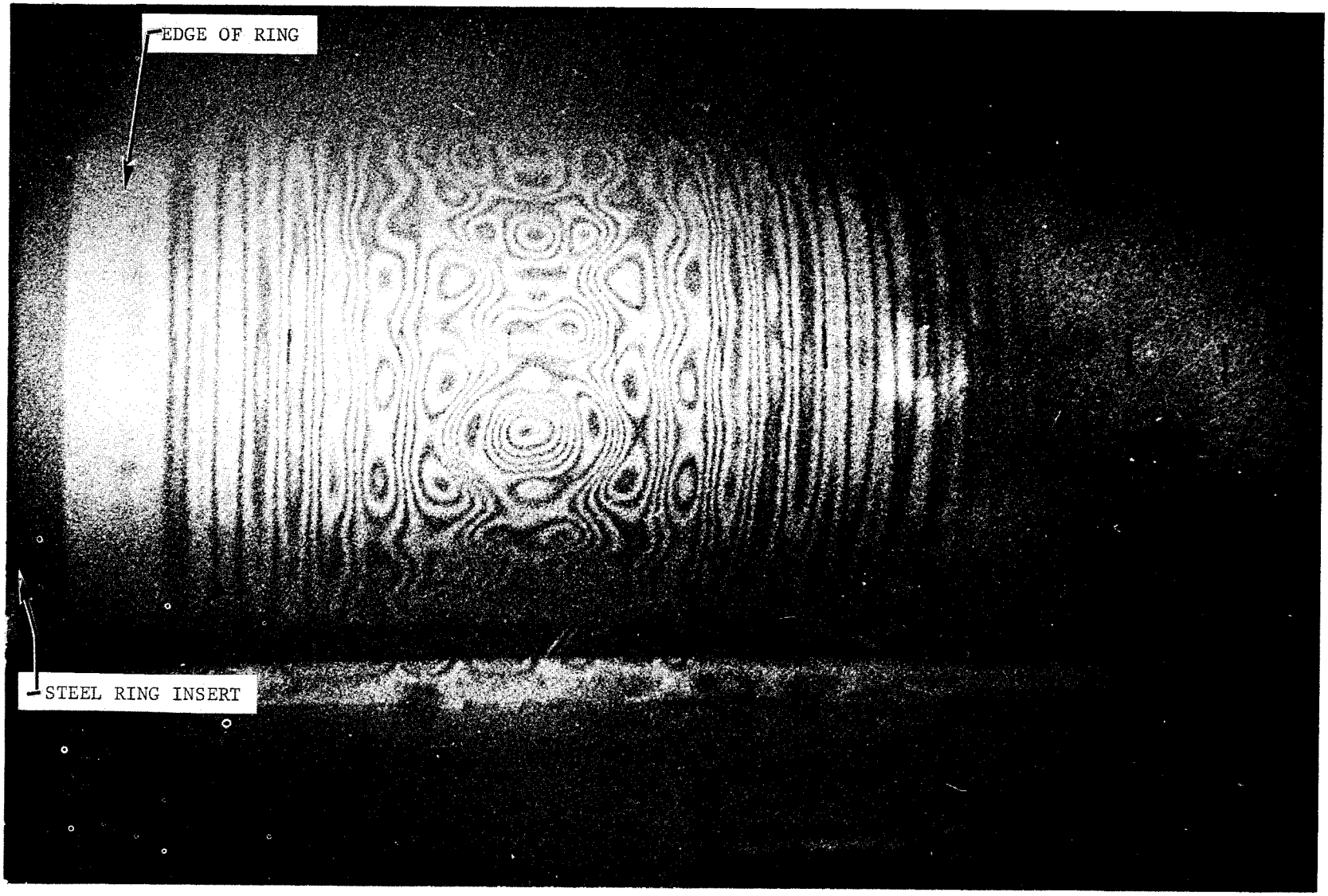

Figure 20: Wave interacting with a "clamped" boundary. (Steel ring is at the left of the shell. Time t = 90 μsec.)

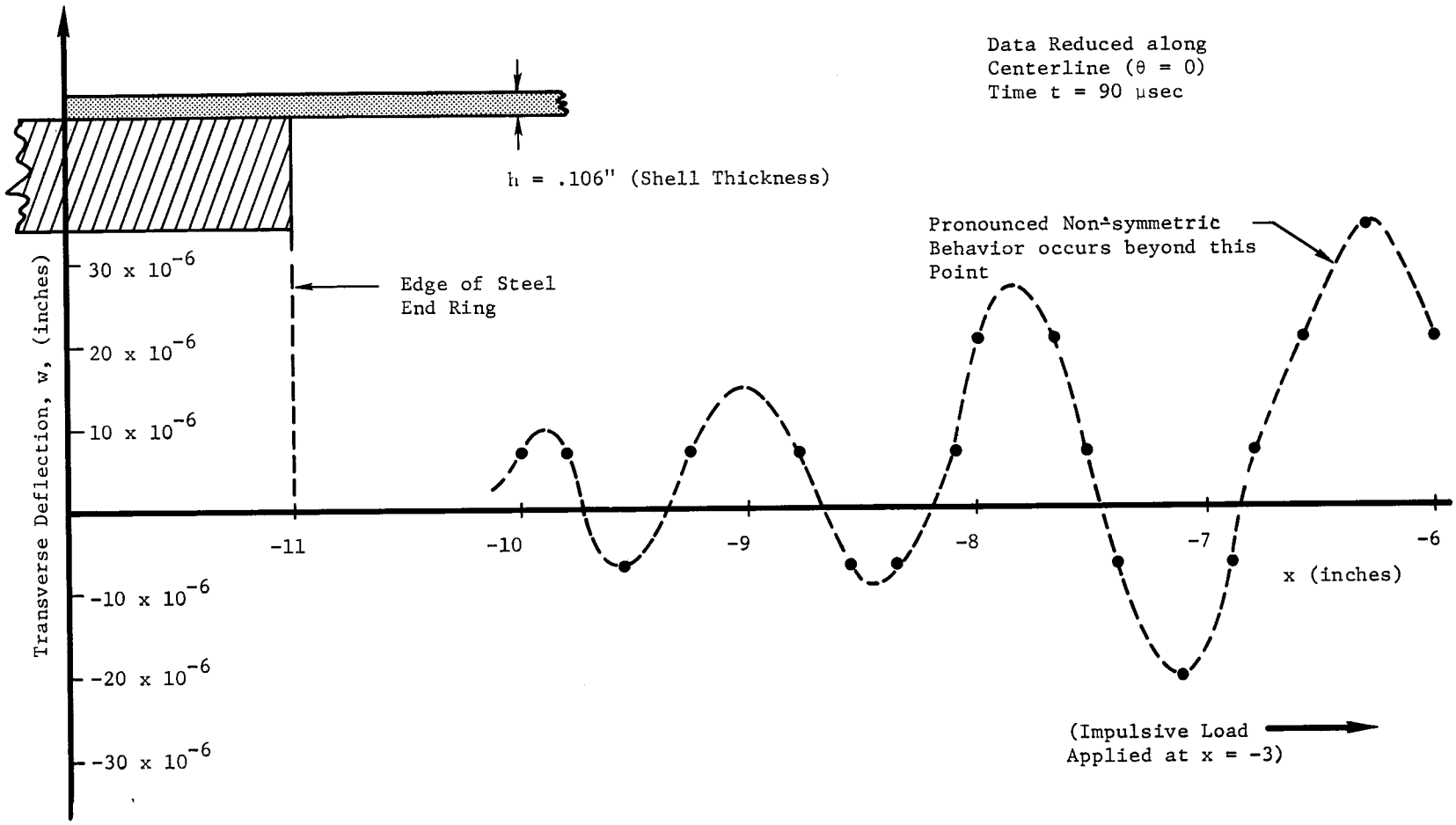

Figure 21: Radial Deflection, w, as a Function of Position along the Shell. (Wave Reflecting from a fixed Boundary; see Interferogram Figure 20.)

A typical interferogram (showing the wave reflecting from a free edge) taken at time t = 105 μsec is given in Figure 22. The corresponding deflection data (w vs x) is plotted in Figure 23. The radial load was applied at x = 2.5 inches, to the right of the center of the shell. At time t = 105 μsec, the transverse wavefront (which moves at approximately $c_s \cong .1$ inch/μsec) has reached the edge of the shell and is reflecting back toward the center of the shell.

Additional interferograms (for this same free-edge boundary condition) are presented in Appendix C and show the wavefront at various times, t_i.

Reflections from a Simply-Supported Boundary - Another edge condition which is commonly used in analysis is the simply-supported boundary:

$$M_x = 0 \qquad \text{(moment - free)}$$

$$w = 0 \qquad \text{(zero radial displacement)}$$

The accompanying in-plane boundary condition is either

$$u = 0 \qquad \text{(zero displacement)}$$

or

$$N_x = 0 \qquad \text{(zero axial force)}$$

An attempt was made to simulate the "simply-supported" boundary experimentally by machining vee grooves around the circumference of the shell. The grooves (i.e., "notches") produce a significant (local) reduction in the flexural stiffness, since

(i) the shell thickness is reduced by a factor of 5 or 10 at the groove

and (ii) the bending stiffness varies as the third power of the wall thickness, i.e., $\sim h^3$

Enough material is left (at the bottom of the vee) to approximate the restraints

$$w \approx 0$$

$$u \approx 0$$

prescribed in the analysis. This is a common technique of approximating simply-supported edges experimentally.

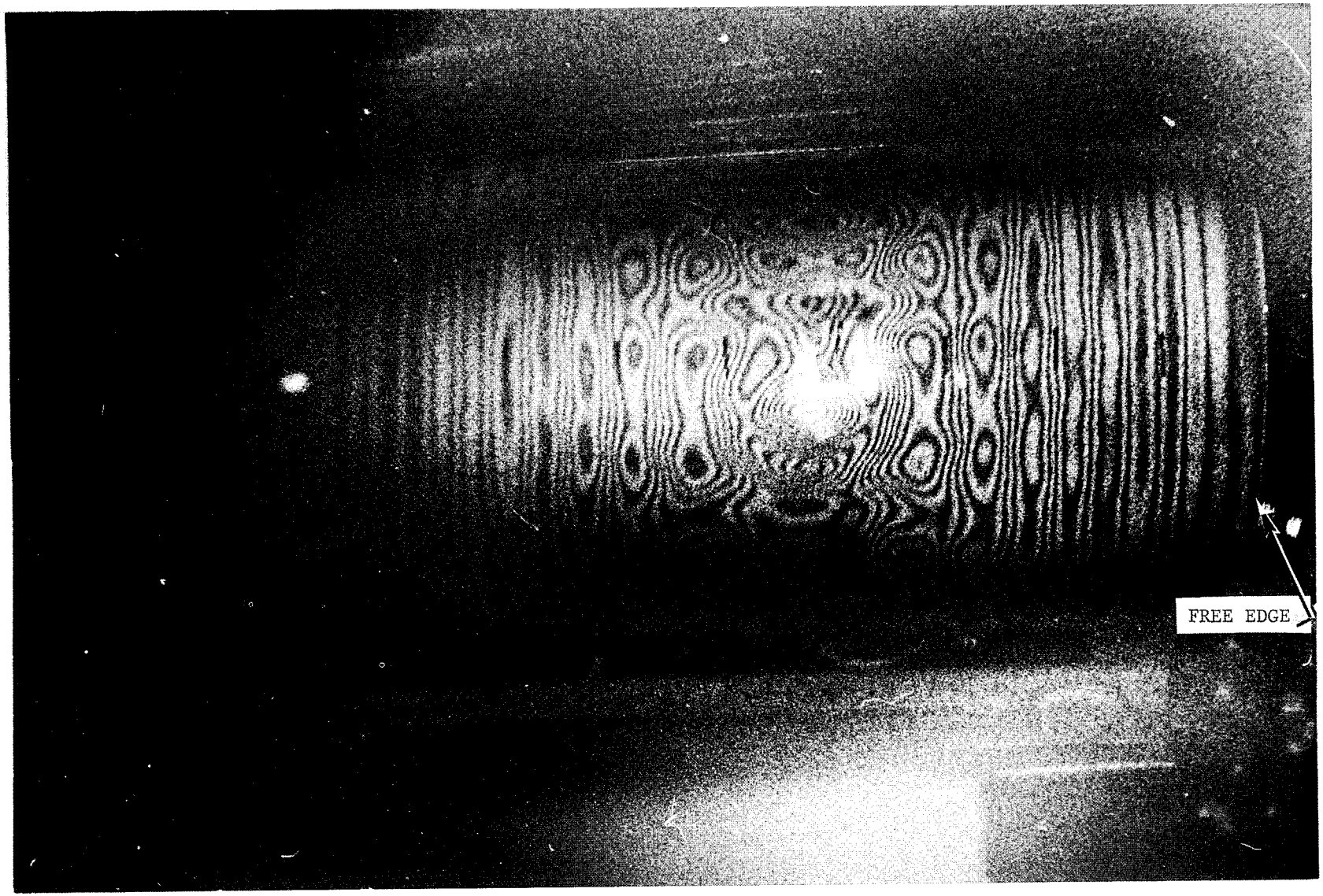

Figure 22 : Wave interacting with a "free" edge (at the right). Time t = 105 μsec.

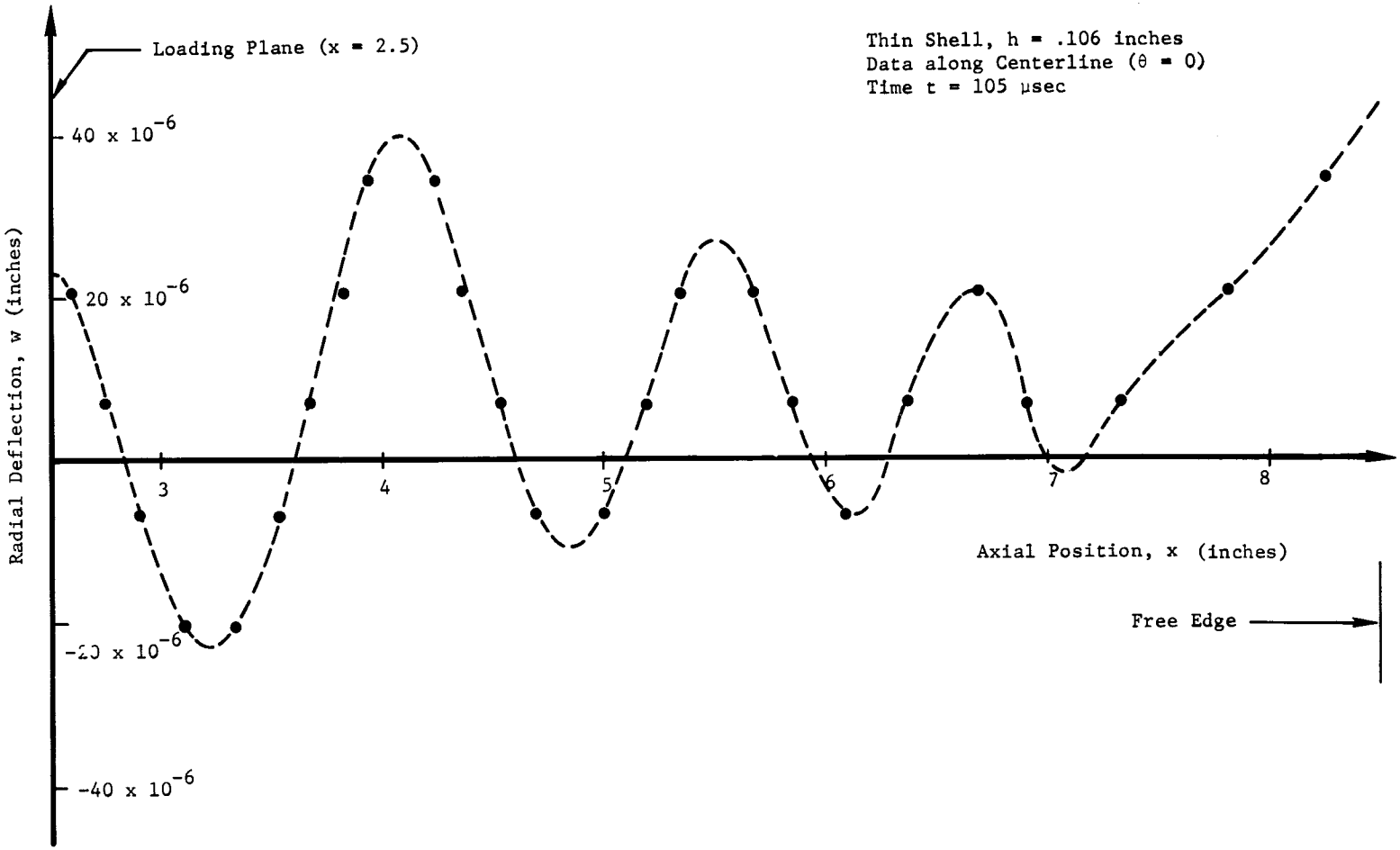

Figure 23: Radial displacement, w, as a function of axial position, x. Load applied at x = 2.5 inches, free-edge at x = 8.5 inches. (See interferogram, Figure 22.)

The vee groove was situated at the left end of the shell, close to the steel end ring. A typical interferogram (showing a wave reflecting from the vee groove) at time t = 39 μs is given in Figure 24. The corresponding deflection data (w vs x) is plotted in Figure 25. The impulsive load was applied at a location 4 inches to the right of the vee groove, as illustrated in Figure 25. Additional interferograms (for this boundary condition) are included in Appendix C.

Comparison with Computer Analysis

One objective of the experimental work was to provide data for comparison with computer analyses. The tests on the "thin" shell (h = .106 inch wall thickness) were co-ordinated with NASA/Langley for comparison with an axi-symmetric, finite-difference analysis (Reference 25). Quantitative details of this comparison are presented herein.

Input Data for the Analysis - The computer program used the following input data:

Radius, a = 5.0 inches

Thickness, h = .106 inches

Length, L = 12.0 inches (total length between ends)

Radius/Thickness Ratio, a/h = 47.1

Length/Radius Ratio, L/a = 2.4

The applied loading was modeled as a pressure, p(x, t) as follows:

$$p(x, t) = \rho k \left[16\left(\frac{t}{T}\right)^2 - 32\left(\frac{t}{T}\right)^3 + 16\left(\frac{t}{T}\right)^4 \right] h \qquad (3\text{-}19)$$

for $0 \leq t \leq T$ (the pulse duration)

in a region 1/4 - of an inch wide, centered at x = 6 inches. (That is, the load was a uniform band of pressure, located mid-way between the ends of the 12 inch long shell.) The factor, ρ, in Equation (3-19) represents the mass density of the shell and the constant k was used as a scaling factor to adjust the amplitude of the impulsive loading.

Equation (3-19) is a polynomial representation of the applied pulse time-history, and it is quite similar to the expression

$$p(x, \theta, t) = A \sin^2 \frac{\pi t}{T}$$

discussed previously (c.f. Figure 3).

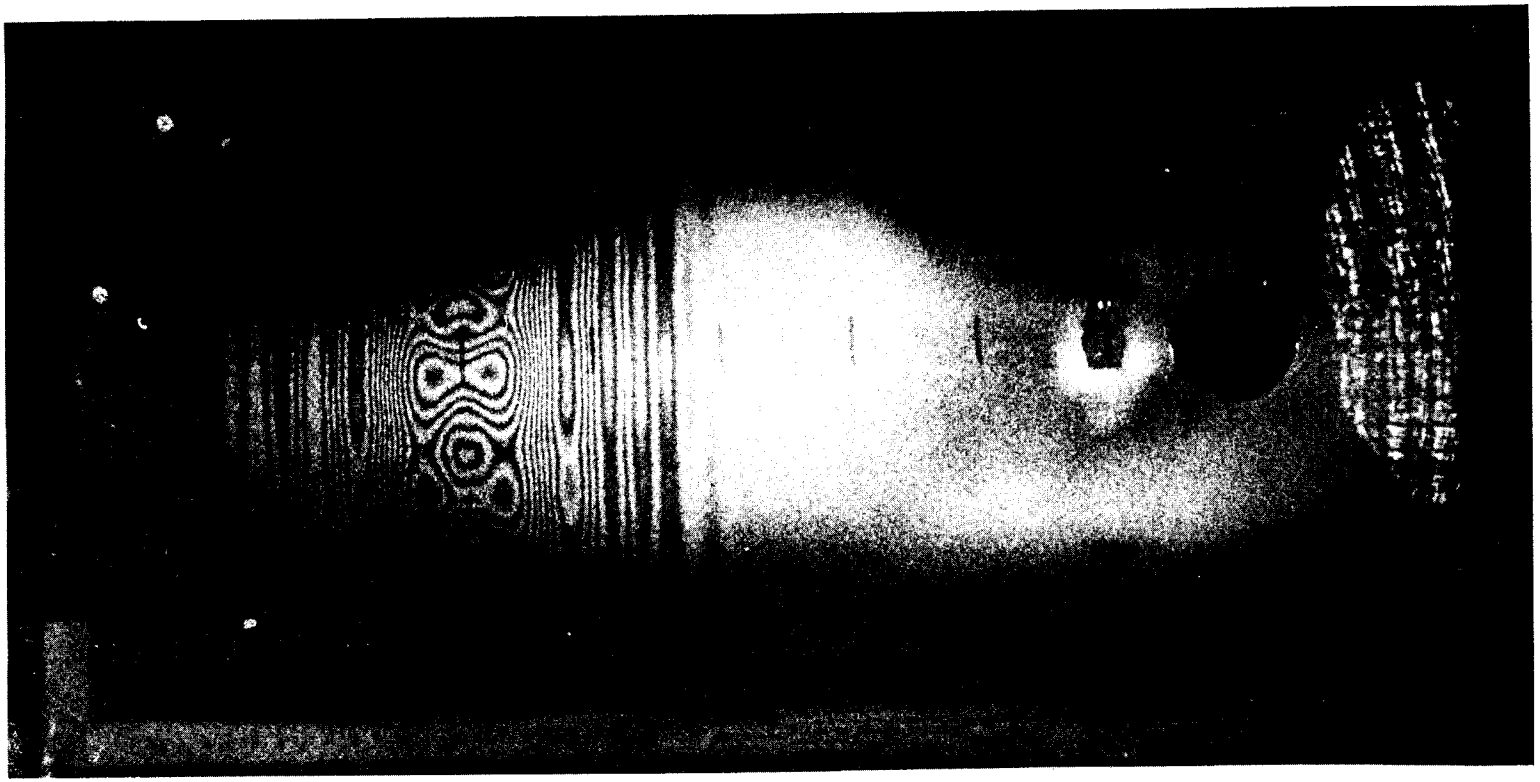

Figure 24: Wave interacting with a simply-supported boundary (vee groove) at the left. (Time t = 39 μsec.)

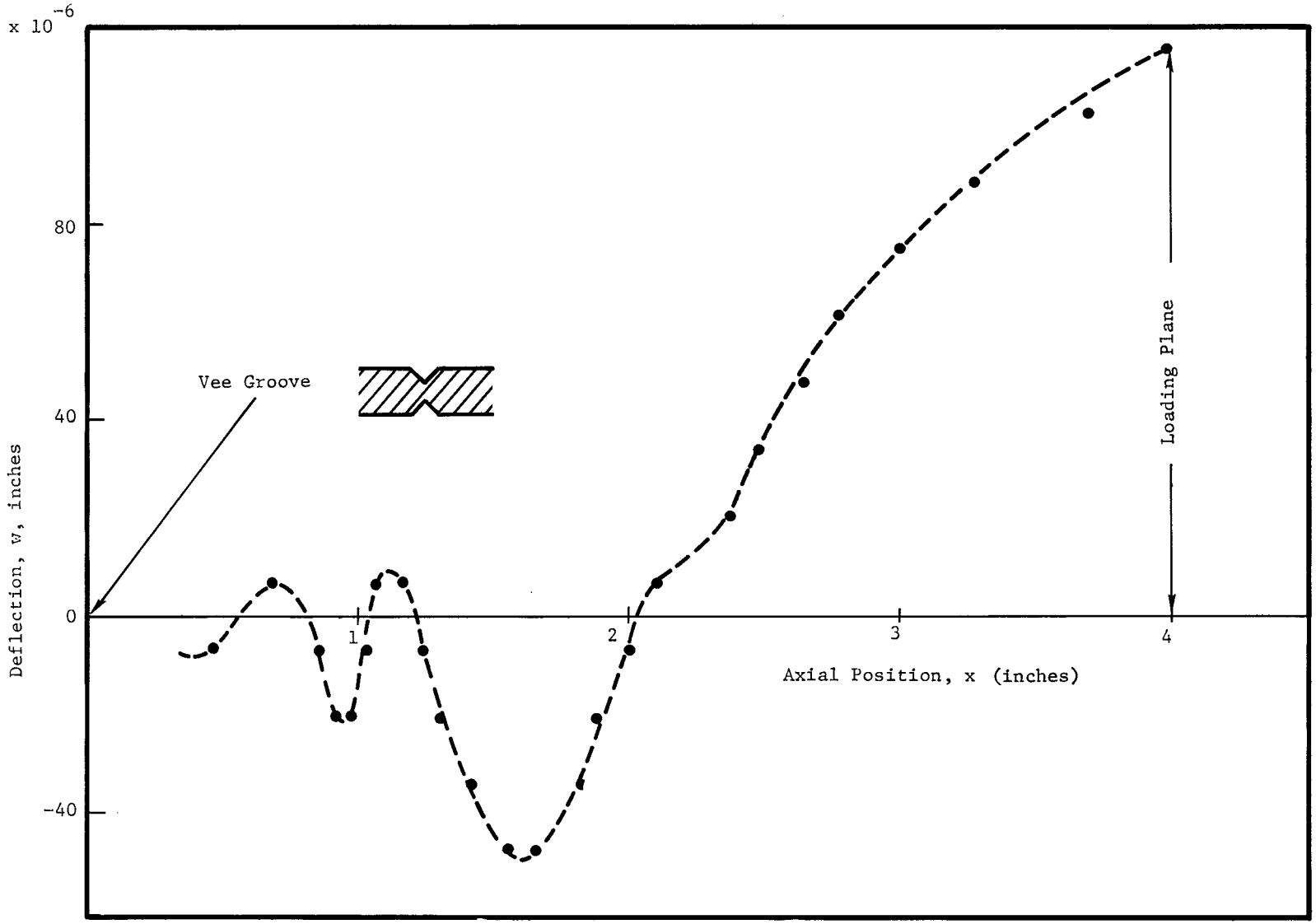

Figure 25: Radial deflection, w, as a function of position, x. (Wave reflecting from a simply-supported boundary, t = 39 μsec.)

The pulse duration, T, used in the analysis was T = 10 μsec, which closely represents the experimental result; (see Appendix A). The material properties used were nominal values for aluminum, namely

$$E = 10 \times 10^6 \text{ lb/in}^2 \qquad \text{(Young's Modulus)}$$

$$\nu = 0.3 \qquad \text{(Poisson's Ratio)}$$

$$\rho g = 0.10 \text{ lb/in}^3 \qquad \text{(Density by weight)}$$

The applied impulsive load, $p(x,\theta,t)$ is characterized by its "specific impulse," I_o which was calculated as follows:

$$I_o = \int_o^T \int_{-\varepsilon}^{\varepsilon} p(x,t)\, dx\, dt \tag{3-20}$$

When Equation (3-19) is substituted for $p(x,t)$ in Equation (3-20) and the integral is evaluated, the result is

$$I_o = \rho h \left(\frac{1}{4}\right) k \left(\frac{8}{15}\right) \times 10^{-5} \tag{3-21}$$

where the (1/4) comes from integrating on x from $\varepsilon = -1/8$ to $\varepsilon = +1/8$ (i.e., the width of the applied load). The product (ρh) represents the shell (mass/unit area), and the factor $8/15 \times 10^{-5}$ results from integrating the polynomial from t = 0 to T = 10 sec. The constant k was chosen to be 3.65×10^6, which yields a value

$$I_o = 1.34 \times 10^{-4} \text{ lb-sec/in} \tag{3-22}$$

when used in Equation (3-21) along with the nominal values of h and ρ. Thus, the scaling constant k was chosen such that the analysis used the same "impulse" as given by the pendulum measurements. (See Equation A-12, Appendix A.)

Ratio Between Experimental/Theoretical Responses

With the scaling constant k adjusted in this fashion, the ratio between experimental and computed deflections was expected to be 1:1. However, the computer solutions were noticeably lower in magnitude than the response measured experimentally. This result was disturbing, expecially in view of the fact that previous holographic measurements of wave propagation (in beams, Ref. 7, and plates, Ref. 8) had shown excellent correlation with analysis.

At this point, it was suspected that the pendulum calibration of the specific impulse might be in error (see Appendix A). The calculation of the specific impulse (using electromagnetic theory and the measured current, I(t), in the repelling-wire device) resulted in

$$2.06 \times 10^{-4} \leq (I_o)_{calc} \leq 2.39 \times 10^{-4} \qquad (3\text{-}23)$$

where the units are lb-sec/inch and the inequality (3-23) depends on the limits of an integration, discussed in Appendix A.

When the value

$$(I_o)_{calc} = 2.39 \times 10^{-4} \quad \text{lb-sec/in}$$

is used to "scale up" the computer results, (by the ratio $K = \frac{2.39}{1.34} = 1.8$) fairly good agreement is achieved between theory and experiment, as illustrated in Figure 26.

Figure 26 shows the computed results (Ref. 25) and the holographic data, for times t = 5, 10, and 20 μsec. As shown in Figure 26, qualitative agreement between theory and experiment is quite good, and the data agree quantitatively as well, providing we scale the theory to correspond with the impulse $I_o = 2.39 \times 10^{-4}$ lb-sec/in given in Appendix A.

Further comparison between theory and experiment (for the thin-walled shell) was hampered by two considerations:

(i) The computer program was based on axial symmetry, whereas non-symmetric responses occurred (at the later times) experimentally.

(ii) The computer program involved long running times (e.g. on the order of 30 minutes to propagate the wave for t = 20 μsec) and it was not practical to compute the response at the later times.

Additional comparisons between theory and experiment (but for the thick-walled shell) are given in Section 4.0 which follows.

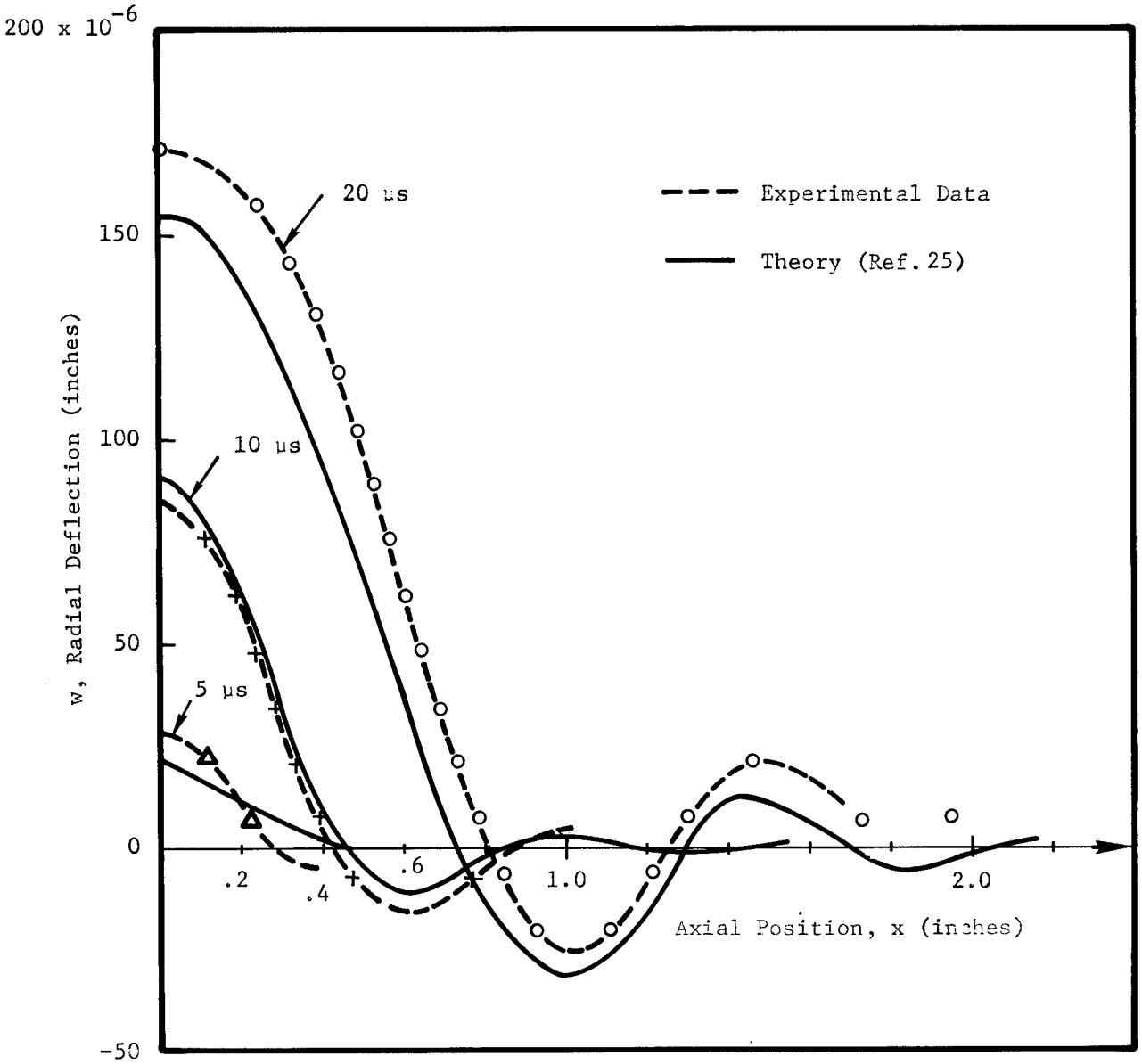

Figure 26: Radial deflection along the shell: comparison of theory and experiment. (Thin aluminum shell, h = .106 inches.)

4.0 WAVE PROPAGATION PAST CUT-OUTS AND STIFFENERS

Background and Summary

The problem of axi-symmetric wave propagation in a thin-walled shell of revolution represents a rather idealized situation from a practical standpoint. This is to say, that many practical problems (in actual engineering applications) involve shells with cut-outs, stiffeners, eccentricities, etc. that depart from a mathematical model which requires axial symmetry. Computer programs for non-symmetric wave propagation in such shells are of fairly recent development (e.g., Ref. 17). One of the objectives of the present experimental study was to provide data for comparison with such analyses.

Experimental data are given in this section for transverse wave propagation past square cut-outs, circular cut-outs, and an (axi-symmetric) ring stiffener. Tests run on a thick-walled shell (h = .25 inches) were compared with analytical results of Ref. 17. Qualitative argeement between theory and experiment was obtained, and the quantitative discrepancies are largely attributed to rotary inertia and transverse shear effects not included in the analysis.

Other tests on the thin-walled shell (h = .106 inches) are also presented herein, but analytical results for this geometry were not available. The "thin" wall thickness (h $\approx$ .1 inch) requires a very "fine" finite-difference mesh in the analysis, which results in "long" computer run times. As faster computer analyses become available, efforts should be made to correlate them with the present experimental data.

Tests on a Thick-Walled Cylinder

Background - Concurrent with our experimental work, NASA/Langley funded an analytical study (involving a two-dimensional, finite-difference approach) for nonsymmetric wave propagation in shells (See Ref. 17). It was understood that TRW and Lockheed personnel would coordinate these programs and provide each other with their results. Discussions were held with the NASA Technical Monitor (Dr. J. P. Raney) and with T. L. Geers (Lockheed, Palo Alto) until we agreed upon a shell configuration which was acceptable for both the holographic experiments and the computer calculations. The present section deals with the holographic results and their comparison with analysis.

Shell Specimen and Test Procedure - The cylindrical shell used in these tests was aluminum tubing, and it had a nominal wall thickness $h = .25$ inches. The shell was 24 inches long and had an average inside diameter $D_i = 9.496$ inches. Thus, the radius to the mid-surface of the shell was $a = 4.87$ (inches) and the radius/thickness ratio was $a/h = 19.5$. The shell was supported at the ends by flexible aluminum discs (1/16-in. thick) which were designed to provide "freely-supported" boundary conditions (see Ref. 4). (A photograph of the "thick-shell" specimen is given in Figure 27).

Since the "thick shell" specimen was two-and-one-half times as thick as the "thin shell" (Section 3.0), the stiffness and mass were also 2-1/2 times larger. Elementary response calculations show that the radial displacement for our problem is inversely proportional to the shell thickness. Thus, in order to maintain an adequate response (and produce sufficient fringes on the interferogram) it was desirable to increase the impulse applied to the shell and thereby compensate for its increase in thickness. The repelling-wire loading technique (described in Section 3.0 and Appendix A) was used, and the impulse was increased by using (i) a higher charging voltage, $V_o = 25$ kilovolts, and (ii) a smaller wire spacing, $d = 0.27$ inches. Using these values in equations (A-6) and (A-7) of Appendix A results in a specific impulse of (approximately)

$$I_o = 6.0 \times 10^{-4} \quad \text{lb.sec./in} \qquad (4\text{-}1)$$

applied to the thick shell.

The optical arrangement, timing of the laser pulse, and test procedure were identical to that described previously in Section 3.0. Experiments were performed first on the virgin shell (without cutouts), and then rectangular cut-outs were machined in the shell and the tests repeated. Typical results are discussed in the following paragraphs.

Response Without Cut-Outs - Typical holographic interferograms of the thick-walled cylinder are shown in Figures 28 through 30. Figure 28 (recorded at $t = 9$ μs) illustrates the axisymmetric nature of the initial response. Slight nonsymmetric behavior is evident in Figure 29 ($t = 15$ μs) and Figure 30 ($t = 38$ μs). The corresponding curves of radial displacement (w) vs axial position (x) are given in Figure 31. Additional interferograms showing the response at other times are presented in Appendix D.

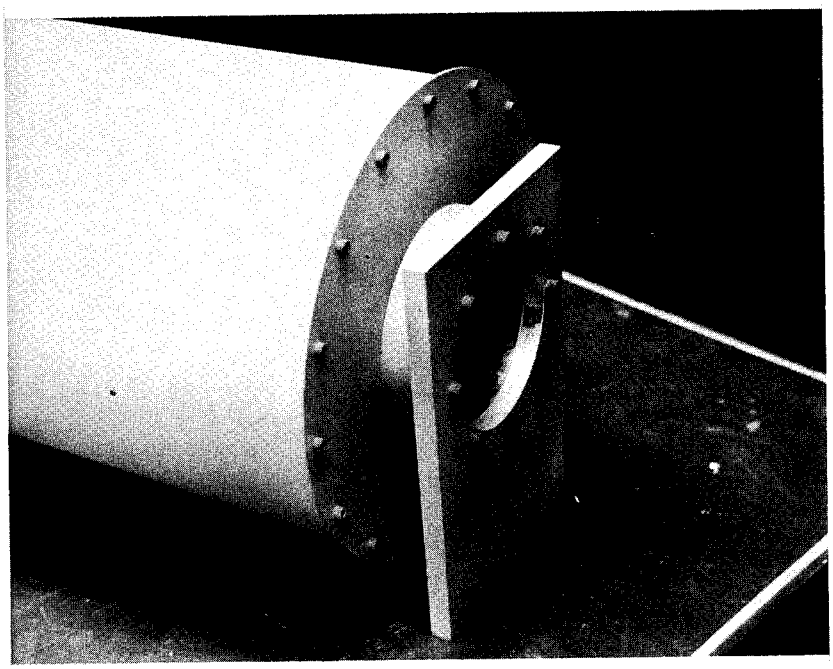

Figure 27: Thick-walled shell specimen (aluminum, a = 4.87 inches, h = .25 inches).

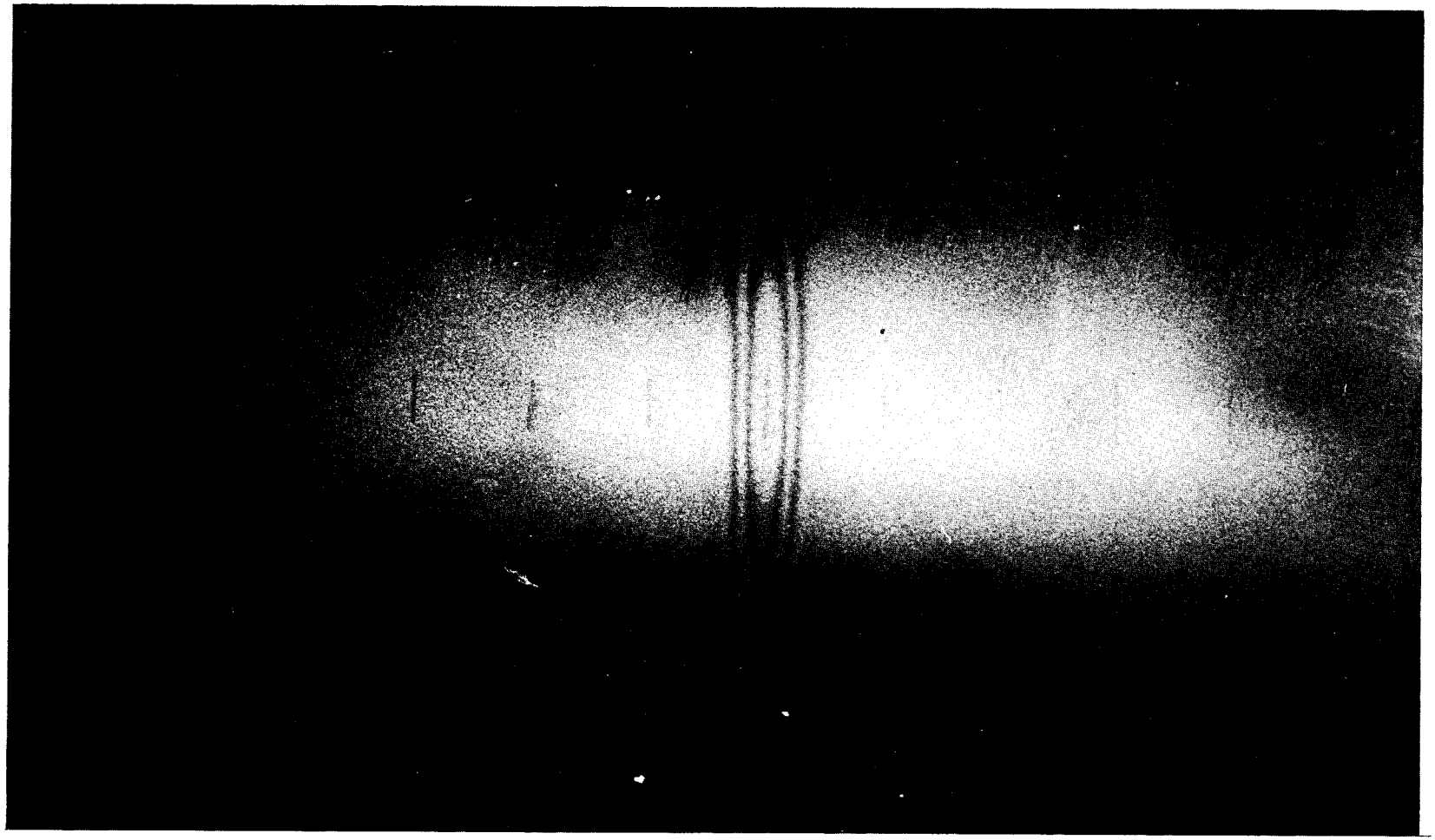

Figure 28 : Wave propagation in the thick-walled shell. (h = .25 inches). Time t = 9 μsec.

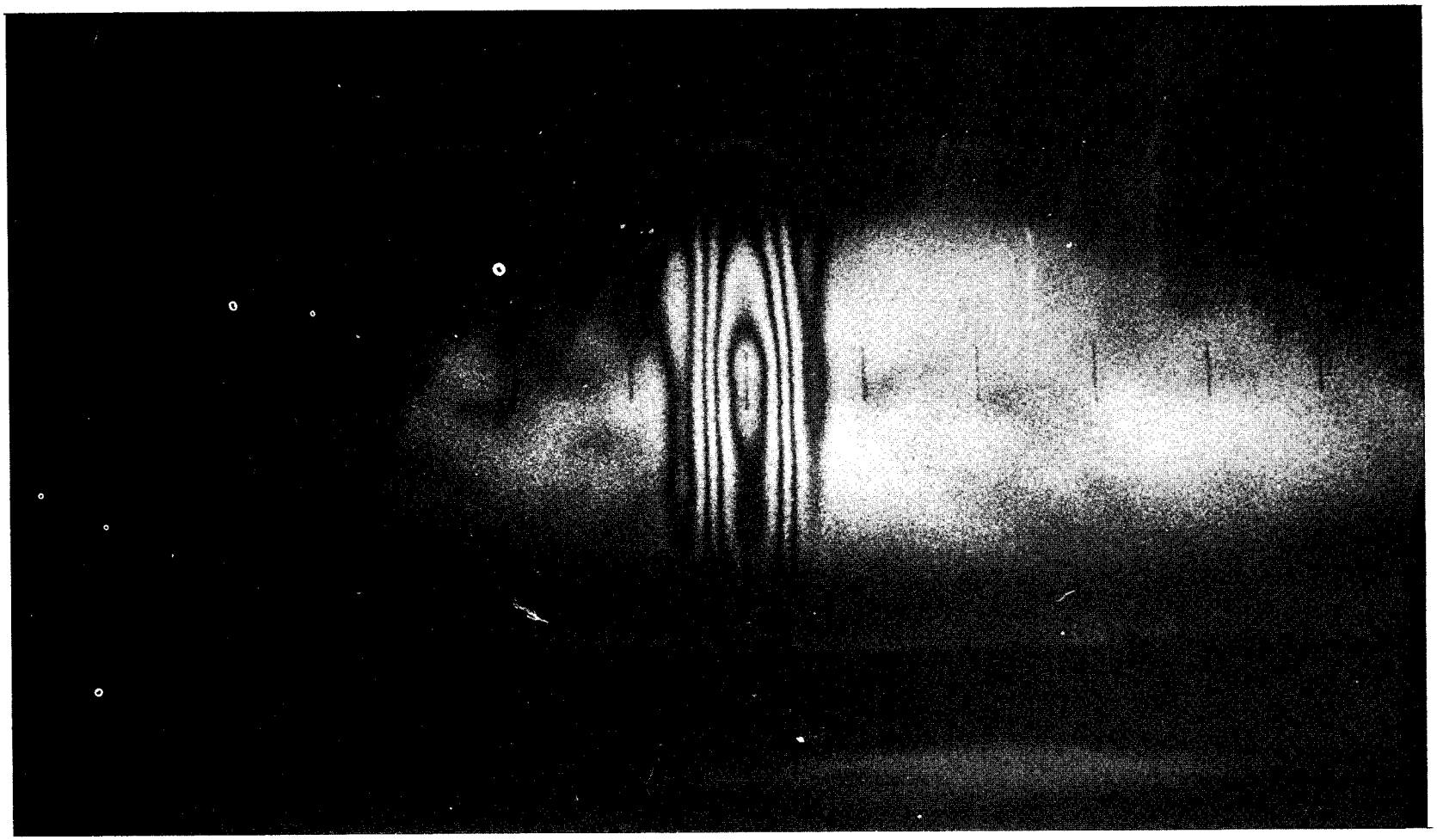

Figure 29: Wave propagation in the thick-walled shell. (h = .25 inches). Time t = 15 μsec.

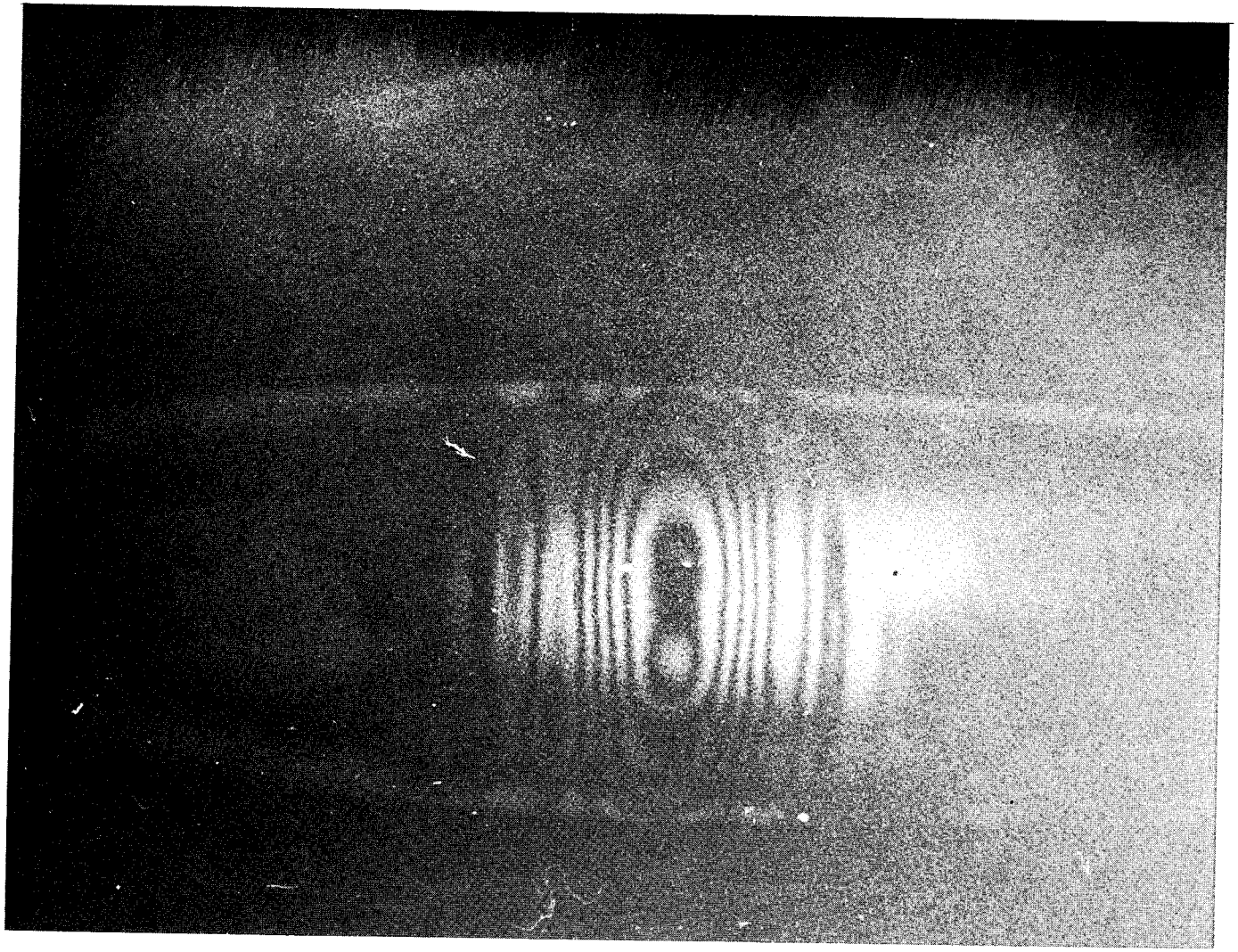

Figure 30: Wave propagation in the thick-walled shell. (h = .25 inches). Time t = 38 μsec.

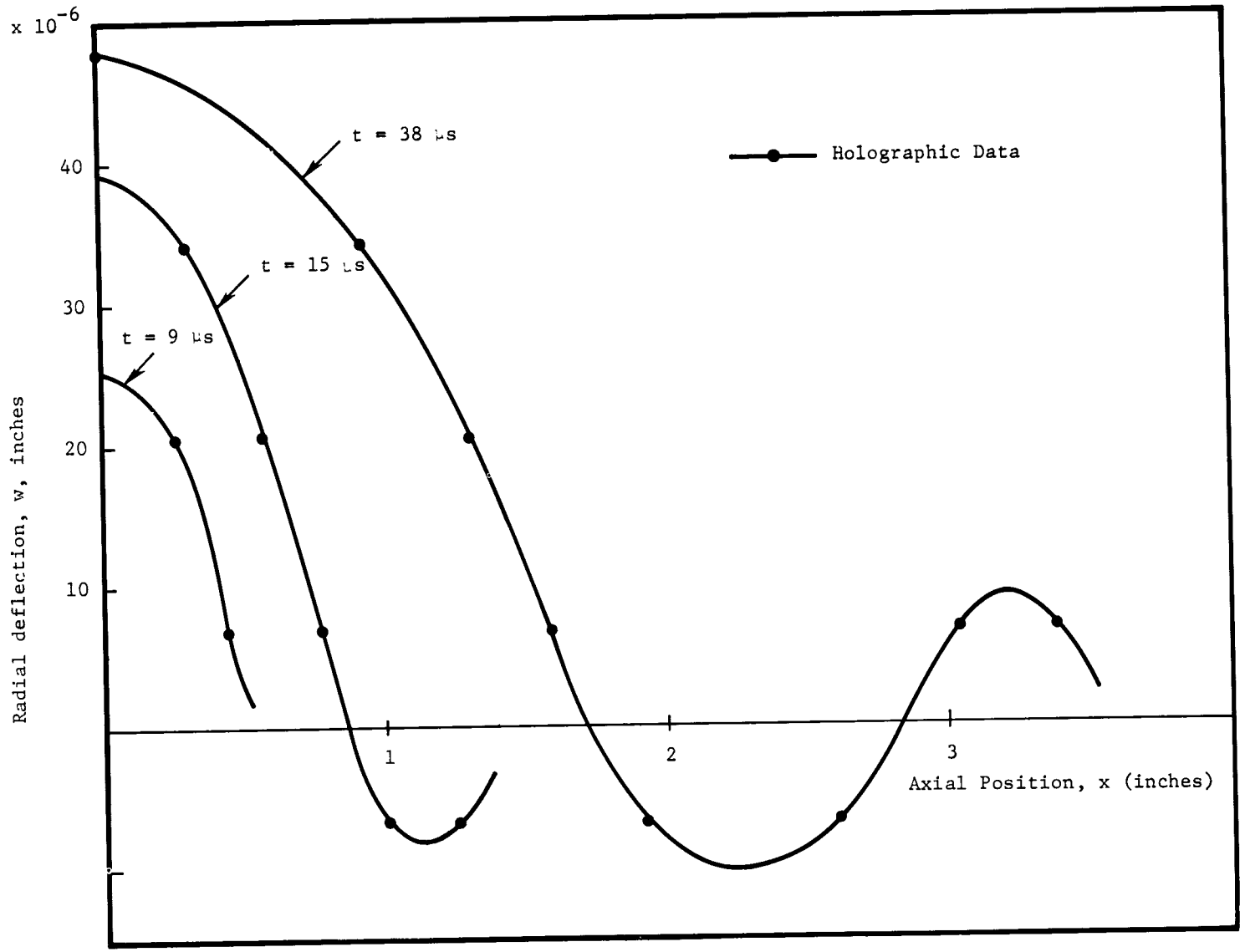

Figure 31 : Radial deflection, w, vs. axial position, x. Thick-walled shell, h = .25 inches, without cut-outs.

The displacement curves just discussed (Figure 31) illustrate a technical difficulty encountered previously: Each structural wavelength of the deformation is defined by very few data points (i.e., fringes). This problem could be overcome by increasing the impulse to the shell, but this approach was complicated by the fact that the electrical circuitry would not permit higher voltages (as it was, we operated well above the ratings of several components). An alternative means of increasing the impulse was to decrease the wire spacing, d, still further but such an approach magnifies the circumferential variations in the loading, which is undesirable. Thus, the decision was made to keep the experimental design fixed and proceed to tests using the shell with cut-outs. The results of those experiments are reported in the following paragraphs.

Response with Cut-Outs - The same thick-walled aluminum cylinder was used for these tests, except that it was machined as shown in Figure 32. (A photograph of the shell with cut-outs is given in Figure 33). Eight symmetrically placed cut-outs were used, since the mathematical model (see Ref. 17) required several planes of symmetry to minimize the number of degrees-of-freedom (i.e., to cut down on the extent of the finite-difference mesh).

The holographic results are shown in Figures 34 through 38, which graphically illustrate the waves approaching and propagating past the cut-outs. Reflected waves leaving the cut-out and traveling back to the center of the shell are also apparent in the interferograms. Since the shell response is clearly two-dimensional (involving both x and θ), it was necessary to reduce the experimental data for various "cuts" along the shell. This was accomplished by determining the fringe order, n, and calculating the corresponding displacement (as outlined previously in Section 3.0. Cuts were taken parallel to the axis of the cylinder, and primarily at two angular stations, $\theta = 0$, and $\theta = \pi/12$. These values of θ correspond to the middle of the cut-out and the top edge of the cut-out, respectively.

Plots of the radial deflection vs x are shown in Figures 39 through 47. Until the wavefront reaches the cutouts, the response of the shell is basically axisymmetric (cf. Figure 34). As the wave interacts with the cutout, the transverse response tends to be large near the edge of the cutout, as might be expected (cf. Figure 37). These experimental results are in qualitative agreement with the computer analysis, as discussed in the next section.

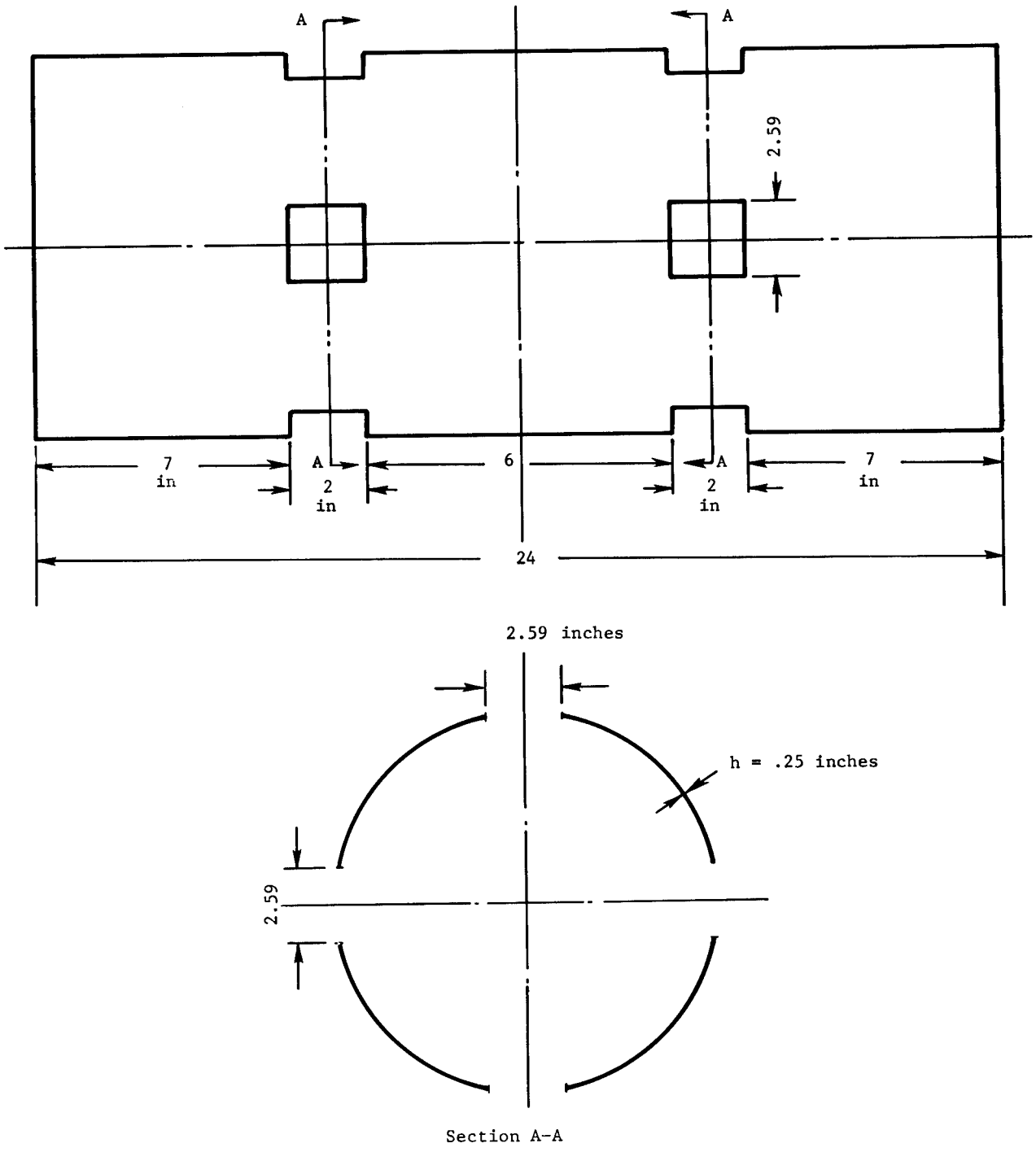

Figure 32: Sketch showing location of cut-outs in the thick shell. (All dimensions are given in inches.)

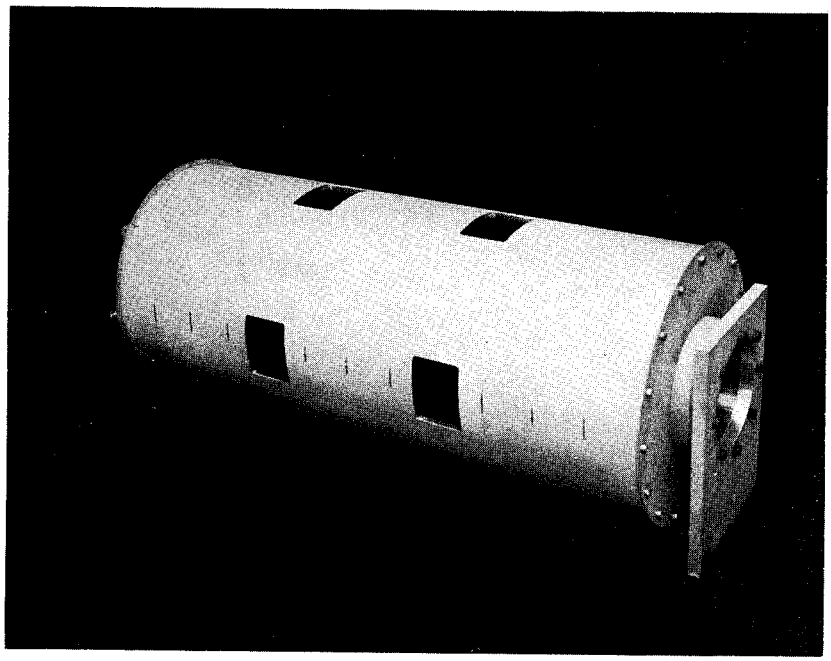

Figure 33: Photograph of thick-walled shell specimen with symmetrical cut-outs (c.f. Figure 32).

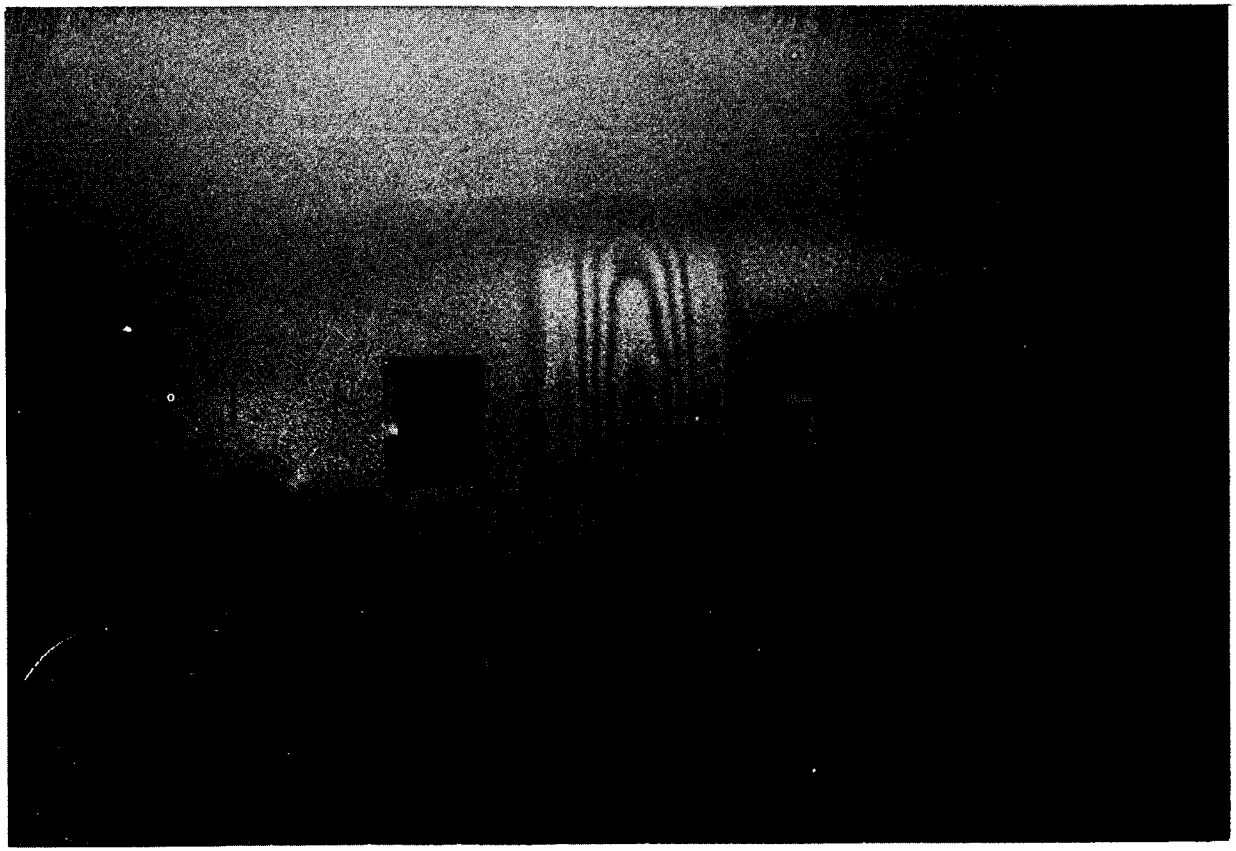

Figure 34 : Wave interacting with cut-outs. Thick-walled shell, h = .25 inches. Time t = 20 μsec.

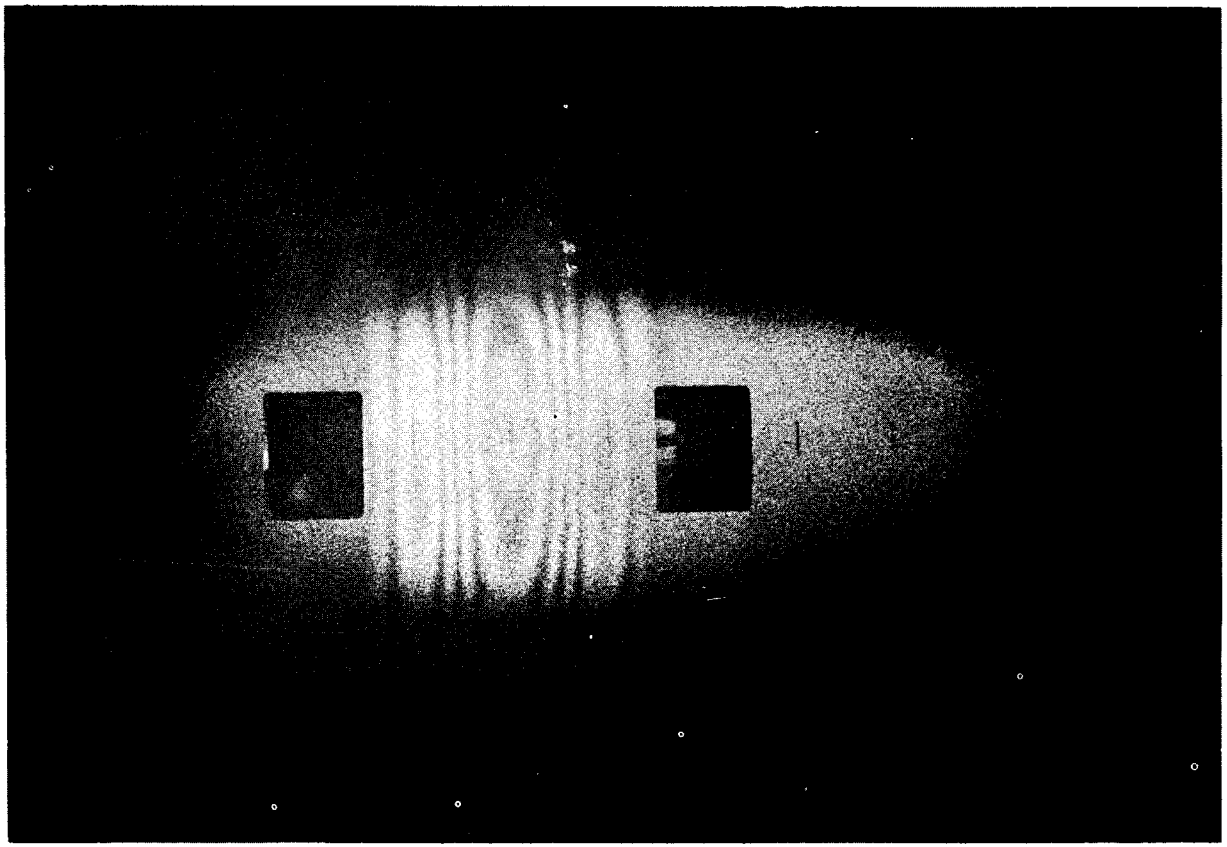

Figure 35 : Wave interacting with cut-outs. Thick-walled shell, h = .25 inches. Time t = 29 μsec.

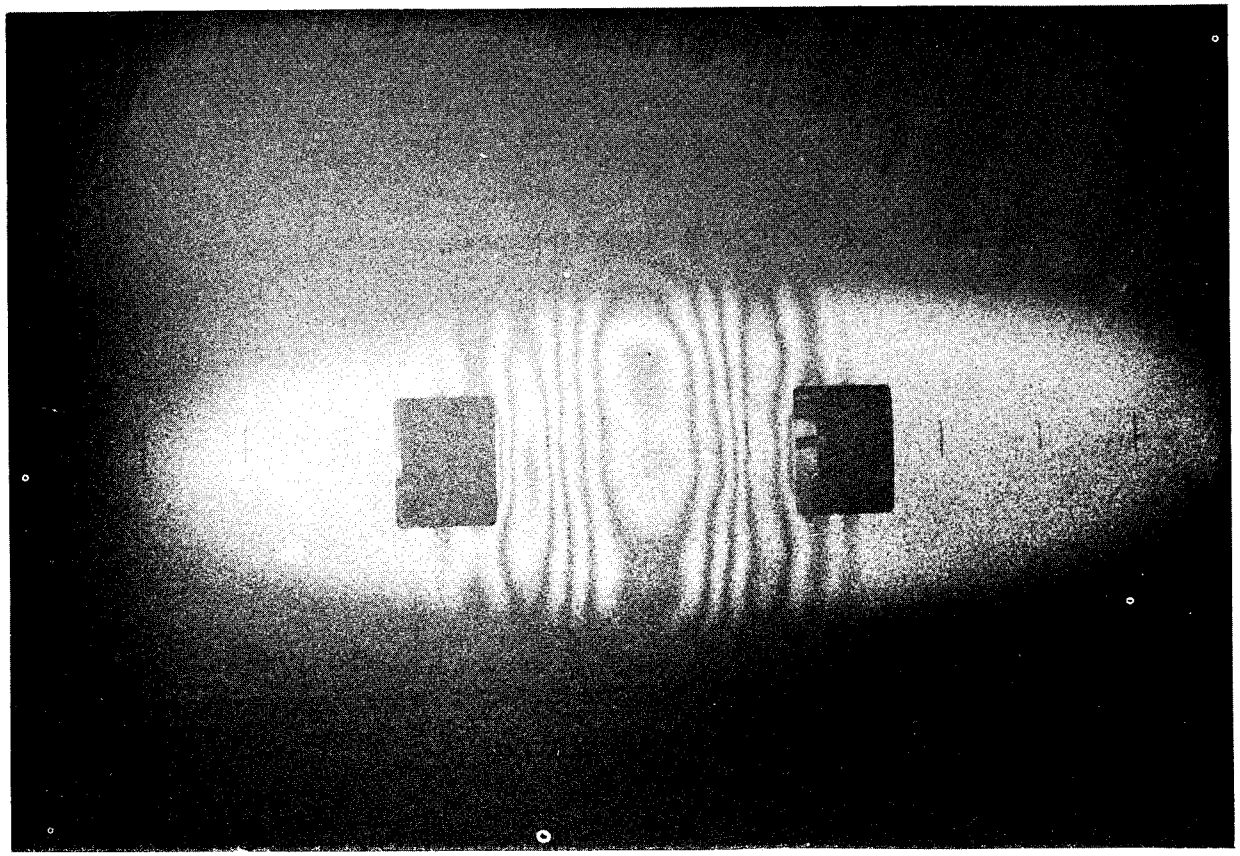

Figure 36: Wave propagation past cut-outs in the thick-walled shell. Time t = 41 μsec.

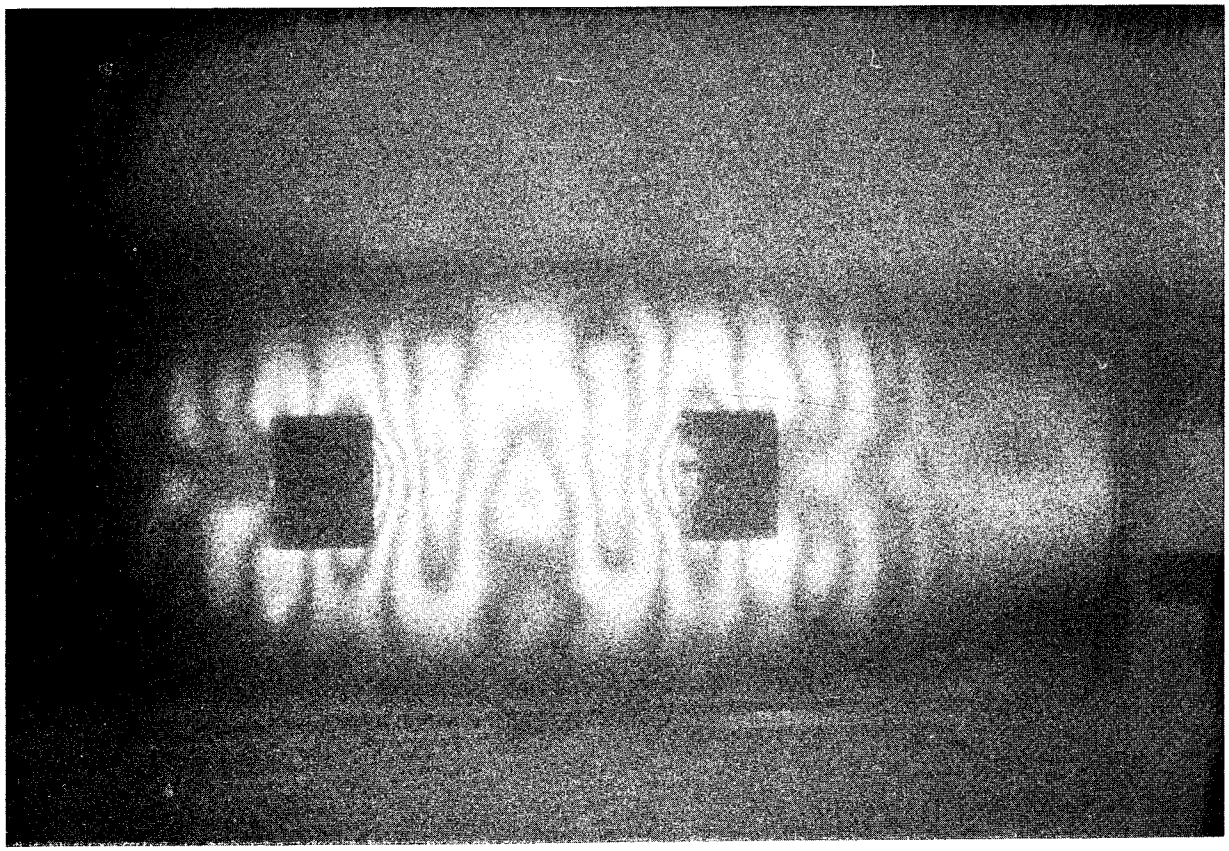

Figure 37 : Wave propagation past cut-outs in the thick-walled shell.
Time t = 72 μsec.

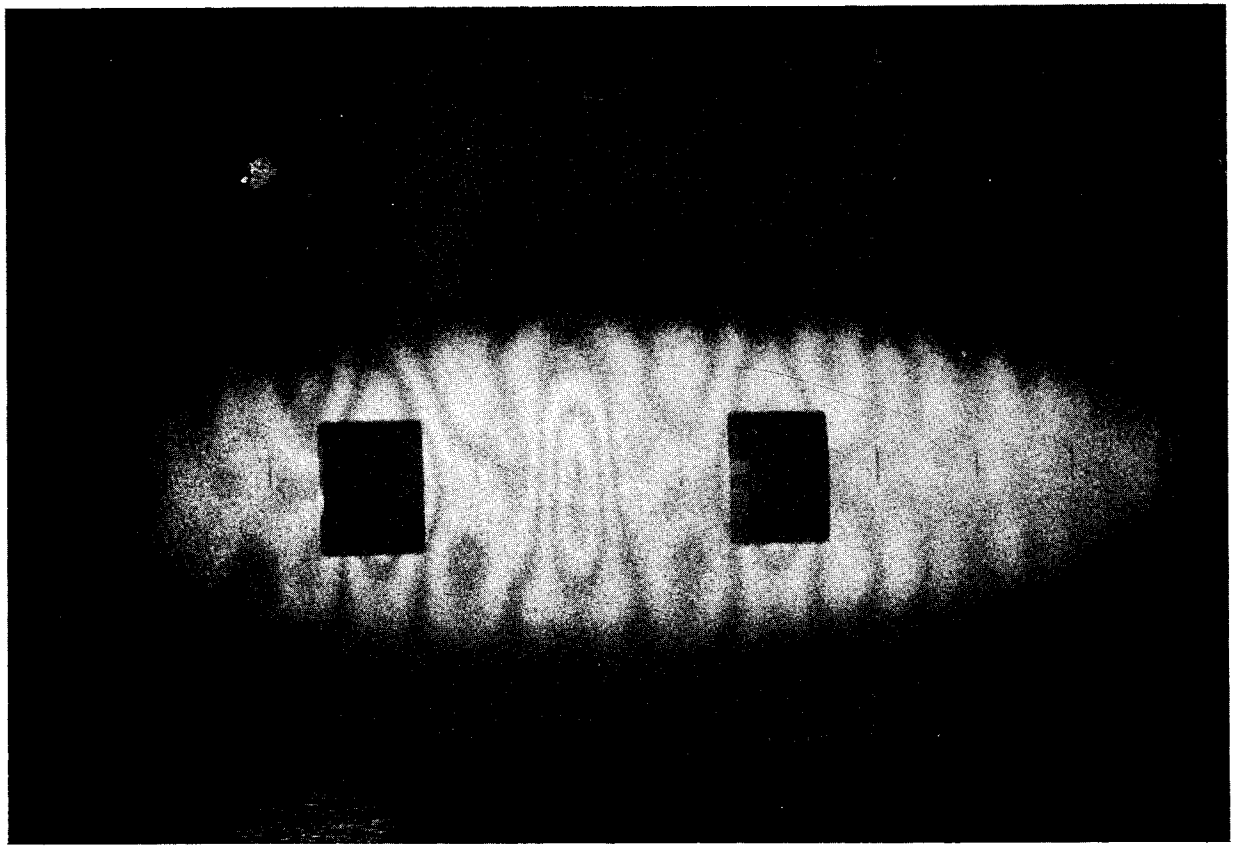

Figure 38: Wave propagation past cut-outs in the thick-walled shell. Time t = 82 μsec.

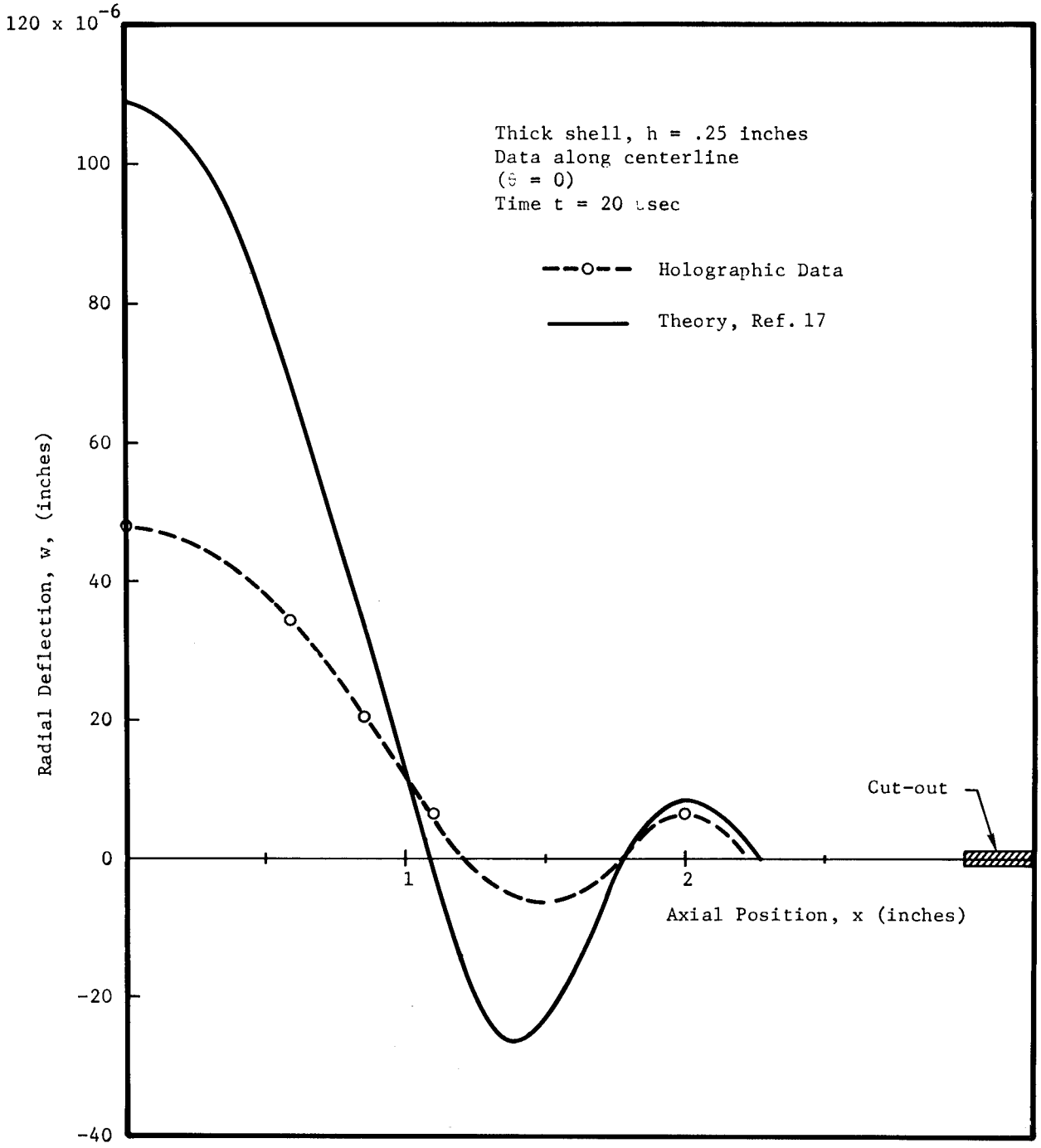

Figure 39: Radial deflection, w, as a function of x. Thick shell, with cut-outs.

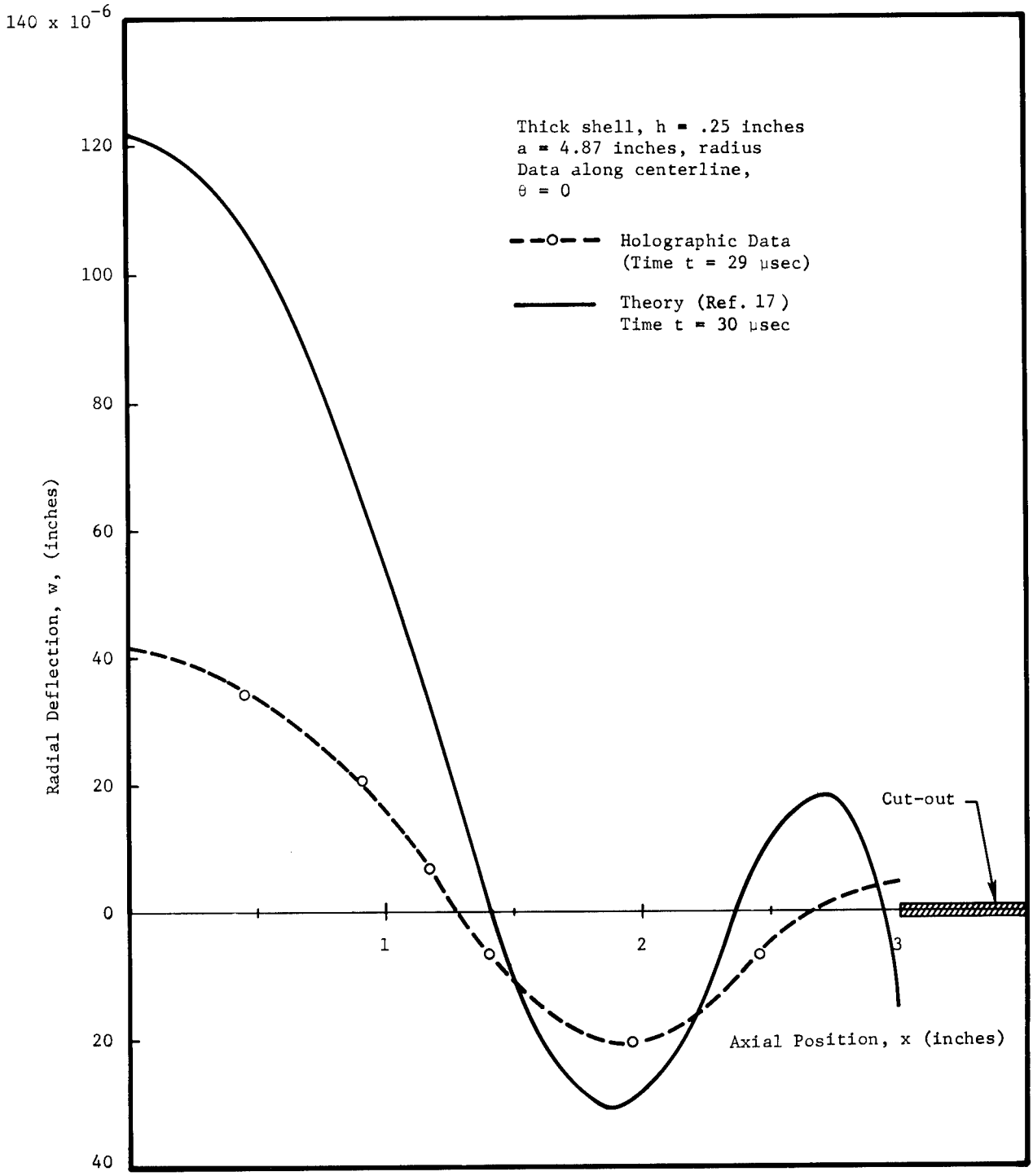

Figure 40 : Radial deflection, w, as a function of axial position, x. Comparison of theory and experiment, thick shell with cut-outs.

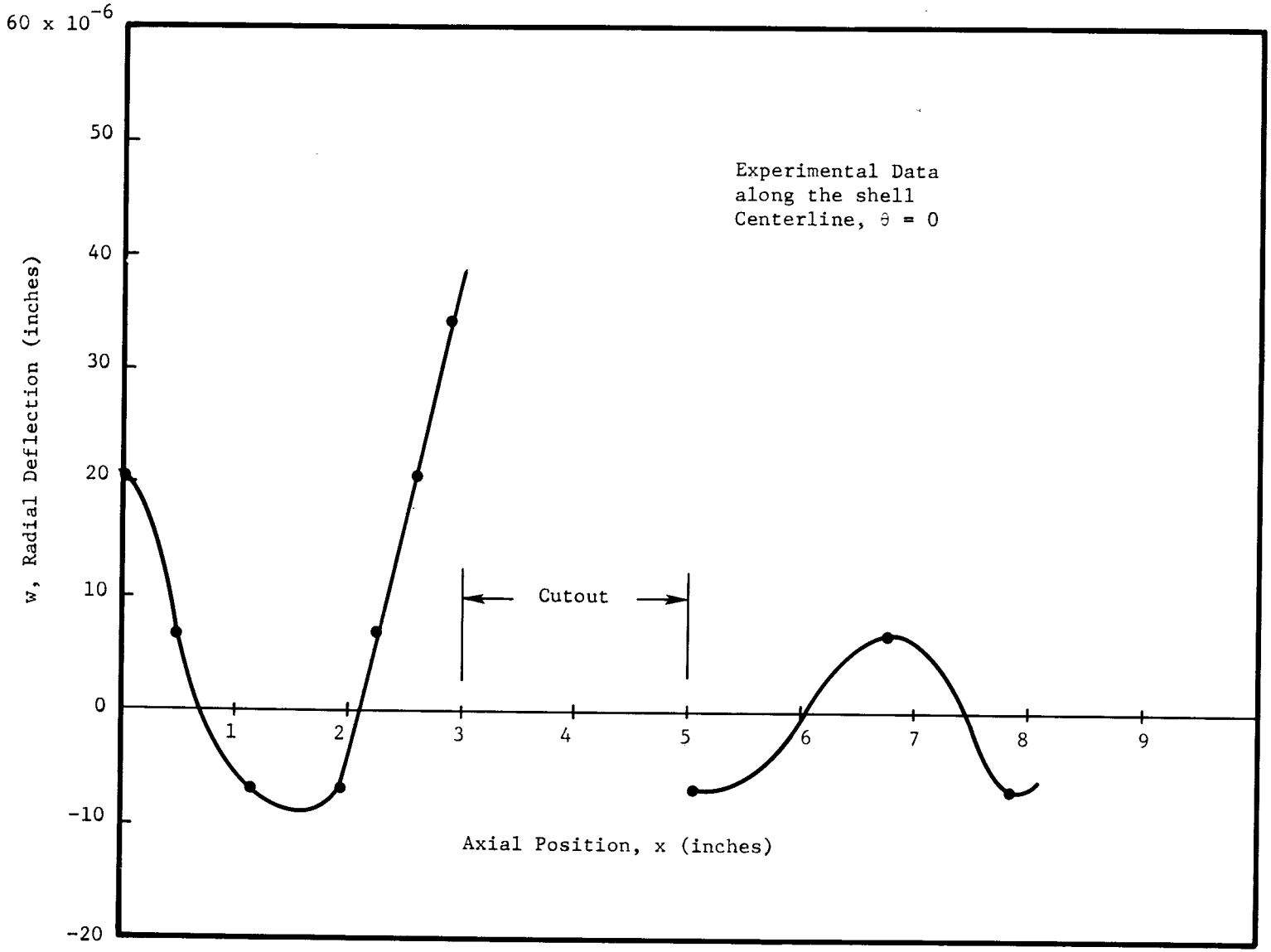

Figure 41: Radial deflection, w, vs. axial position, x, at time t = 72 μsec. Thick shell with cut-outs

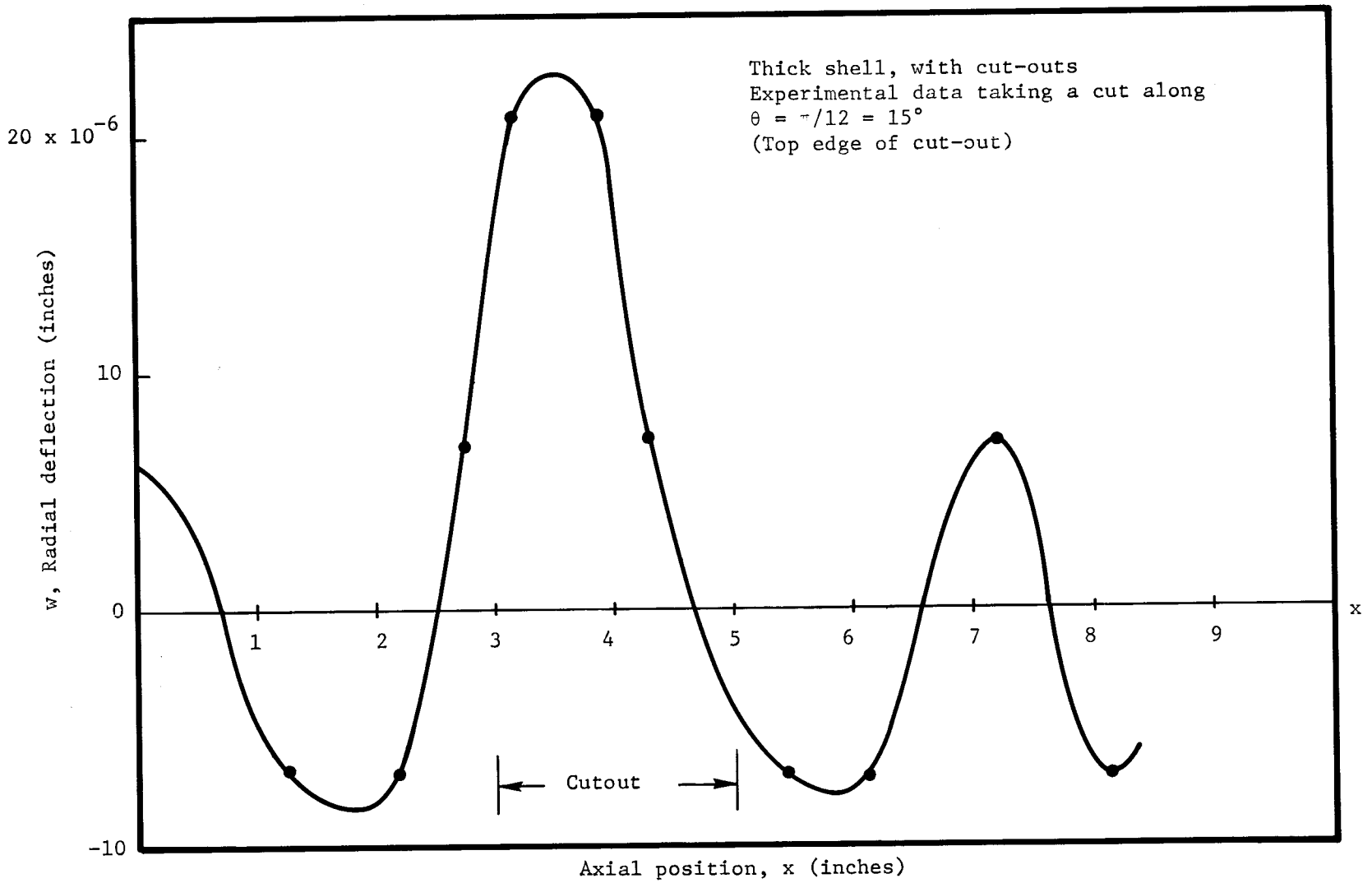

Figure 42 : Radial deflection, w, bs. axial position, x, at time t = 72 μsec. Thick shell with cut-out.

Comparison with the STAR Code

As indicated previously, one objective of the experimental work was to provide data for comparison with computer analyses. In particular, the tests on the "thick shell" (h = .25 inches) were designed for comparison with the STAR code (Ref. 17). Quantitative details of this comparison are presented herein.

Input Data for the Analysis - The shell which was analyzed used the following input data:

Radius/Thickness Ratio, a/h = 20

Length/Radius Ratio, L/a = 4.8 (total length between ends)

Conditions of symmetry were applied on the following planes:

- The plane x = 0, which contains the radial loading,
- The plane $\theta = 0$, which passes through the cut-out and contains the cylinder axis,
- The plane $\theta = \pi/4$, which passes mid-way between the cut-outs and also contains the cylinder axis.

The applied loading was modeled as a transverse shear, Q_α, as follows:

$$\frac{1 - \nu^2}{Ea} Q_\alpha(0,\theta,t) = \begin{cases} 5 \sin^2 \frac{\pi t}{T} & 0 \leq t \leq T = .4 \frac{a}{c} \\ 0 & t > T \end{cases}$$

Boundary conditions of "free-support", i.e.,

$$\left.\begin{aligned} w &= 0 \\ N_x &= 0 \\ v &= 0 \end{aligned}\right\} \quad \text{at } x = \pm L/2$$

were applied at the ends of the shell.

Ratio Between Experimental/Theoretical Responses - To compare theory and experiment, the following factors were used:

$a = 5$ inches (radius)

$c = .2$ in/μs (wave speed)

$L/2 = 12$ inches (half length of the shell)

$E = 10 \times 10^6$ lb/in^2 (Young's Modulus)

$\nu = .3$ (Poisson's Ratio)

Thus, $T = .4 \frac{a}{c} = 10$ μs, the duration of the applied loading. The pressure loading, $p(x,t)$, (assumed axisymmetric) can be related to the shear force Q_α as follows:

$$\int_{-\varepsilon}^{\varepsilon} p(x,t)dx = 2Q_\alpha(0,\theta,t) \tag{4-2}$$

where ε is a small quantity representative of the width of the applied load. Equation (4-2) is obtained by considering equilibrium of a shell element in the radial direction.

If we now integrate both sides of this equation in time, we obtain

$$\int_0^T \int_{-\varepsilon}^{\varepsilon} p(x,t)dxdt = I_o = 2\int_0^T Q_\alpha(0,\theta,t)dt \tag{4-3}$$

where I_o is the "specific impulse", in lb-sec/inch. (See Section 3.0. Equation 3-20, for example.) Thus, Equations (4-2) and (4-3) can be combined to give

$$I_o = \frac{2Ea}{(1-\nu^2)} \int_0^T 5 \sin^2 \frac{\pi t}{T} dt$$

$$I_o = \frac{10Ea}{(1-\nu^2)} \left(\frac{T}{2}\right) \tag{4-4}$$

Using the nominal values of E, a, ν, and T (given previously) we have

$$I_o = \frac{10(10 \times 10^6)(5)}{(.91)} \left(\frac{10 \times 10^{-6}}{2}\right) = 2.75 \times 10^3 \ \frac{\text{lb-sec}}{\text{in}}$$

which characterizes the (analytical) input.

The experimental value of the specific impulse was calculated using Equation (A-6) and (A-7), following the procedures outlined in Appendix A. Thus, from Equation (A-7) we have

$$I_o = \int_0^{t_{final}} F(t)dt = \left(\frac{V_o}{.6}\right)^2 \left(\frac{2 \times 10^{-7}}{\omega}\right) \left(\frac{1}{d}\right) \begin{Bmatrix} .409 \\ .475 \end{Bmatrix} \qquad (4\text{-}5)$$

where for the thick shell V_o = 25,000 volts and d = .691 x 10^{-2} meters, which gives

$$I_o = \begin{Bmatrix} 5.86 \\ 6.80 \end{Bmatrix} \times 10^{-4} \ \frac{\text{lb-sec}}{\text{in}}$$

when expressed in English units.

The ratio of experimental to theoretical values is

$$R_{t/e} = \frac{w_{expt}}{w_{theory}} = \frac{I_{expt}}{I_{theory}} = \frac{\begin{Bmatrix} 5.86 \\ 6.80 \end{Bmatrix} \times 10^{-4}}{2.75 \times 10^3} = \begin{Bmatrix} 2.14 \\ 2.48 \end{Bmatrix} \times 10^{-7}$$

The results of Ref. 17 are given in terms of deflection/radius, (i.e., w/a), and in order to compare theory with experiment we have

$$w_{theory} = \left(\frac{w}{a}\right) (R_{t/e}) (a)$$

$$= \left(\frac{w}{a}\right) \begin{Bmatrix} 2.14 \\ 2.48 \end{Bmatrix} \times 10^{-7} \times 5 \qquad (4\text{-}6)$$

$$w_{theory} = \left(\frac{w}{a}\right) (1.125 \times 10^{-6}) \qquad (4\text{-}7)$$

where the values of (w/a) are read from Ref. 17.

Equation (4-7) states that the analytical results of Ref. 17 should be scaled by (approximately) a factor of 10^{-6} to correspond with the experimental input conditions.

Analytical Results and Comparison with Experiment - Typical experimental data obtained holographically are shown in Figures 43 through 45, along with analytical values which have been scaled from Reference 17. (The scaling factor used was $K = 1.125 \times 10^{-6}$, which was used to multiply the analytical values of w/a. (See Equation (4-7) and the related discussion.) The analytical and experimental curves have many features in common, but certain basic discrepancies are also apparent. In order to understand these differences, it is worthwhile to review some of the limitations of thin shell theory, which is used in the computer analysis.

As discussed in Section 3.0, thin shell theory is an approximation to the more exact linear elasticity theory. In terms of the structural wavelengths (say Λ) involved, shell theory will apply when the ratio (Λ/h) is sufficiently large. For example, Bernoulli-Euler type shell theory (Ref. 11) neglects rotary inertia and shear effects, and is expected to be accurate when the wavelength/thickness ratio (Λ/h) is approximately 10 (or larger). Timoshenko type shell theory (Ref. 12) which includes rotary inertia, etc., is valid for shorter wavelengths, say Λ/h on the order of 2 (or perhaps 1). And finally, for yet shorter wavelengths, more exact theories are required.

If we keep these limitations in mind and now refer to Figure 40, we observe that the analytical curve possesses rather "high-frequency" (i.e., short wavelength) ripples near the front of the wave. For example, near $x = 2$ inches (Fig. 40) the analysis exhibits a local structural wavelength $\Lambda \approx 1$ inch. Since the thickness $h = .25$ inches, we have (locally) $\Lambda/h \approx 4$, which is outside the range of validity ($\Lambda/h \geq 10$) of the Bernoulli-Euler shell theory used in the analysis (Ref. 17). In other words, the analytical curve (c.f. Fig. 40) is not expected to be valid in the high-frequency, short-wavelength region near the front of the wave. Accordingly, one would not expect the present experimental data to agree with Ref. 17 near the wavefront.

When rotary inertia and transverse shear are included in the analysis, the "high-frequency ripples" (predicted by Bernoulli-Euler theory) are removed (Ref. 12). The short-wavelength ripples of the less-accurate (Bernoulli-Euler) theory are replaced by longer-wavelength deflections with smaller amplitudes. These effects (of shear and rotary inertia) are well-documented in the literature of elastic wave propagation (c.f., Ref. 26).

Thus, the disagreement between analysis and experiment (at the wavefront) is attributed primarily to the shortcomings of Bernoulli-Euler shell theory. Of greater concern was the lack of quantitative

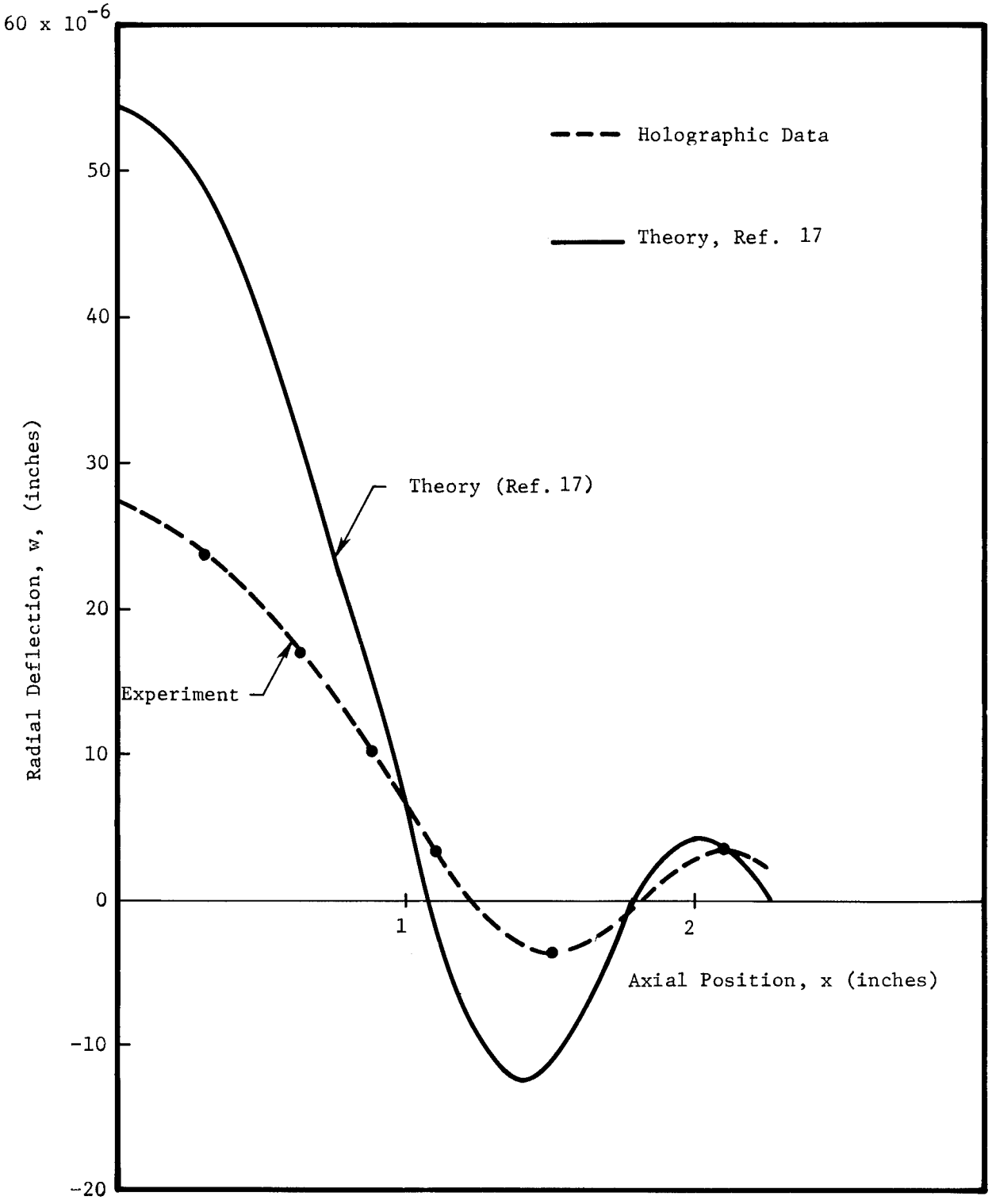

Figure 43: Comparison of theory and experiment, at time t = 20 μsec.

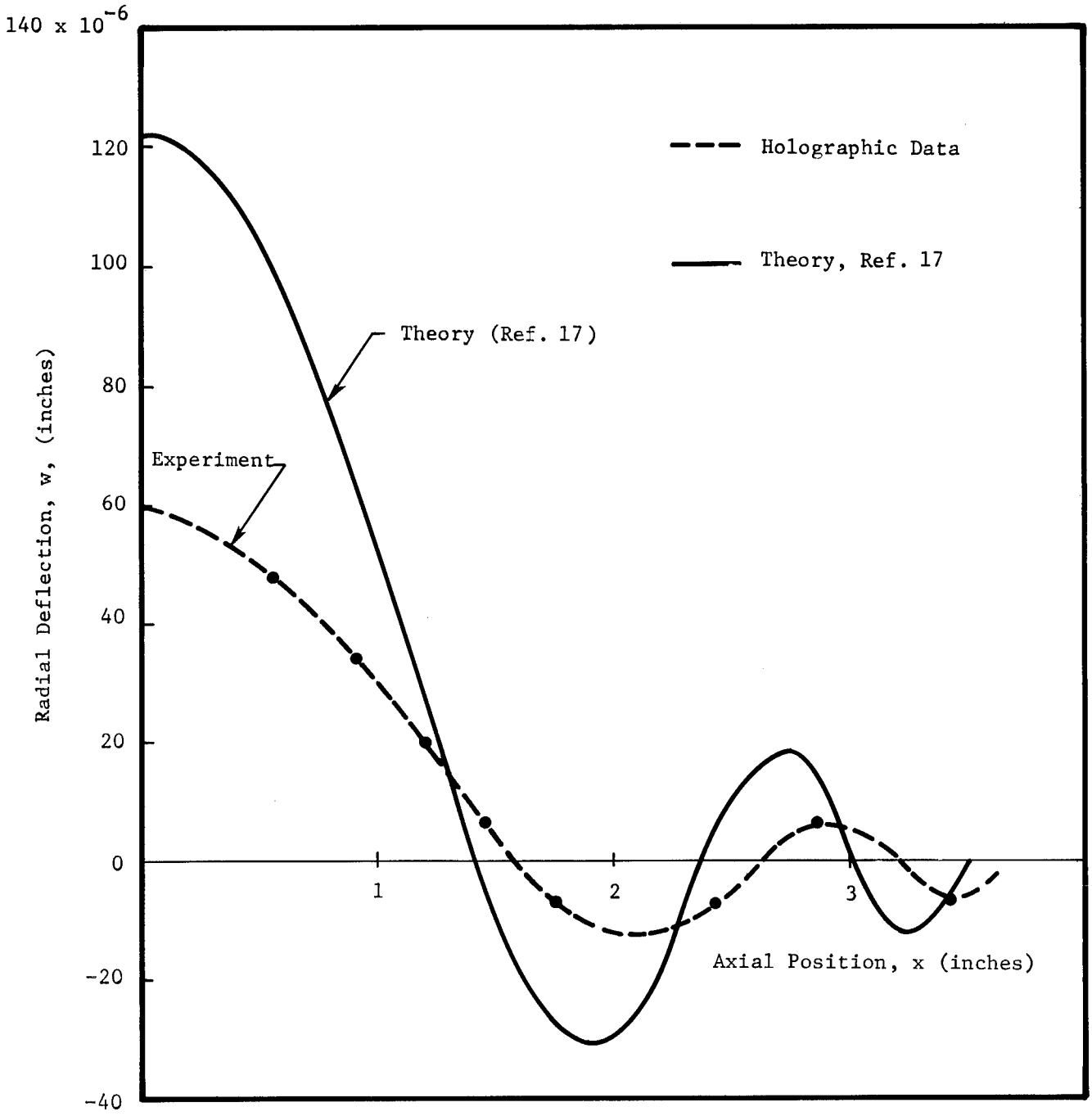

Figure 44: Comparison of theory and experiment, at time t = 30 μsec.

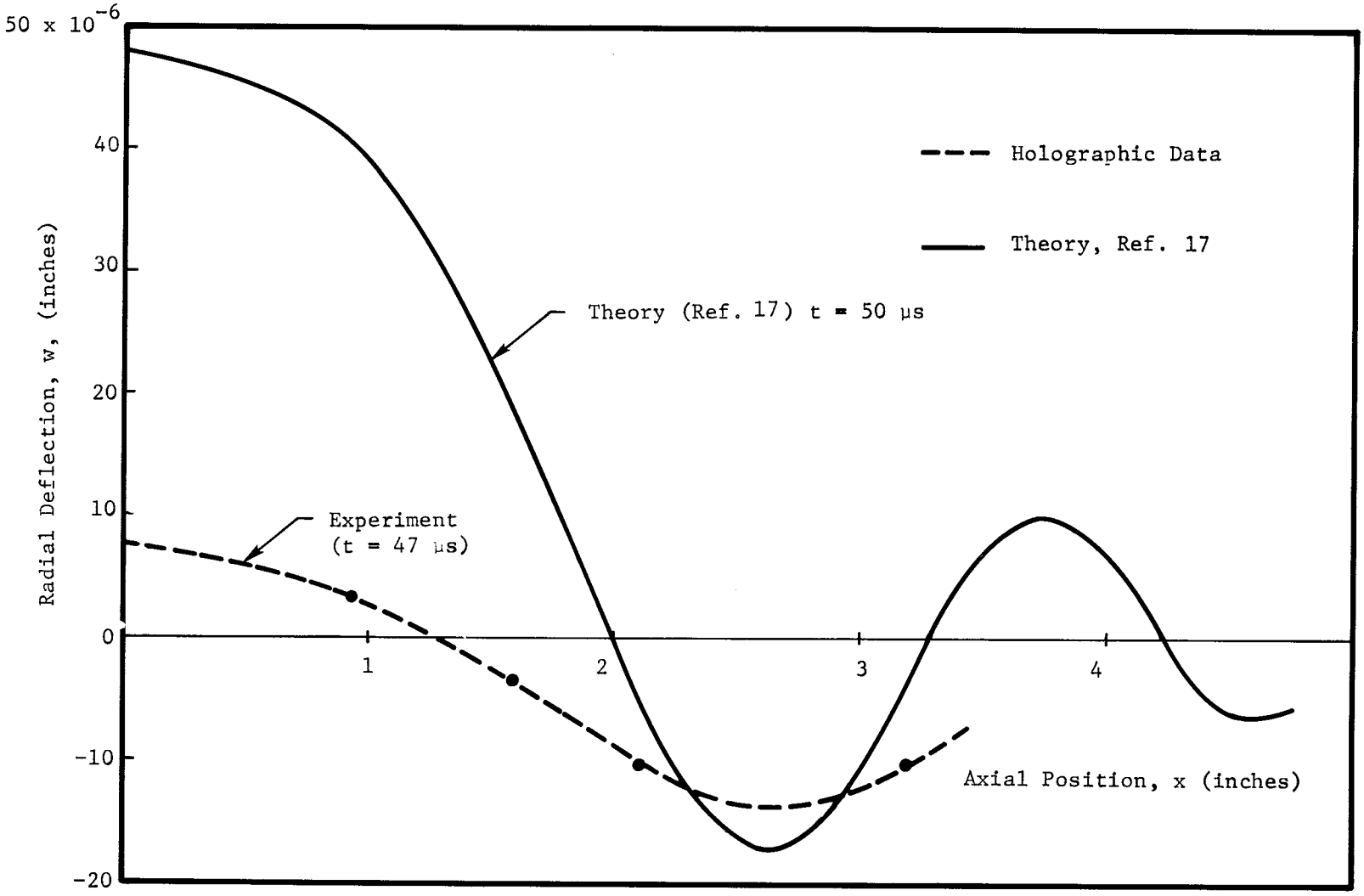

Figure 45: Comparison of theory and experiment (theory at 50 μsec, tests at t = 47 μsec).

agreement between theory and experiment near the center of the shell (i.e., $x = 0$) where the load was applied. In this "center" region, the structural wavelengths are fairly long (at least for the later times, such as $t \geq 20$ μsec) and the analysis (Ref. 17) was originally expected to apply. However, discussion of this problem with several colleagues* has lead the authors to conclude that an analysis of the subject problem (using Bernoulli-Euler shell theory) may in fact be inadequate even in the "long-wavelength" region near $x = 0$. Time would not permit an adequate study of this problem, (from an analytical standpoint) but some simple "demonstrative examples" are discussed in the following section to support the authors' conclusions.

Some Simple Wave Propagation Problems in Thick and Thin-Walled Shells

Consider the (idealized) problem of an infinitely long, circular cylindrical shell with thickness h and radius, a, subjected to an axisymmetric impulsive ring load applied at $x = 0$. (See, for example Figure 2). The shell itself has just <u>two</u> characteristic lengths, namely h, (thickness) and a, (radius).

If the impulsive load is idealized as

$$p(x, \theta, t) = I_o \, \delta(x) \, \delta(t) \tag{4-8}$$

where $\delta(x)$ and $\delta(t)$ are Dirac-delta functions in space and time, then there is no characteristic length (or characteristic time) associated with the loading. Finally, suppose that we consider only a single wave speed, c, associated with wave propagation.

When such an idealized problem is analyzed by Bernoulli-Euler shell theory, wave propagation through the thickness, h, is ignored. Thus, there exists only <u>one</u> characteristic length (namely a, the radius) in the Bernoulli-Euler problem, and the corresponding characteristic time is

$$T_{B.E} = \frac{2\pi a}{c} \tag{4-9}$$

which is the time for a wave to travel once around the shell. In fact, if we use

$$c = c_p = \sqrt{\frac{E}{\rho(1 - \nu^2)}} \tag{4-10}$$

* Including Drs. T. L. Geers (Lockheed, Palo Alto), G. A. Hegemier (Univ. of Calif, San Diego) and J. P. Jones (Aerospace Corp., El Segundo).

(see Ref. 17) for the wave speed in Equation (4-9), the result is

$$T_{ring} = \frac{2\pi}{\omega_o} \tag{4-11a}$$

where

$$\omega_o = \frac{1}{a}\sqrt{\frac{E}{\rho(1 - \nu^2)}} \tag{4-11b}$$

is the frequency of the axi-symmetric, plane strain, "ring mode" (c.f., Ref. 21). (This simplified discussion is based on the tacit assumption that the shell is very "thin", in the sense that the thickness/radius ratio, h/a, is very small - i.e., $h/a \rightarrow 0$.)

Now consider the same problem when analyzed by a Timoshenko-type shell theory. Wave propagation through the thickness is not ignored, and the problem contains <u>two</u> characteristic lengths (h and a) with the associated times

$$T_{ring} = \frac{2\pi a}{c} = \frac{2\pi a}{c_p} = \frac{2\pi}{\omega_o} \tag{4-12}$$

(around the circumference)

and

$$T_{ts} = \frac{2h}{c} = \frac{2h}{c_s} = \frac{2\pi}{\omega_s} \tag{4-13a}$$

where

$$\omega_s = \frac{\pi c_s}{h} \tag{4-13b}$$

is the lowest simple thickness-shear frequency (see Ref. 15) discussed in Section 3.0. (Again it is assumed that the ratio h/a is small, tending toward zero.)

In writing Equations (4-12) and (4-13a) we have actually used <u>two</u> wave speeds, c_p and c_s, for the speed, "c". We could equally well define two additonal characteristic times, namely

$$T_{s/\theta} = \frac{2\pi a}{c_s} \tag{4-14a}$$

and

$$T_{o/h} = \frac{2h}{c_p} \tag{4-14b}$$

(which together with Equations (4-12) and (4-13) make a total of <u>four</u>). However, the latter two (Equations 4-14a and b) are of minor significance for the problem under discussion.

The preceding paragraphs suggest that Bernoulli-Euler shell will have a time-dependence of the form

$$w(x, t) \sim A_o \cos(\omega_o t + \phi) \tag{4-15}$$

(since ω_o is the <u>only</u> characteristic frequency in this case) whereas the Timoshenko theory will give

$$w(x, t) \sim A_o \cos(\omega_o t + \phi) + B \cos(\omega_s t + \psi) \tag{4-16}$$

since it possesses <u>two</u> characteristic frequencies, ω_o and ω_s. (The phase angles, ϕ and ψ, depend upon the initial conditions for w and $\frac{\partial w}{\partial t}$.)

The idea that the Bernoulli-Euler theory (Equation 4-15) is included within the more exact, Timoshenko theory (Equation 4-16) is conveyed by the fact that the latter reduces to the former as the "amplitude" B tends to zero in Equation (4-16). Of course, the appropriateness of one theory or the other now depends upon the relative magnitudes of A_o and B.

In fact, these "amplitudes" are actually functions of space, i.e.,

$$A_o = A_o(x)$$

$$B = B(x)$$

and it was pointed out previously that the ratio B/A_o is significant near the wavefront, where shear and rotary inertia are important. Furthermore, for "short" times i.e., on the order of

$$T_{ts} \leq t \leq T_{ring} \tag{4-17}$$

the wavefront is still relatively near the plane of loading ($x = 0$) and short wavelength, high-frequency waves are still present near the origin to give difficulty for Bernoulli-Euler theory. Thus, it is clear that the deflection at the origin, namely $w(0, t)$, cannot coincide identically for the two theories, at least beginning from time $t = 0$ and until time $t = T_{ts}$.

At the later times, i.e., $t >> T_{ts}$, the thickness-shear mode has undergone many vibration cycles and indeed the ratio B/A_o may then approach zero at the origin ($x = 0$). In this case, the more exact Timoshenko theory may degenerate into Bernoulli-Euler theory and the displacement time histories coincide at $x = 0$, (i.e., at least well away from the wavefront).

This intuitive discussion can be put on a more rigorous basis by using the Fourier Transform (k, x) and Laplace Transforms, (s, t) in conjunction with the appropriate shell theories. Approximate results (i.e., asymptotic expansions) can be obtained by expanding the transforms as the Laplace parameter $s \rightarrow \infty$, i.e., time $t \rightarrow 0$, etc. Indeed, readers thoroughly familiar with elastic wave propagation may be able to provide references where such an approach has been carried out for the loading

$$p(x, \theta, t) = I_o \, \delta(x) \, \delta(t)$$

and geometry considered here. However, it was beyond the scope of the present contract to generate or extensively search for such analytical solutions.

Additional Experimental Results for the Thick-Walled Shell

The lack of quantitative agreement between theory and experiment for the thick-walled shell was somewhat disturbing, especially in view of the following items:

- Previous holographic measurement of wave propagation (in beams and plates, Refs. 7, 8) had been successfully correlated with computer solutions.
- The results presented herein (Section 3.0) for the thin-walled shell, agree reasonably well with calculations (e.g., see Figure 26).
- The computer program (Ref. 17) has been amply verified by testing it against known, previous solutions, and finally
- Examples are available (e.g., Ref. 27) which show that (at

least for specific problems) the solutions using Timoshenko shell theory approach those of Bernoulli-Euler theory (at sufficiently long wavelengths).

In an effort to clarify and to better understand the thick shell results, additional interferograms were analyzed to provide more deflection data. The experimental results, showing the radial deflection, w, vs. axial position, x, (for several discrete times) are shown in Figure 46. This family of curves illustrates typical wave propagation behavior, with the wavefront advancing (to the right) along the shell. This high-frequency, short-wavelength region occurs at the front of the wave, with the longer waves propagating more slowly and lagging behind. A feature of some interest is the behavior at the origin ($x = 0$), as a function of time, t. The central deflection(s) $w(0, t_i)$ from Figure 46 have been cross-plotted to give the time-history, $w(0, t)$, shown in Figure 47. The relatively smooth, continuous nature of the (albeit limited) experimental data in Figure 49 give strong support to the "consistency" of the present tests.

Also shown in Figure 47 is the calculated half-period, $T_o/2 = 75$ μsec, of the axi-symmetric ring mode of the shell. From the discussion of length scales and "characteristic times" presented previously, one might expect Bernoulli-Euler shell theory to predict a deflection time-history $w(0, t)$ involving a half period of $T_o/2$. On the other hand, Timoshenko theory will involve half-periods of $T_o/2$ and $T_{ts}/2$, and combinations thereof.

From an experimental standpoint, there are many more "characteristic times" in the physical problem than are indicated by Equations (4-12) and (4-13). For example, the input pulse has a duration $T = 10$ μsec, which may have a significant effect on the shell behavior. In addition, the finite width of the load, $-\varepsilon \leq x \leq \varepsilon$, of about 1/4 of an inch, introduces another characteristic length (for example, a flexural wavelength) which has an associated frequency, etc. Thus, it is not surprising to find an experimental "half-period" of approximately 50 μsec vs. an (idealized) result of $T_o/2 = 75$ μsec.

A thorough (analytical) study of this problem, including the effects of a finite width of the loading (in space) and a finite pulse duration (in time) would be of considerable interest, but such an analysis was beyond the scope of the present study.

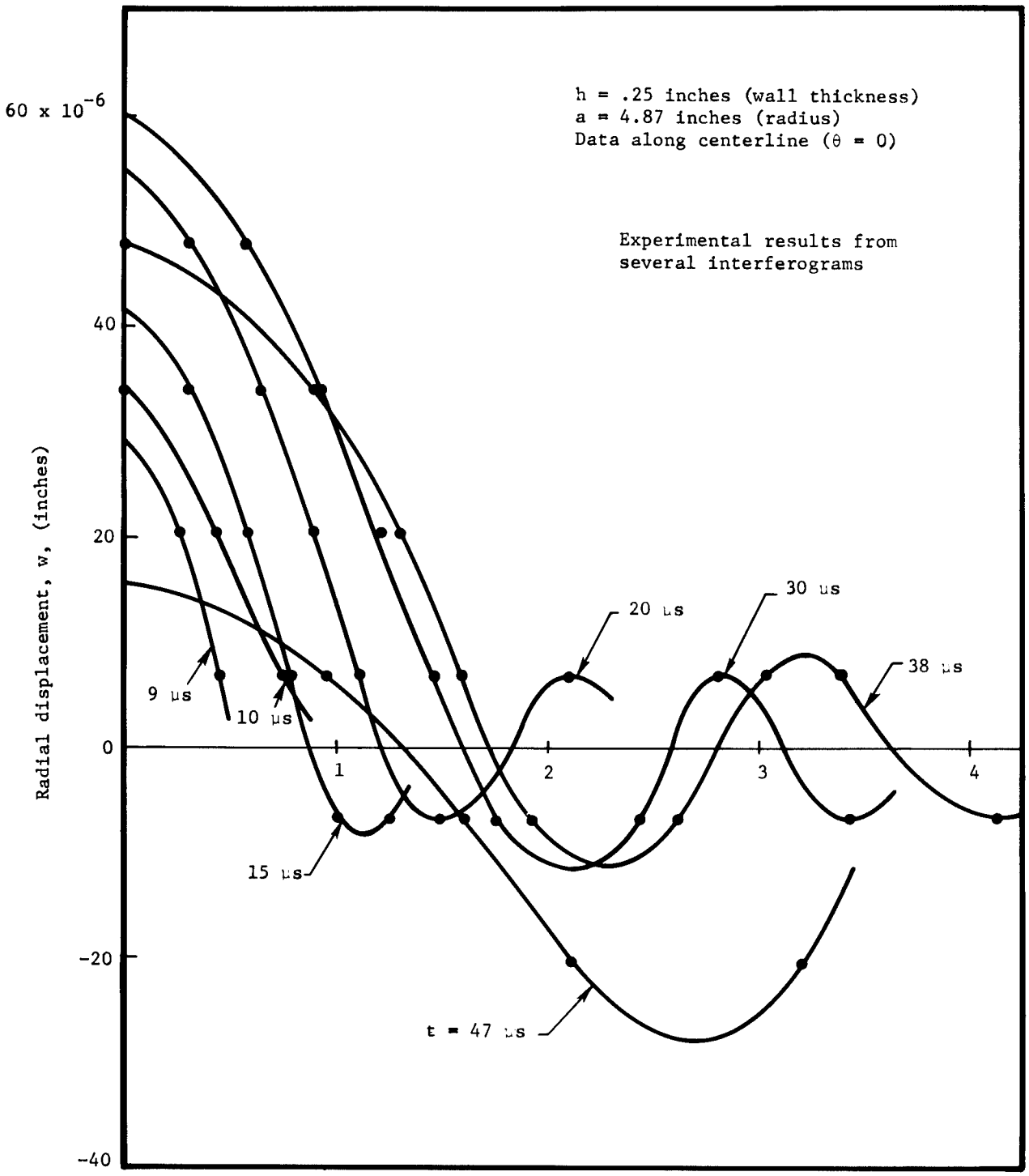

Figure 46: Radial deflection, w, vs. axial position, x. (Thick shell, no cut-outs.)

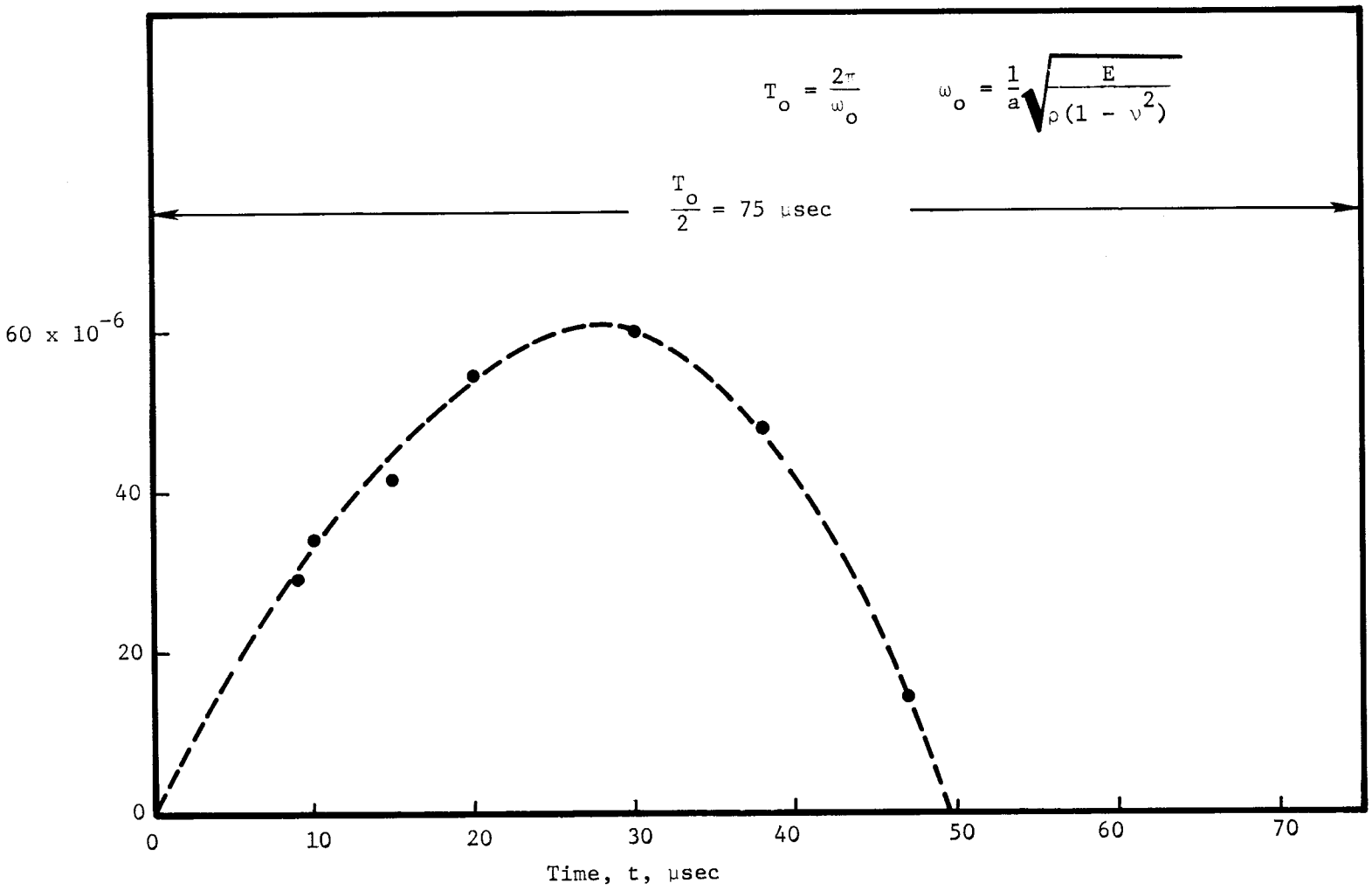

Figure 47: Radial deflection (at x = 0) vs. time, t. Thick-walled shell, no cut-outs.

Results from Elasticity Theory

Consider the following argument. The pulse duration, T = 10 μsec, is a characteristic time, which can be used to calculate a structural wavelength, Λ. In other words,

$$\Lambda_s = 2c_sT = 2(.1 \text{ in/}\mu\text{sec})(10\ \mu\text{sec})$$

$$\Lambda_s = 2 \text{ inches, based upon the shear wave speed, } c_s$$

Having this value of Λ, and knowing the radius $a \cong 5.0$ inches, the thickness $h = .25$ inches, we have

$$\frac{h}{a} = \frac{.25}{5} = .05$$

$$\frac{h}{\Lambda} = \frac{.25}{2} = .125$$

With these values, we enter Ref. 28 and use the tabulated results for the $n = 0$ (axi-symmetric) mode. Page 20, of Ref. 28 then gives

$$\Omega_1 = .034$$

for the corresponding frequency. But

$$\Omega_1 = \frac{\omega}{\omega_s} = .034$$

where $\omega_s = \frac{\pi c_s}{h}$ = Fundamental thickness/shear frequency.

Thus $$\omega = .034\ \omega_s$$

and the corresponding period of vibration is

$$T_{elast} = \frac{2\pi}{\omega} = \frac{2\pi}{\omega_s} \times \frac{1}{.034}$$

But $\frac{2\pi}{\omega_s} = T_s = 4.1$ μsec, (see Section 3.0) and we then have

$$T_{elast} = 4.1 \text{ μsec} \times \frac{1}{.034} = 120 \text{ μsec}$$

which results in a half-period of

$$\frac{T_{elas}}{2} = 60 \text{ μsec}$$

which is very close to the experimental result (T/2 = 50 μsec) shown in Figure 47.

Of course, it is recognized that the duration of the input pulse, namely T = 10 μsec is actually 10 μsec $\pm$ (some fraction) which influences the structural wavelength Λ. Furthermore, the theory of Ref. 28 is calculated for the assumption of steady, traveling wave trains with wavelength Λ. Thus, it is considered to be good agreement when the experimental half period is 50 μsec and the elasticity theory gives T/2 = 60 μsec.

Test Results for the Thin-Walled Cylinder

Wave Propagation Past a Circular Cut-Out - Experiments were conducted in which transverse waves were excited (and deflections recorded holographically) to study waves interacting with a circular cut-out. The thin-walled cylinder ($h = .106$ inches) was used in these tests, and the diameter of the cut-out was $d = 2.0$ inches. The impulsive load was applied at the longitudinal station $x = 0$, and the cut-out was centered at $x = 6.0$ (inches) to the right of the loading plane.

Tests were conducted following the procedures outlined previously in Section 3.0. A typical interferogram of the transverse wave interacting with the cut-out (at time $t = 59$ μsec) is shown in Figure 48. The corresponding deflection data (w vs x) are presented in Figure 49, for the centerline, i.e., $\theta = 0$. Non-symmetric behavior, caused by the interaction of an axi-symmetric wavefront with the cut-out, is evident in the interferogram. The high-frequency, short-wavelength, ripples (in the circumferential direction, θ, Figure 48) indicates the presence of circumferential harmonics (i.e., $w \sim \cos n\theta$) of high wave-number, n.

Additional interferograms, showing the wave passing the cut-out and the formation of a "shadow zone" to the right (beyond the cut-out) are presented in Figures 50 through 52. (For the earlier times, $t \leq 59$ μsec, see Appendix E.) The presence of short-wavelength, circumferential harmonics near the cut-out are evident in the interferograms.

Wave Propagation Past a Square Cut-Out - Similar tests were conducted on wave propagation past a square cut-out in the thin-walled shell. The square cut-out was 2.0 inches (on a side) and centered at $x = -4$ (inches). That is, the cut-out was centered 4 inches to the left of the loading plane, $x = 0$. Several interferograms (which show the wave approaching and engulfing the cut-out) are presented in Figures 53 through 58.

A typical plot of the radial deflection for this problem is given in Figure 59, $t = 60$ μsec. Note the large gradients $\left(\frac{\partial w}{\partial x}\right)$ near the edge of the cut-out; see Figures 54 and 55. Non-axisymmetric behavior is apparent in the interferograms, as indicated by the circumferential ripples in the dark interference fringes. The "shadow zone" caused by the cut-out is quite evident as well, c.f. Figure 58. Although it would be desirable to reduce these highly "two-dimensional" results to give quantitative data (e.g., in both x and θ) such a reduction was not possible during the present study.

Additional results (showing the behavior at other times, t_i) are given in Appendix E. When computer programs become available which can (economically) handle such non-symmetric, two-dimensional behavior, it is hoped that they will be compared with the holographic results given herein.

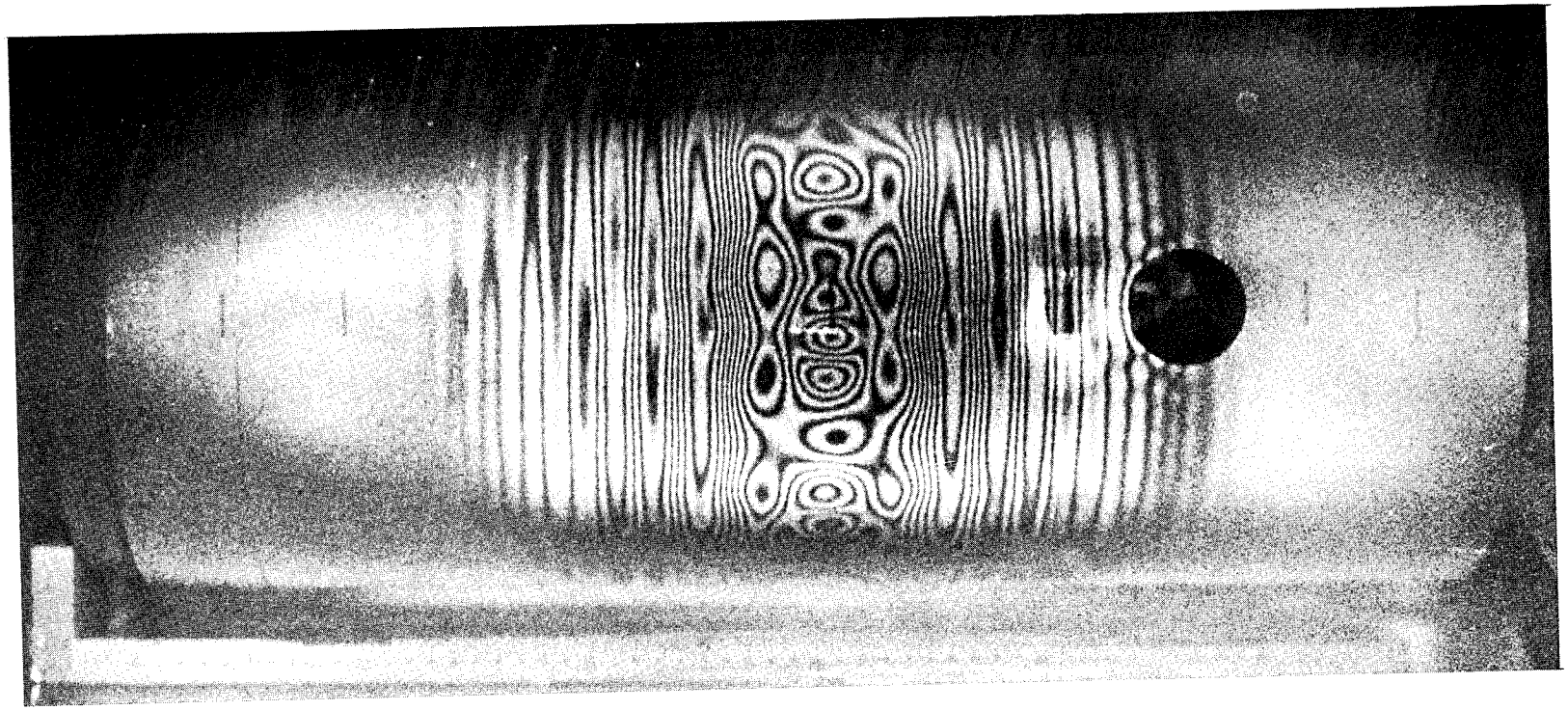

Figure 48: Wave interacting with circular cut-out. (Thin shell, h = .106 inches, wall thickness. Cut-out diameter, d = 2.0 inches. Time t = 59 μsec.)

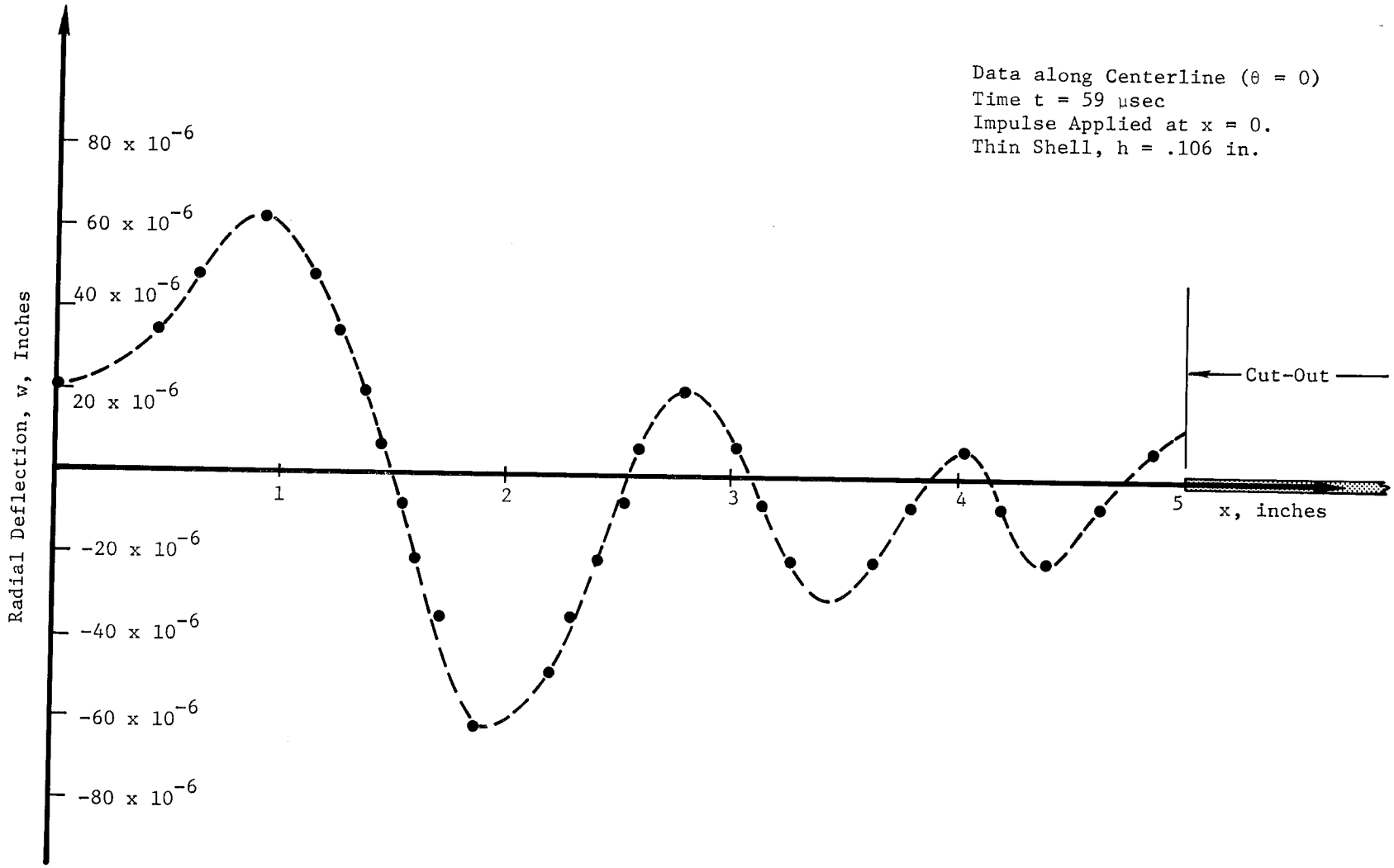

Figure 49: Radial Deflection, w, as a Function of Position along the Shell. (Wave Interacting with a Circular Cut-Out; see Figure 48).

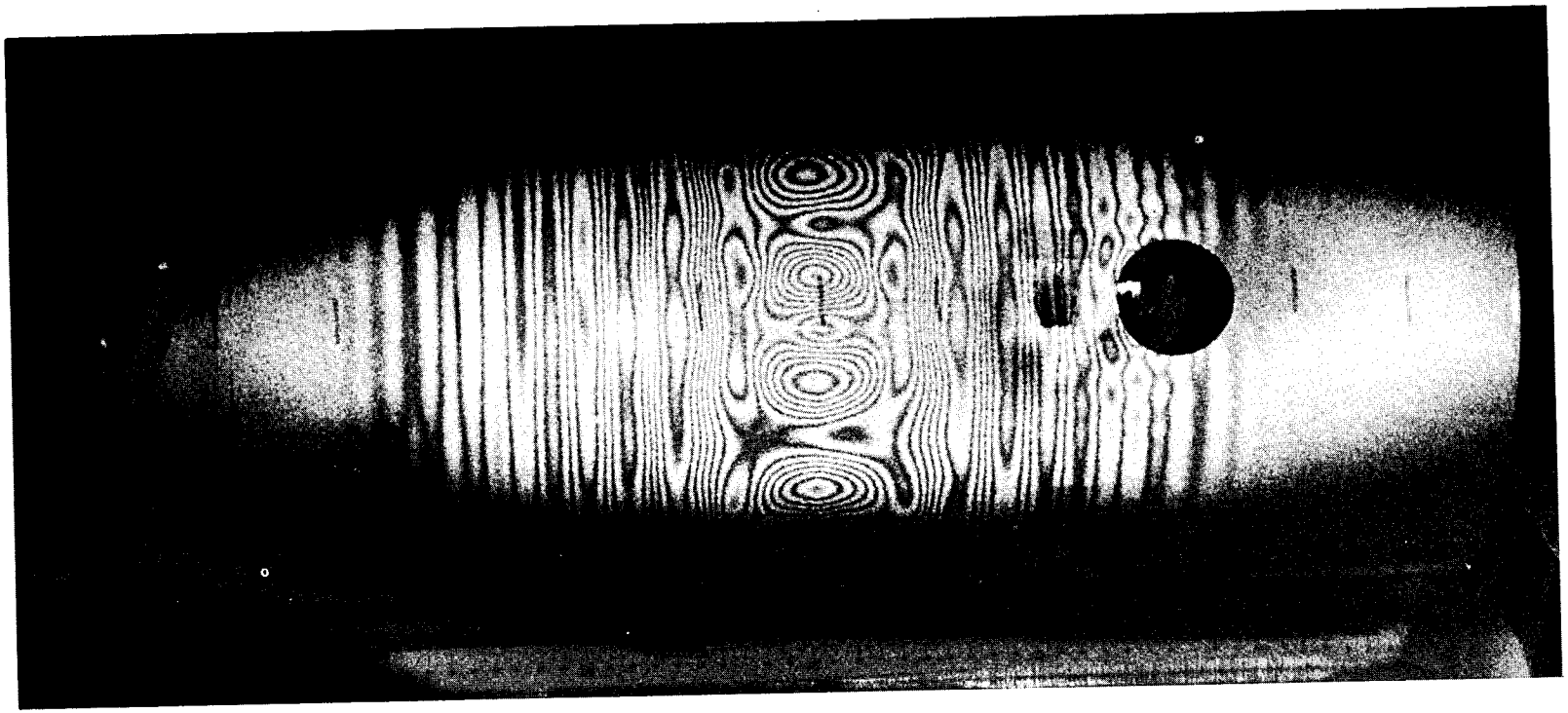

Figure 50: Transverse Wave Interaction with a Circular Cut-Out.
Time t = 70 μsec

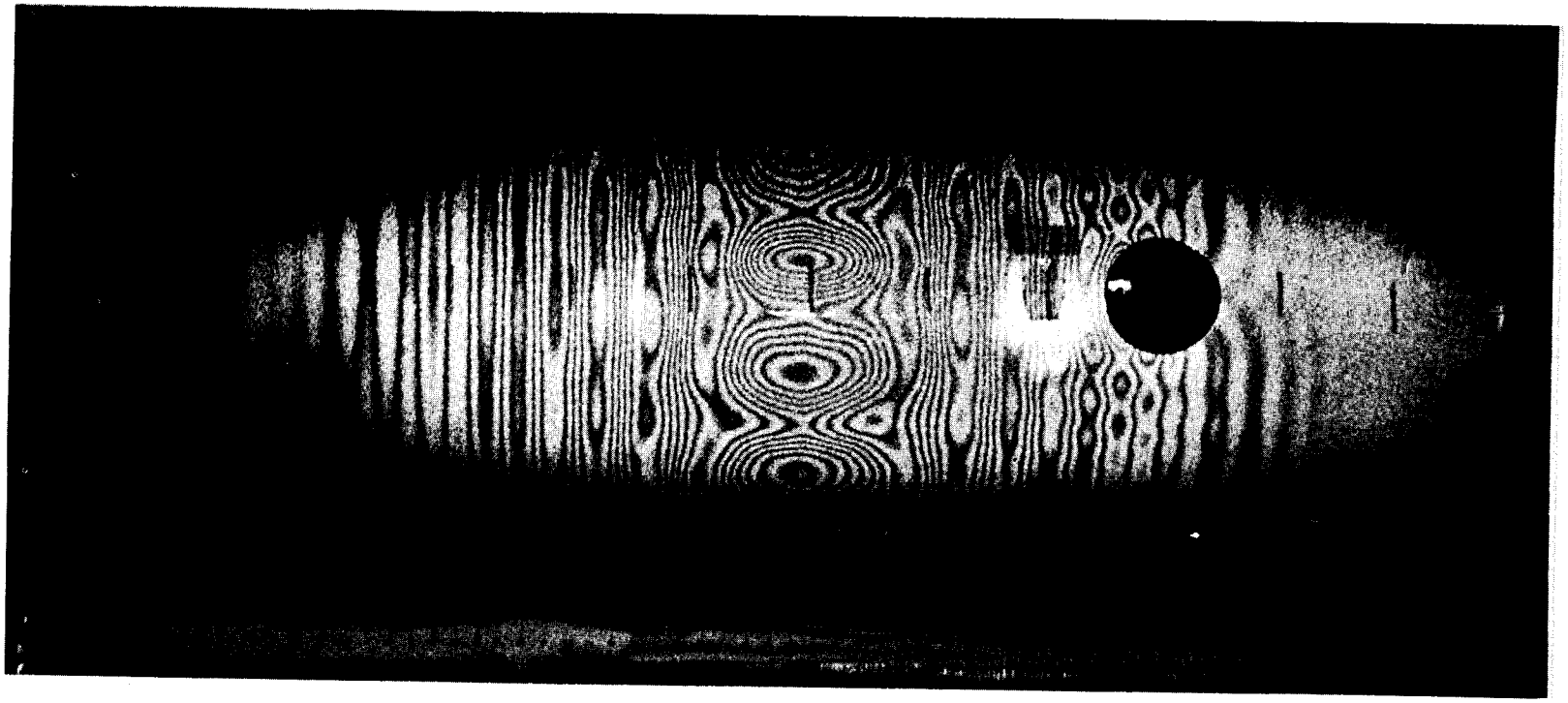

Figure 51: Transverse Wave Interaction with a Circular Cut-Out.
Time t = 80 μsec

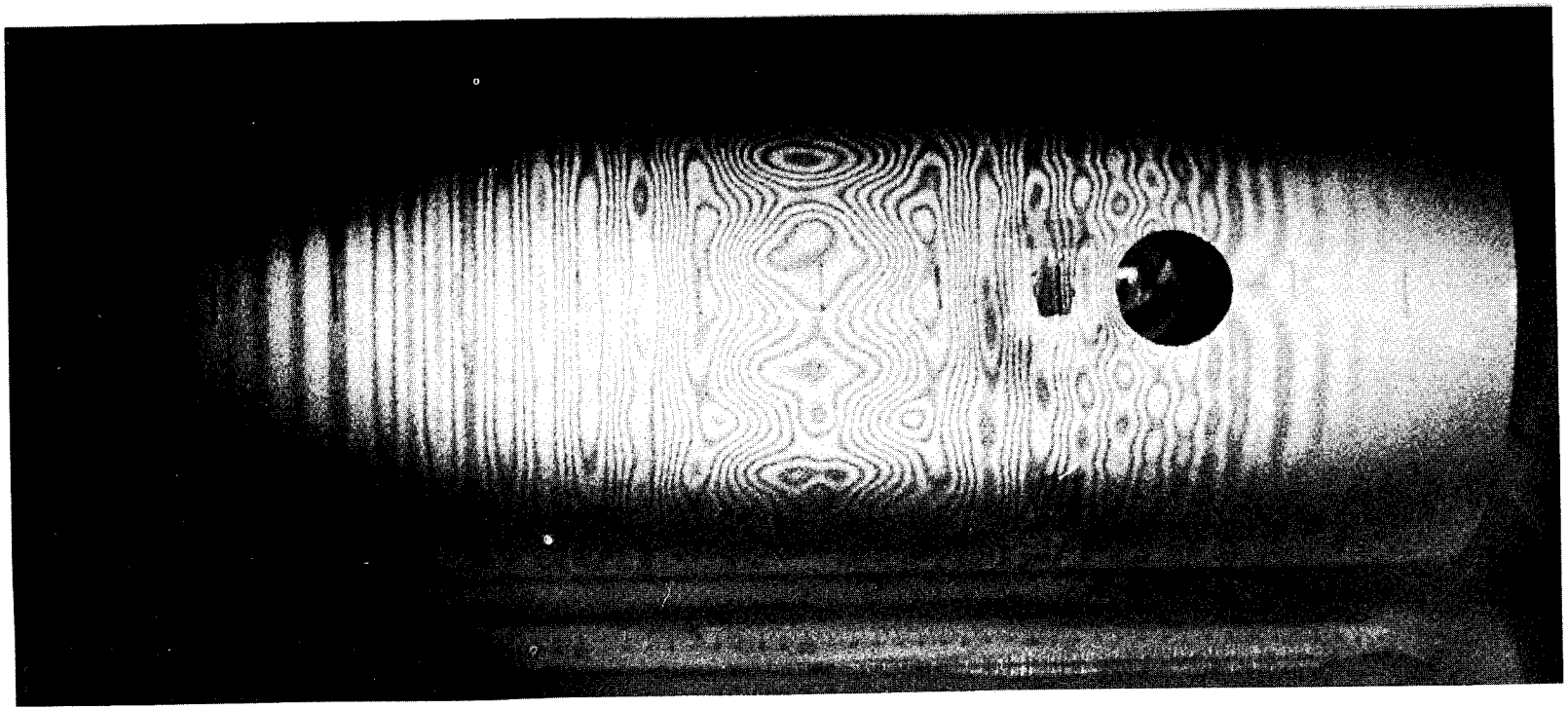

Figure 52: Transverse wave interaction with a circular cut-out. Time t = 92 μsec.

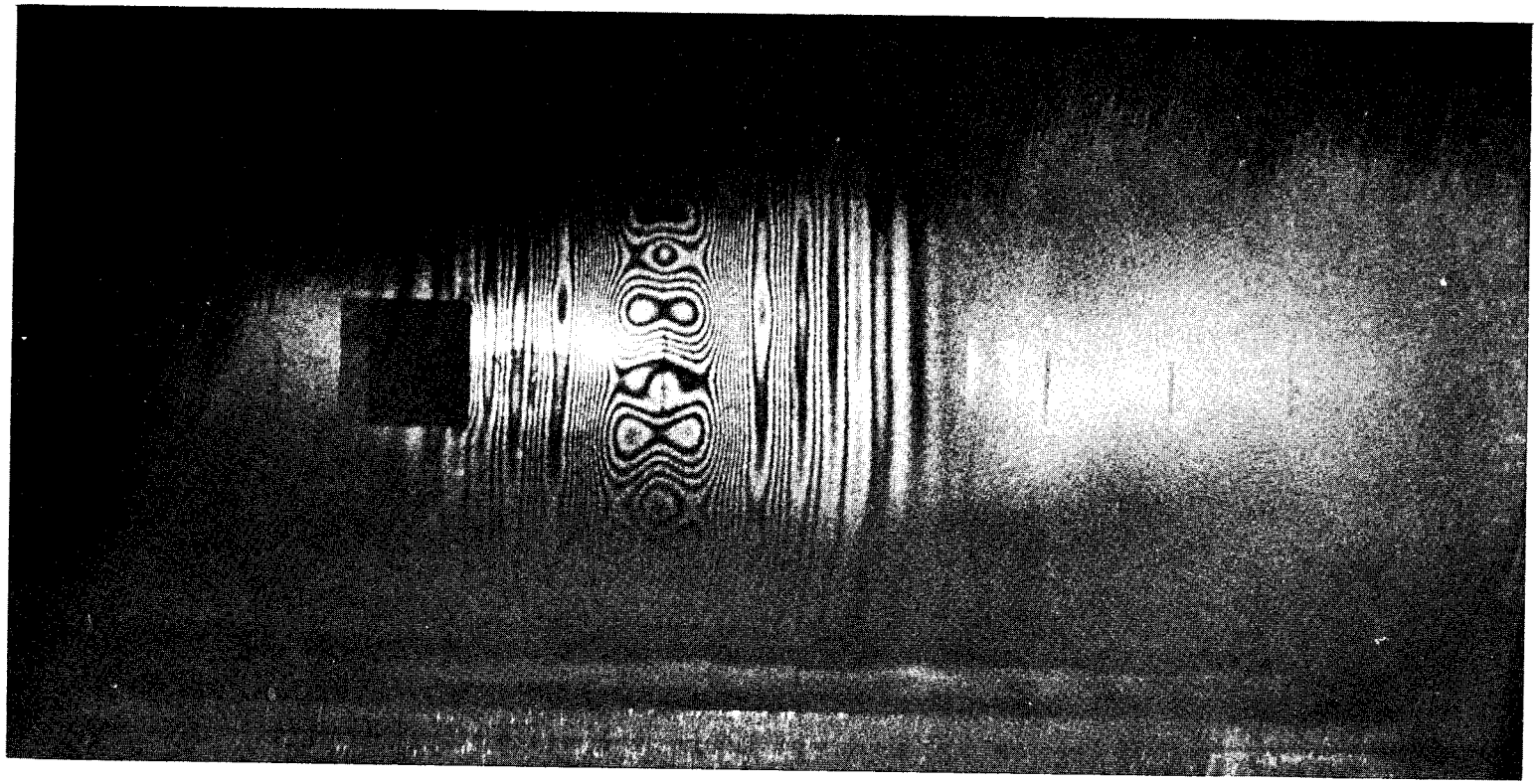

Figure 53: Wave propagation past a square cut-out. Time t = 39 μsec. (Thin shell, h = .106 wall thickness.)

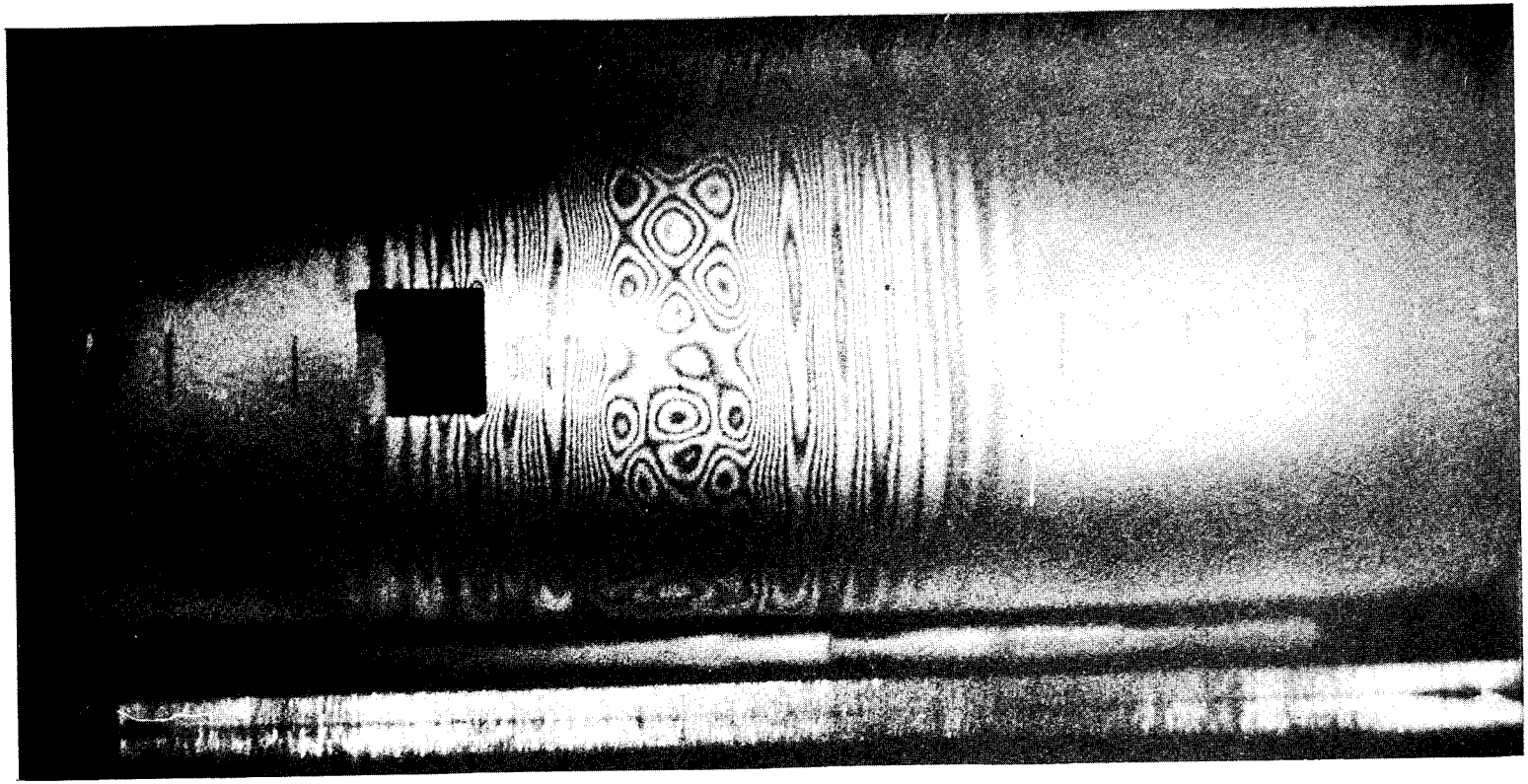

Figure 54: Wave propagation past a square cut-out. Time t = 50 μsec. (Thin shell, h = .106 wall thickness.)

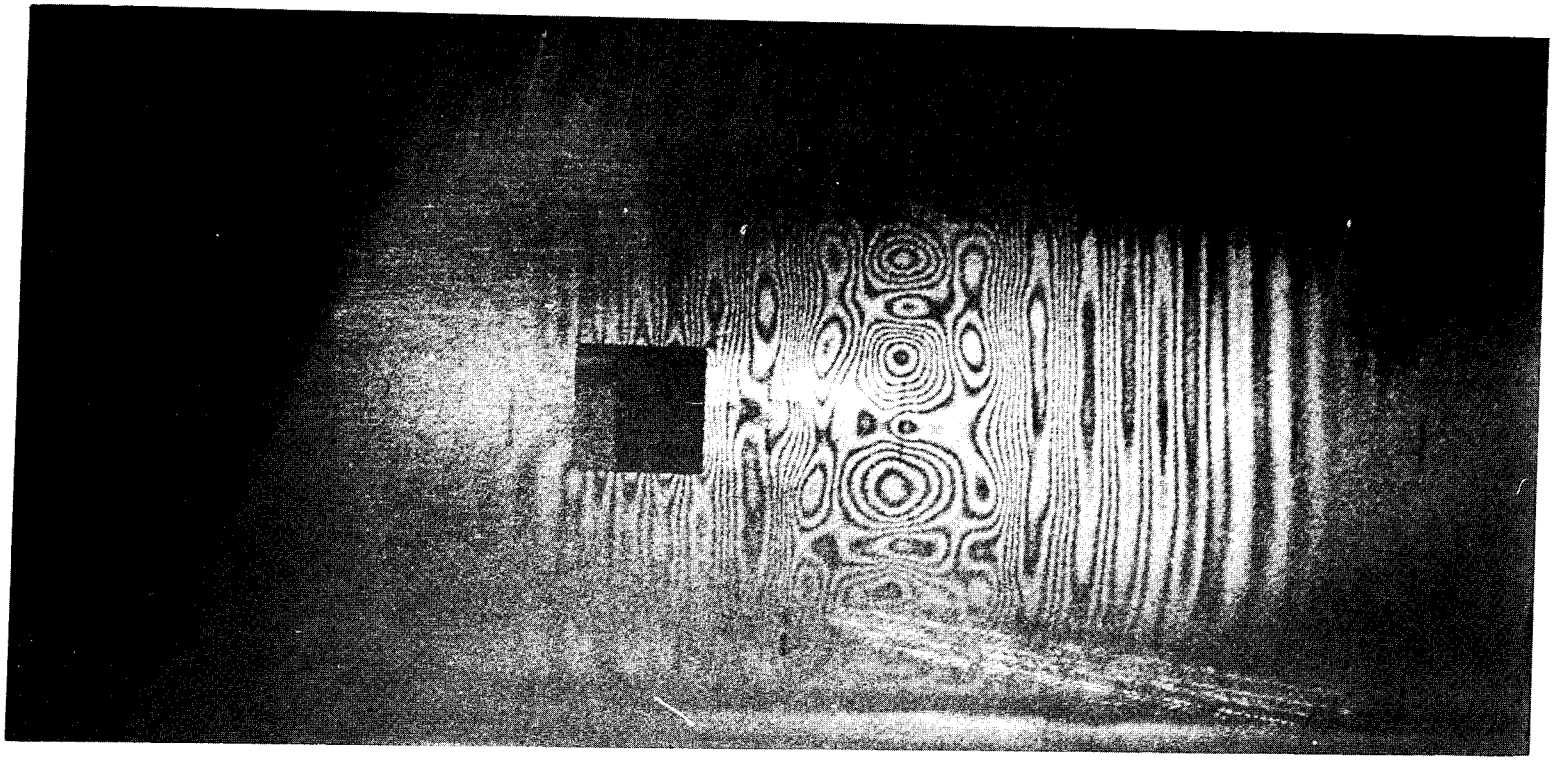

Figure 55: Wave propagation past a square cut-out. Time t = 60 μsec. (Thin shell, h = .106 wall thickness.)

Figure 56: Wave propagation past a square cut-out. Time t = 71 μsec. (Thin shell, h = .106 wall thickness.)

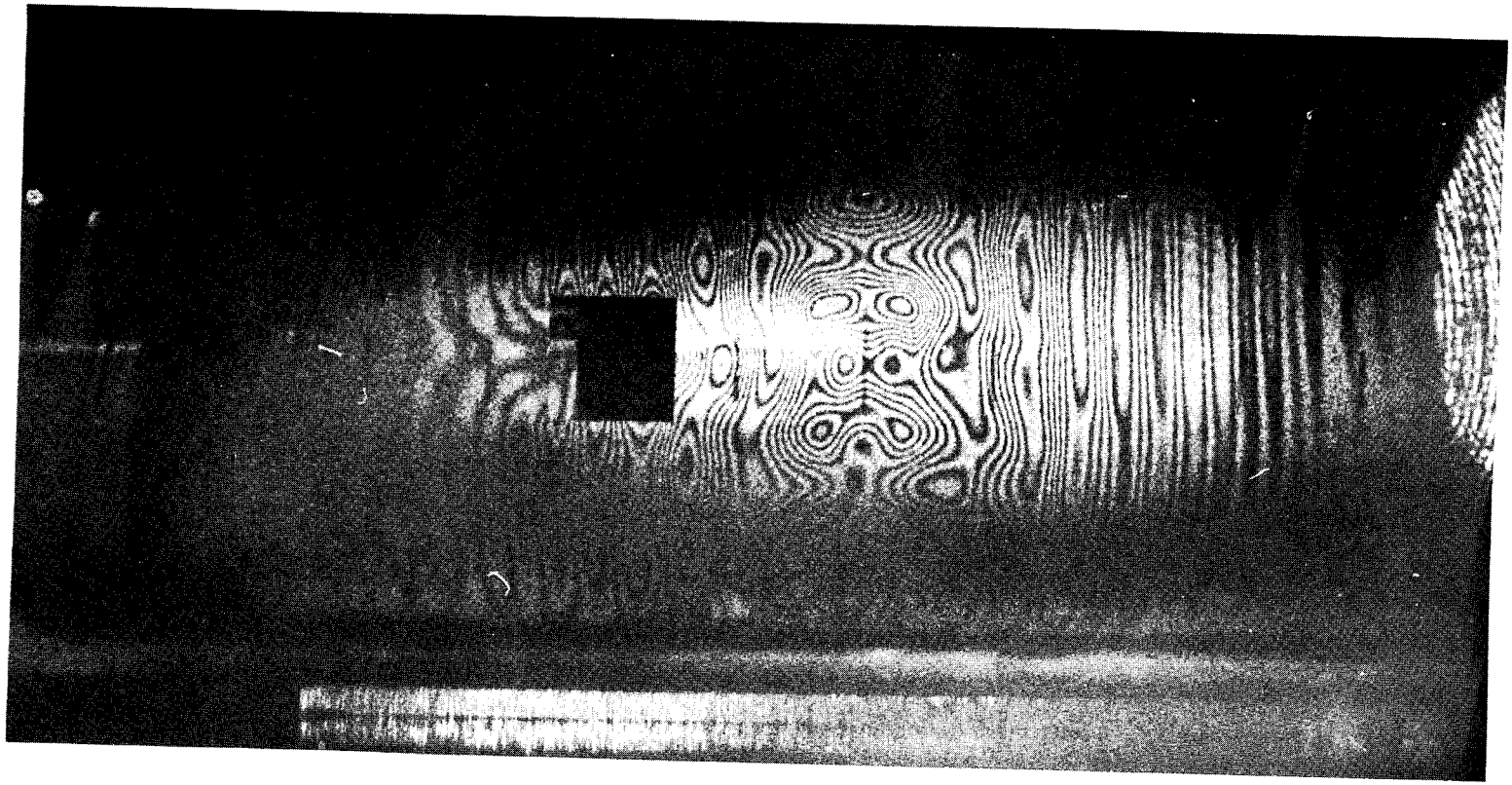

Figure 57: Wave propagation past a square cut-out. Time t = 81 μsec. (Thin shell, h = .106 wall thickness.)

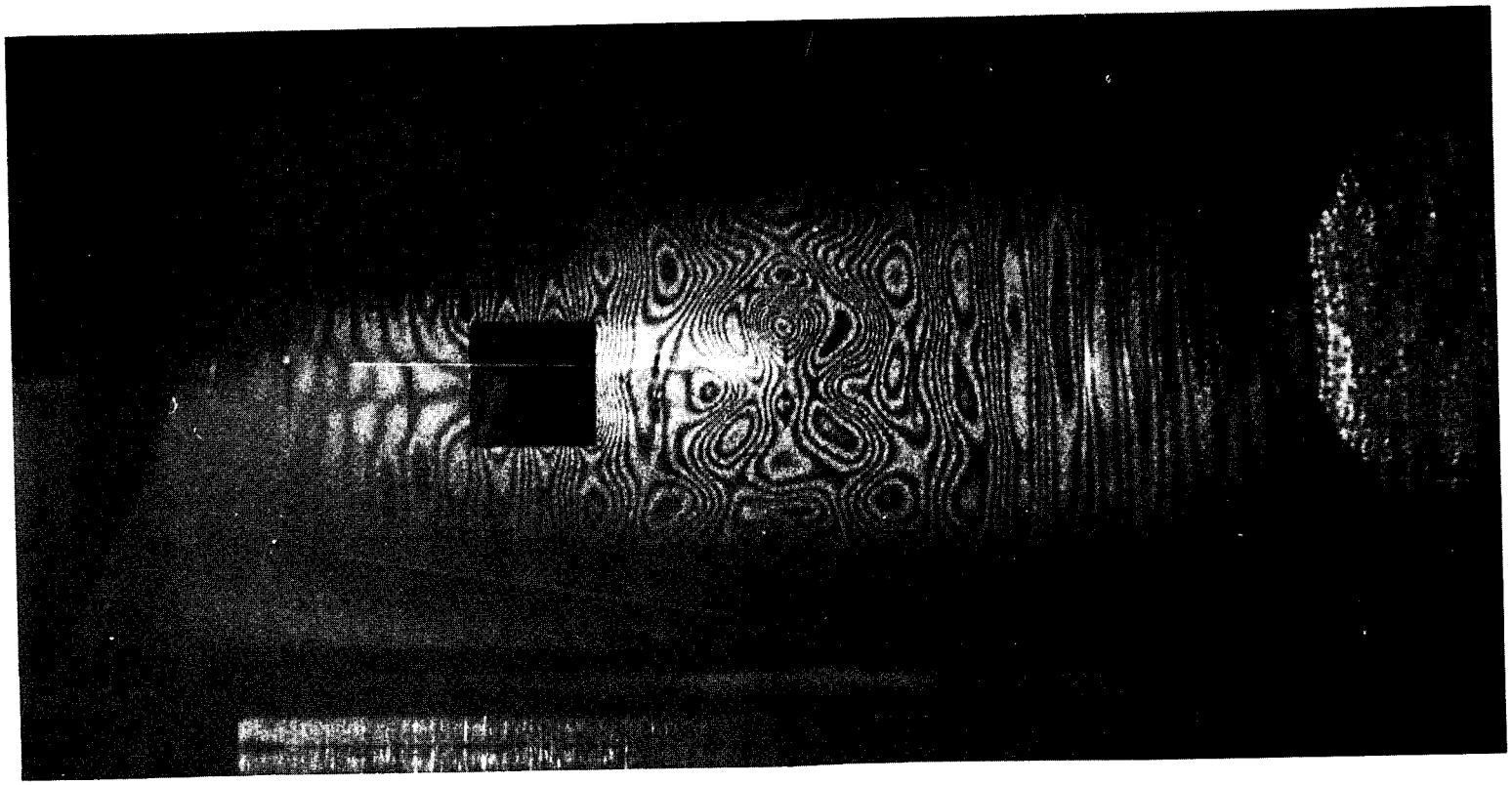

Figure 58: Wave propagation past a square cut-out. Time t = 92 μsec. (Thin shell, h = .106 wall thickness.)

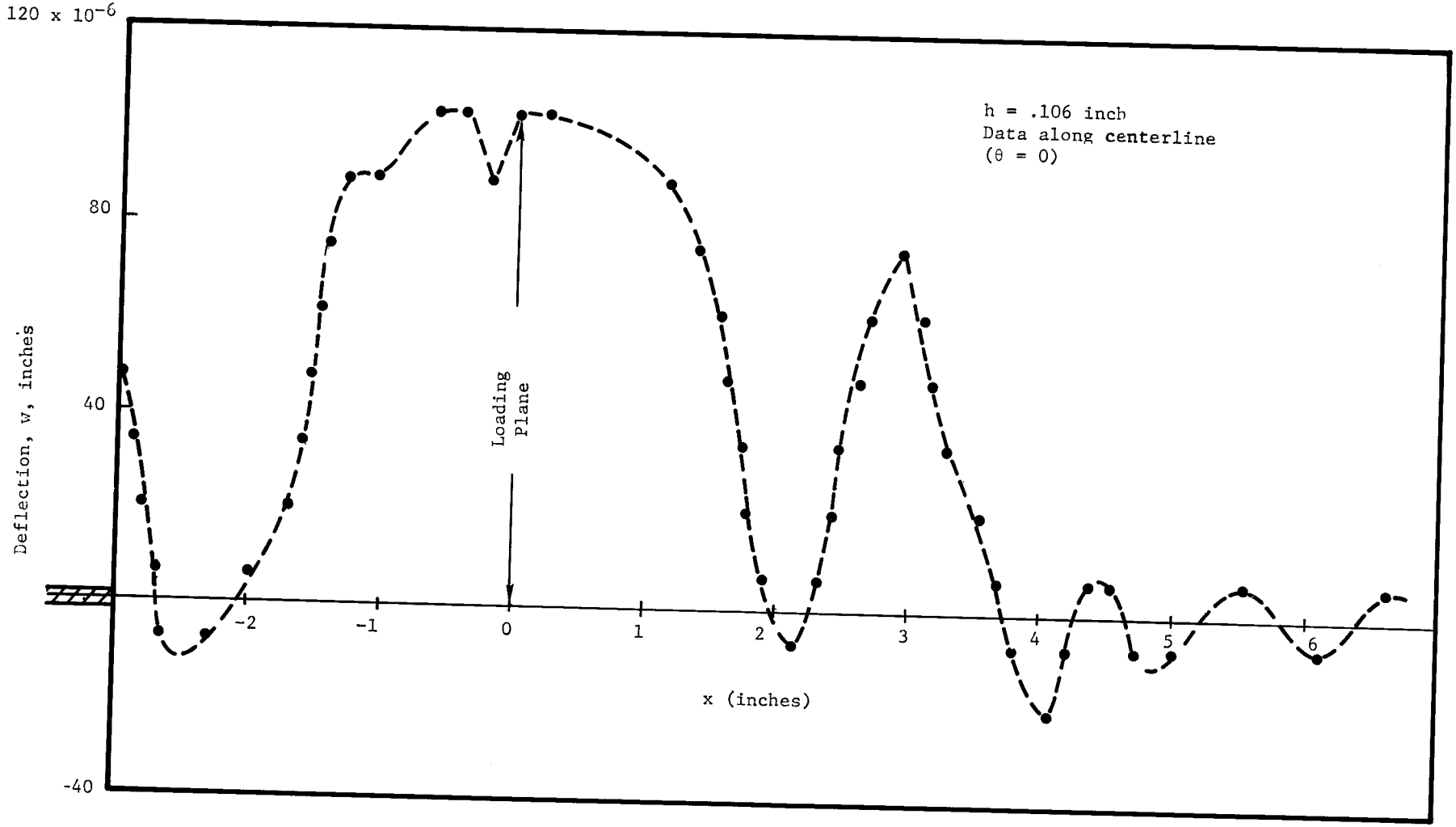

Figure 59: Radial deflection, w, vs. axial position, x. (Thin-walled shell, square cut-out, t = 60 μsec, c.f. Figure 55.)

Wave Interaction with a Stiffening Ring - The final test series (using the thin-walled shell) was designed to record the interaction of an axisymmetric wave with an axisymmetric ring stiffener. The ring stiffener had a rectangular cross-section with a width of .5 inches and a depth of 1.0 inches. It was centered approximately 4.0 inches to the left of the loading plane (x = 0).

Typical interferograms for this problem are shown in Figures 60 through 63. The appearance of non-symmetric modes (i.e. cosnθ) when the wave hits the stiffener are evident in Figure 62. Deflection data (w vs. x) for one interferogram are shown in Figure 64. Additional interferograms are presented in Appendix E.

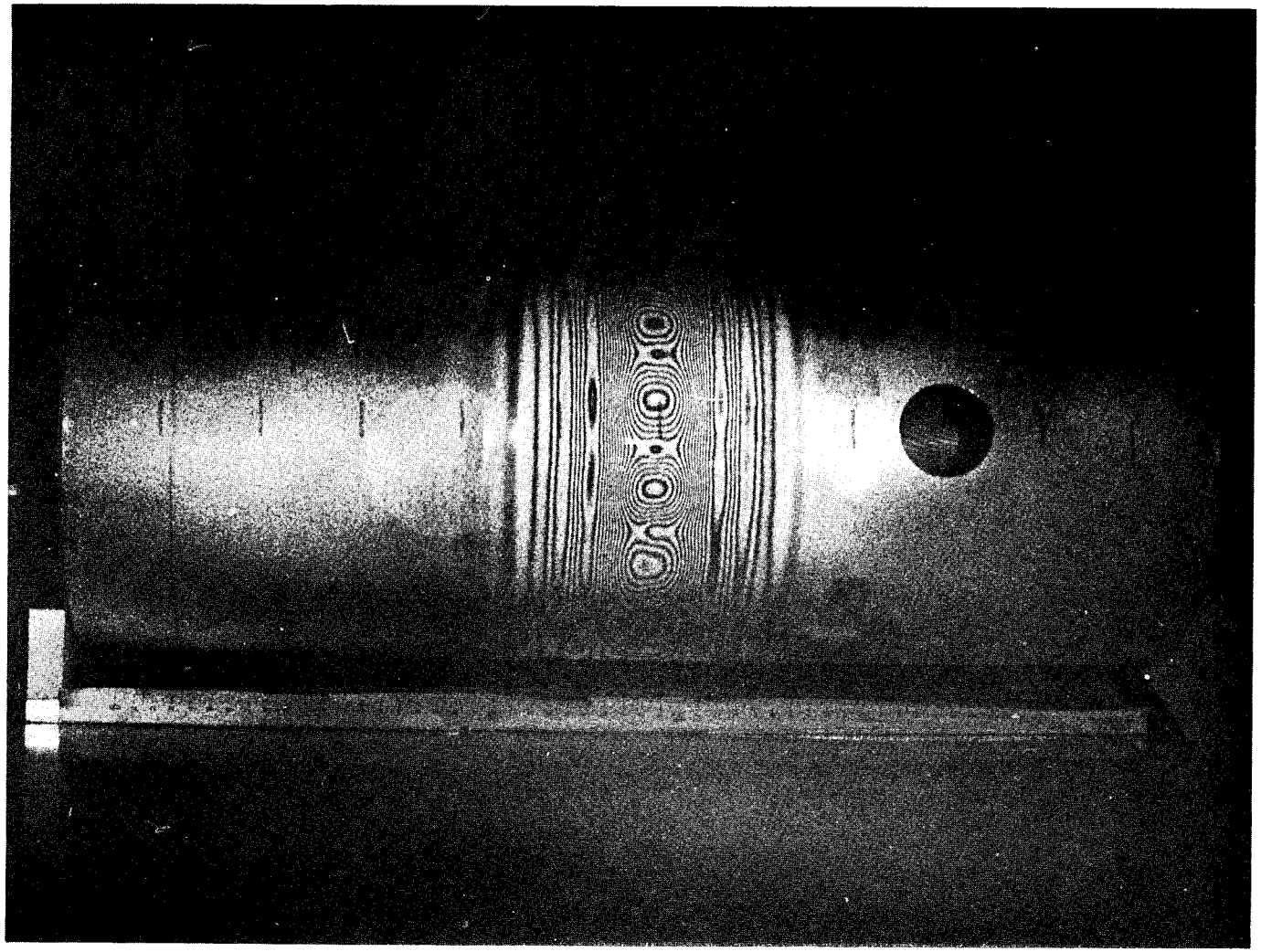

Figure 60: Wave Interacting with the (Internal) Stiffening Ring (on the left, at x = -4 inches) and the Cut-Out (on the right). Time t = 30 μsec

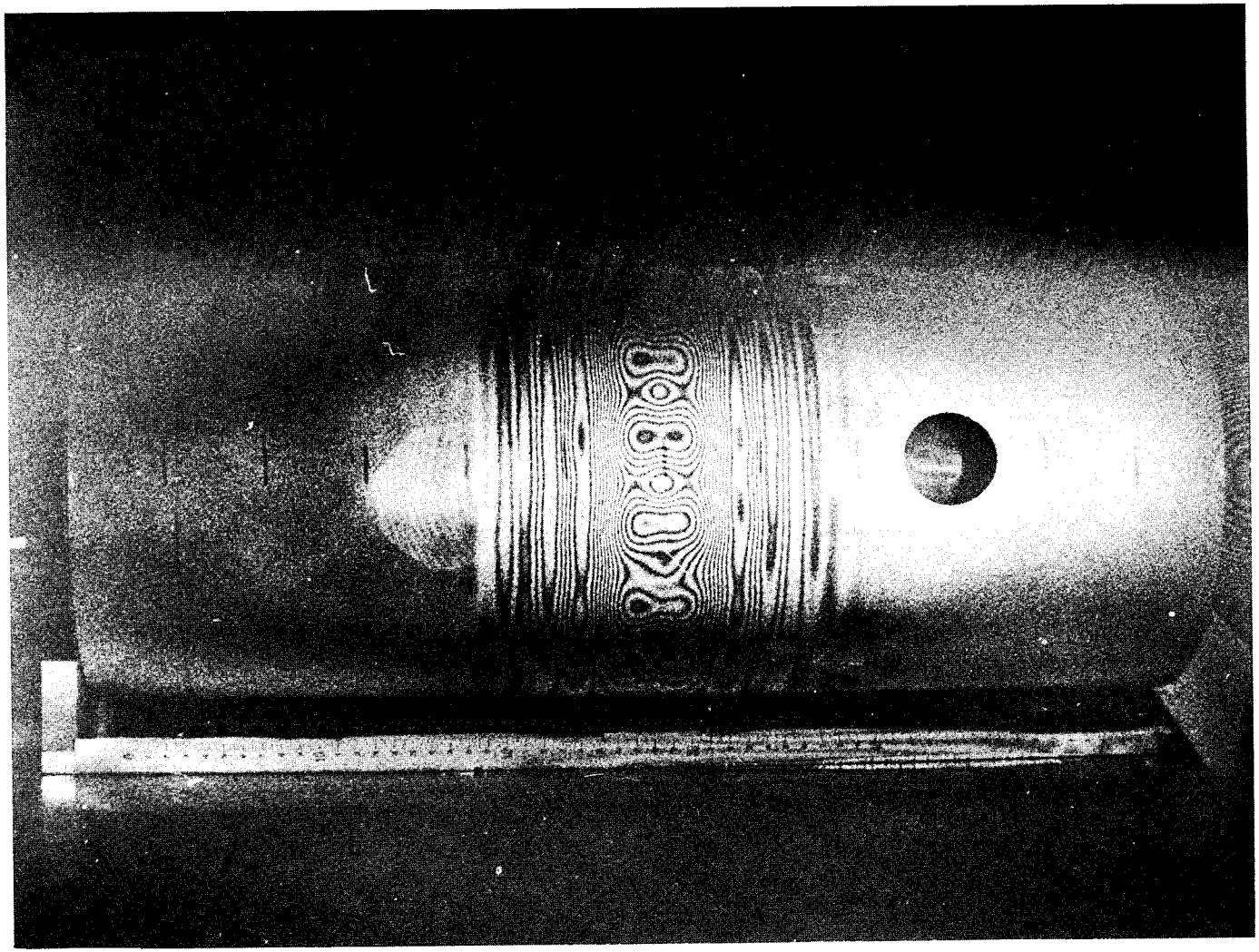

Figure 61: Wave Interacting with the (Internal) Stiffening Ring (on the left, at x = -4 inches) and the Cut-Out (on the right). Time t = 40 μsec

Figure 62 : Wave Interacting with the (Internal) Stiffening Ring (on the left, at x = -4 inches) and the Cut-Out (on the right). Time t = 49 μsec

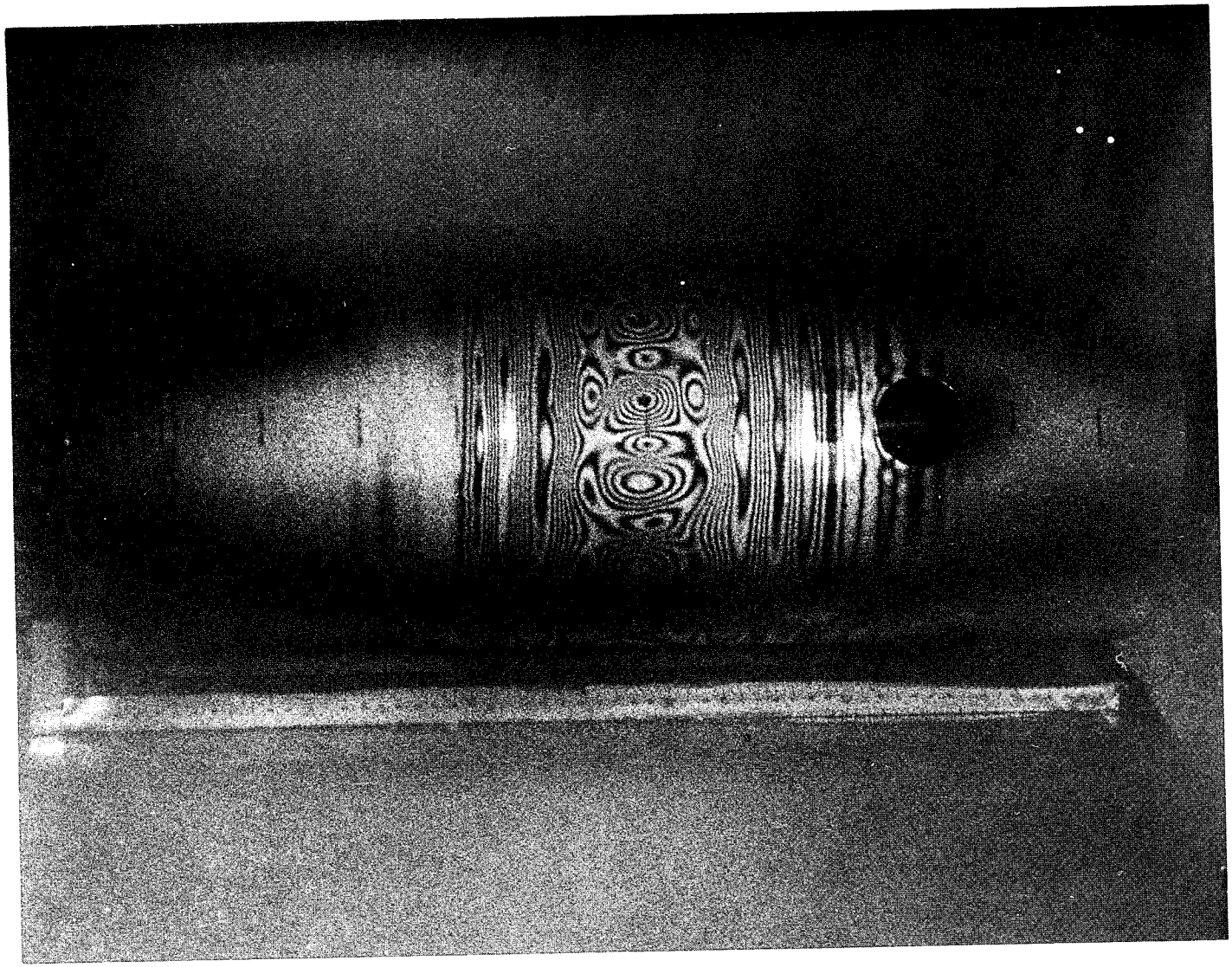

Figure 63: Wave interacting with the (internal) stiffening ring (on the left, at x = -4 inches) and the cut-out (on the right). Time t = 60 μsec.

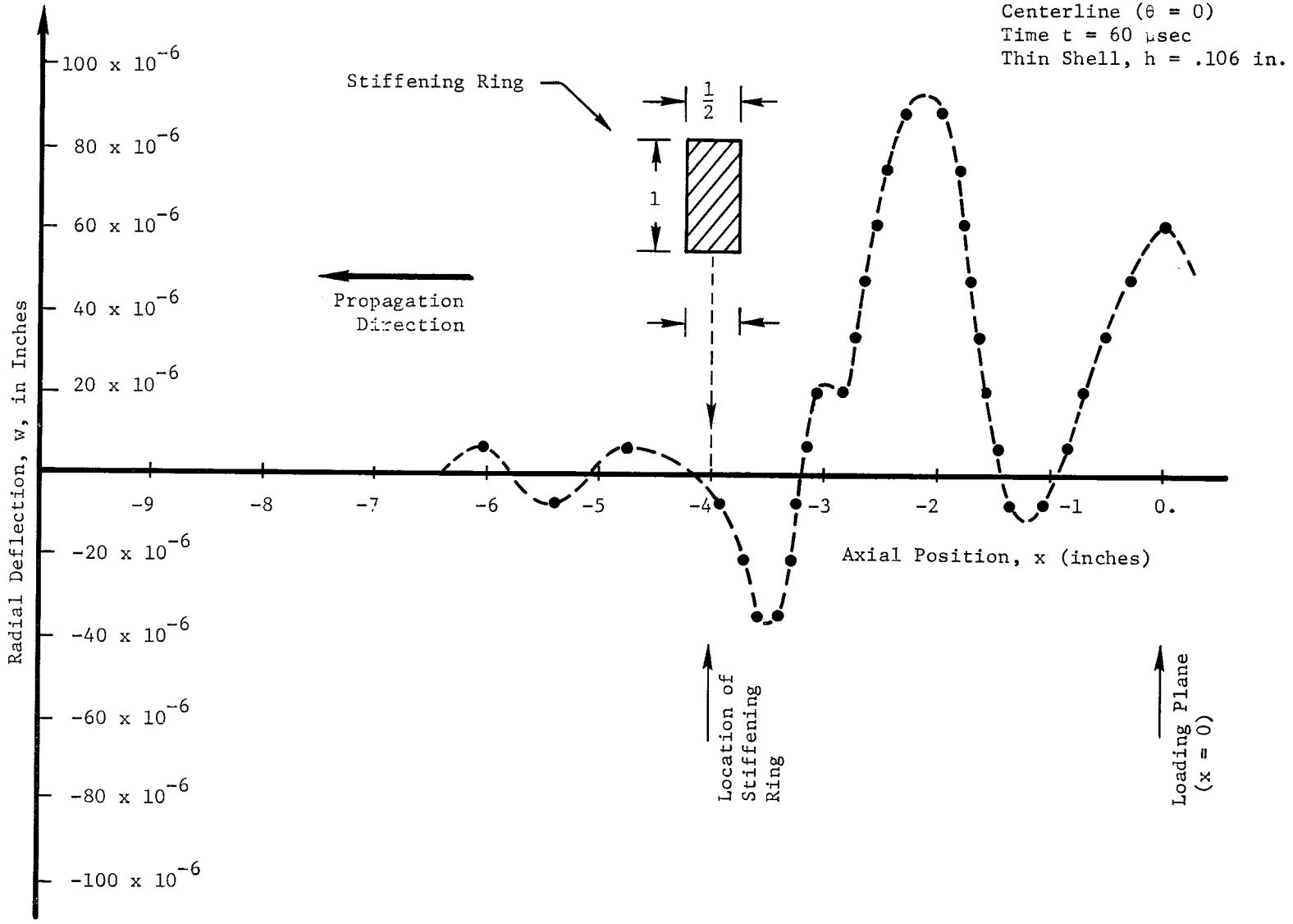

Figure 64: Radial Deflection, w, as a Function of Position along the shell. (Wave Propagating to the left, past the Stiffening Ring at x = -4.)

5.0 WAVE PROPAGATION IN CONICAL SHELLS

Introduction and Background

In addition to the tests on cylindrical shells, it was desired to obtain data for wave propagation in conical shells as well. Two conical specimens were tested, and the results of the tests are given in the following paragraphs.

Tests on the Cone-Cylinder Specimen

A thin-walled cone-cylinder specimen was obtained for use in these tests. The dimensions of the specimen are given in Figure 65, and a photograph of the actual model is given in Figure 66.

In order to apply the loading pulse (electromagnetically) the loading wire was located in the larger end of the specimen. Initial tests were conducted with the load applied at $x = 1.0$, i.e., approximately 1 inch from the large end of the cone.

A typical interferogram for this test arrangement is given in Figure 67. The corresponding deflection data are given in Figure 68. As the waves propagate longitudinally along the cone, the appearance of non-symmetric modes (i.e., cos n θ) becomes evident. The development of the non-symmetric response is evident in Figures 69 through 72. Additional interferograms are given in Appendix F.

Tests on the Large Conical Shell

In order to investigate waves propagating in a larger shell, another conical specimen was built. A sketch showing the shell geometry is given in Figure 73. A photograph of the shell itself is given in Figure 74.

The test procedure and experimental set-up were similar to those discussed previously. The shell has a thickness $h = .094$ inches, and it was loaded with the repelling-wire device discussed previously. A typical hologram for this test series is given in Figure 75. The corresponding deflection w (as a function of the length, s, along the cone) is given in Figure 76.

Additional interferograms are given in Figures 77 through 79, which again demonstrate non-symmetric behavior (i.e., cos n θ modes). Finally, additional interferograms are presented in Appendix F.

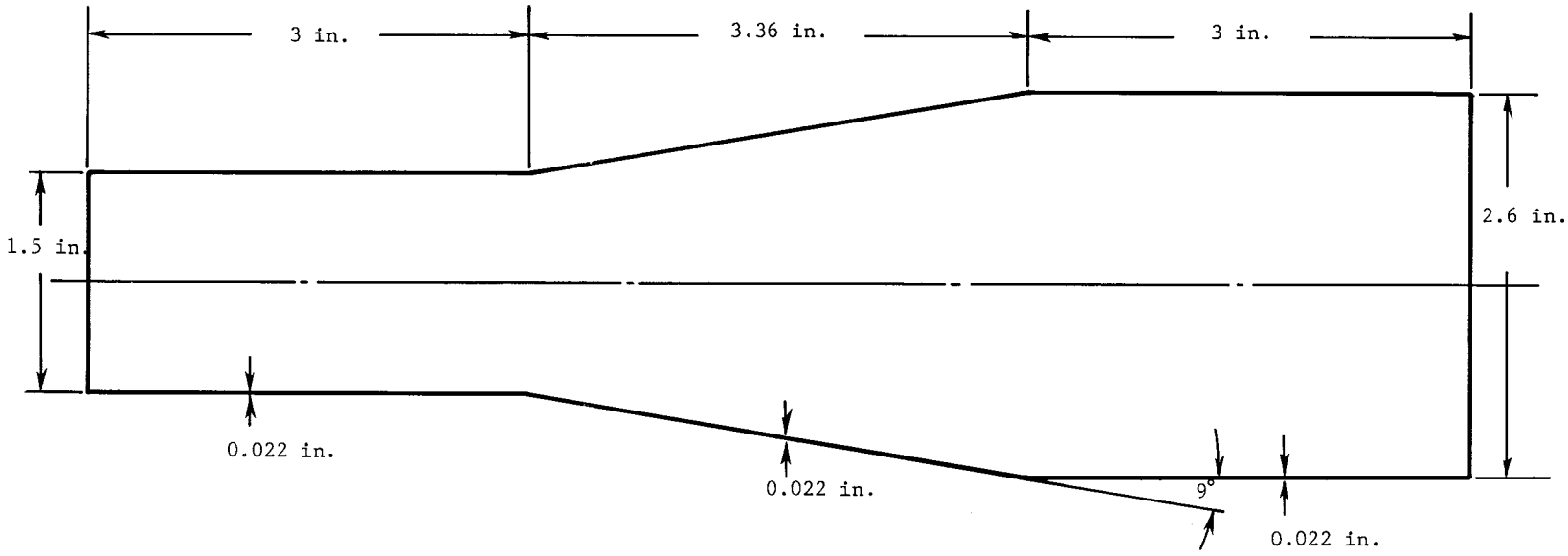

NOTE:

1. Circular Section
2. Aluminum

Figure 65: Dimensions for the thin-walled cone cylinder.

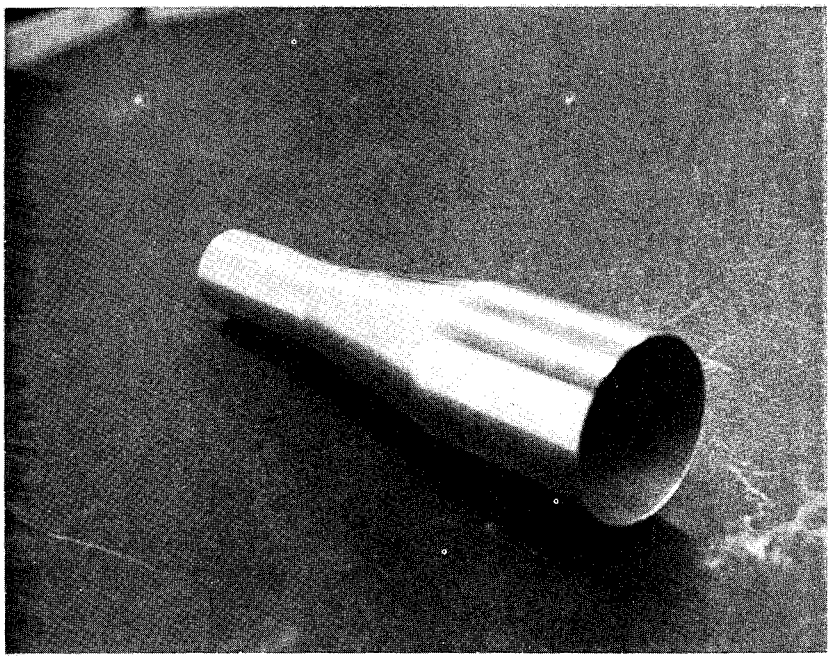

Figure 66: Photograph of the thin-walled cone-cylinder (diameter of large end is 2.6 inches).

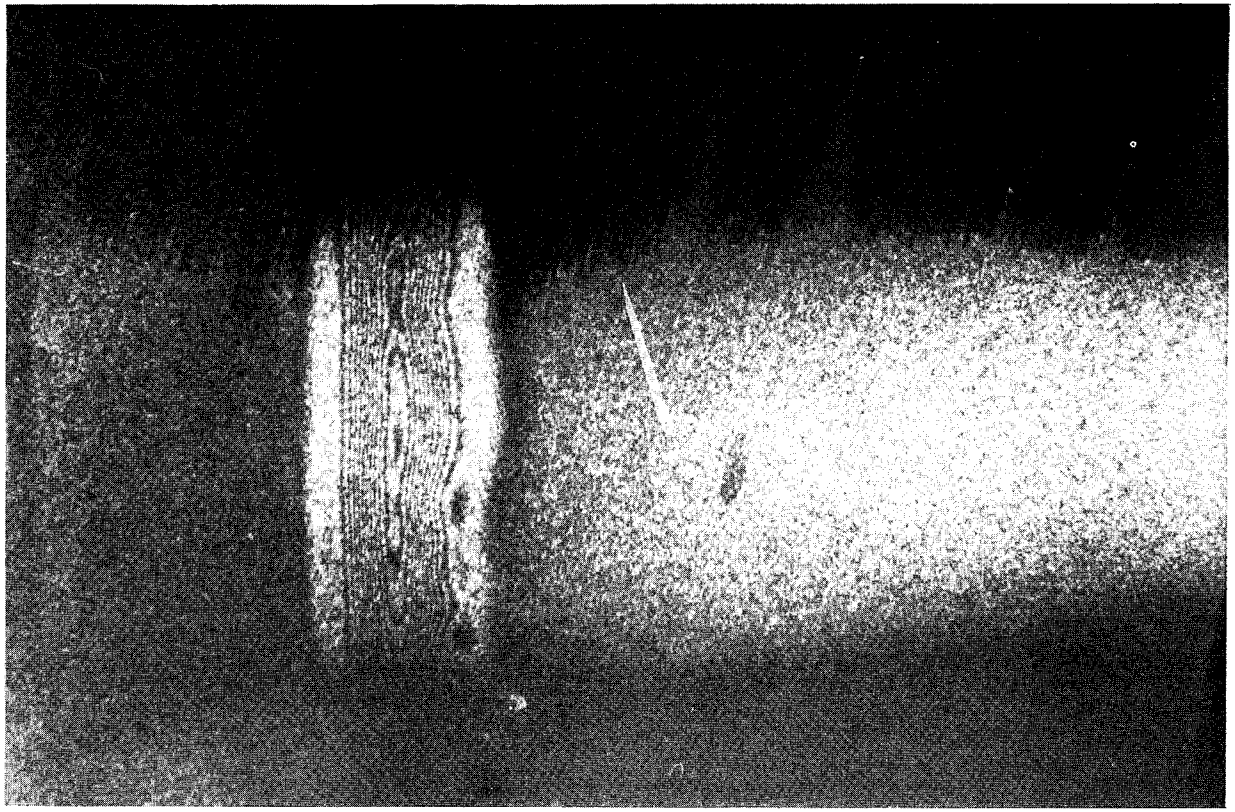

Figure 67: Wave propagation in the thin-walled cone-cylinder. Time t = 10 μsec.

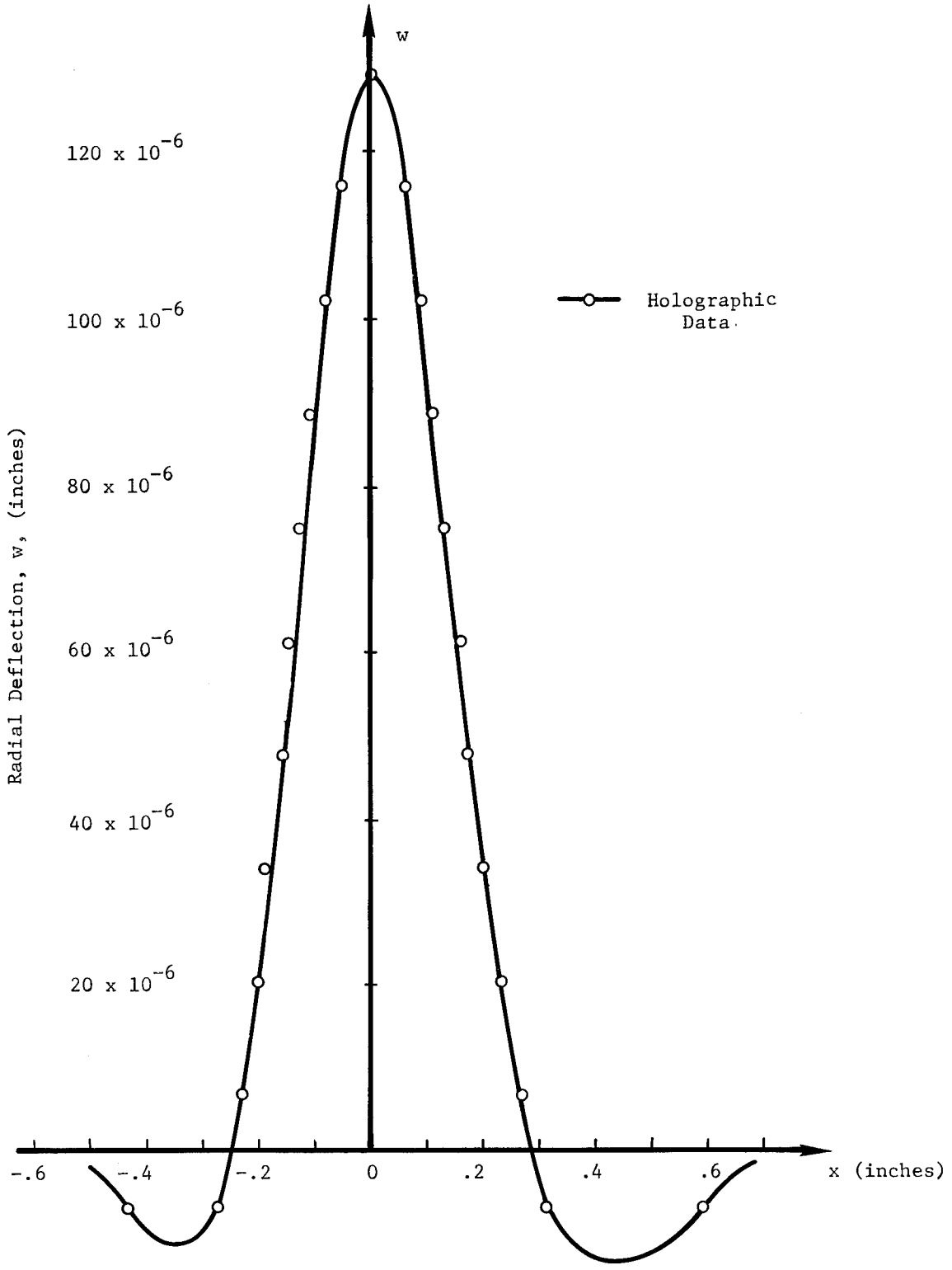

Figure 68: Radial deflection, w, vs. axial position, x. (Load centered at x = 0.) Cone cylinder combination, time t = 10 μsec.

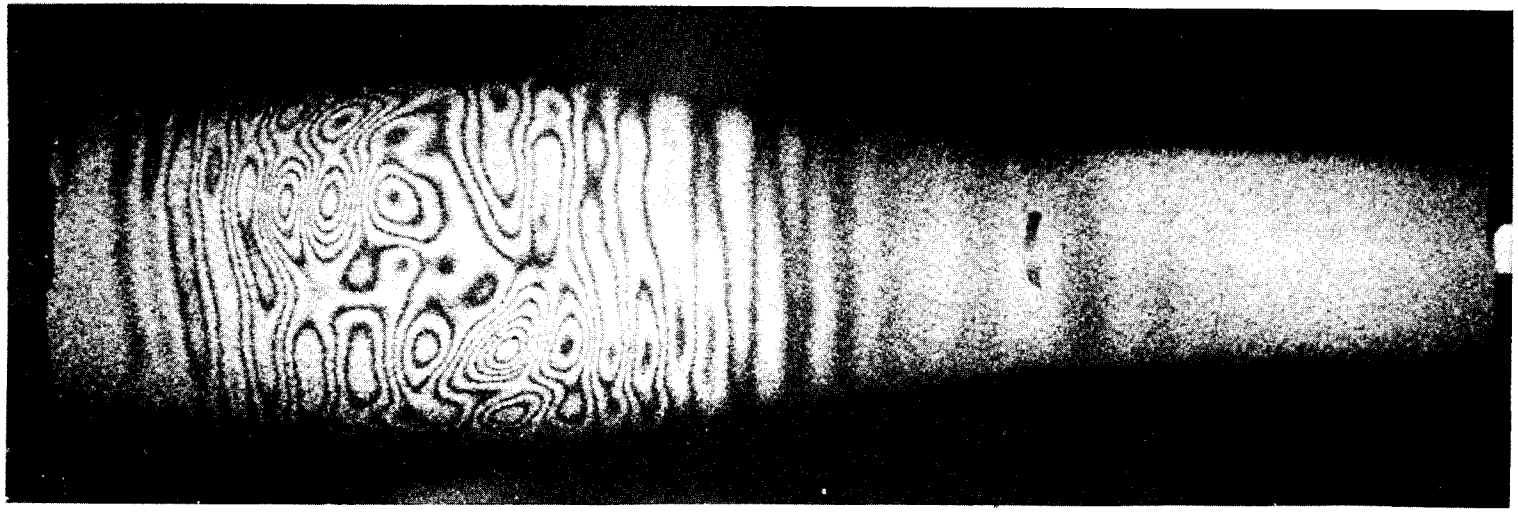

Figure 69: Wave propagating in a thin-walled cone-cylinder. Time t = 48 μsec.

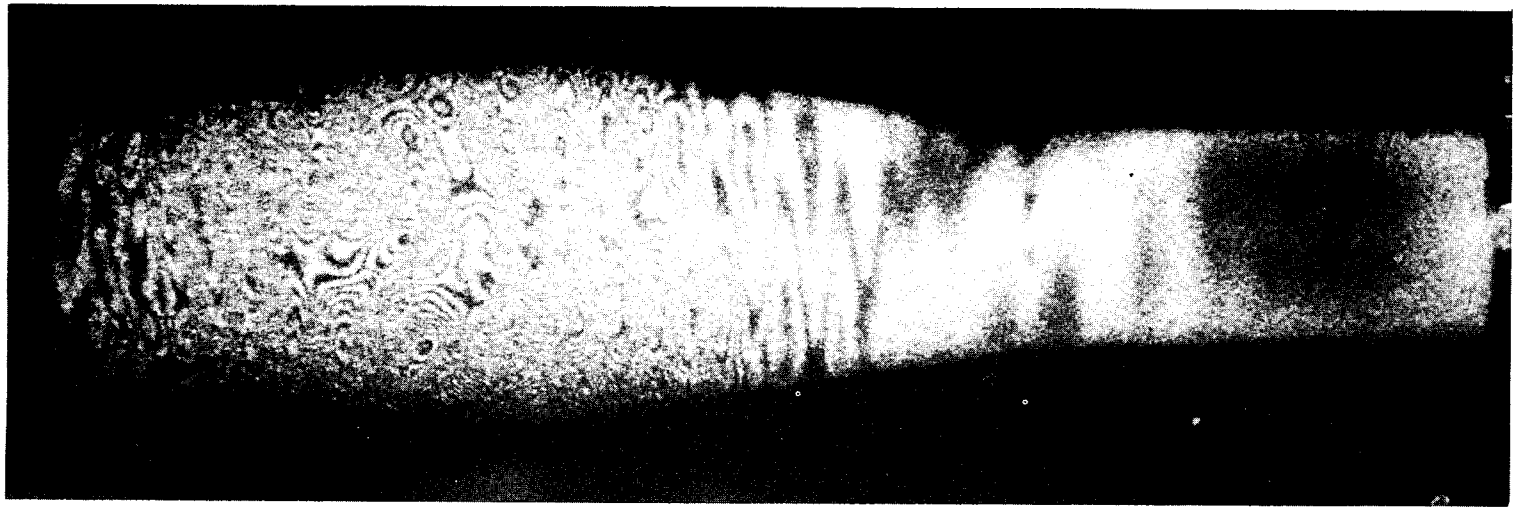

Figure 70: Wave propagating in a thin-walled cone-cylinder. Time t = 51 μsec.

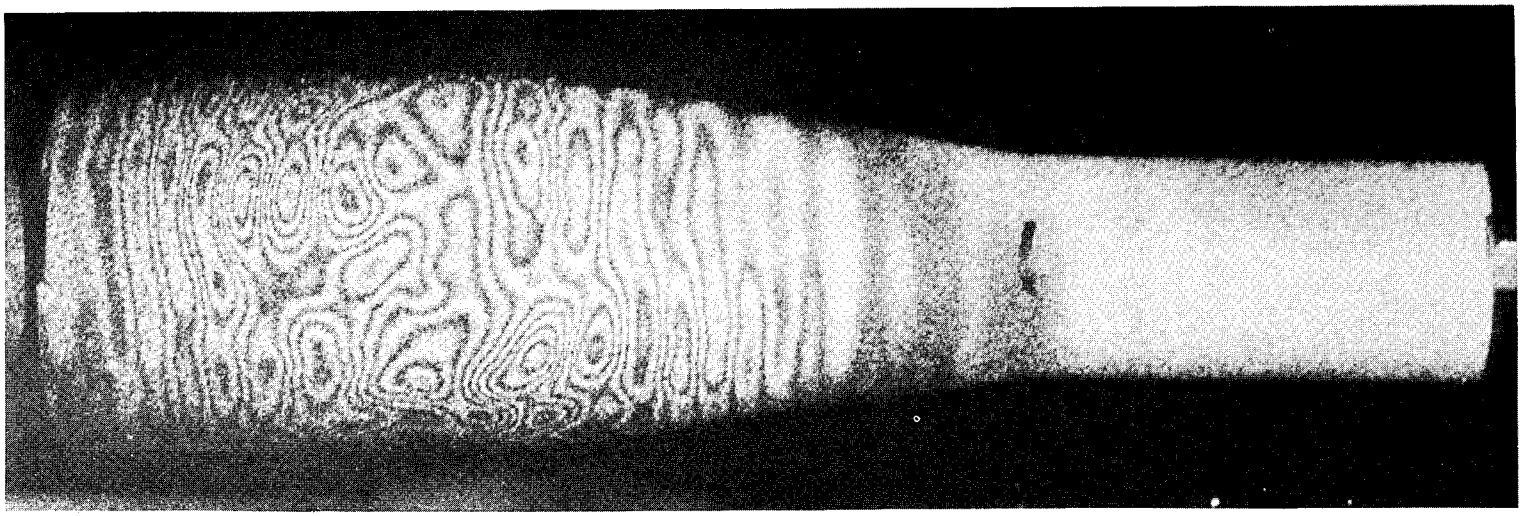

Figure 71: Wave propagating in a thin-walled cone-cylinder. Time t = 58 μsec.

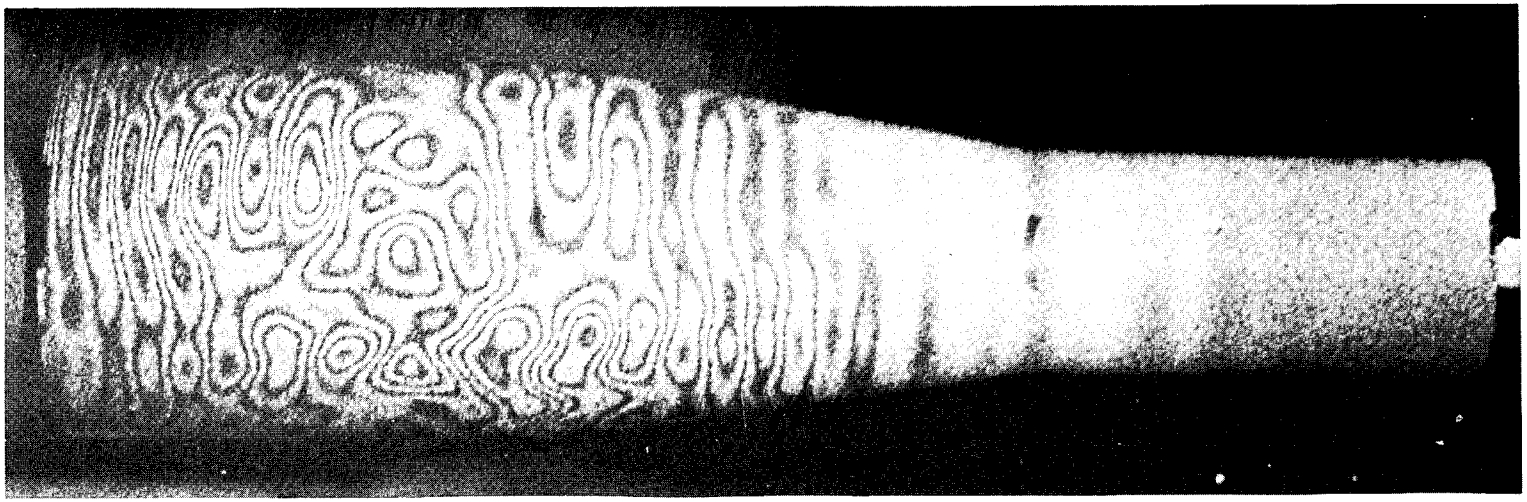

Figure 72: Wave propagating in a thin-walled cone-cylinder. Time t = 70 μsec.

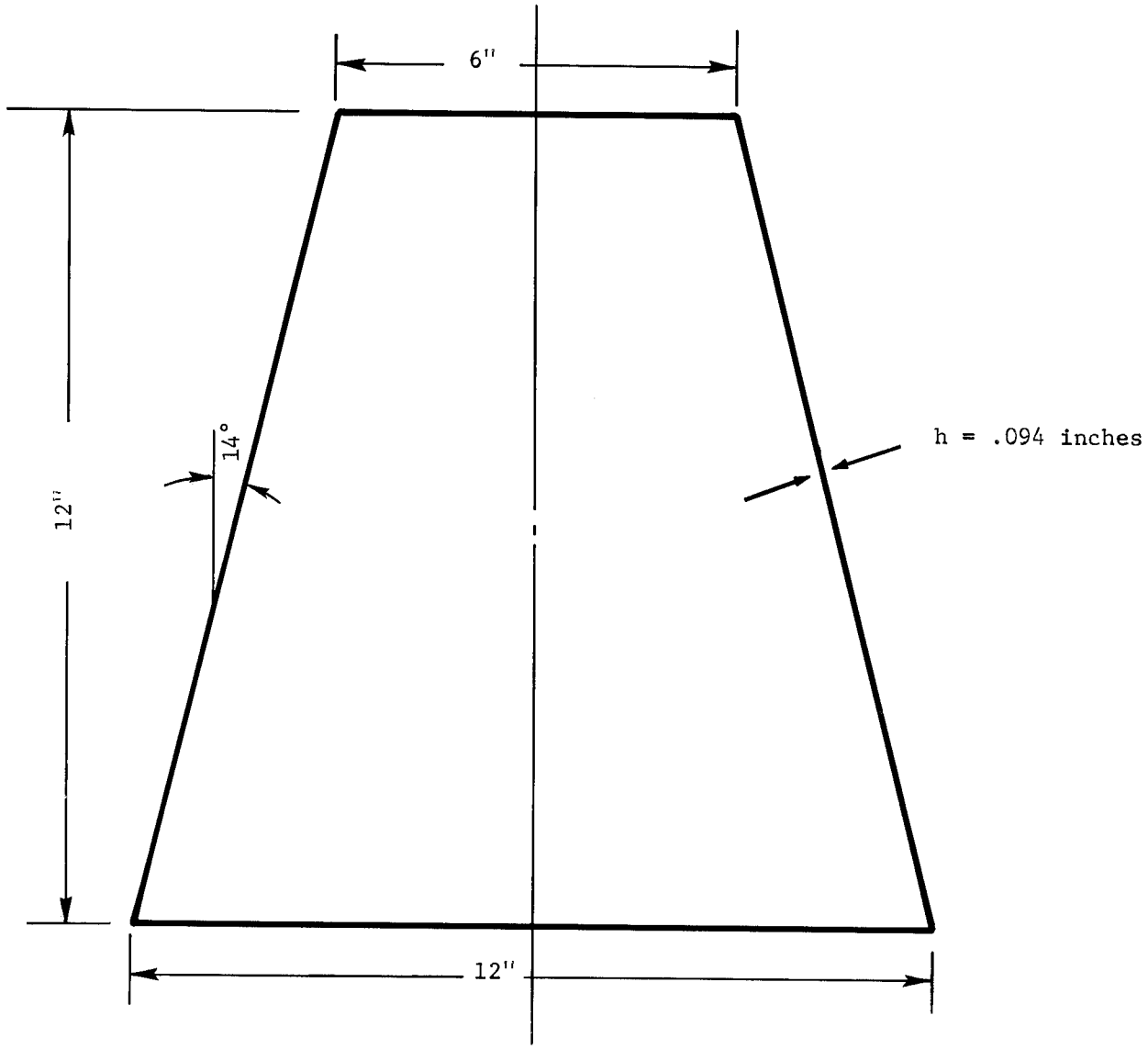

Figure 73: Sketch of conical shell geometry.

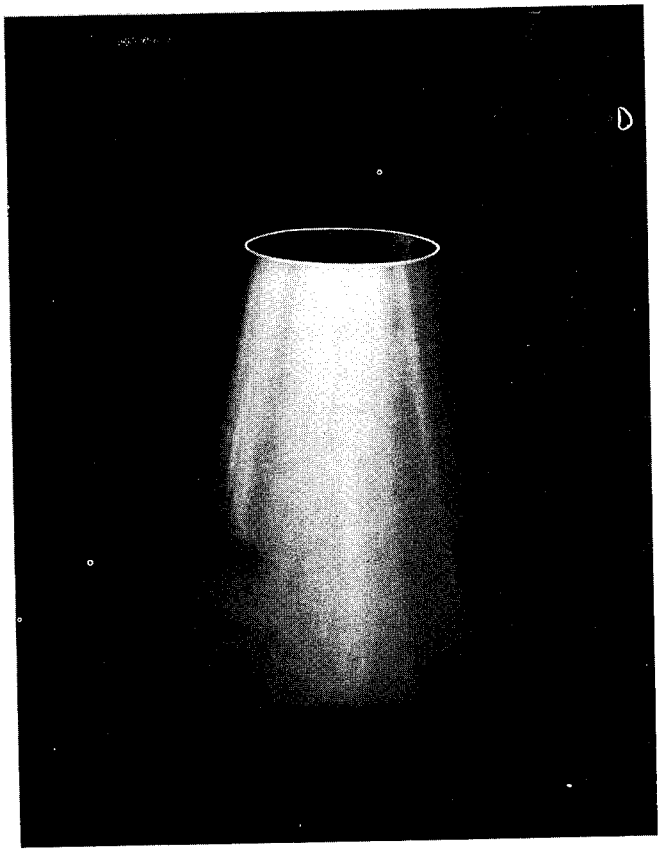

Figure 74: Conical shell specimen (14° half-angle, conical frustrun).

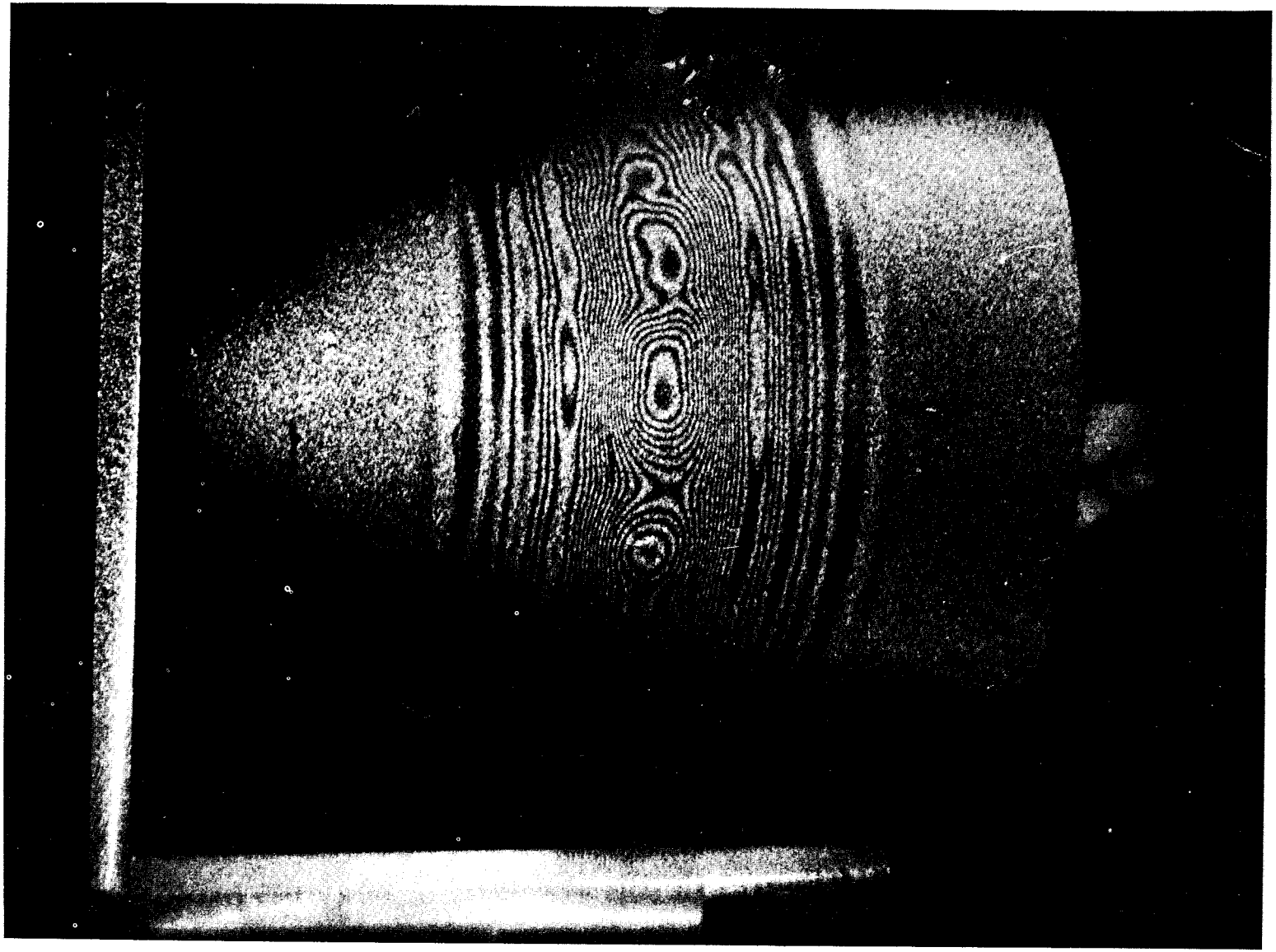

Figure 75: Wave propagation in a conical shell. Time t = 29 μsec.

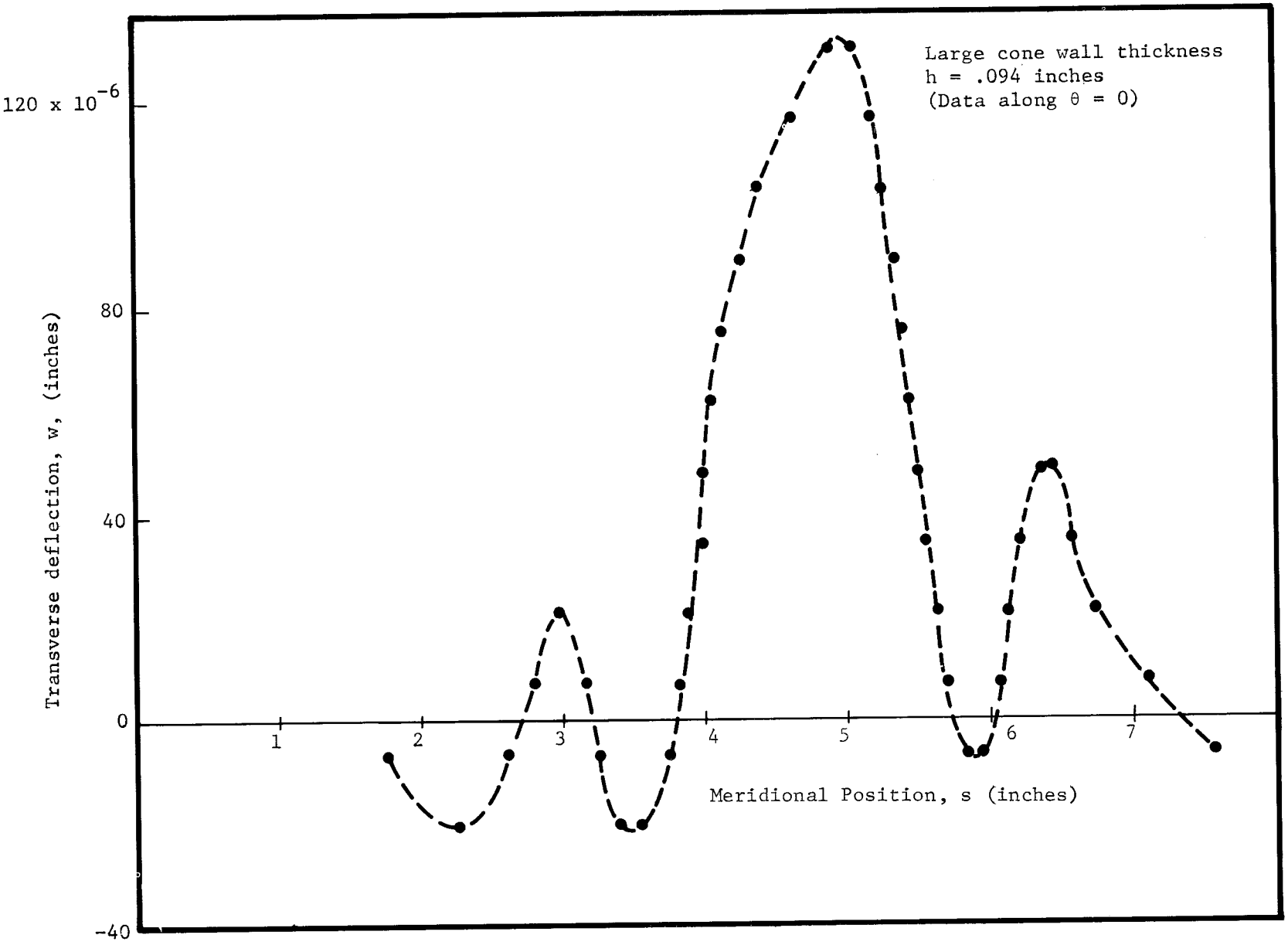

Figure 76: Transverse deflection, w, vs. position along the shell. Conical shell, t = 29 μsec.

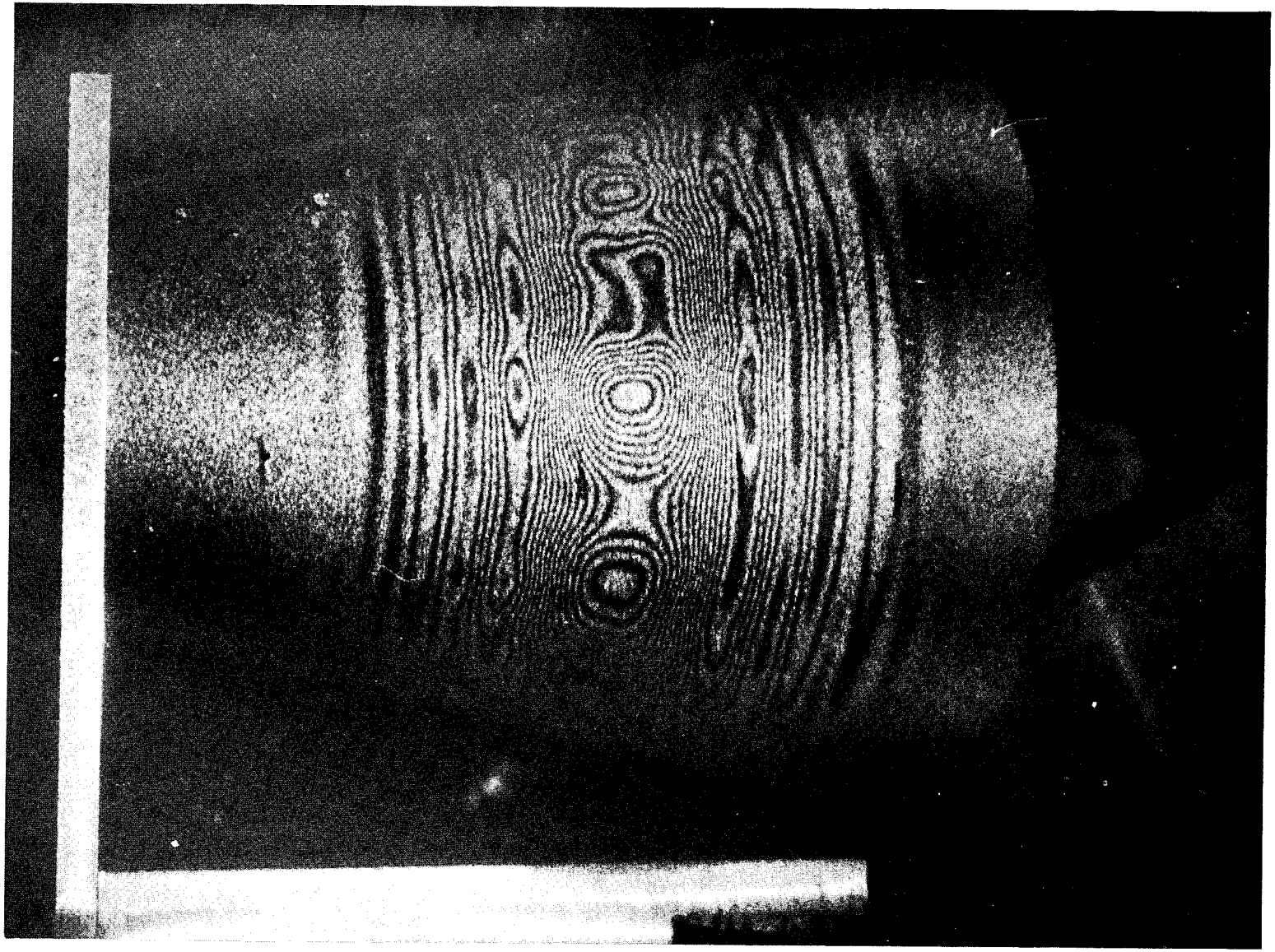

Figure 77: Wave propagating in a large conical shell. Time t = 40 μsec.

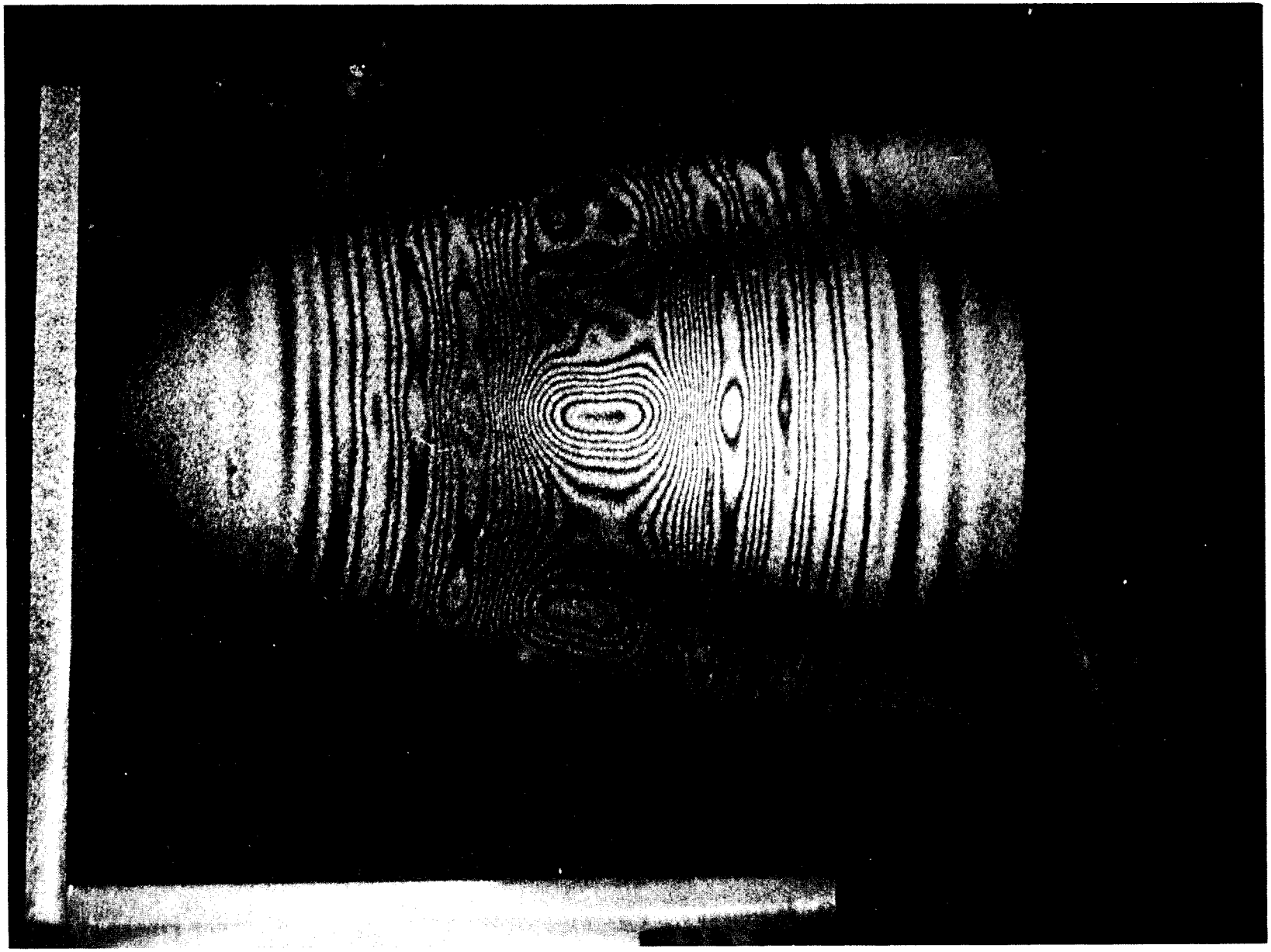

Figure 78: Wave propagating in a large conical shell. Time t = 48 μsec.

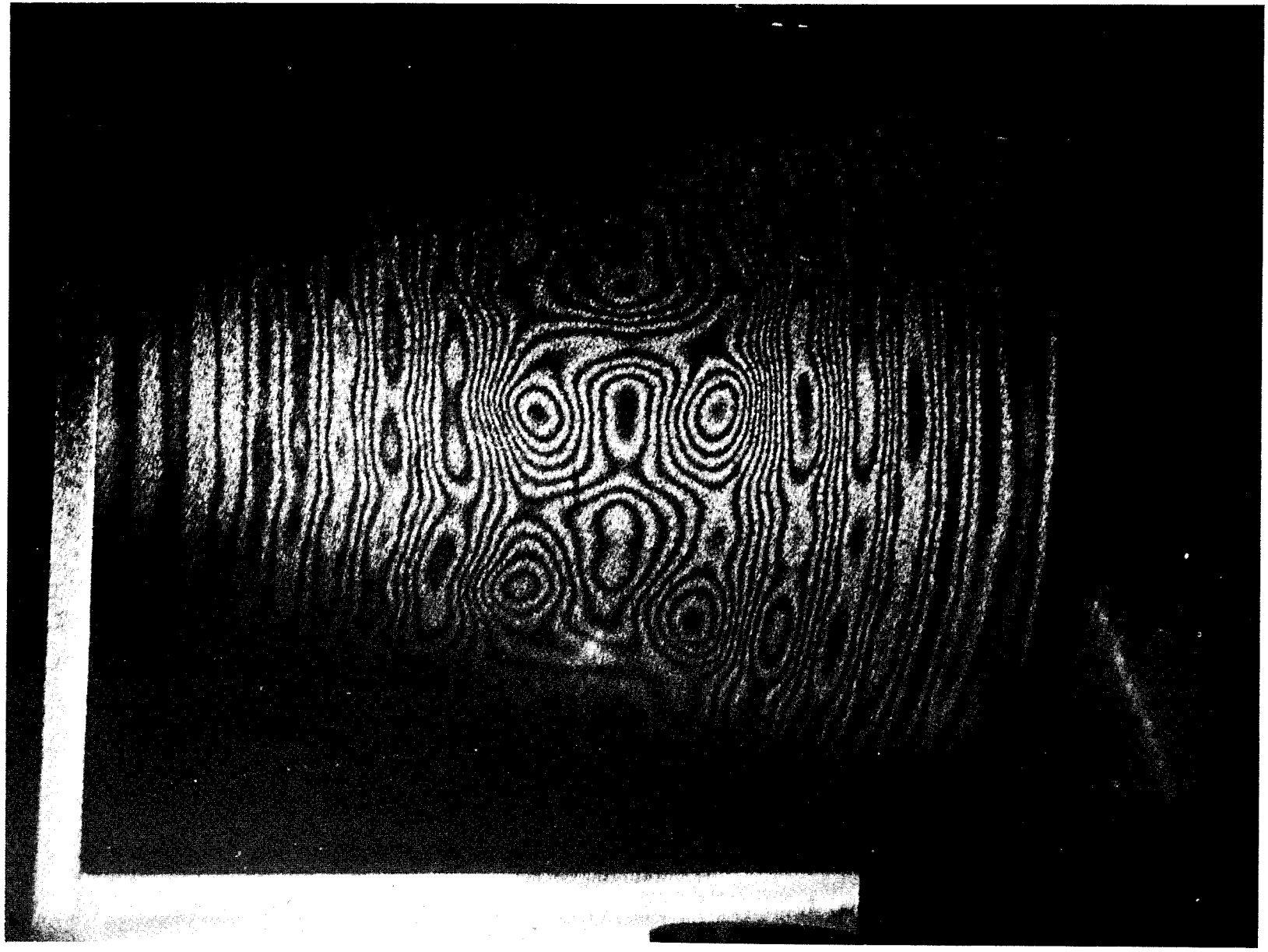

Figure 79: Wave propagating in a large conical shell. Time t = 70 μsec.

6.0 CONCLUDING REMARKS

In an attempt to extract the major conclusions found in this study, the following points stand out:

- Transverse wave propagation in shells can be accurately measured using pulsed laser holography. From an engineering standpoint, this means that holography can provide engineering data on the effects of cut-outs, discontinuities, etc.

- The axi-symmetric response of a circular shell to an axi-symmetric loading pulse may subsequently become unstable and excite circumferential harmonics in the shell. This is a problem in dynamic stability, and may be worth investigating analytically. The presence of non-symmetric modes might be of practical importance since they will affect stress distributions, circumferential bending, etc.

- When the input pulse is of sufficiently short duration, it is possible to excite responses that are beyond the scope of conventional shell theories. In this case, it is necessary to use "elasticity-type" solutions, as discussed in Section 4.0. The reader should note that elementary shell theory (Bernoulli-Euler) overpredicted the thick-shell deflections (as compared with the experimental data). Thus it seems that the elementary theory is overconservative (at least for this problem) and might result in a non-optimum design.

- Holography can be used to measure waves propagating past cut-outs and/or stiffening rings, which exhibit pronounced non-symmetric responses. Dynamic stress concentration caused by cut-outs, discontinuities, bolt holes, etc., can be accurately evaluated using pulsed laser holography. Such stress concentration factors often have a major impact on the design of shell structures.

7.0 REFERENCES

1. J. B. Develis and G. O. Reynolds, Theory and Applications of Holography, Addison-Wesley Publ., Reading, Mass., 1967.

2. J. W. Goodman, Introduction to Fourier Optics, McGraw-Hill, 1968 pp. 209-268.

3. H. Smith, Principles of Holography, John Wiley & Sons, 1969.

4. D. A. Evensen and R. Aprahamian, "Applications of Holography to Vibrations, Transient Response, and Wave Propagation," NASA CR-1671, December, 1970.

5. K. A. Haines and B. P. Hildebrand, "Surface Deformation Measurement Using the Wavefront Reconstruction Technique," Applied Optics, Vol. 5, No. 4, April 1966, pp. 595-602.

6. W. G. Gottenberg, "Some Applications of Holographic Interferometry," Experimental Mechanics, Proc. Soc. for Experimental Stress Analysis, September, 1968. Also published as TRW Report No. EM 17-13, August 1967.

7. R. Aprahamian, D. A. Evensen, J. S. Mixson and J. E. Wright, "Application of Pulsed Holographic Interferometry to the Measurement of Propagating Transverse Waves in Beams," Experimental Mechanics, J. Soc. for Experimental Stress Analaysis, July 1971, pp. 309-314.

8. R. Aprahamian, D. A. Evensen, J. S. Mixson and J. L. Jacoby, "Holographic Study of Propagating Transverse Waves in Plates," Experimental Mechanics, J. Soc. for Experimental Stress Analysis, August 1971, pp. 357-362.

9. A. B. Witte, J. Fox, and H. Rungaldier, "Localized Measurements of Wake Density Fluctuations Using Pulsed Laser Holographic Interferometry," (AIAA Paper No. 70-727) to appear in AIAA Journal. Paper presented at the AIAA Reacting Turbulent Flows Conference, San Diego, CA, June 17-18, 1970.

10. A. B. Witte, J. Fox, and H. Rungaldier, "Holographic Interferometry Measurements of Mean and Localized Fluctuating Wake Density Field for Cones Fired at Mach 6 in a Ballistic Range," (AIAA Paper No. 71-564) to appear in AIAA Journal. Paper presented at the AIAA 4th Fluid and Plasma Dynamics Conference, Palo Alto, CA, June 12-23, 1971.

11. A. E. H. Love, "On the Small Free Vibrations and Deformations of Thin Elastic Shells," Phil. Trans., Roy. Soc. (London), Vol. 17A, 1888, pp. 491-546.

12. A. Kalnins and H. Kraus, "Effect of Transverse Shear and Rotary Inertia on Vibration of Spherical Shells," Proc. 5th U.S. Nat'l. Cong. Appl. Mech., A.S.M.E., 1966.

13. D. C. Gazis, "Three-Dimensional Investigation of the Propagation of Waves in Hollow Circular Cylinders - I. Analytical Foundation, II. Numerical Results," J. Acous. Soc. Amer. Vol. 31, 1959, pp. 568-578.

14. H. Kraus, Thin Elastic Shells, Wiley and Sons, New York, 1967.

15. R. D. Mindlin, "Waves and Vibrations in Isotropic, Elastic Plates," in Structural Mechanics, Proc. 1st Symp. Naval Struct. Mech., (Ed. J. N. Goodier and N. J. Hoff) Pergamon Press, 1960, pp. 199-232.

16. Erdelyi, et. al., Tables of Integral Transforms, Bateman Manuscript Project, McGraw-Hill, 1954.

17. T. L. Geers and L. H. Sobel, "Analysis of Transient, Linear Wave Propagation in Shells by the Finite Difference Method," NASA CR-1885, 1971.

18. J. S. Bendat and A. G. Piersol, Measurement and Analysis of Random Data, Wiley & Sons, 1966.

19. E. B. Aleksandrov and A. M. Bonch-Bruevich, "Investigation of Surface Strains by the Holographic Techniques," Soviet Physics, Technical Physics, Vol. 12, No. 2, August, 1967, p. 258.

20. E. G. Lovell and I. K. McIvor, "Nonlinear Response of a Cylindrical Shell to an Impulsive Pressure," Jour. Appl. Mech., Vol. 36, Trans. A.S.M.E., Series E, No. 2, June 1969, pp. 277-284.

21. J. N. Goodier and I. K. McIvor, "The Elastic Cylindrical Shell Under Nearly Uniform Radial Impulse," Jour. Appl. Mech., Vol. 31, No. 2, Trans. A.S.M.E., Series E, June 1964, pp. 259-266.

22. R. W. Mortimer and J. F. Hoburg, "MCDIT 21 - A Computer Code for One-Dimensional Elastic Wave Problems," NASA CR-1306, April 1969.

23. W. E. Baker, W. C. L. Hu, and T. R. Jackson, "Elastic Response of Thin Spherical Shells to Axi-symmetric Blast Loading," J. Appl. Mech., Vol. 33, No. 4, Trans. A.S.M.E., Series E, December 1966, pp. 800-806.

24. Y. C. Fung, Foundations of Solid Mechanics, Prentice-Hall, 1965.

25. J. P. Raney and J. T. Howlett, "Modal Solutions for Wave Propagation in Finite Shells of Revolution," J. Spacecraft and Rockets, Vol. 8, No. 6, June 1970, pp. 650-656.

26. H. N. Abramson, H. J. Plass, and E. A. Ripperger, "Stress Wave Propagation in Rods and Beams," Advances Applied Mechanics, Vol. 5, 1958, pp. 111-194.

27. M. J. Sagartz and M. J. Forrestal, "Transient Stresses at a Clamped Support of a Circular Cylindrical Shell," Trans. A.S.M.E. Jour. Appl. Mech., June 1969, pp. 367-369.

28. A. E. Armenakas, D. C. Gazis, and G. Herrmann, Free Vibrations of Circular Cylindrical Shells, Pergamon Press, 1969.

29. F. O. Hoese, C. G. Langner, and W. E. Baker, "Simultaneous Initiation over Large Areas of a Spray - Deposited Explosive," Experimental Mechanics, Jour. Soc. Exptl. Stress Analysis, Vol. 8, No. 9, September 1968, pp. 392-397.

30. D. V. Keller and J. R. Penning, "Exploding Foils - The Production of Plane Shock Waves and the Acceleration of Thin Plates," Exploding Wires, Vol. 2, Plenum Press, 1962, pp. 263-277.

31. R. Resnick and D. Halliday, Physics for Students of Science and Engineering, Part II, Wiley & Sons, 2nd Edition, 1962, pp. 761-764.

32. R. C. O'Rourke, et al, "Progress Report Impulsive Load Tests on Cylindrical Assemblies," Technical Report B-3147, EGG-1183-235 Edgerton, Germeshausen and Greer, 24 September 1965.

APPENDIX A

THE EXPERIMENTAL LOADING TECHNIQUE

Introduction

In loading the shell(s), the objective was to produce a radial pressure that was uniform around the circumference, concentrated at a single axial station (x = 0) and of short duration in time (i.e., on the order of a few microseconds). The loading was to generate axisymmetric, transverse waves in the shell(s), which involve the radial displacement, w, and the longitudinal displacement, u. From the standpoint of analysis, the desired loading might be idealized as

$$p(x,\theta,t) = P(t)\delta(x) \tag{A-1}$$

where $\delta(x)$ is a Dirac delta function in space and P(t) represents the time-history of the loading pulse. In practice, P(t) can be approximated by

$$p(t) = \begin{cases} A \sin^2 \frac{\pi t}{T} & 0 \leq t \leq T \\ 0 & T \leq t < \infty \end{cases} \tag{A-2}$$

where T is the time duration of the pulse.

In launch vehicle applications, the loading function $p(x,\theta,t)$ usually results from pyrotechnic shock loads (i.e., explosives). Thus, one of the first loading techniques investigated was a sprayed-on, light-sensitive explosive (Ref. 29). Such explosives have been used previously in structural applications, but we experienced two main difficulties with this technique:

(1) To cause detonation, high-intensity light (i.e., 7×10^6 lumens/in^2) must be applied over all areas covered by the explosive.

(2) A long turn-around time is required between tests, which involves spraying the explosive, drying it, etc.

As a means of detonating the explosive simultaneously (around the circumference of the shell) an exploding wire (Ref. 30) was considered. The possibility of loading the shell directly (by an exploding wire) led in turn to the development of the final loading device, which involves an electromagnetic impulse.

The Repelling-Wire Loading Device

Consider two parallel, current-carrying conductors, a distance d apart (see Fig. A.1). If one conductor carries a current $I_1(t)$ in one direction,

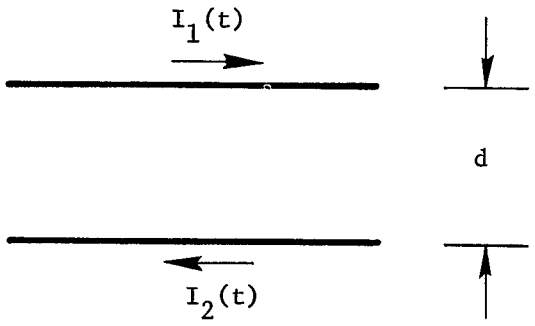

Figure A.1: Parallel, current-carrying conductors, spaced a distance d apart

and the other conductor carries $I_2(t)$ in the other direction, then the force (per unit length) between the conductors is given by (Ref. 31)

$$F(t) = \frac{\mu_o I_1 I_2}{2\pi d} \qquad \text{(A-3)}$$

where $\mu_o = 4\pi x 10^{-7}$ in the rationalized MKS system. F(t) is force of magnetic repulsion, since the interacting electromagnetic fields of the conductors cause them to fly apart (when I_1 and I_2 are in opposite directions). If one conductor is held fixed in space and the other is nestled against the structure to be loaded, it is possible to generate pressure-time histories of the desired magnitude and duration.

To initiate waves in our circular shell structures, a flat aluminum conductor was formed in the shape of two concentric circles (see Fig. A.2). The conductor did not form a complete circle, since it was necessary to bring the current in at one point on the circle and take it out at another. Thus, the circular conductor was made of one continuous piece of aluminum (1/4-inch wide) looped back upon itself. A rubber tube was installed between the conducting loops of aluminum; the tube and conductors were held in place by a circular plexiglas disc (see Fig. A.3). The rubber tube was pressurized to force the loading wire into close contact with the shell.

The generation of significant force pulses with a repelling wire device requires very high electrical currents, e.g., on the order of 50,000 amps. These currents are produced by charging a capacitor bank to several kilovolts, and then discharging the capacitors through the repelling wire circuit. The system can be adequately represented by a simple R-L-C circuit, as discussed in Ref. 32. (A circuit diagram is given in Figure A.4).

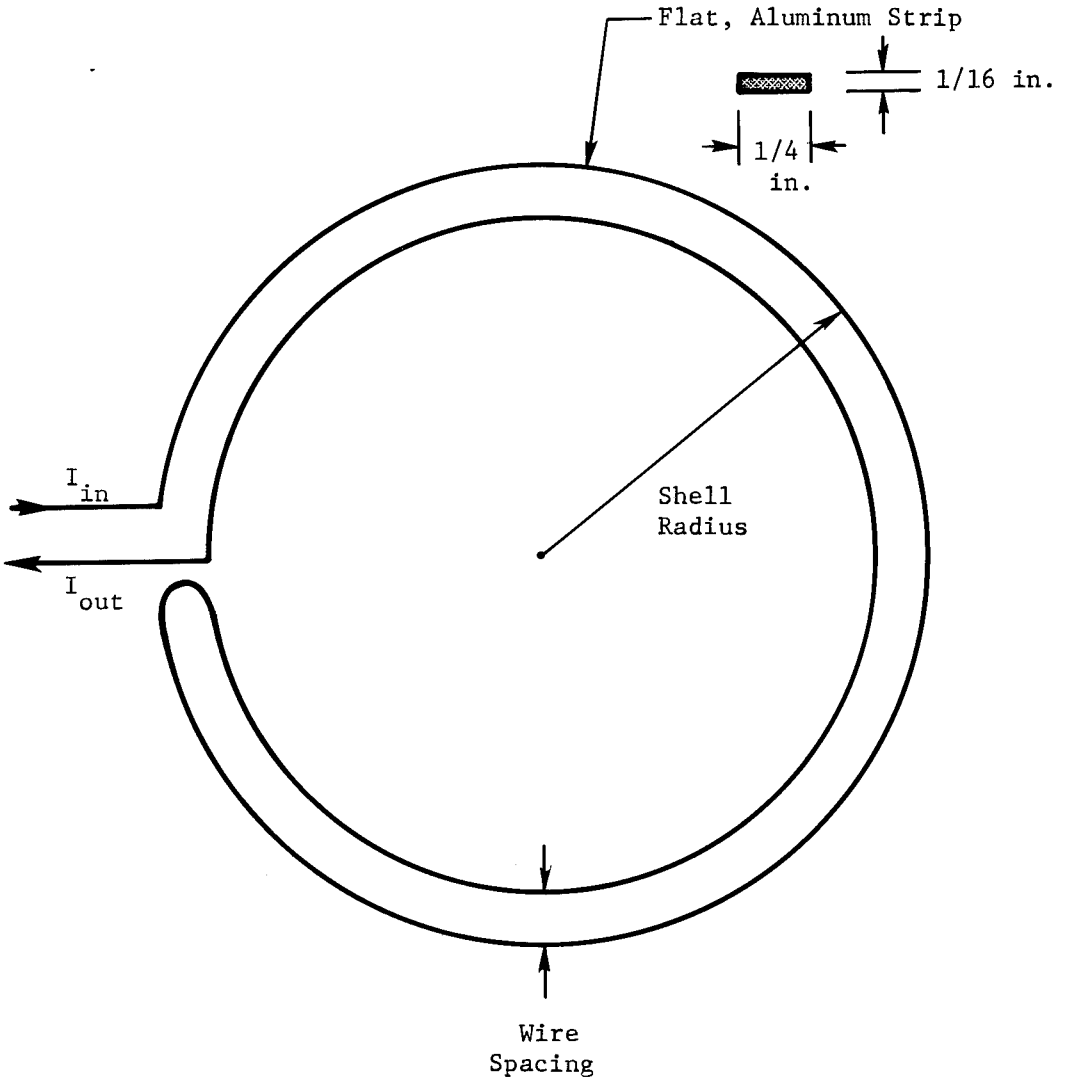

Figure A.2: Concentric current-carrying loop(s) used to load the shell.

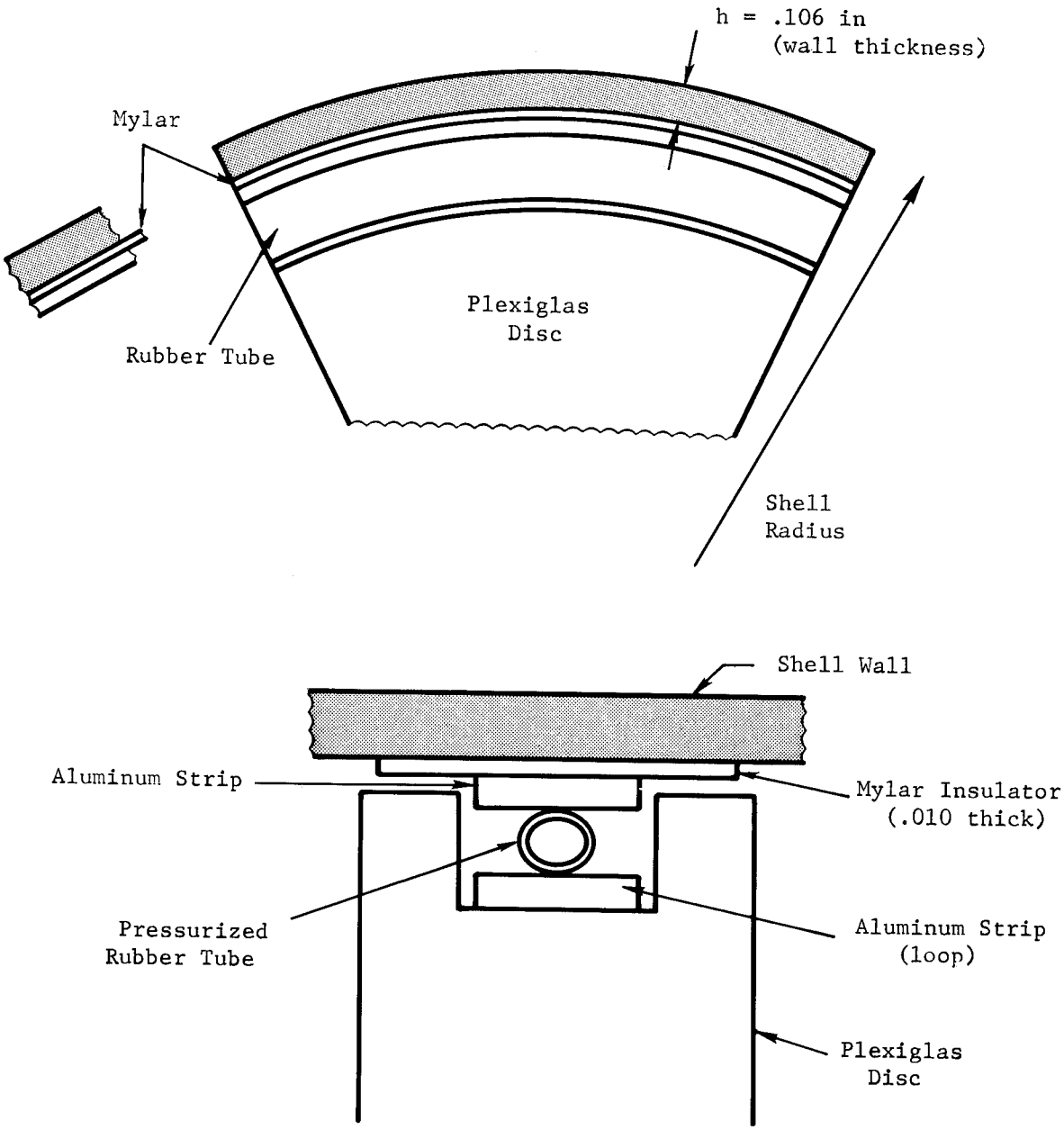

Figure A.3: Schematic showing loading wire (aluminum strips) design details

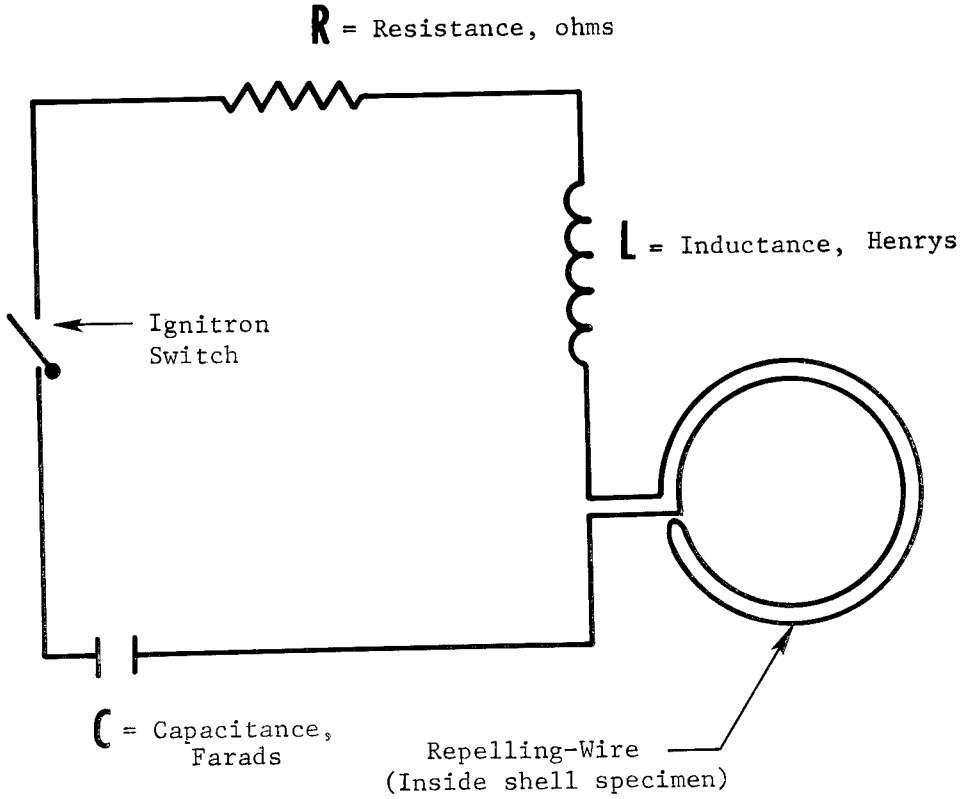

Figure A.4: Schematic R-L-C circuit diagram representing the loading device

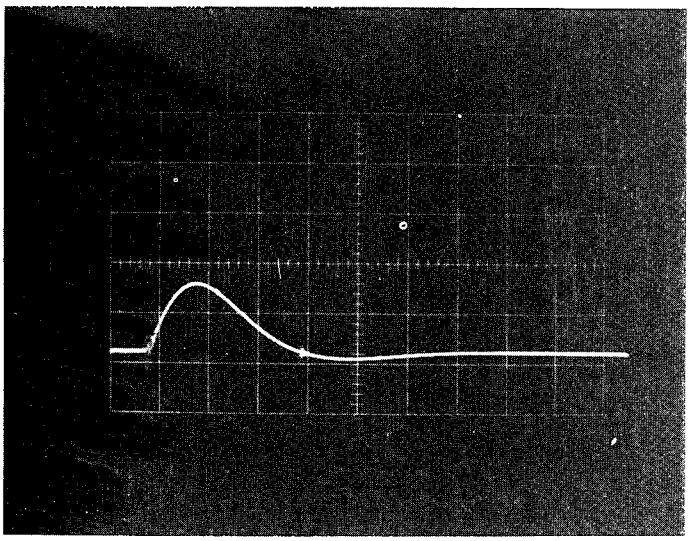

Figure A.5(a): Current vs. time in repelling wire circuit (charging voltage 12 kv, sweep speed 5 μs/cm, scale 50 mv/div).

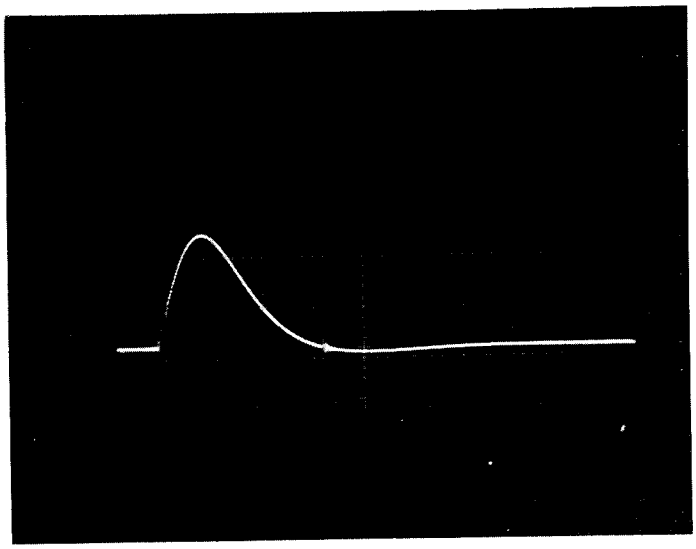

Figure A.5(b): Current vs. time in repelling wire circuit (charging voltage 20 kv, sweep speed 5 μs/cm, scale 50 mv/div).

Current in the Repelling Wire Circuit

The response of the repelling-wire circuit is given by (Ref. 32)

$$I(t) = \frac{V_o}{\omega L} e^{-at} \sin\omega t \qquad \text{(A-4)}$$

where

$\omega = \left(\frac{1}{LC} - \frac{R^2}{4L^2}\right)^{1/2}$ is the circular frequency

$a = \frac{R}{2L}$ is the damping

and V_o is the initial charging voltage.

Equation (A-4) refers to an underdamped circuit, and a typical oscilloscope trace (current vs. time) for the experiment is given in Figure A.5. The damping, R, was adjusted experimentally to yield the desired current-time history. From the trace of Figure A.5, the circuit inductance L was

calculated, using the values $C = 7 \times 10^{-6}$ farads (of the capacitor bank) and $R = .53$ ohms (measured with a micro-ohmmeter), and $\omega = \pi/16\text{x}10^{-6}$ sec. Then the current, I(t) is given by

$$I(t) = \frac{V_o}{(.6)} \; e^{-.0883t} \sin(.2t) \qquad \text{(A-5)}$$

where t is in <u>microseconds</u>.

Calculation of the Force and Impulse

Using Equations (A-3) and (A-4), the force/length is given by

$$F(t) = \frac{2\text{x}10^{-7} I^2}{d}$$

$$= \frac{2\text{x}7^{-10}}{d} \left(\frac{V_o}{.6}\right)^2 e^{-2at} \sin^2 \omega t \qquad \text{(A-6)}$$

The (impulse/unit length) that the wire exerts on the shell is obtained by integration:

$$I_o = \int_o^{t_{final}} F(t)dt \qquad \text{(A-7)}$$

If t_{final} is taken as 16 μsec (the first half-period of the pulse), then

$$I_o = \int_o^{t = 16\ \mu\text{sec}} e^{-2at} \sin^2 \omega t \; dt = \frac{1}{\omega}[.409] \qquad \text{(A-8)}$$

If the upper limit is taken as infinity, (which adds up all the ever-decreasing pulses) then

$$I_o = \int_o^{t = \infty} e^{-2at} \sin^2 \omega t \; dt = \frac{1}{\omega}[.475] \qquad \text{(A-9)}$$

Using the experimental values for the charging voltage, V_o, and the wire spacing, d, we have

$$V_o = 19{,}000 \text{ volts}$$

$$d = .45 \text{ in.} = 1.14 \times 10^{-2} \text{ meters}$$

$$I_o = \left(\frac{1.9 \times 10^4}{.6}\right)^2 \left(\frac{2 \times 10^{-7}}{2 \times 10^5}\right) \left(\frac{1}{1.14 \times 10^{-2}}\right) \left(\frac{.409}{.475}\right)$$

$$I_o = \left\{\begin{matrix} 3.62 \\ 4.20 \end{matrix}\right\} \times 10^{-2} \ \frac{\text{Newton-sec}}{\text{meter}} \qquad \text{(A-10)}$$

where the two values given depend upon the upper limit taken for the integral (see A-8 and A-9).

In English units, the specific impulse is

$$I_o = \left\{\begin{matrix} 2.06 \\ 2.39 \end{matrix}\right\} \times 10^{-4} \ \frac{\text{lb-sec}}{\text{in}} \qquad \text{(A-11)}$$

using equation (A-10) and appropriate conversion factors.

Measurement of the Impulse Using A Ballistic Pendulum

An attempt was made to measure the specific impulse (I_o) directly, using a ballistic pendulum. For this purpose, the repelling wire was installed in a calibration ring (see Figure A.6). The ring was of the same diameter, material, and thickness as the shell to be tested. A small square hole was cut through the wall of the calibration ring to accommodate a small ballistic pendulum. The pendulum mass was a small square piece of aluminum, which was suspended on long strings and then nestled against the repelling wire.

The capacitor bank was charged to a known voltage, V_o, and then the switch was closed to "fire" the circuit. The deflection of the pendulum was measured, and the impulse values (per unit length) were calculated. A plot of I_o (specific impulse) vs V_o (charging voltage) is given in Figure A.7, for a wire spacing of d = .45 inches.

At 19KV, the measured impulse was

$$(I_o)_{meas} = 1.34 \times 10^{-4} \ \frac{\text{lb-sec}}{\text{in}} \qquad \text{(A-12)}$$

vs a calculated value of

$$(I_o)_{calc} = 2.39 \times 10^{-4} \quad \frac{lb\text{-}sec}{in}$$

from equation (A-11).

As things turned out, the experimental deflection data compare more favorably with the analysis when the larger value (2.39×10^{-4}) is used in the computations. This led to the conclusion that the ballistic pendulum technique does not correctly measure the specific impulse, I_o, imparted to the shell. Apparently, the short pendulum mass does not respond the same as the continuous shell. This anomalous behavior is attributed to eddy currents thought to be present in the continuous shell but largely lacking in the pendulum mass.

Description of the Experimental Pulse in a Form Convenient for Analysis

As presented in Section 3.0, it is convenient to represent the applied loading, $p(x, \theta, t)$, as

$$p(x, \theta, t) = A \sin^2 \frac{\pi t}{T} \tag{A-13}$$

within the domain

$$\begin{aligned} -\varepsilon \leq x \leq \varepsilon \\ 0 \leq \theta \leq 2\pi \\ 0 \leq t \leq T \end{aligned} \tag{A-14}$$

and zero everywhere else.

The x-domain (with $\varepsilon = 1/8$ of an inch)

$$-1/8 \leq x \leq 1/8$$

in Equation (A-13) is based upon the fact that the repelling wire (which loaded the shell) was a flat, aluminum strip, 1/4 of an inch wide. No attempt was made to measure the variation of the applied pressure loading in the x-direction. In fact, a more realistic approximation for the x-dependence might be

$$p(x, \theta, t) \sim \cos^2 4\pi x \tag{A-15}$$

within $-1/8 \leq x \leq 1/8$

Similarly, the exact variation of the pressure in the circumferential direction was not measured. The loading wire which applied the pressure was not a complete circle around the circumference. It was necessary to bend the wire (to accommodate electrical leads, etc.) in such a way that a gap existed in the θ-direction. (For example, see Figure A.2.) A more appropriate description of the loading (in the circumferential direction) might thus be given by

$$p(x, \theta, t) \sim \sum_{n=0} A_n \cos n\theta \qquad \text{(A-16)}$$

where the axi-symmetric term (A_o) is much larger than the circumferential harmonics (A_n):

$$A_o >> A_n \qquad n = 1,2,3, \ldots.$$

Finally, the variation in time is more exactly given by Equation (A-6)

$$F(t) = e^{-2at} \sin^2 \omega t$$

where $a \cong .0883 \times 10^6 \text{ sec}^{-1}$

and $\omega \cong .2 \times 10^6 \text{ sec}^{-1}$

Thus it is apparent that the experimental loading approximates (but by no means duplicates) the form given by Equation (A-13) and used in the analysis.

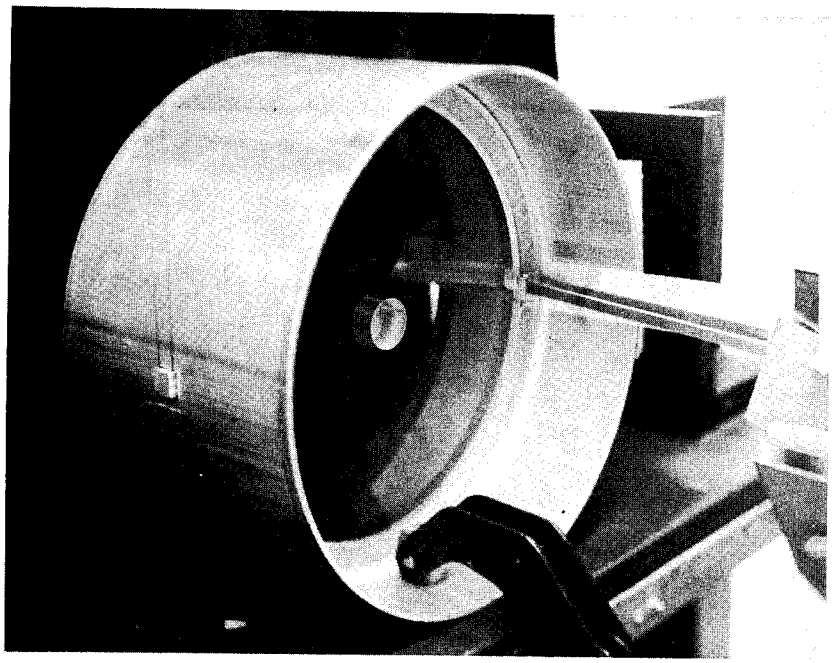

Figure A.6: Repelling Wire in Calibration Ring

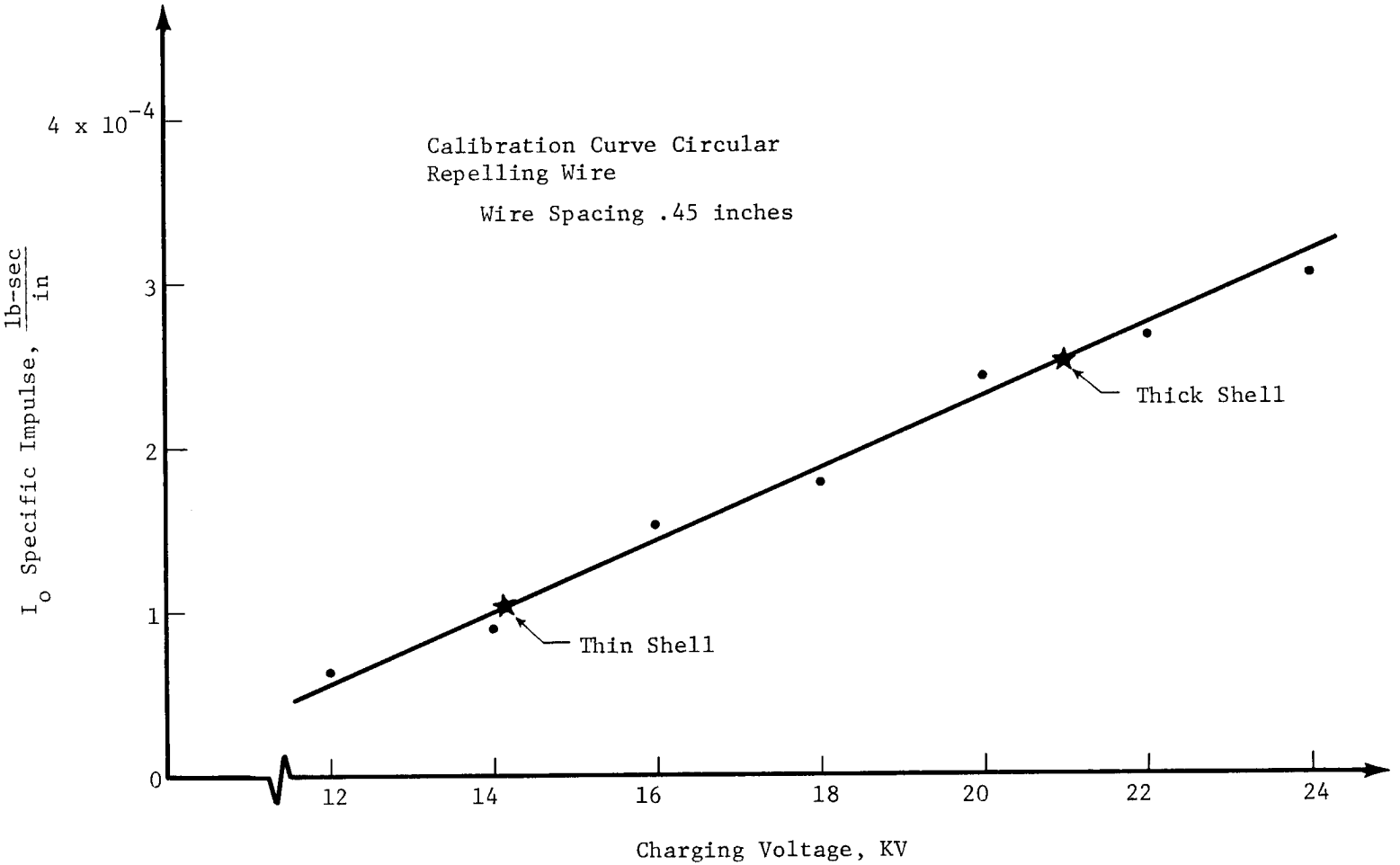

Figure A.7 - Circular Repelling Wire Calibration Curve

APPENDIX B

WAVES IN THE THIN-WALLED CYLINDER
(ADDITIONAL INTERFEROGRAMS)

This Appendix is meant to supplement Section 3.0 of the report, and it contains results for several times, t_i.

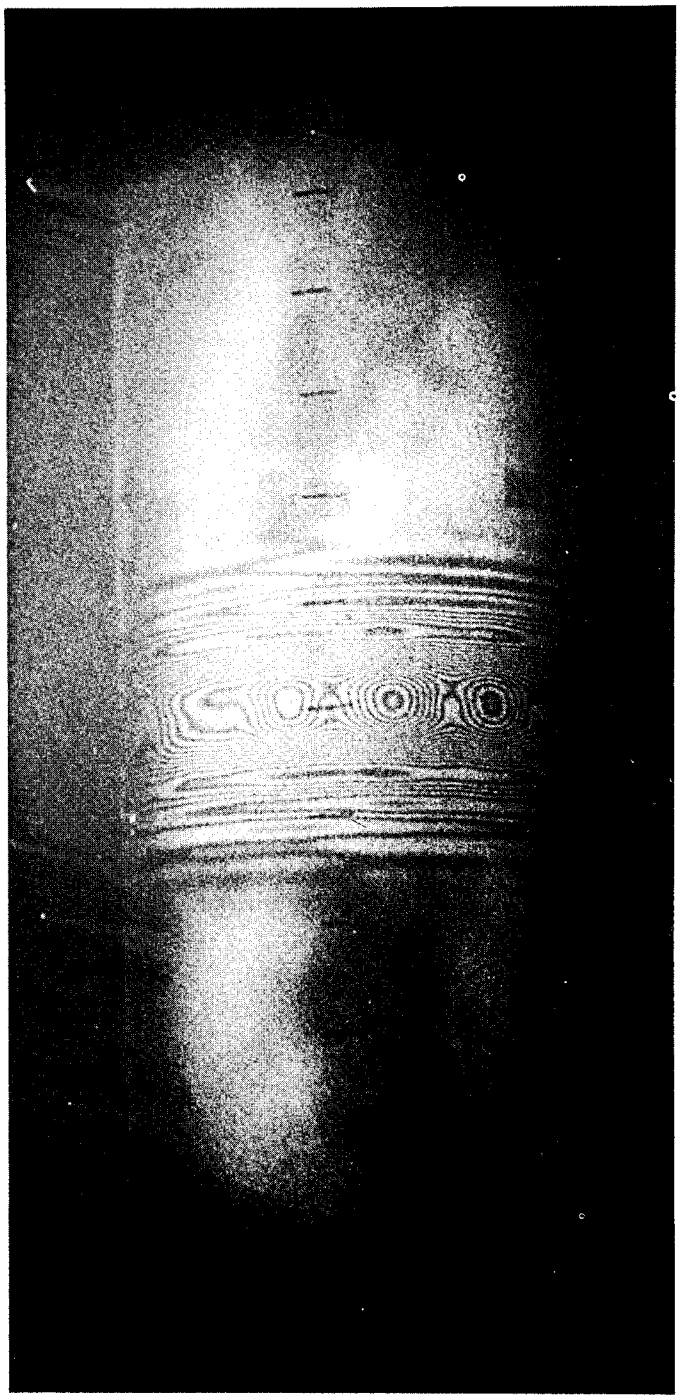

Figure B.1: Wave propagation in the thin-walled cylindrical shell. Time t = 30.5 μsec.

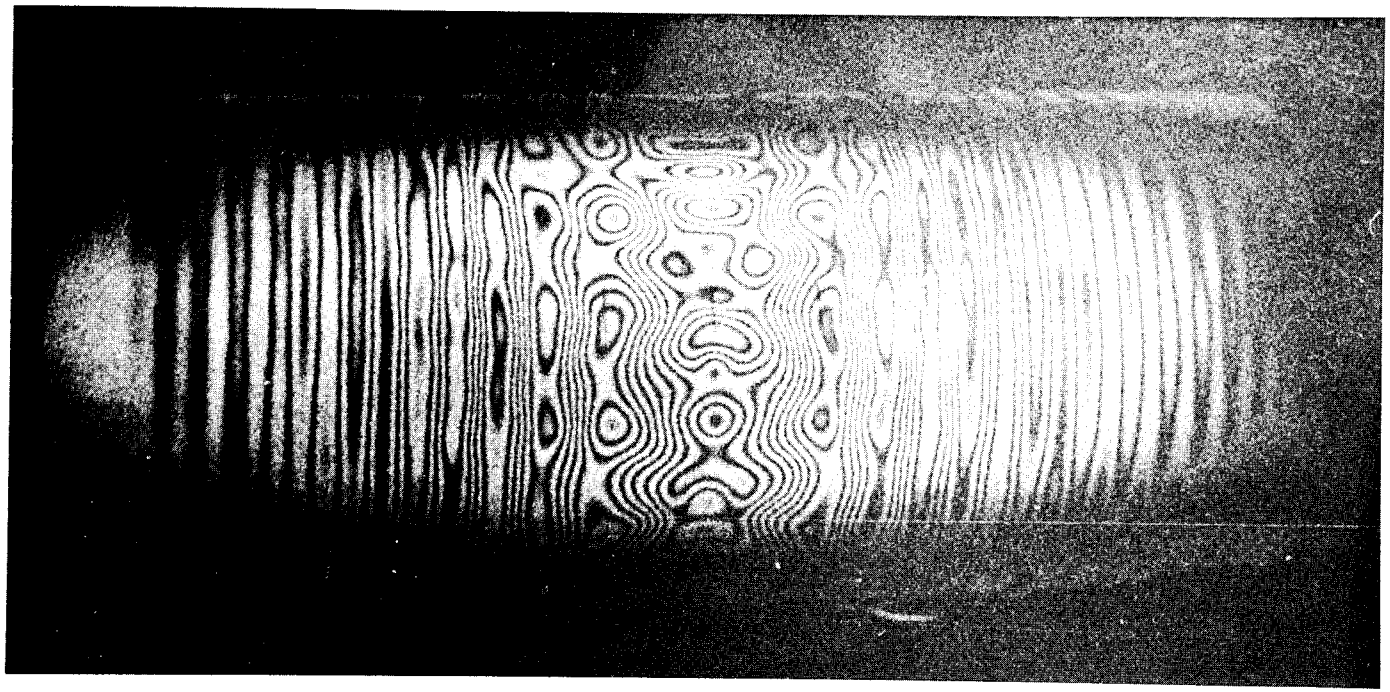

Figure B.2: Wave propagation in the thin-walled cylindrical shell. Time t = 99 μsec.

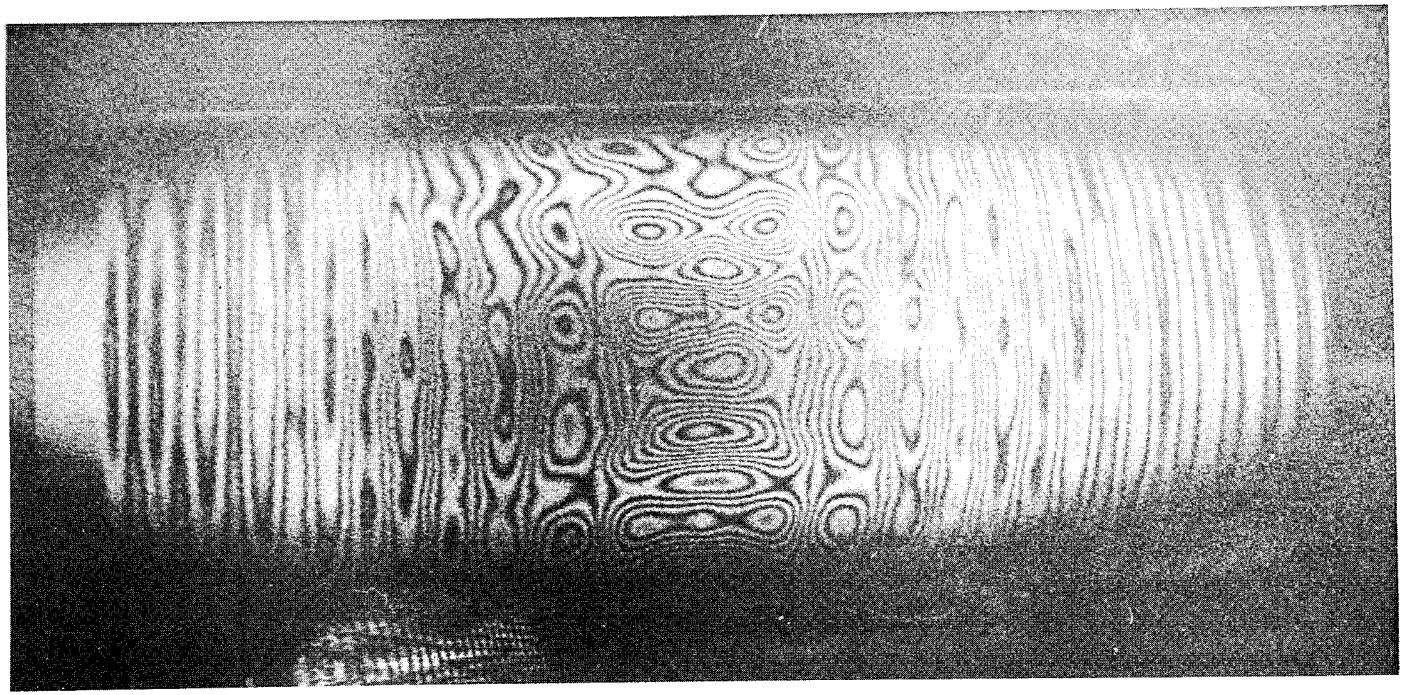

Figure B.3: Wave propagation in the thin-walled cylindrical shell. Time t = 125 μsec.

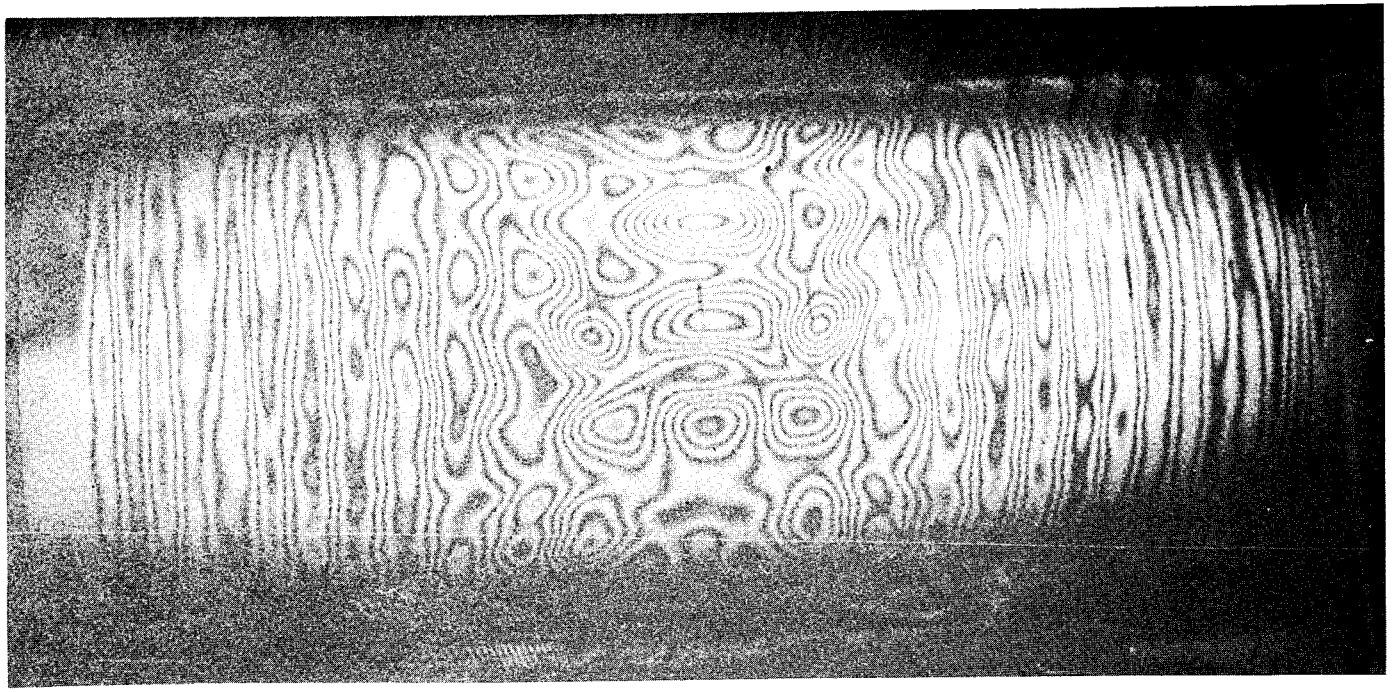

Figure B.4: Wave propagation in the thin-walled cylindrical shell. Time t = 150 μsec.

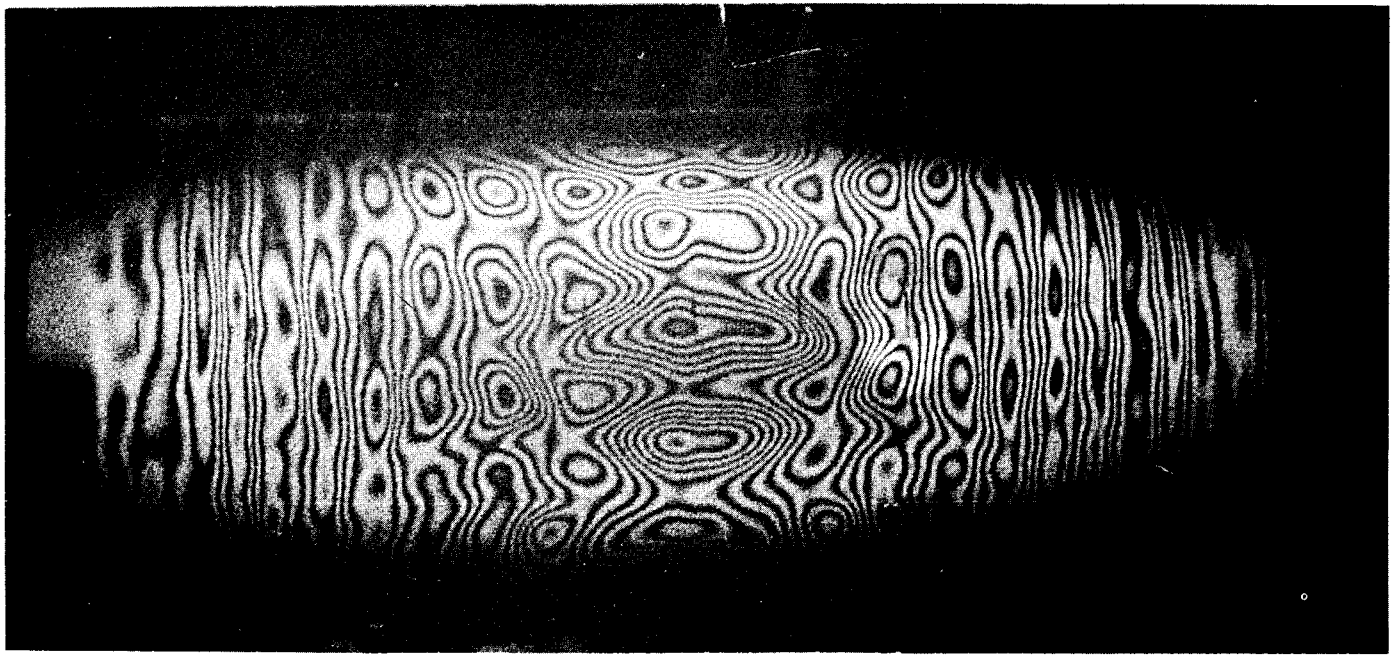

Figure B.5: Wave propagation in the thin-walled cylindrical shell. Time t = 171 μsec.

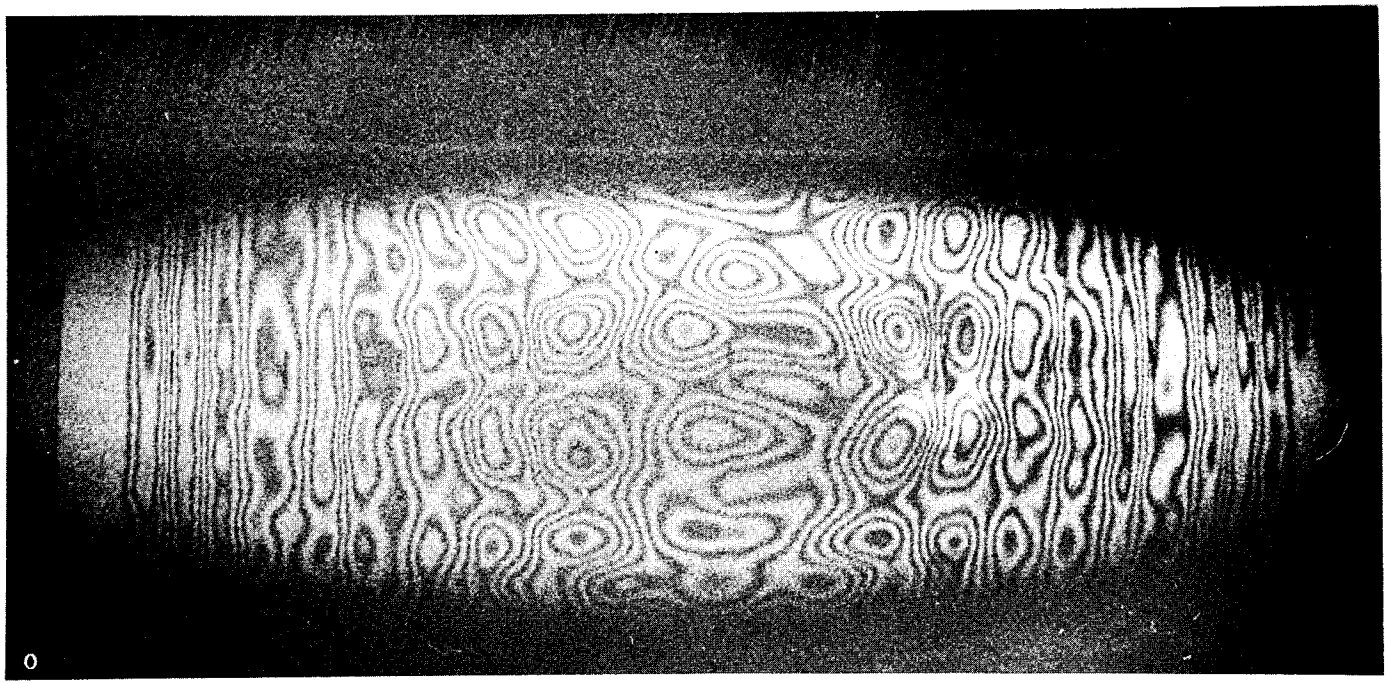

Figure B.6: Wave propagation in the thin-walled cylindrical shell. Time t = 197 μsec.

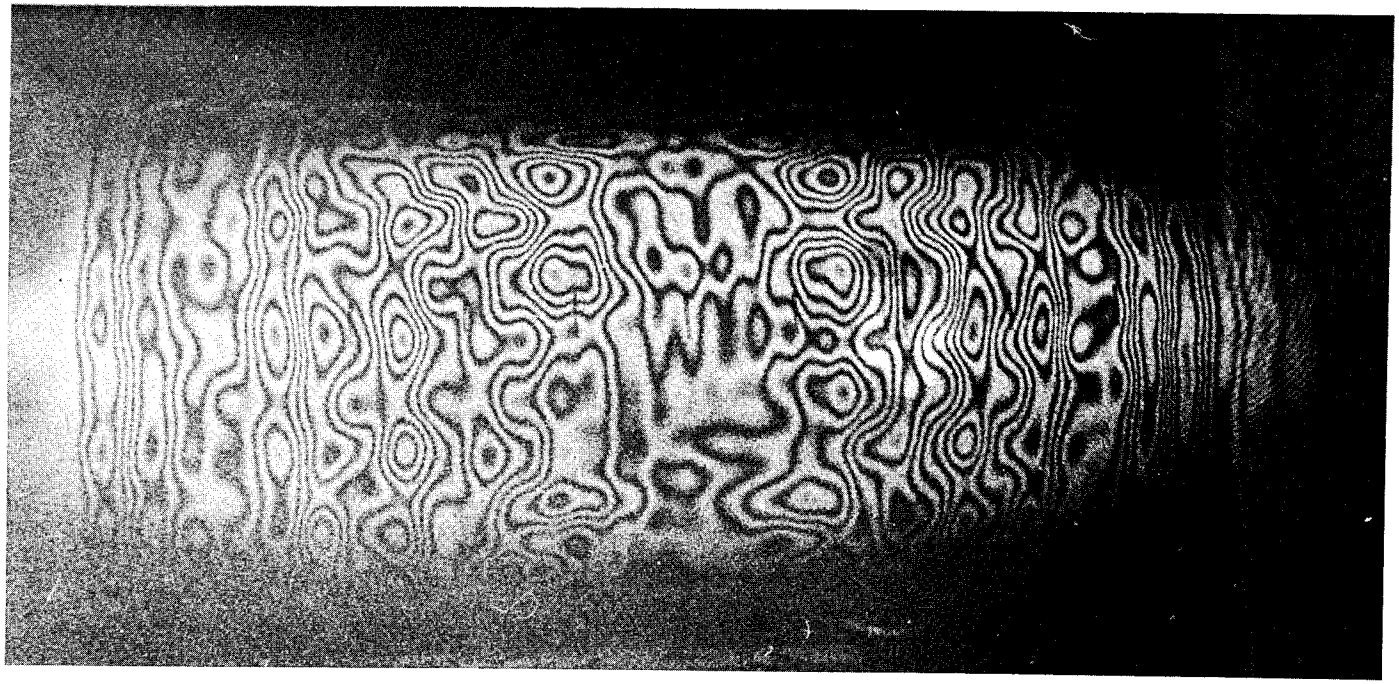

Figure B.7: Wave propagation in the thin-walled cylindrical shell. Time t = 236 μsec.

APPENDIX C

WAVES REFLECTING FROM THE ENDS OF THE SHELL

(ADDITIONAL INTERFEROGRAMS)

The interferograms presented in this appendix show transverse waves reflecting from the ends of the thin cylindrical shell, and they illustrate the structural behavior at various times, t_i. These figures are intended to supplement Figures 20, 22, and 24 in the main body of the text, Section 3.0.

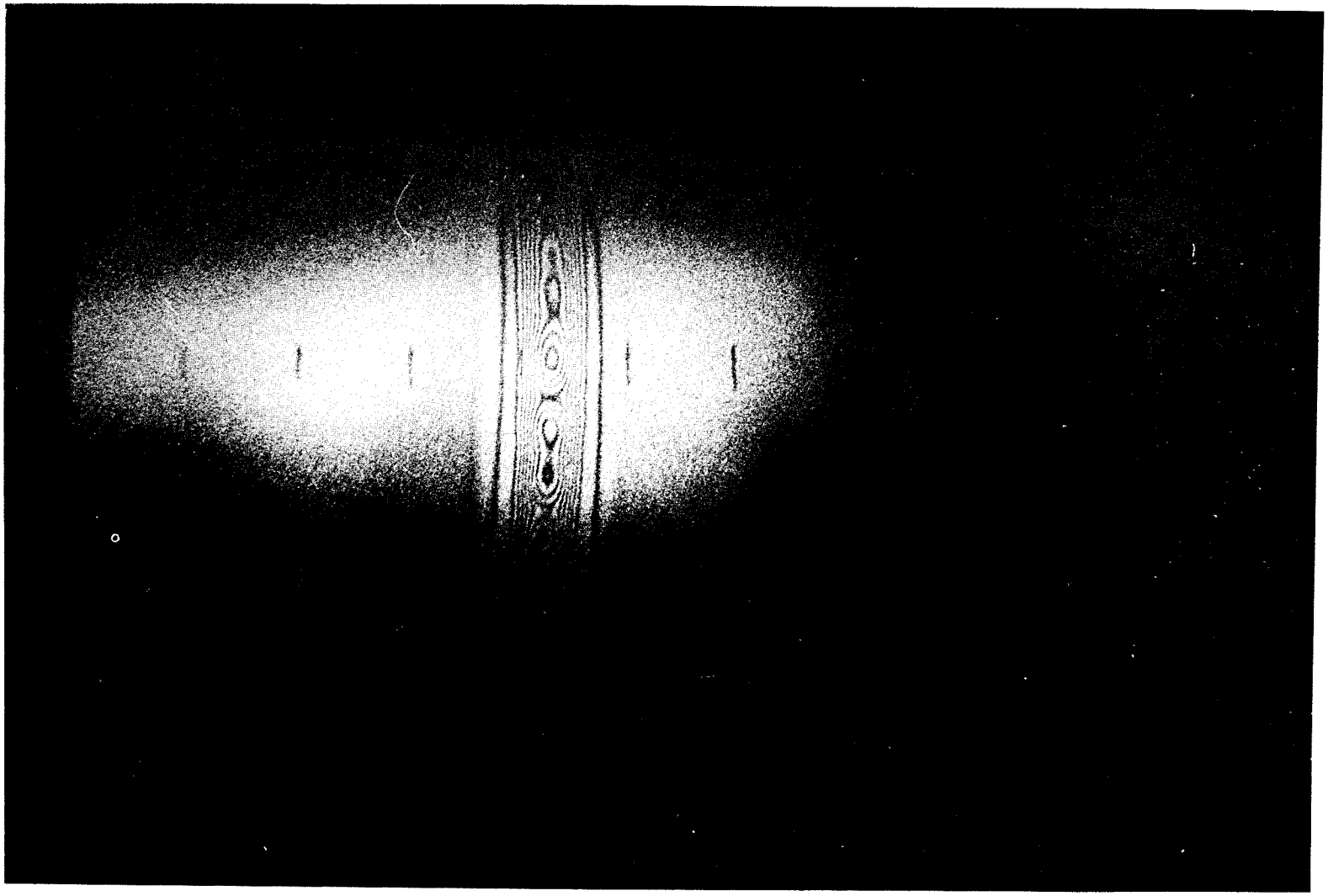

Figure C.1: Wave Propagating Toward the "Clamped" End (at the Left). Time t = 15 μsec.

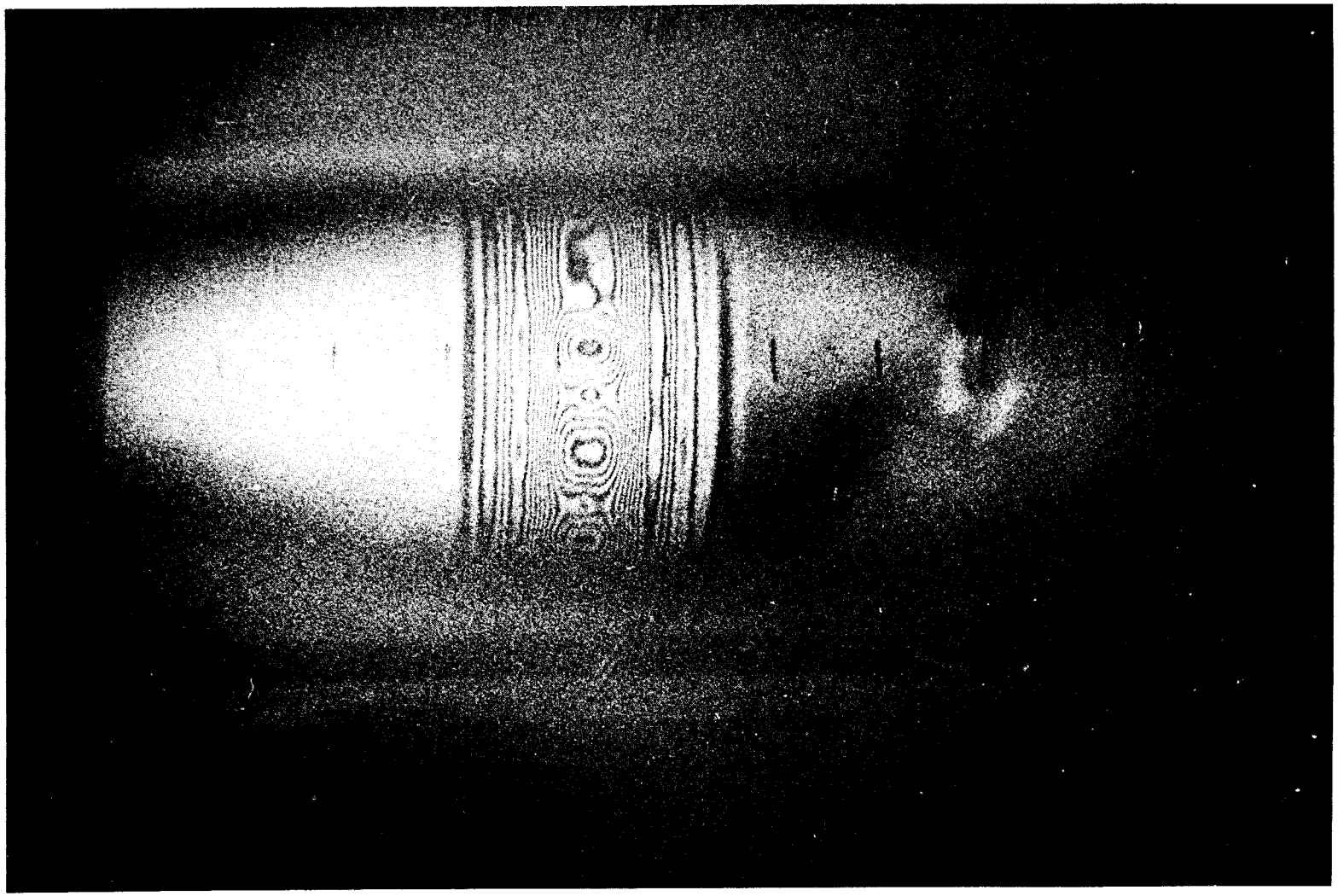

Figure C.2: Wave Propagating Toward the "Clamped" End (at the Left). Time t = 30 μsec.

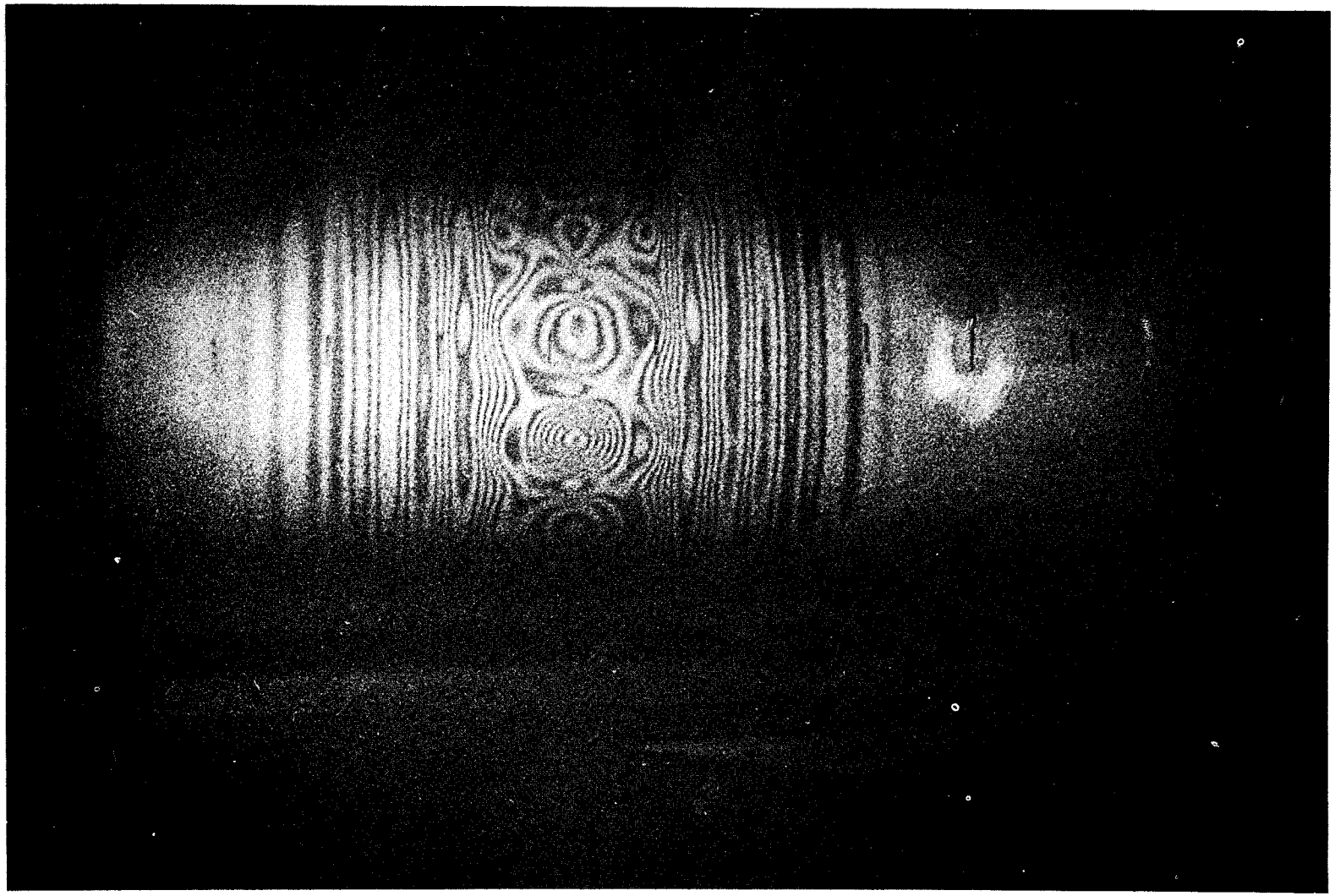

Figure C.3: Wave Propagating Toward the "Clamped" End (at the Left). Time t = 60 μsec.

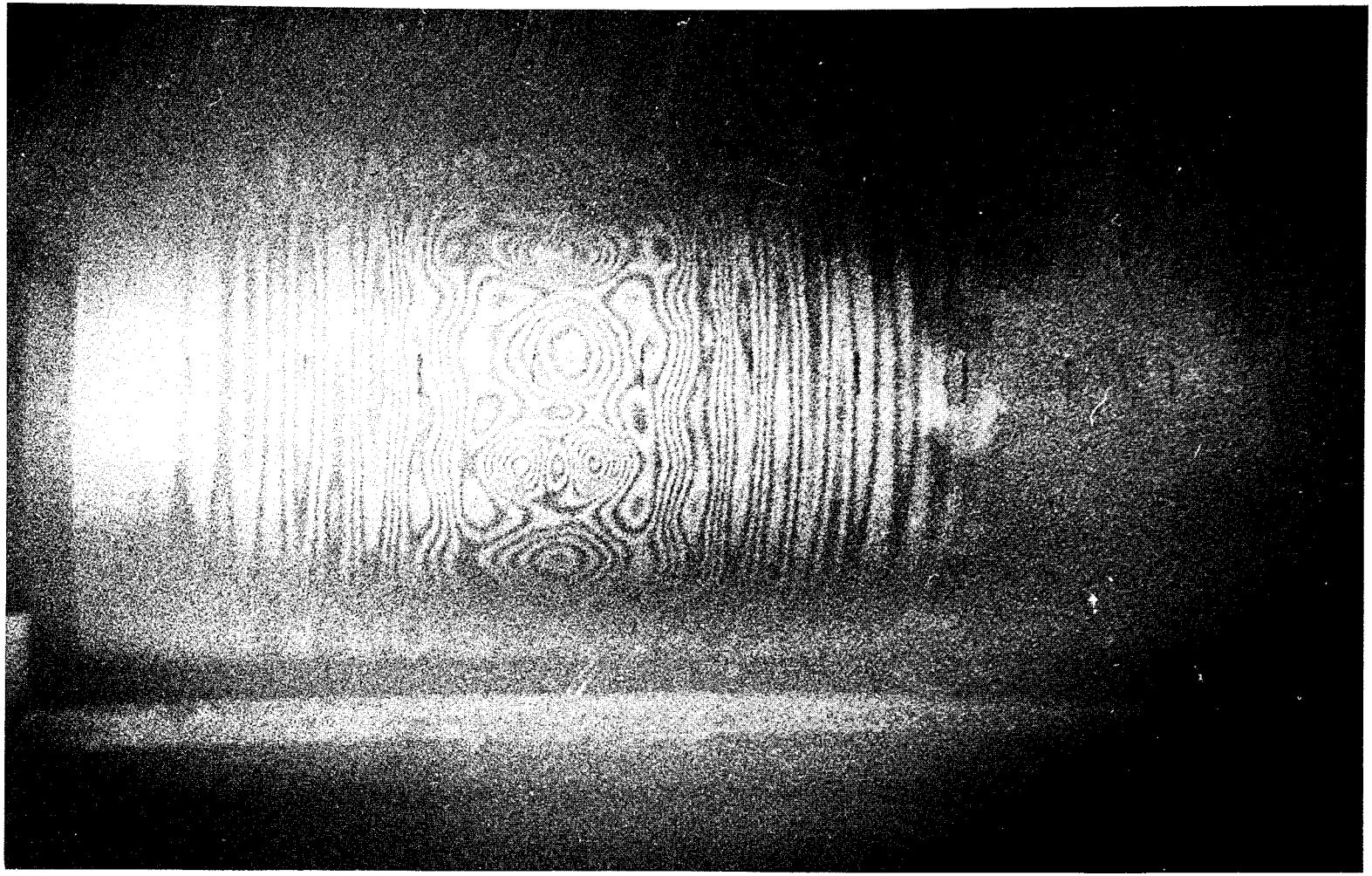

Figure C.4: Wave Propagating toward the "Clamped" End (at the Left). Time t = 75 μsec.

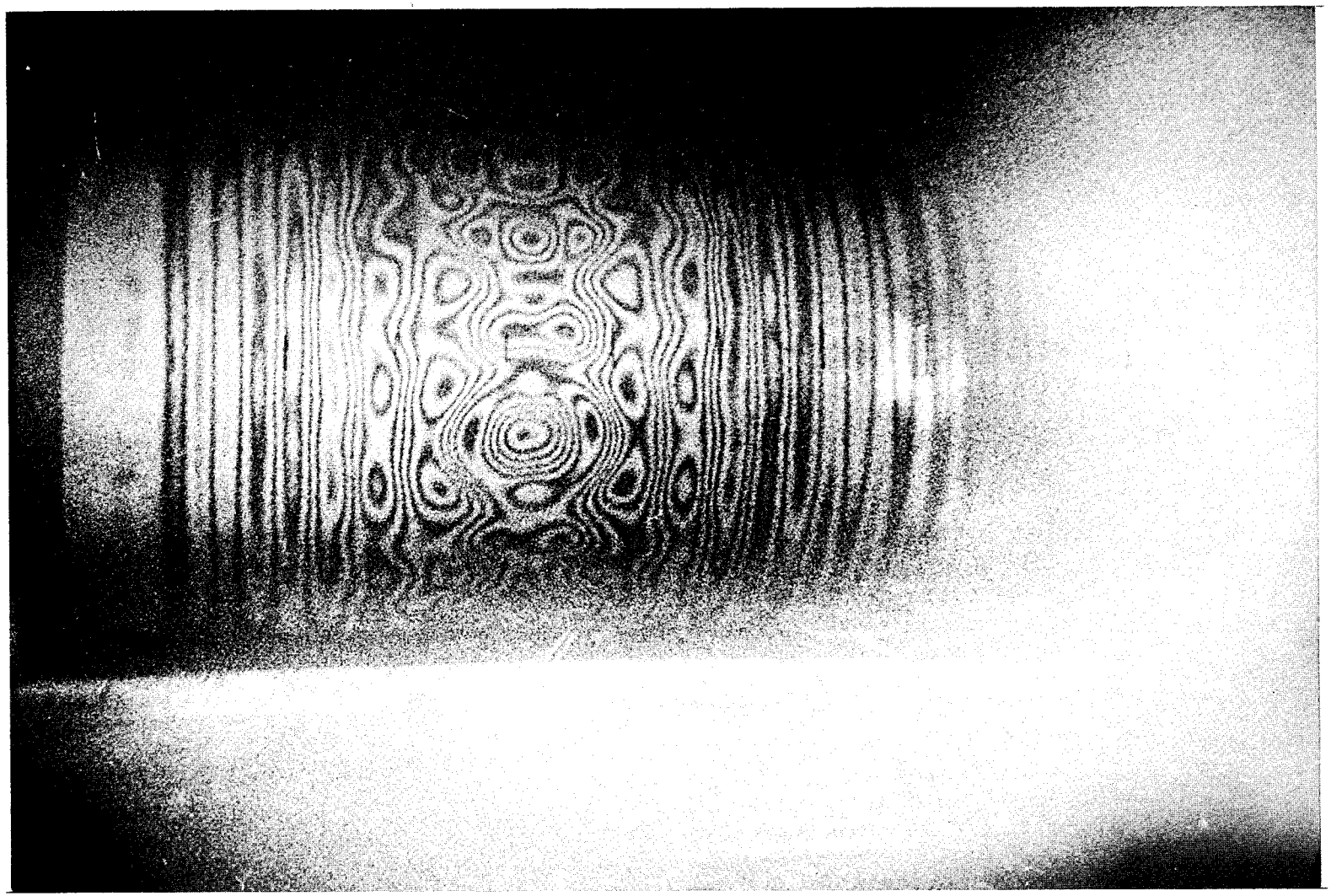

Figure C.5: Wave Propagating toward the "Clamped" End (at the Left). Time t = 90 μsec.

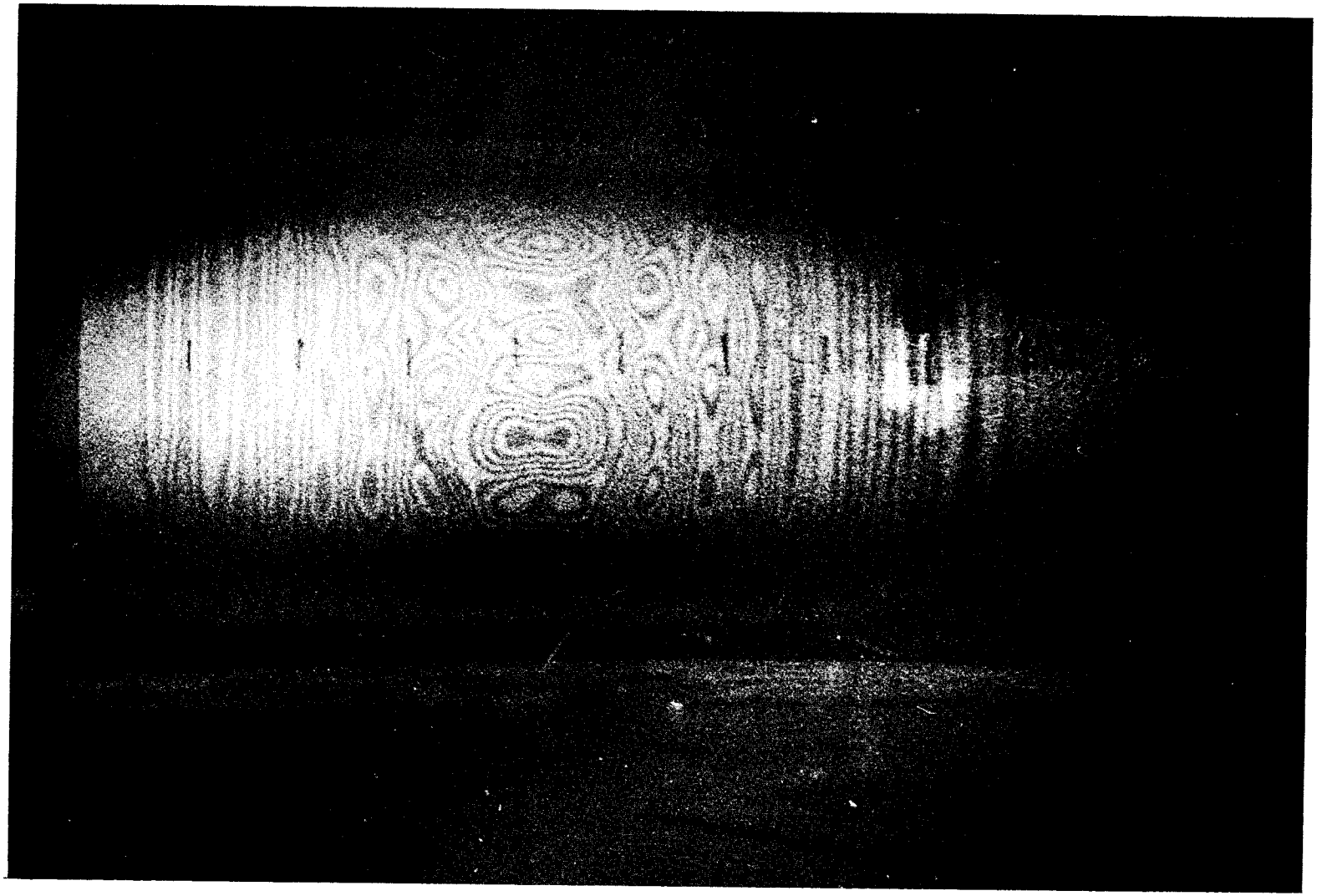

Figure C.6: Wave Propagating toward the "Clamped" End (at the Left)
Time t = 105 μsec.

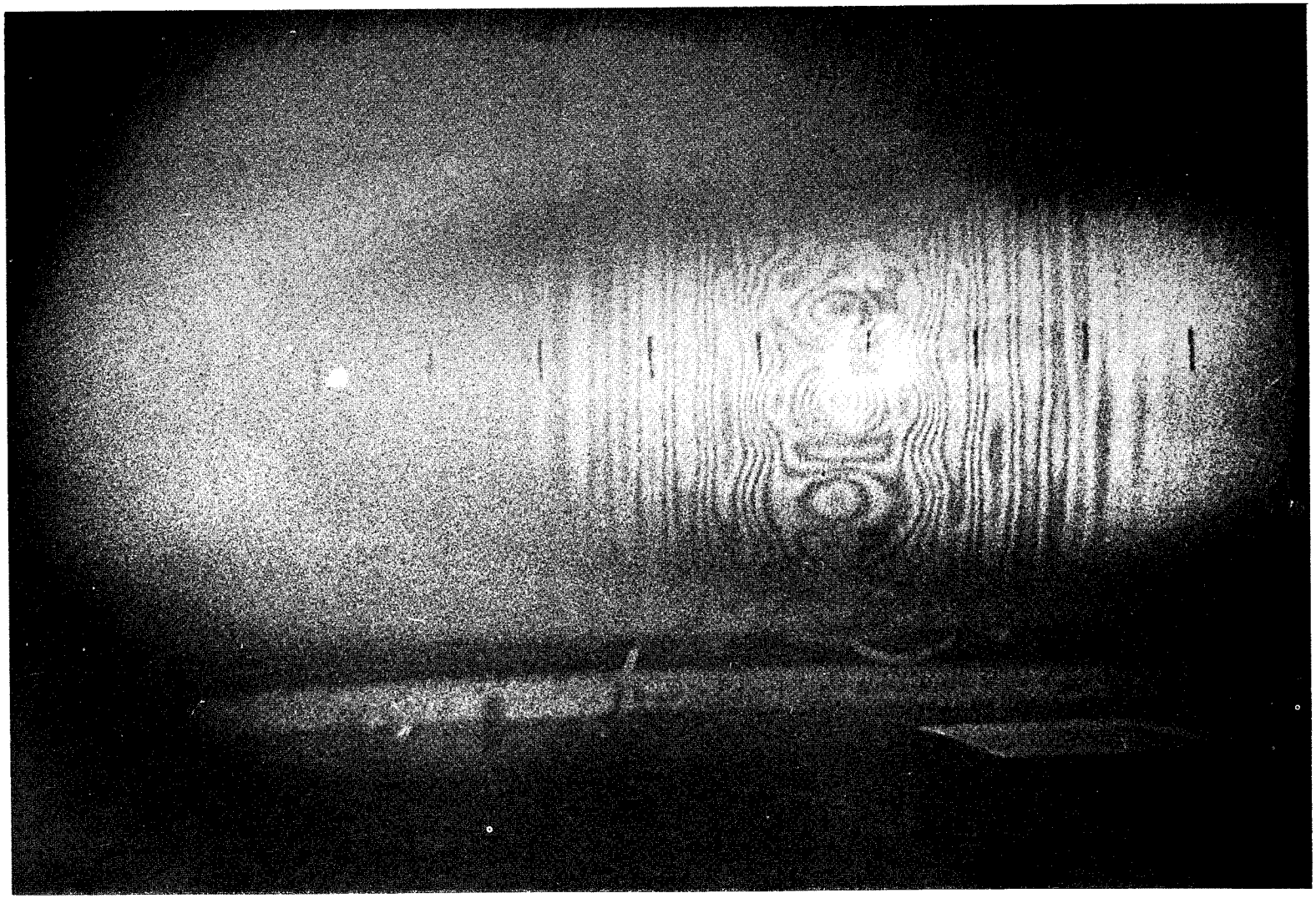

Figure C.7: Wave Propagating toward the Free End (at the Right).
Time t = 60 μsec.

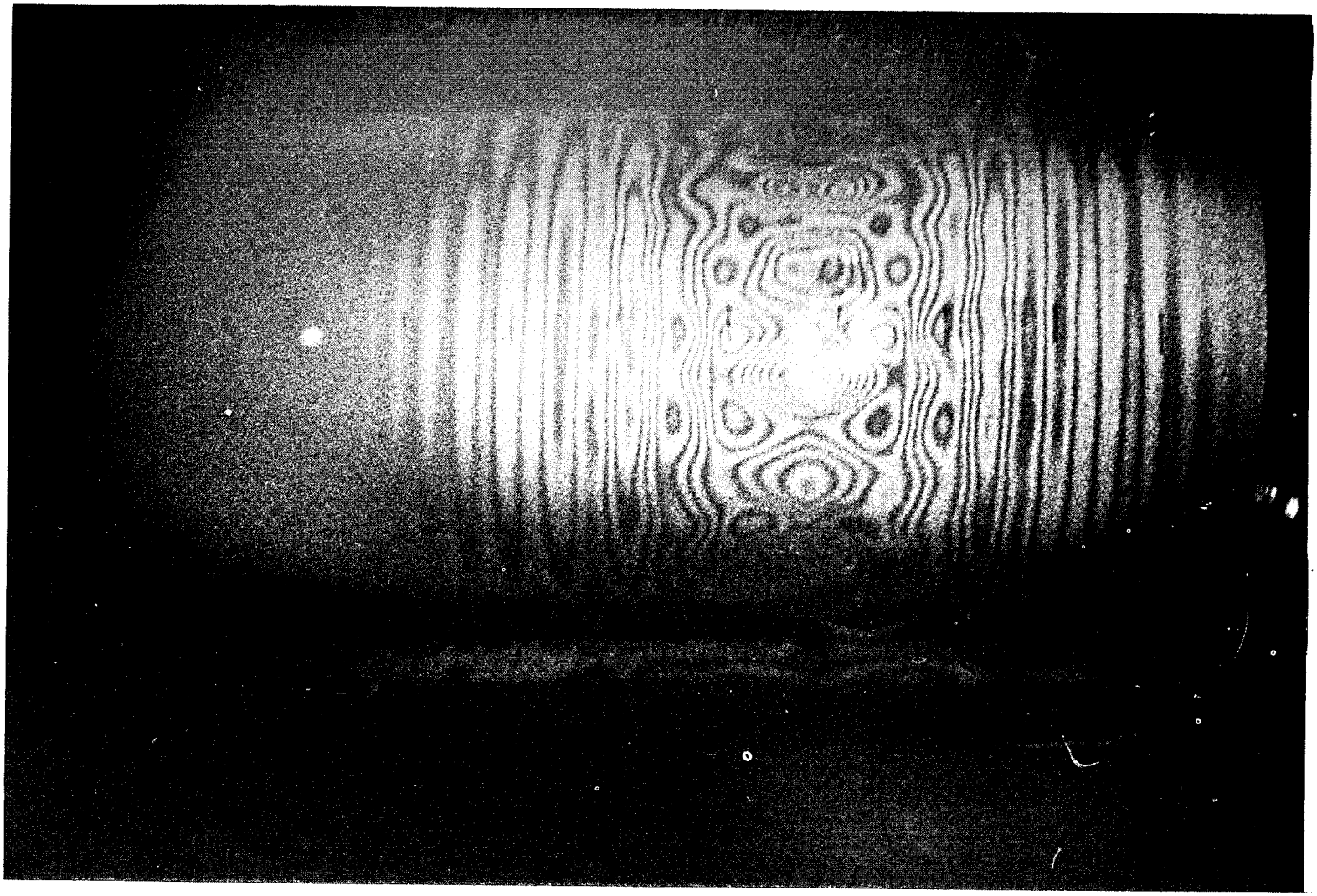

Figure C.8: Wave Propagating toward the Free End (at the Right).
Time t = 75 μsec.

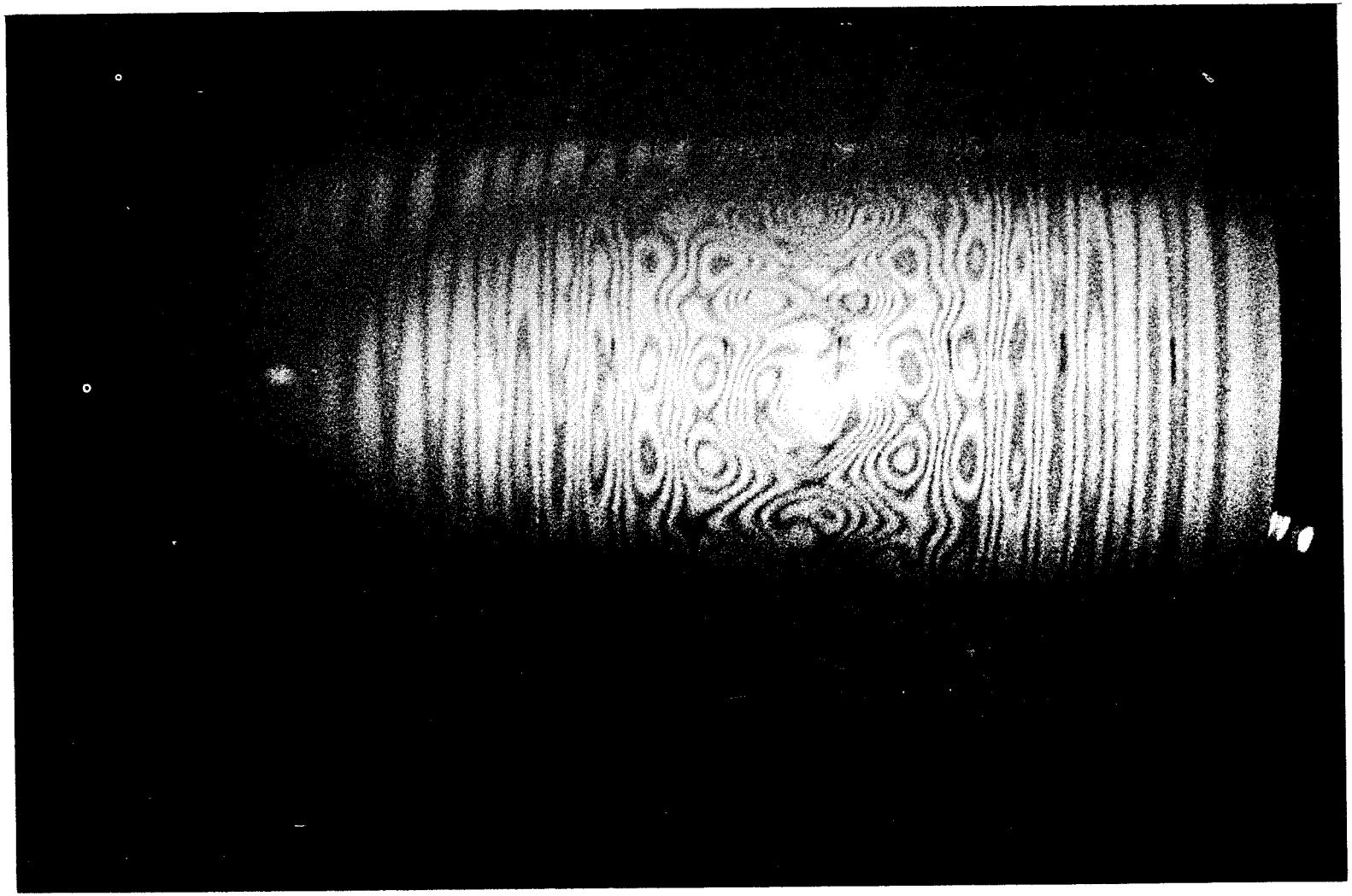

Figure C.9: Wave Propagating toward the Free End (at the Right).
Time t = 90 μsec.

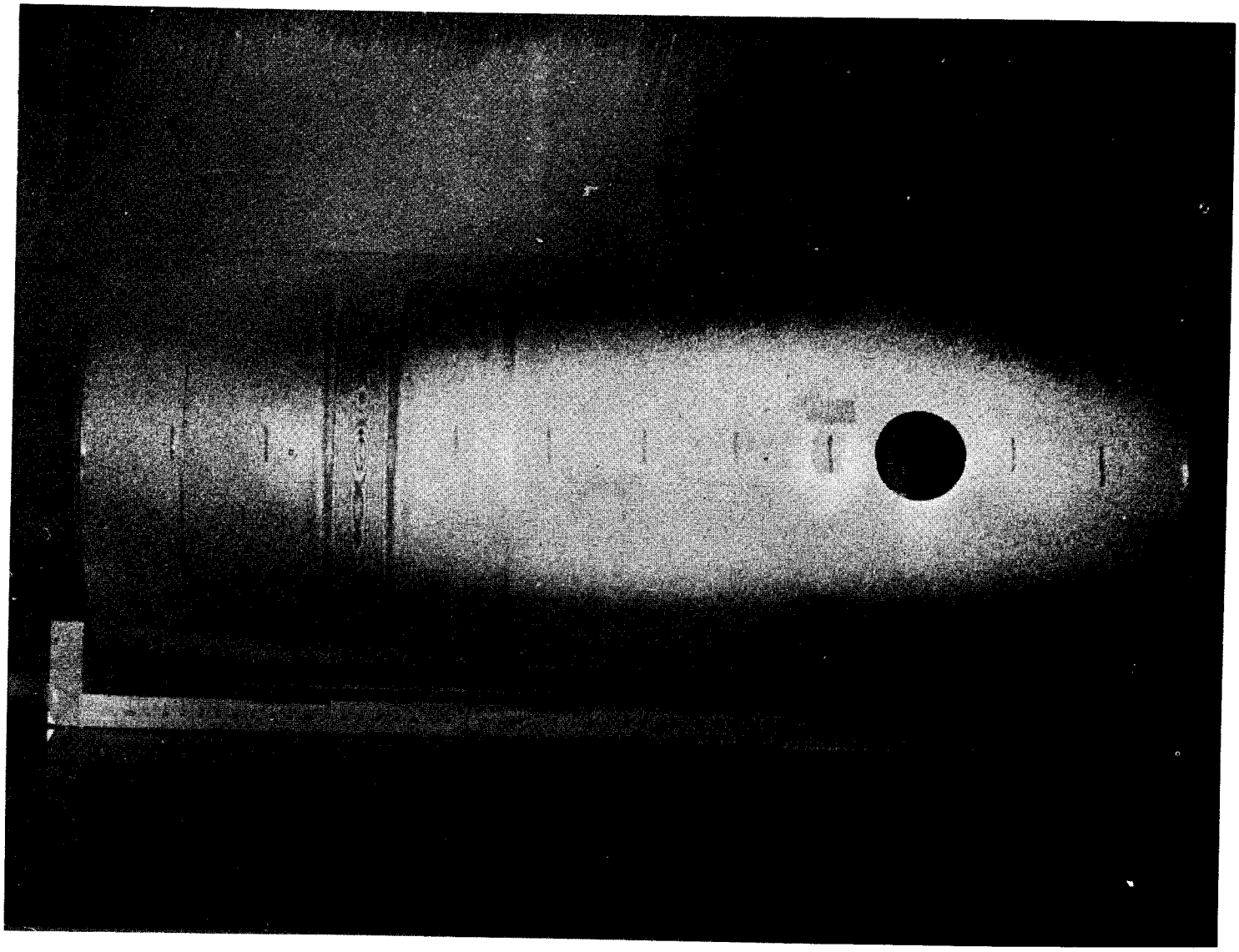

Figure C.10: Wave Propagating toward the Simply-Supported Boundary (Vee-Groove) at the Left. Time t = 11 μsec.

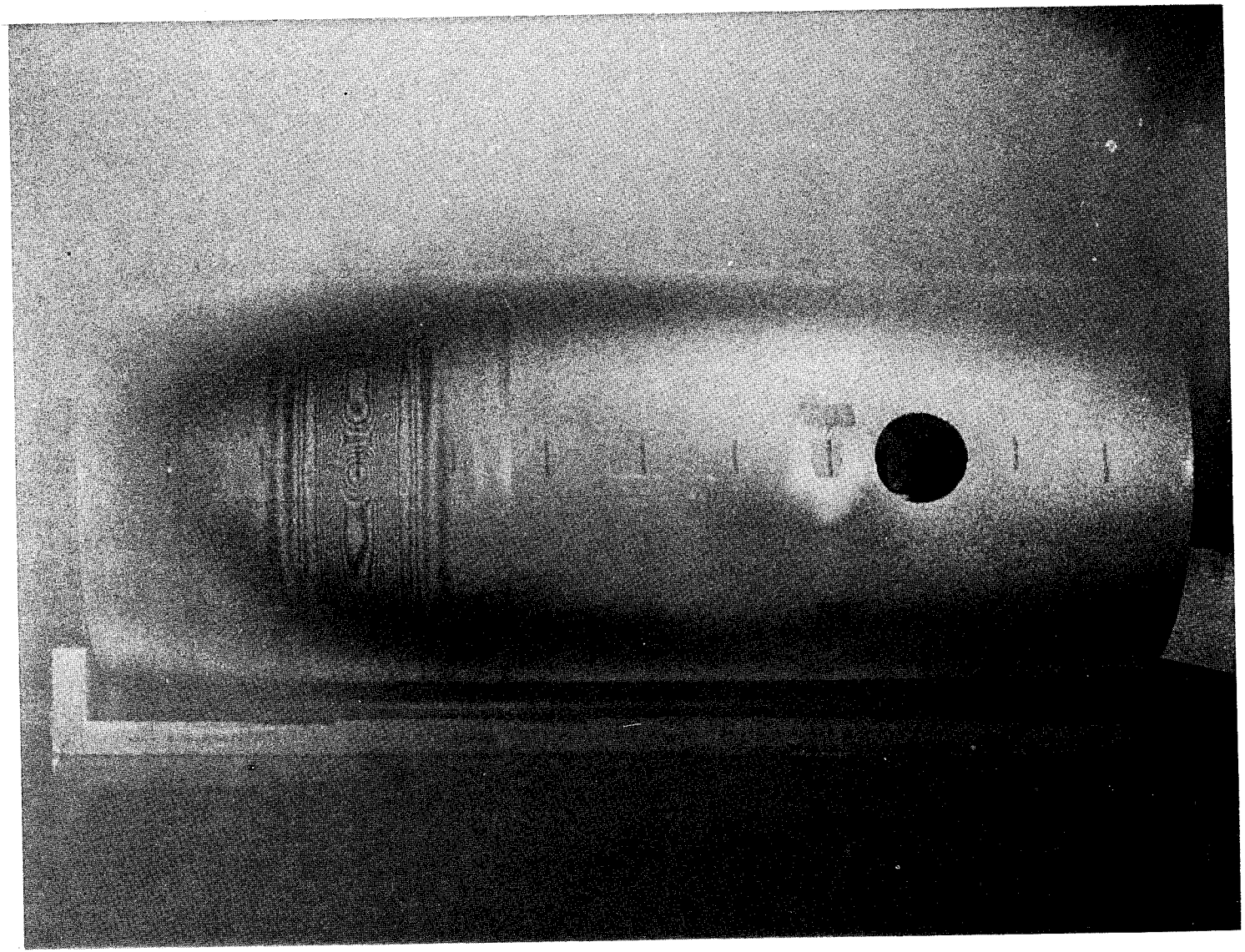

Figure C.11: Wave Propagating Toward the Simply-Supported Boundary (Vee-Groove) at the Left. Time t = 20 μsec.

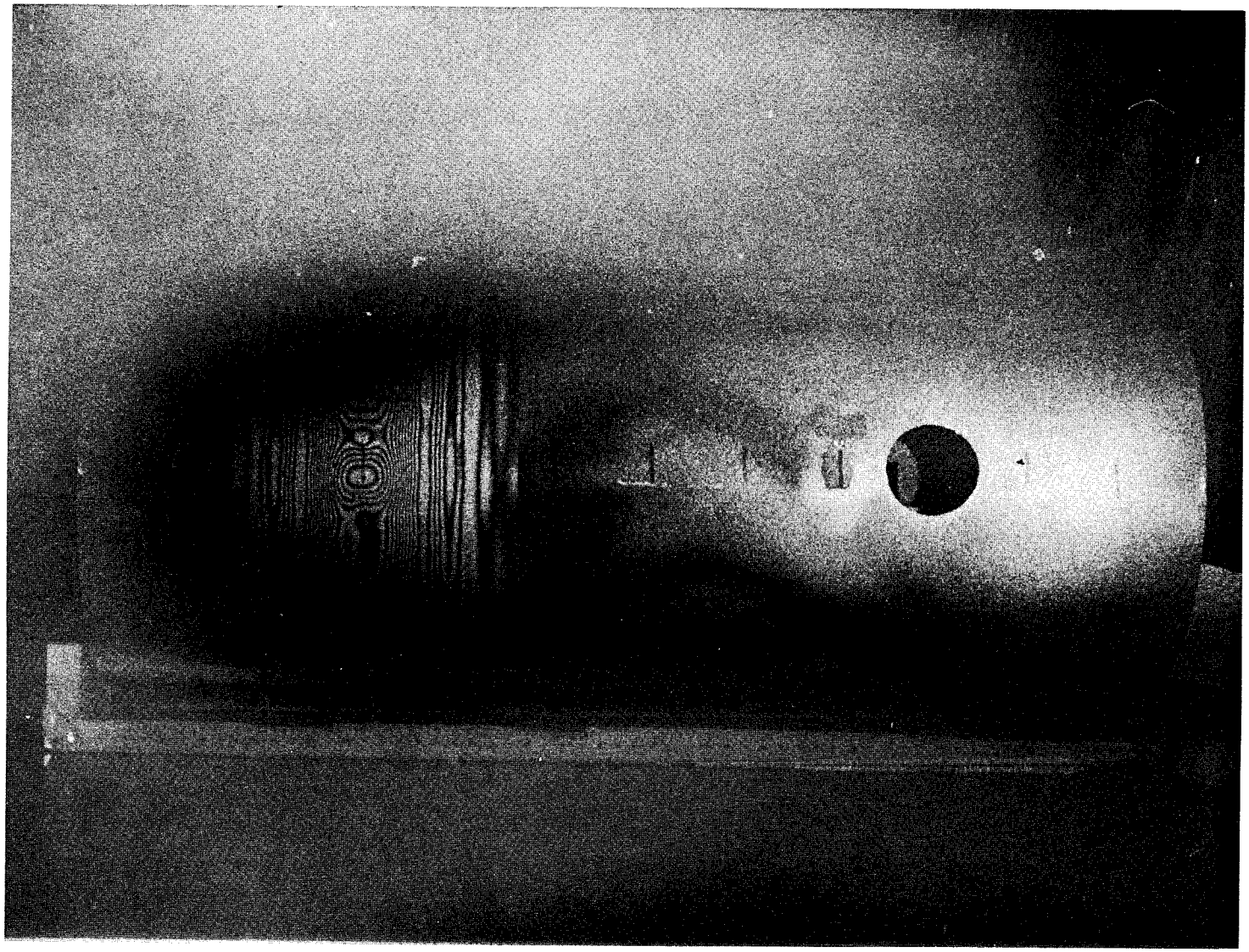

Figure C.12: Wave Propagating Toward the Simply-Supported Boundary (Vee-Groove) at the Left. Time t = 30 μsec.

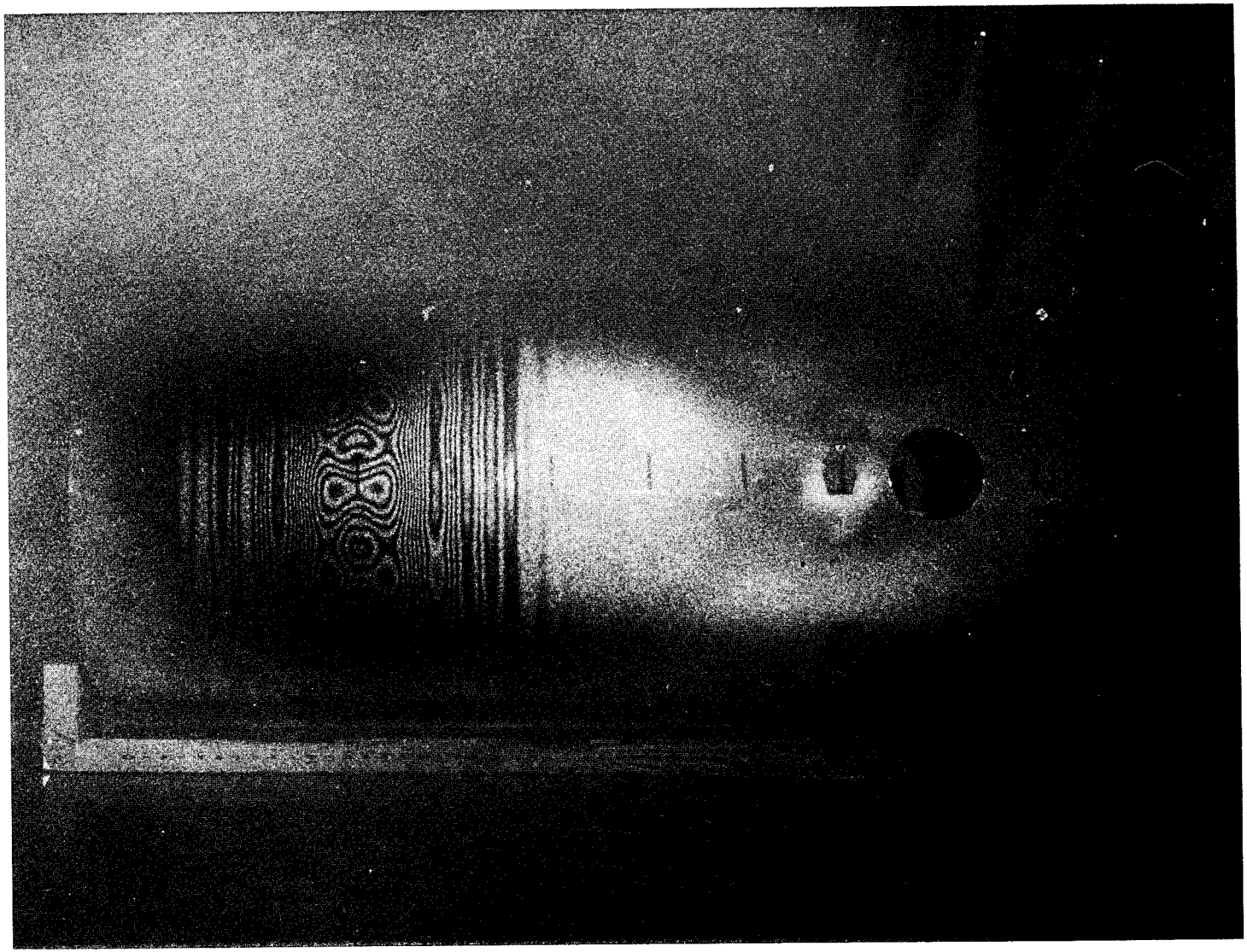

Figure C.13: Wave propagating toward the simply-supported boundary (vee-groove) at the left. Time t = 39 μsec.

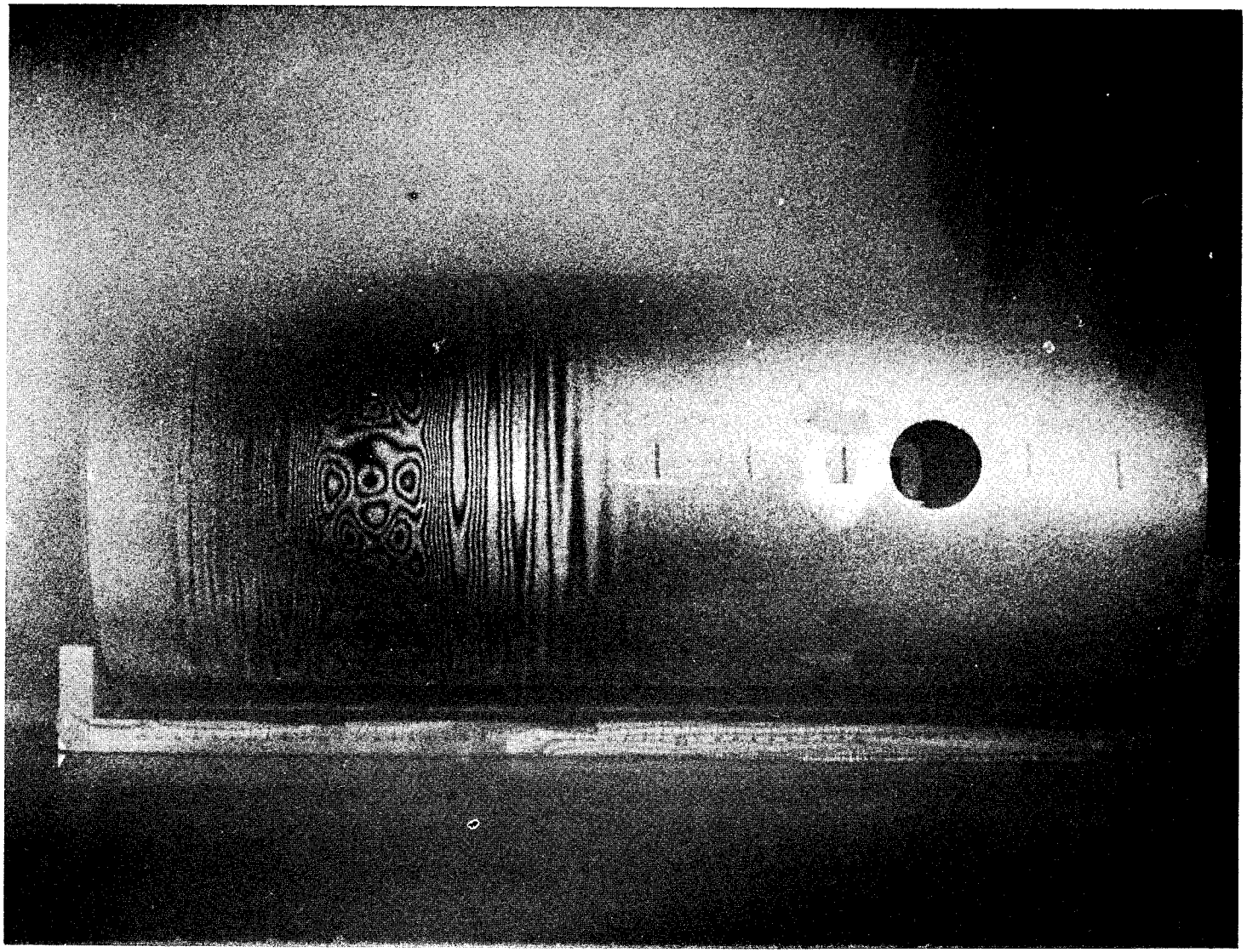

Figure C.14: Wave Propagating Toward the Simply-Supported Boundary (Vee-Groove) at the Left. Time t = 48 μsec.

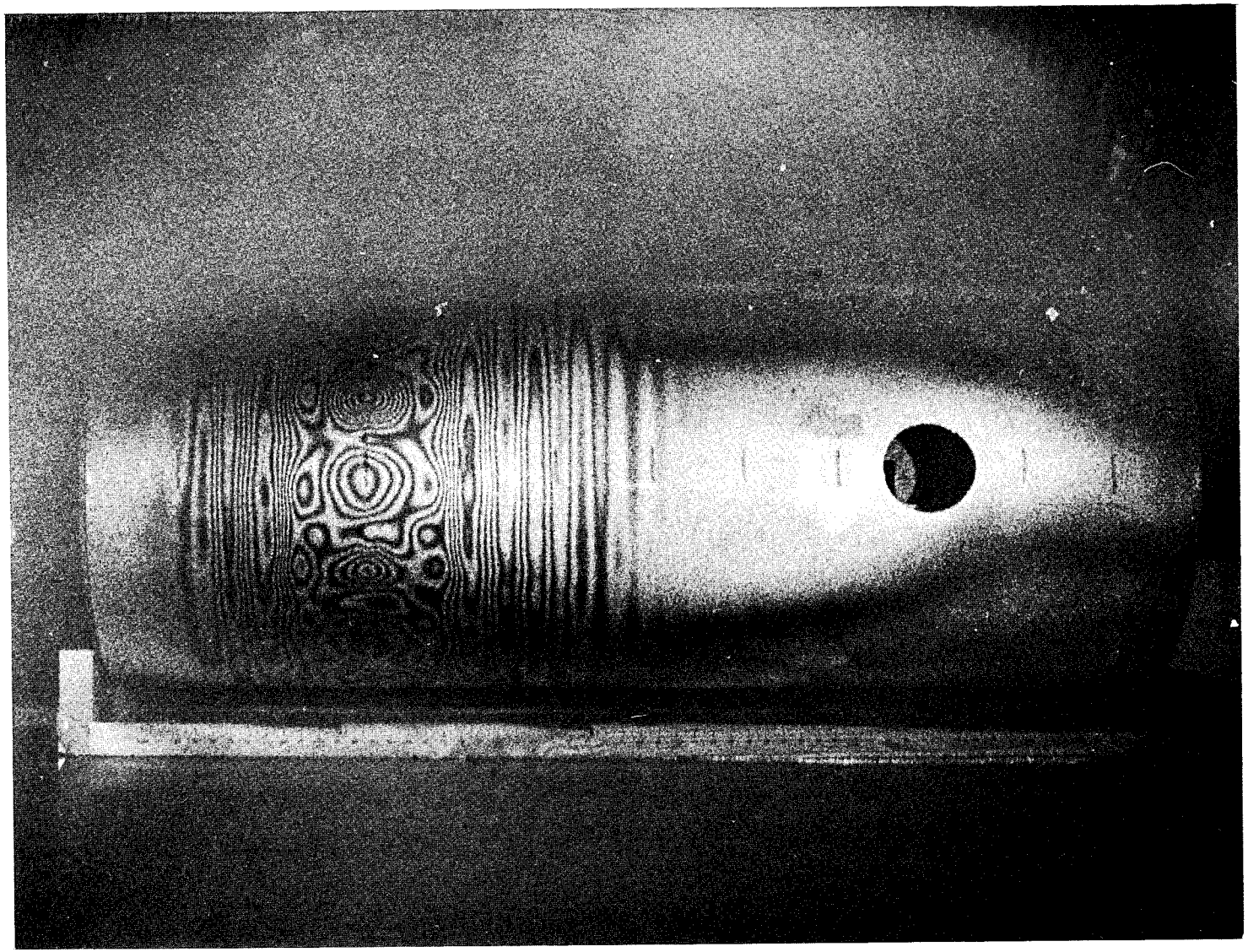

Figure C.15: Wave propagating toward the simply-supported boundary (vee-groove) at the left. Time t = 61 μsec.

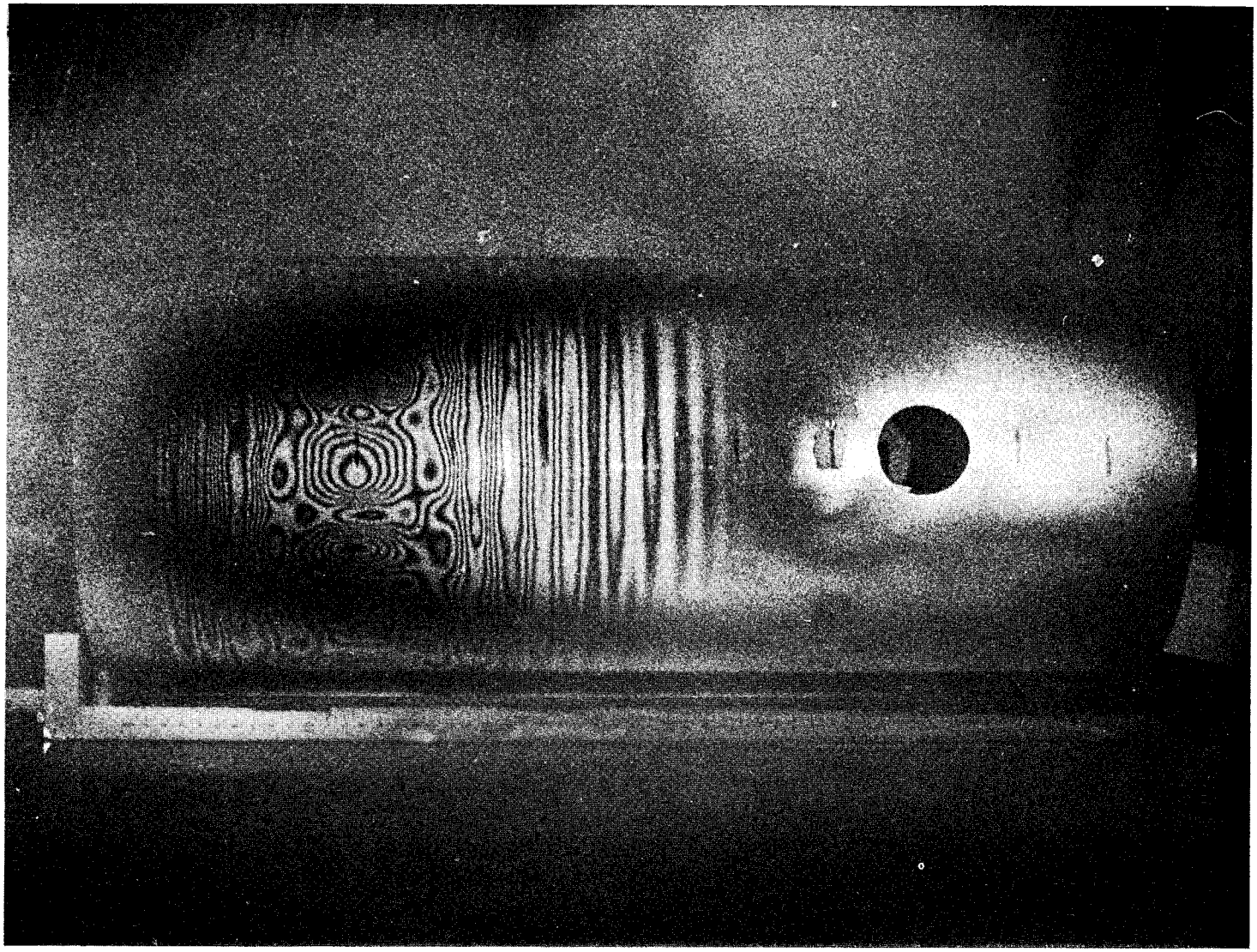

Figure C.16: Wave Propagating Toward the Simply-Supported Boundary (Vee-Groove) at the Left. Time t = 71 μsec.

APPENDIX D

WAVE PROPAGATION IN THE THICK-WALLED SHELL

(ADDITIONAL INTERFEROGRAMS)

This Appendix is meant to supplement the results given in Section 4.0, "Tests on a Thick-Walled Cylinder."

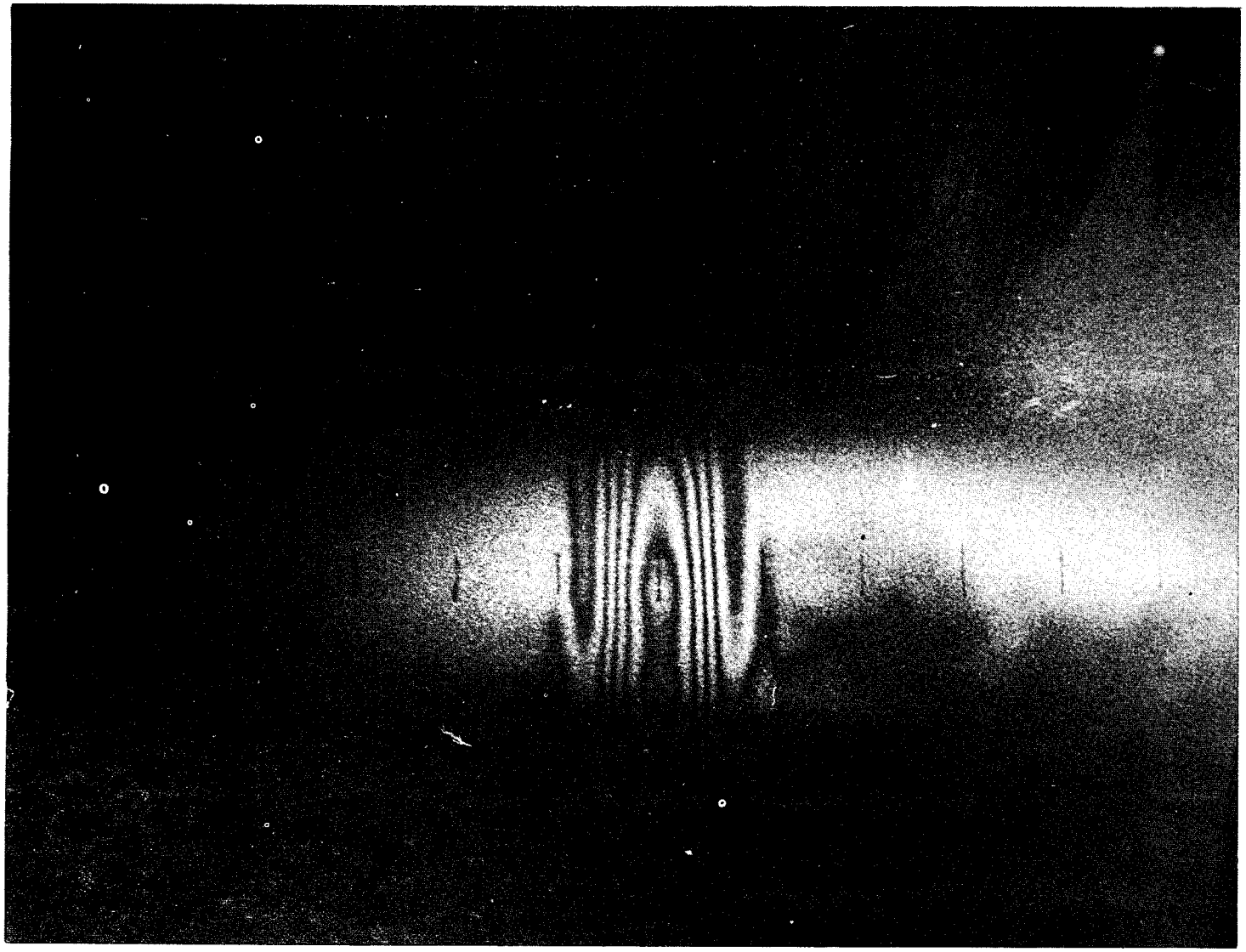

Figure D.1: Wave propagation in the thick-walled shell. (h = .25 inches). Time t = 20 μsec.

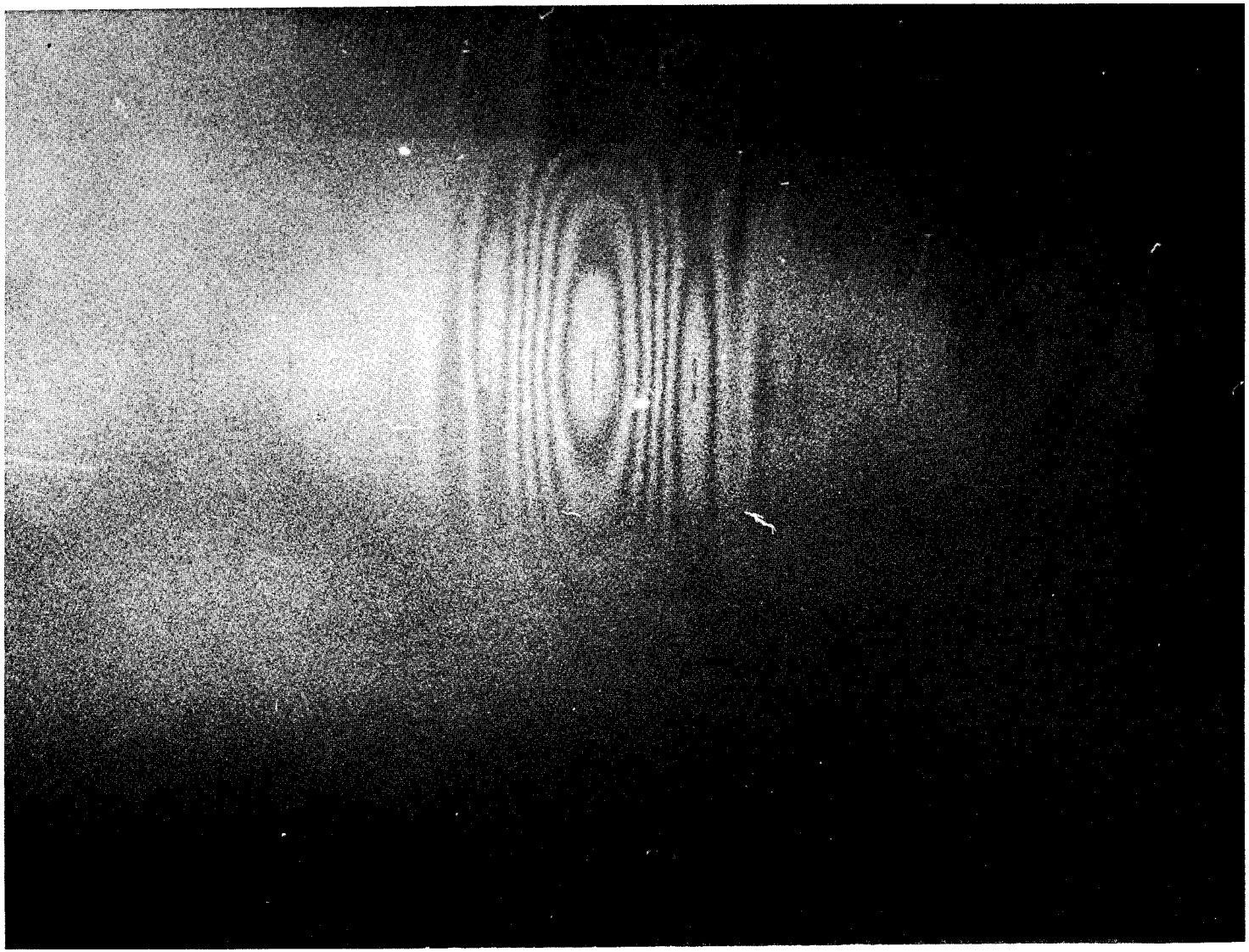

Figure D.2: Wave propagation in the thick-walled shell. (h = .25 inches). Time t = 30 μsec.

Figure D.3: Wave propagation in the thick-walled shell. (h = .25 inches). Time t = 47 μsec.

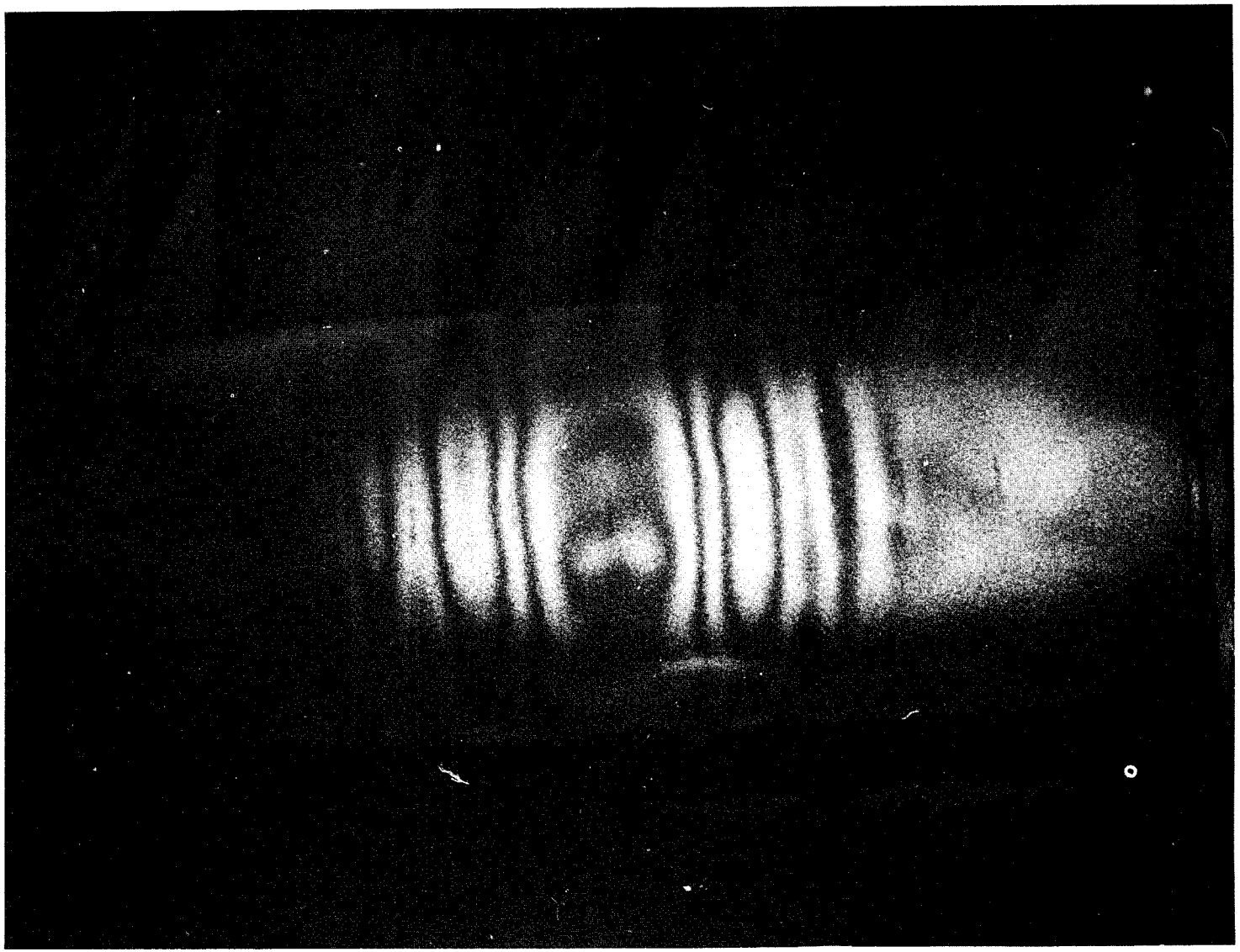

Figure D.4: Wave propagation in the thick-walled shell. Time t = 51 μsec.

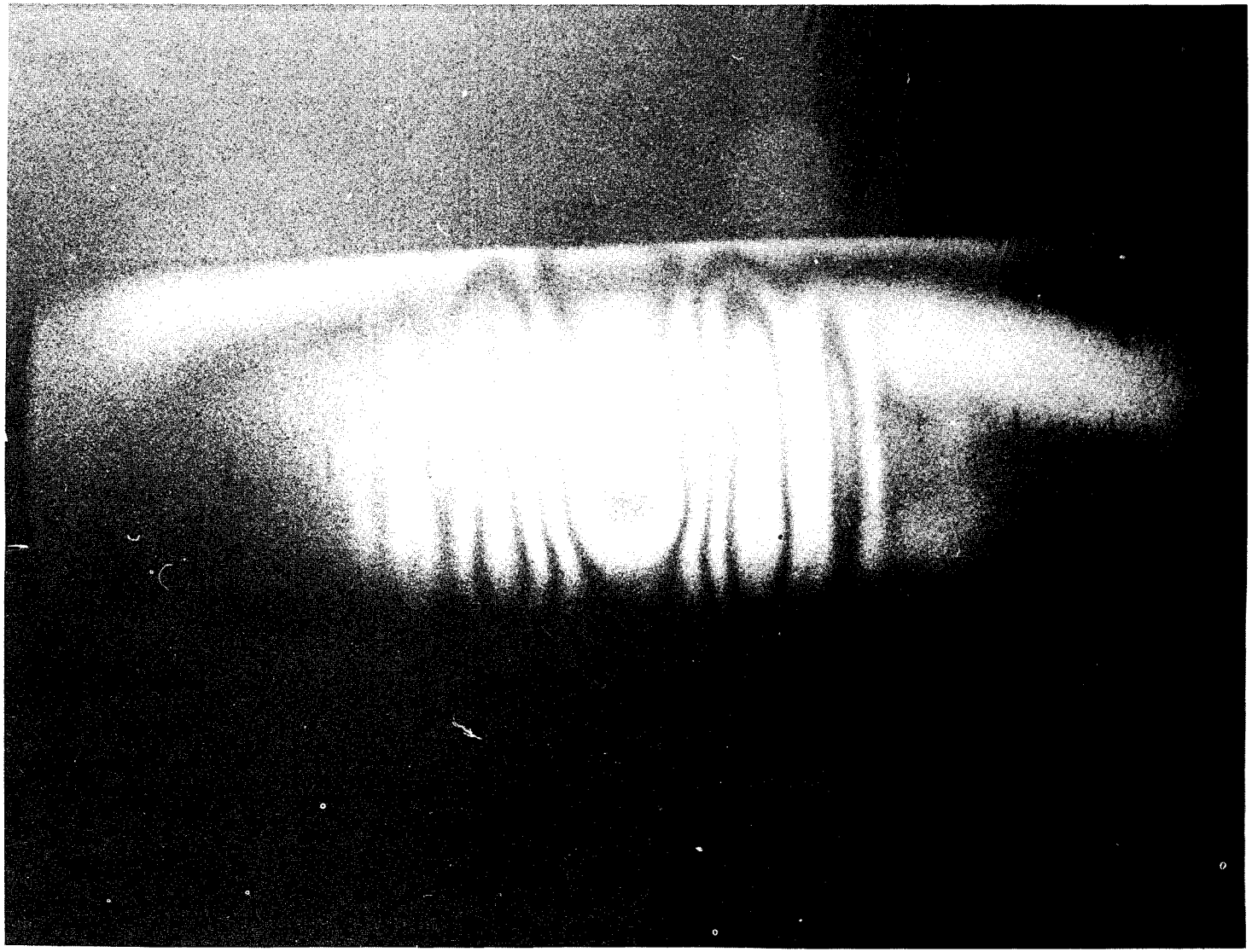

Figure D.5: Wave propagation in the thick-walled shell. Time t = 53 μsec.

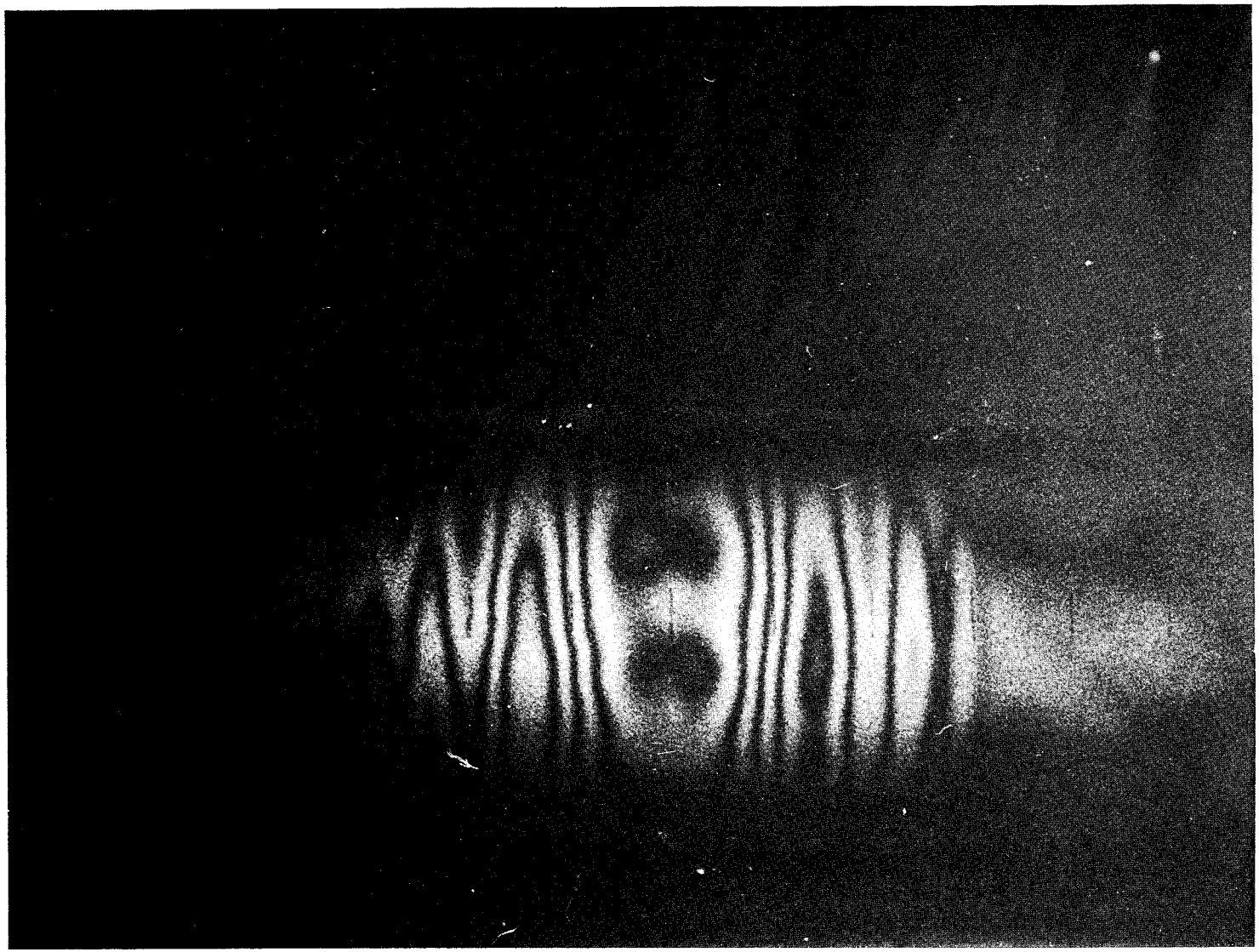

Figure D.6: Wave propagation in the thick-walled shell. Time t = 54 μsec.

Figure D.7: Wave propagation in the thick-walled shell. Time t = 73 μsec.

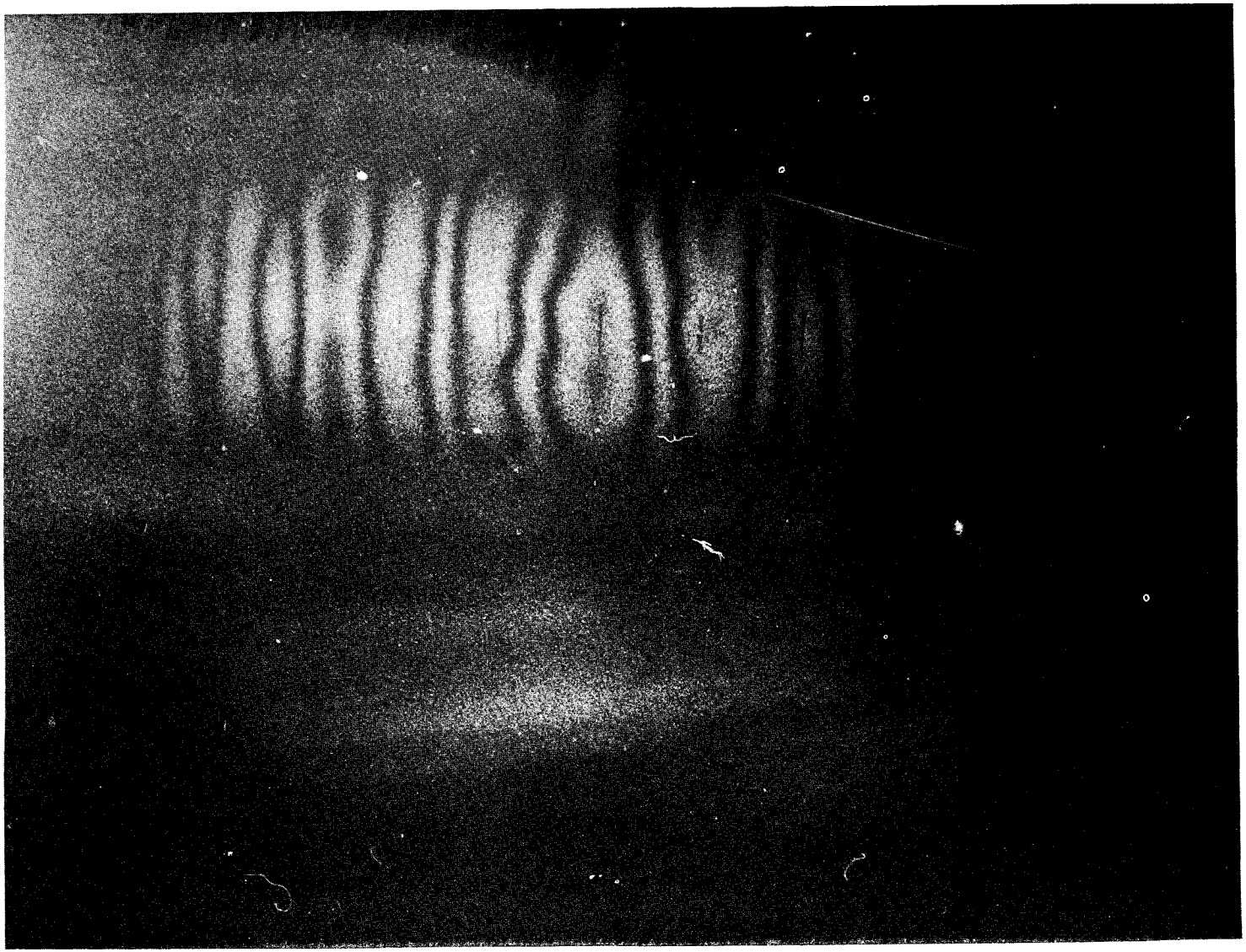

Figure D.8: Wave propagation in the thick-walled shell. Time t = 84 μsec.

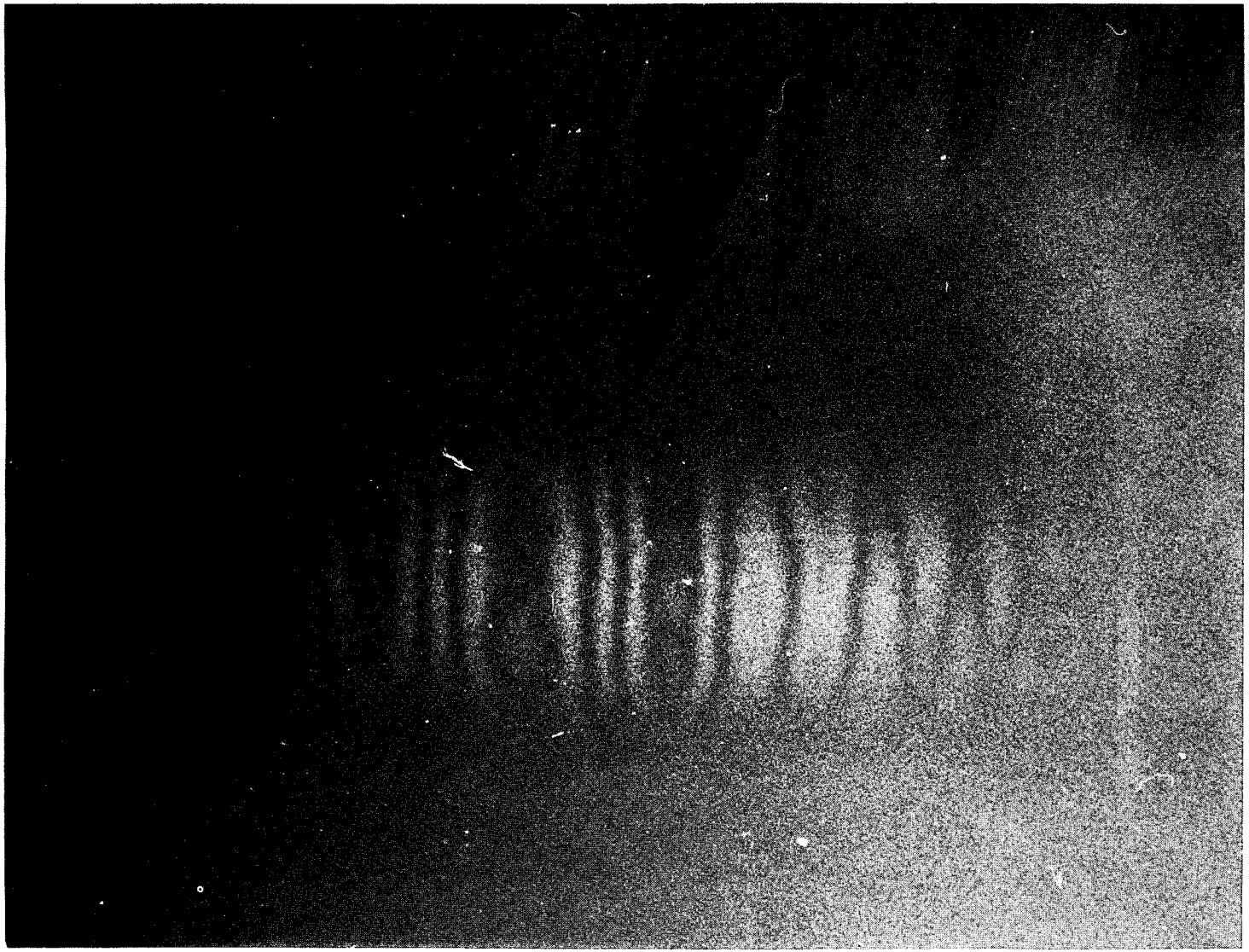

Figure D.9: Wave propagation in the thick-walled shell. Time t = 101 μsec.

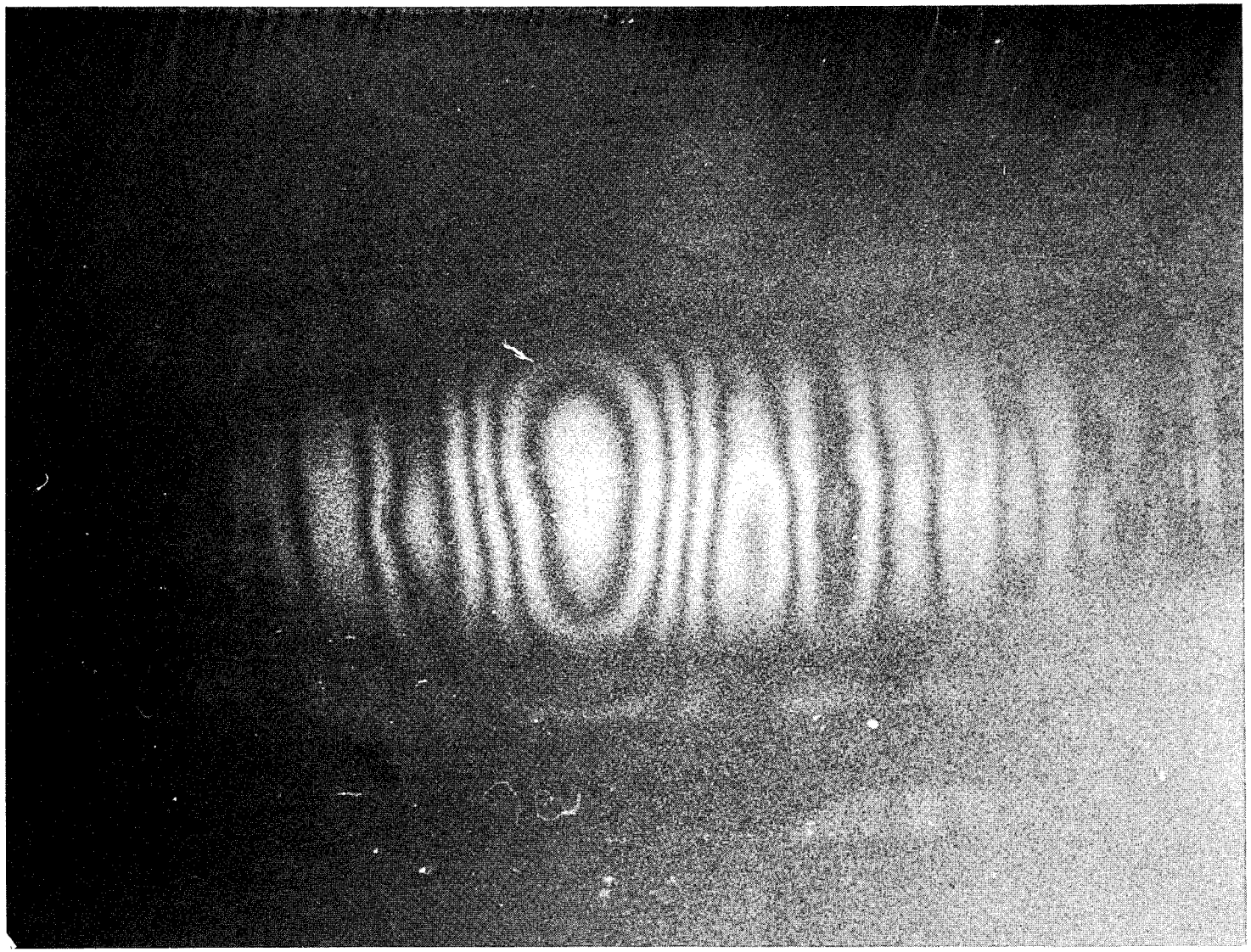

Figure D.10: Wave propagation in the thick-walled shell. Time t = 110 μsec.

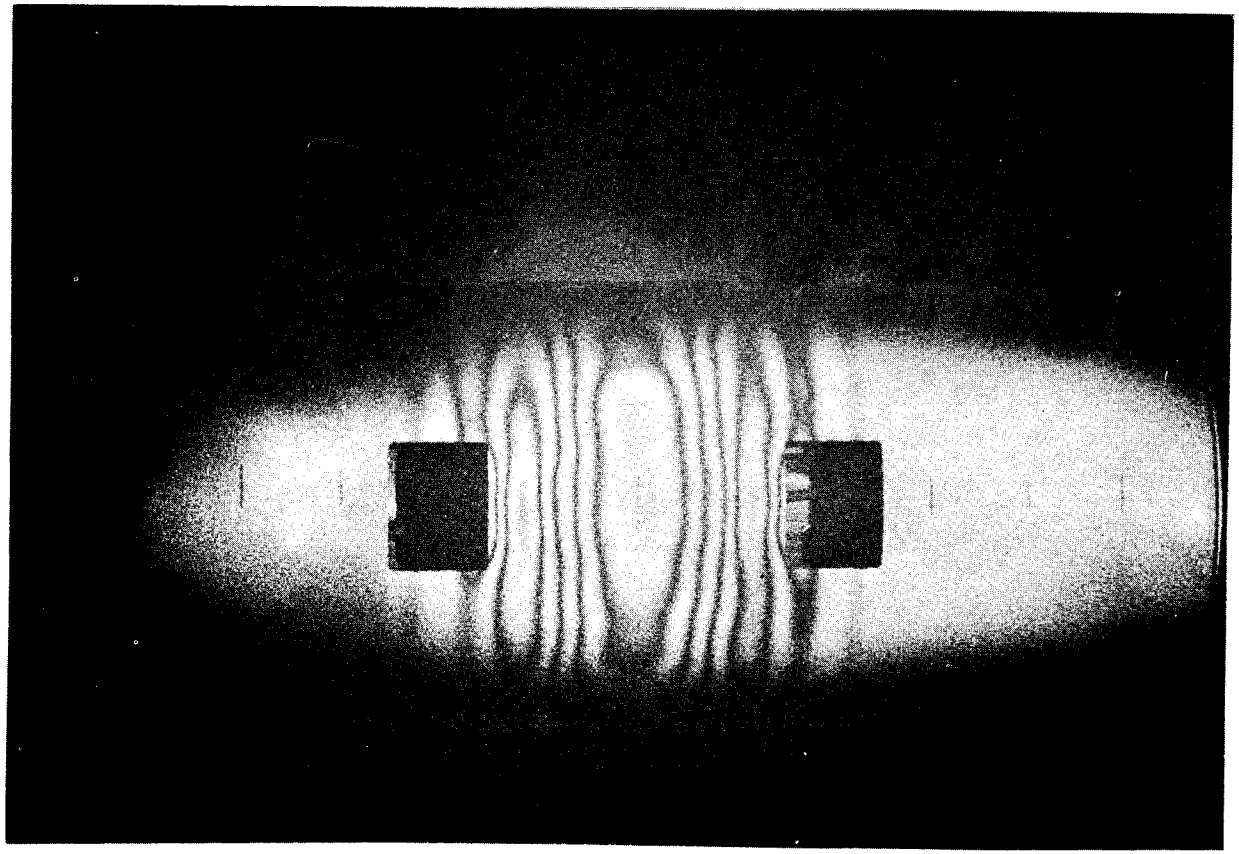

Figure D.11: Wave interacting with cut-outs. Thick-walled shell, h = .25 inches. Time t = 40 μsec.

APPENDIX E

WAVES PAST CUT-OUTS AND STIFFENERS

(ADDITIONAL INTERFEROGRAMS)

This Appendix is to supplement Section 4.0, in particular, "Waves in the Thin-Walled Cylinder."

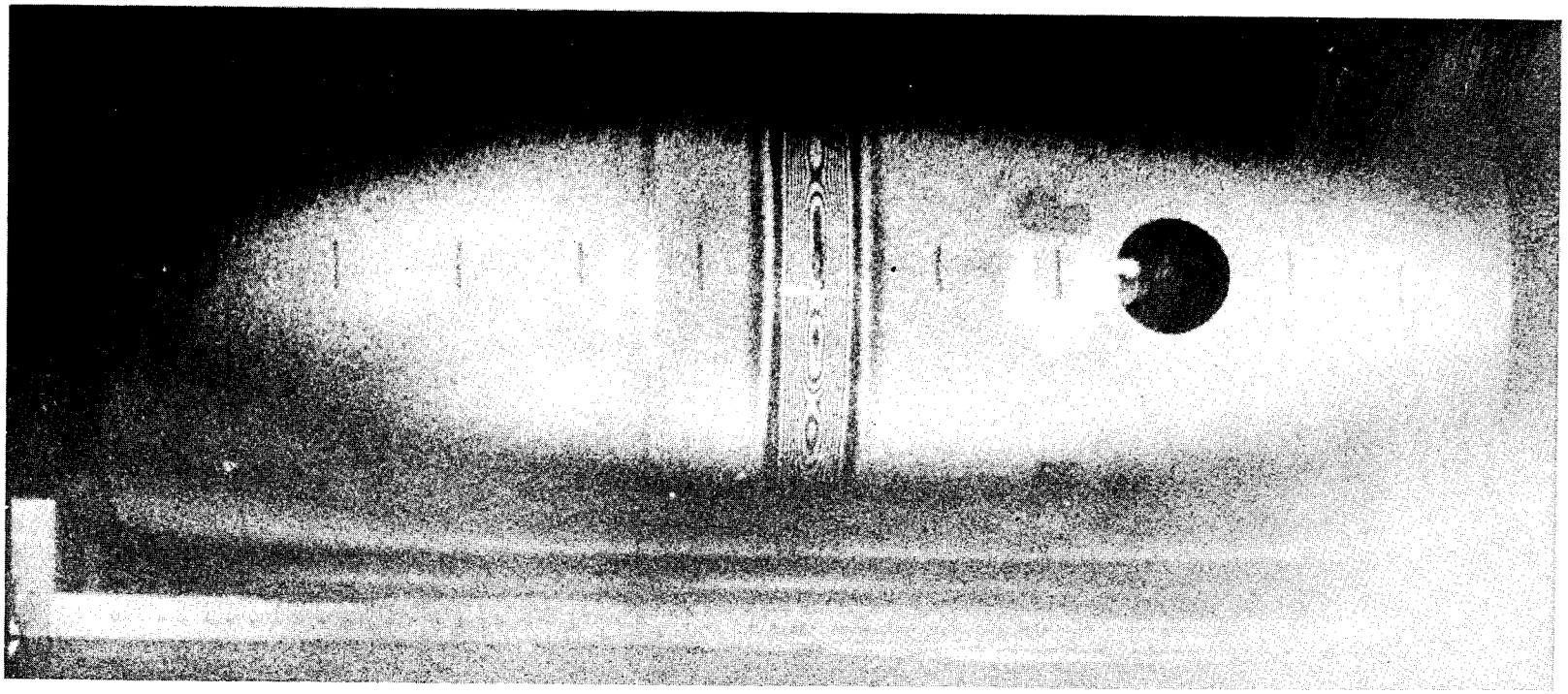

Figure E.1: Transverse Wave Interaction with a Circular Cut-Out.
Time t = 11 μsec

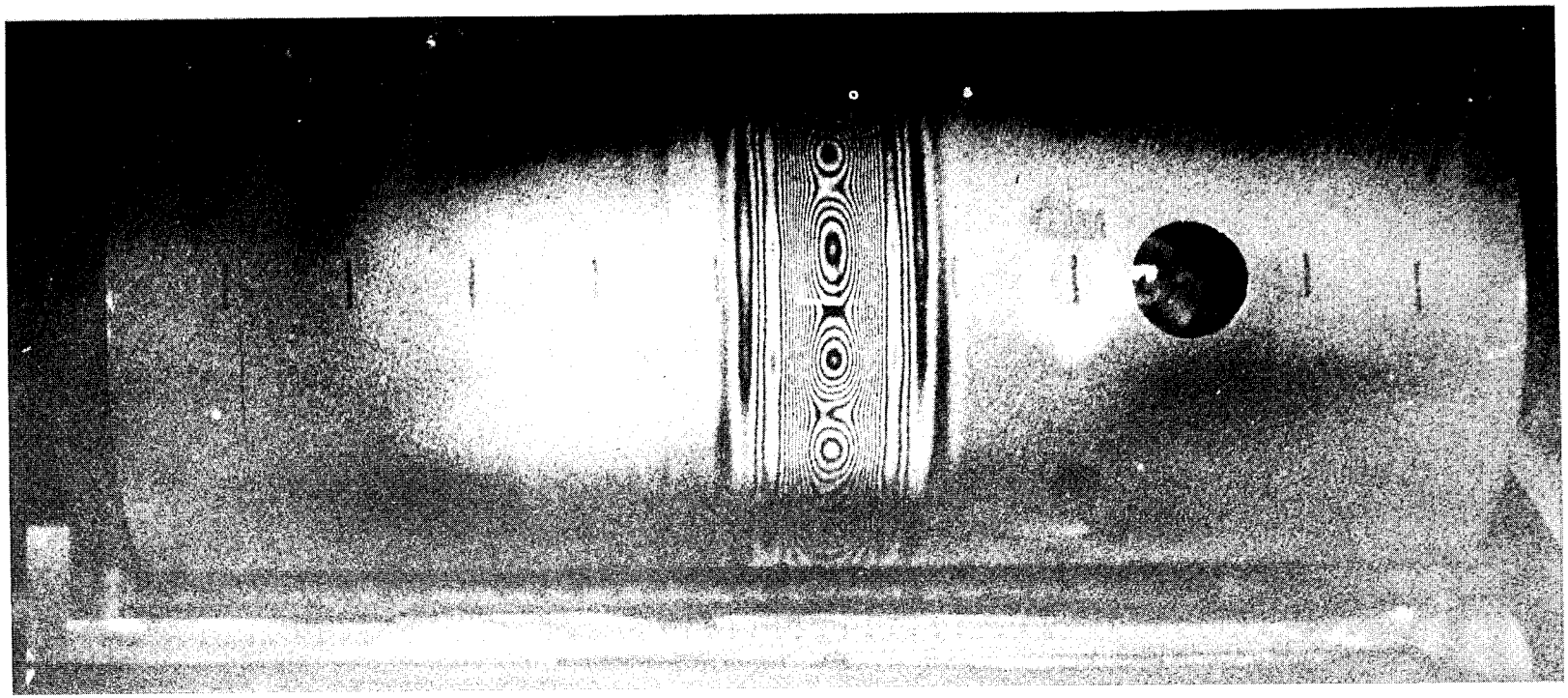

Figure E.2: Transverse Wave Interaction with a Circular Cut-Out.
Time t = 21 μsec

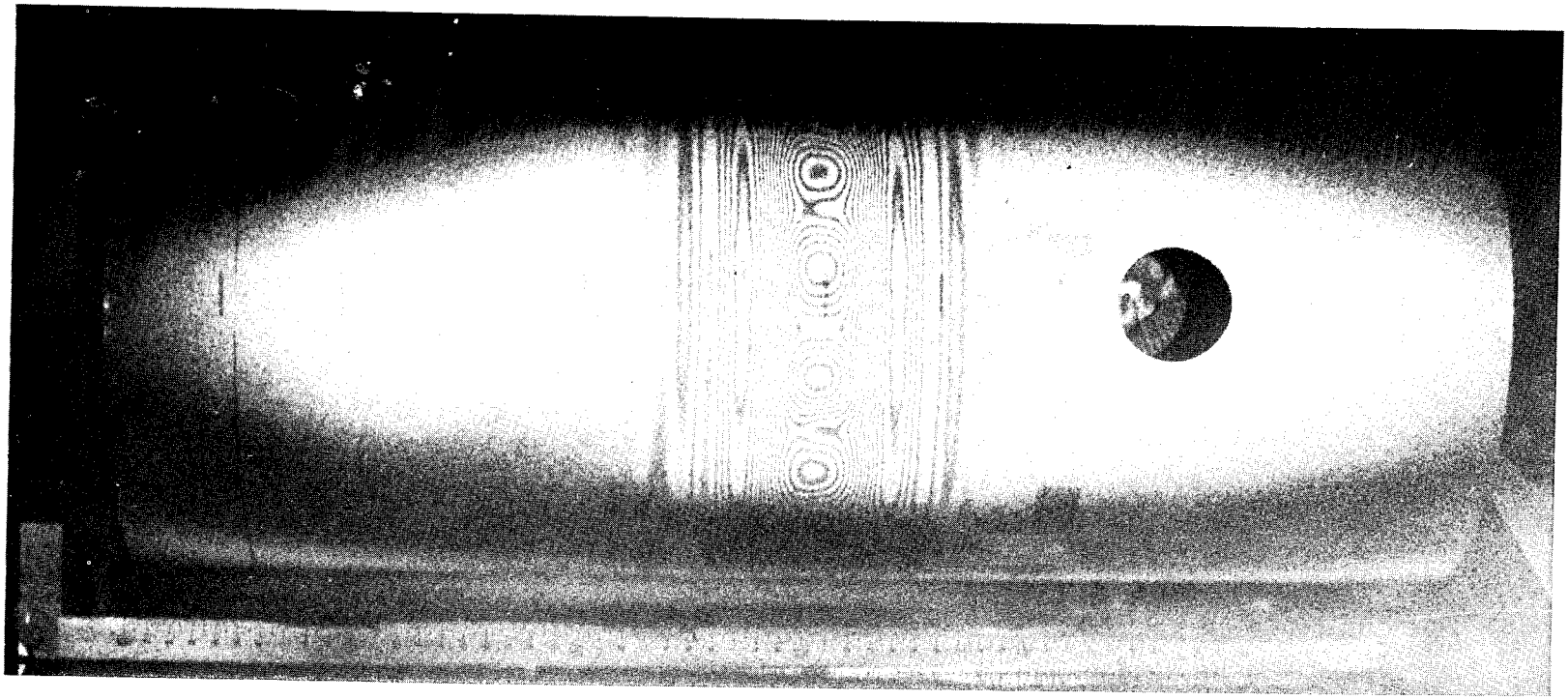

Figure E.3: Transverse Wave Interaction with a Circular Cut-Out.
Time t = 30 μsec

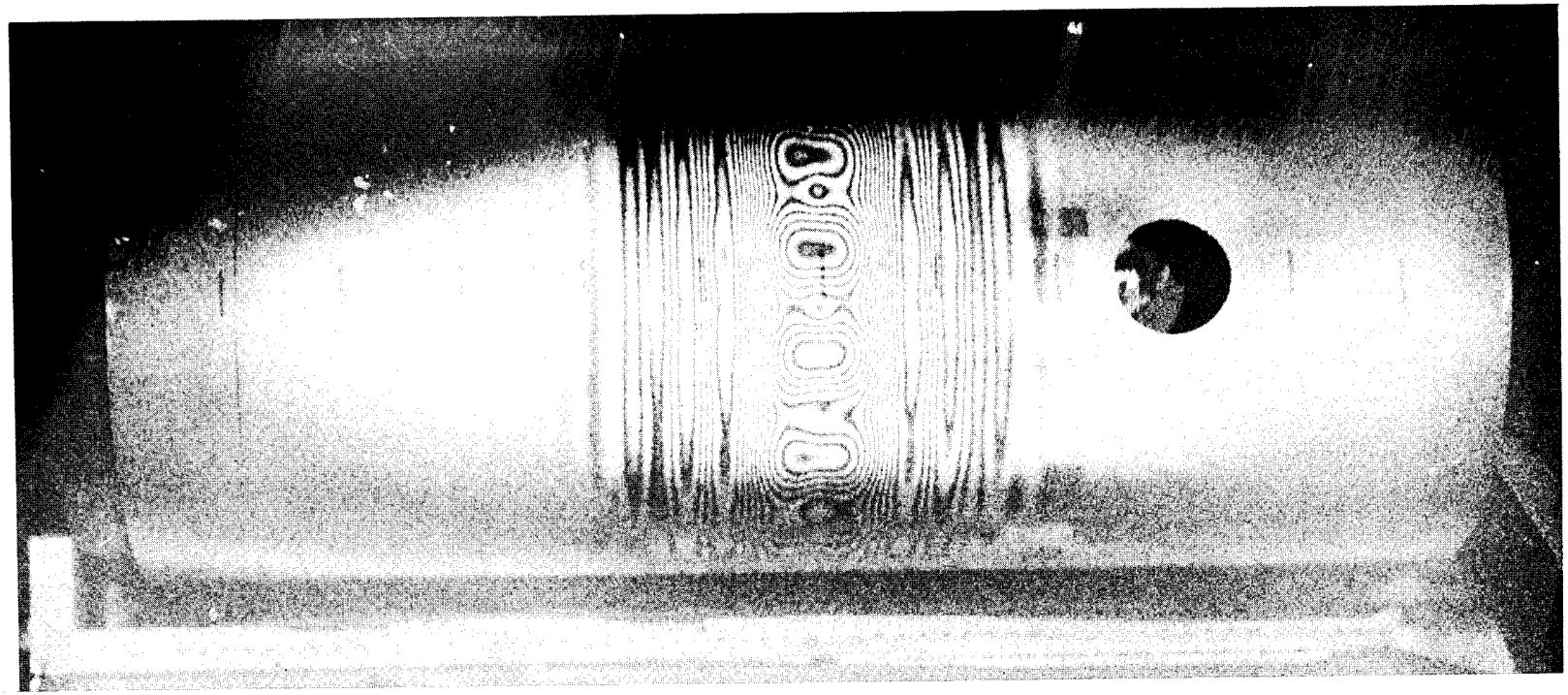

Figure E.4: Transverse Wave Interaction with a Circular Cut-Out.
Time t = 39 μsec

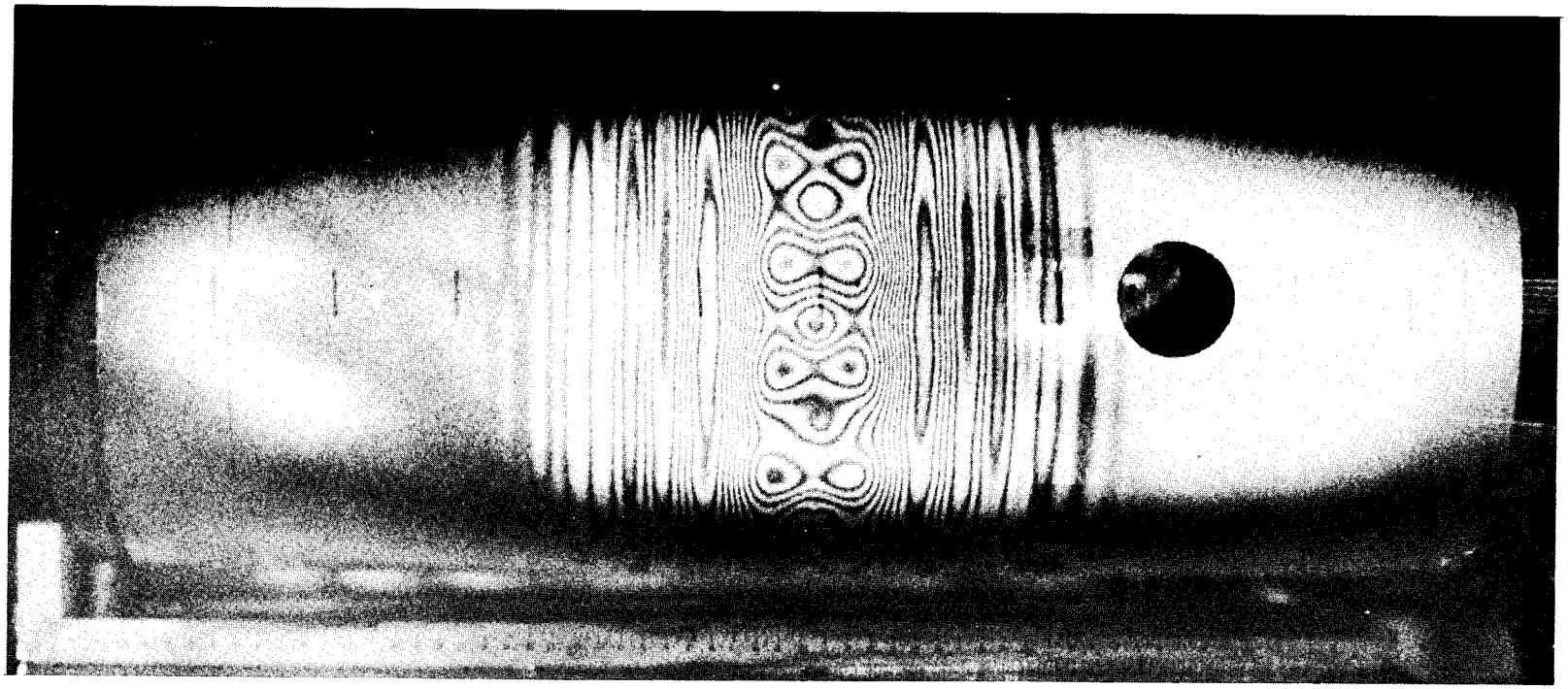

Figure E.5: Transverse wave interaction with a circular cut-out. Time t = 48 μsec.

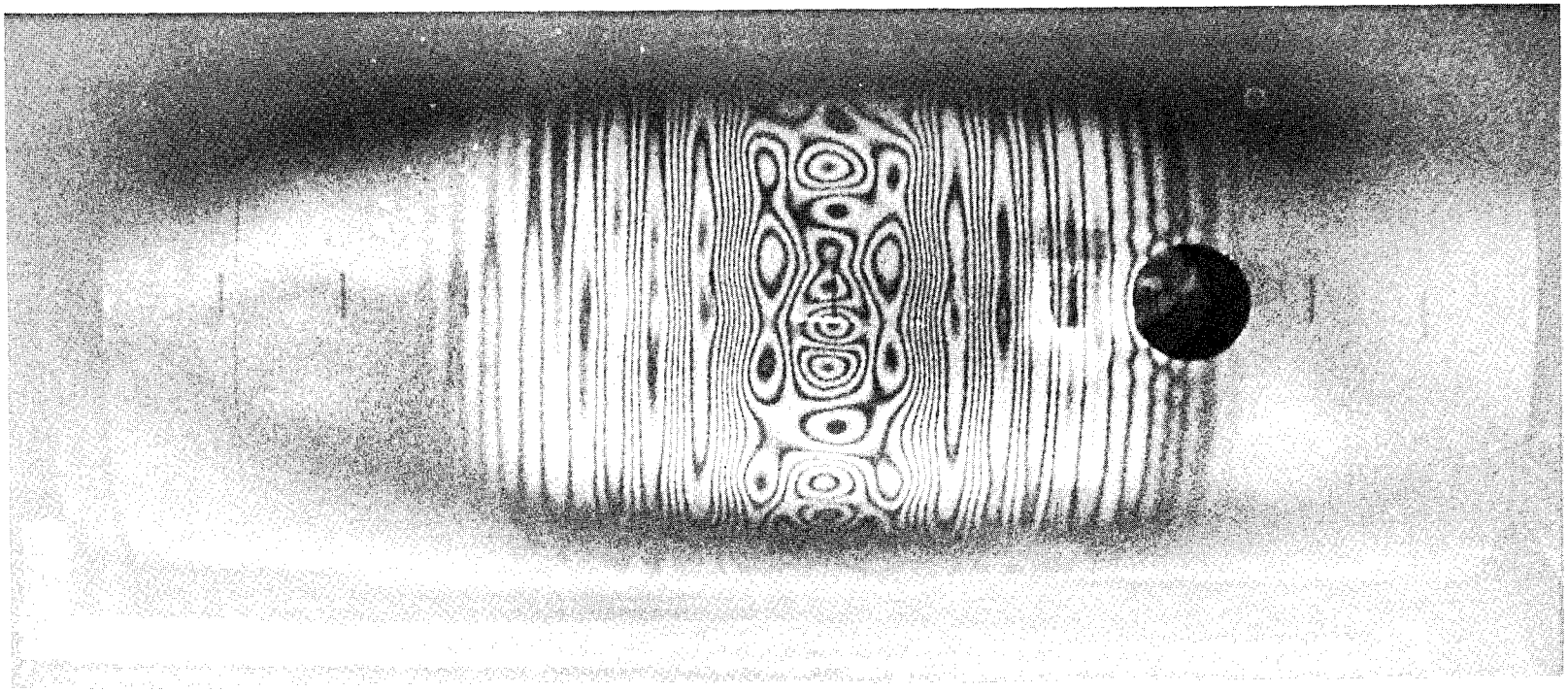

Figure E.6: Transverse Wave Interaction with a Circular Cut-Out.
Time t = 59 μsec

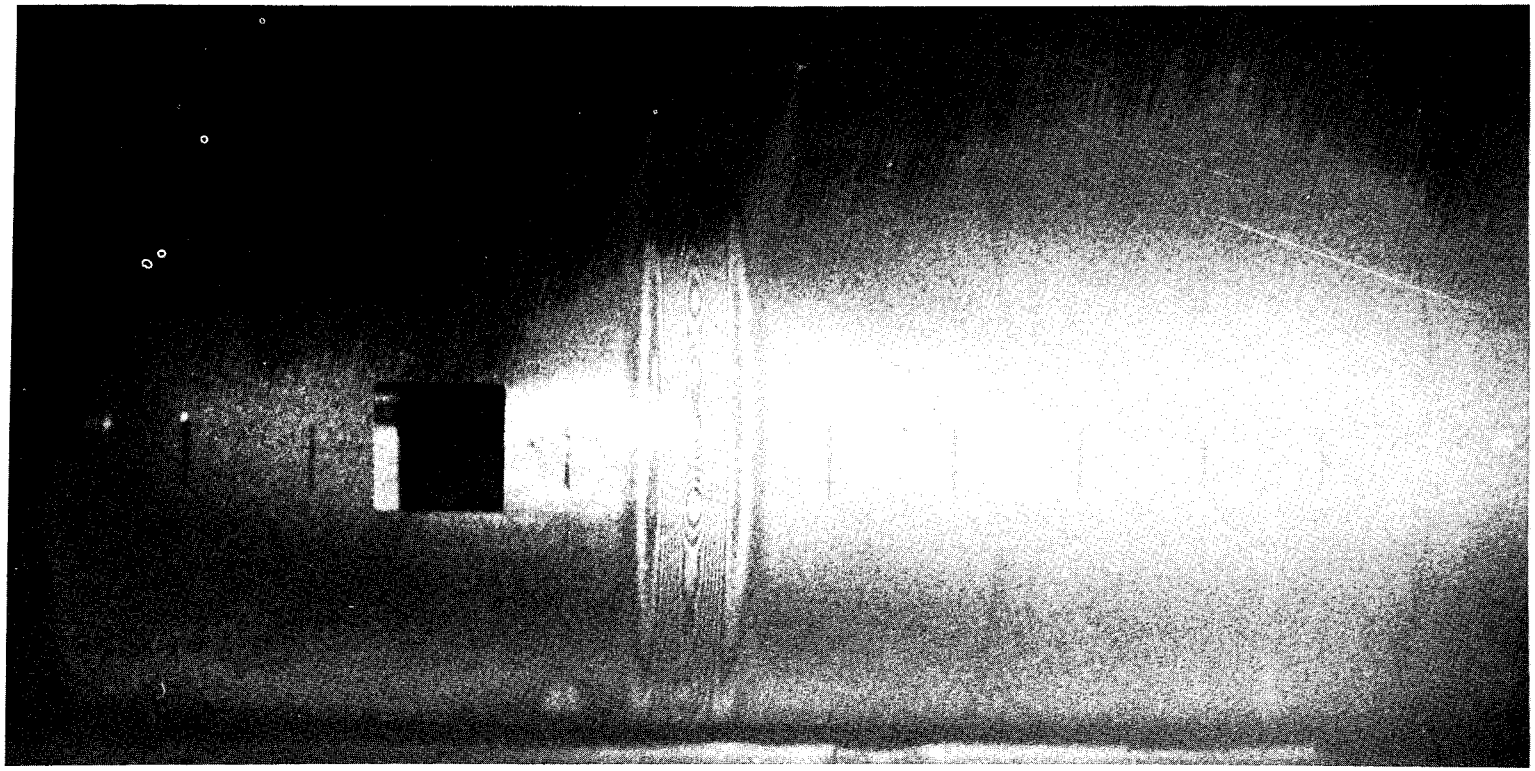

Figure E.7: Wave propagation past a square cut-out. Time t = 11 μsec. (Thin shell, h = .106 wall thickness.)

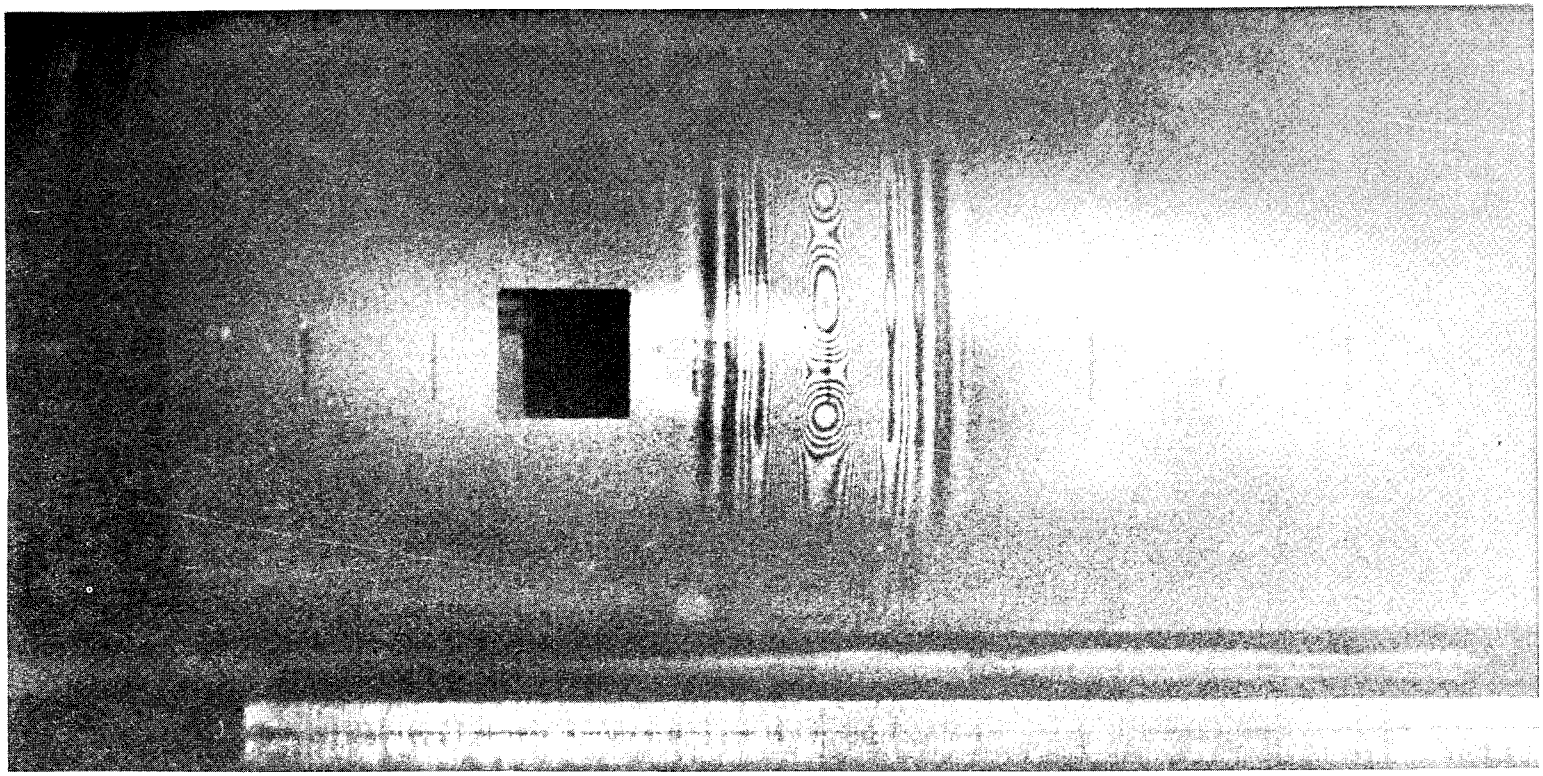

Figure E.8: Wave propagation past a square cut-out. Time t = 21 μsec. (Thin shell h = .106 wall thickness.)

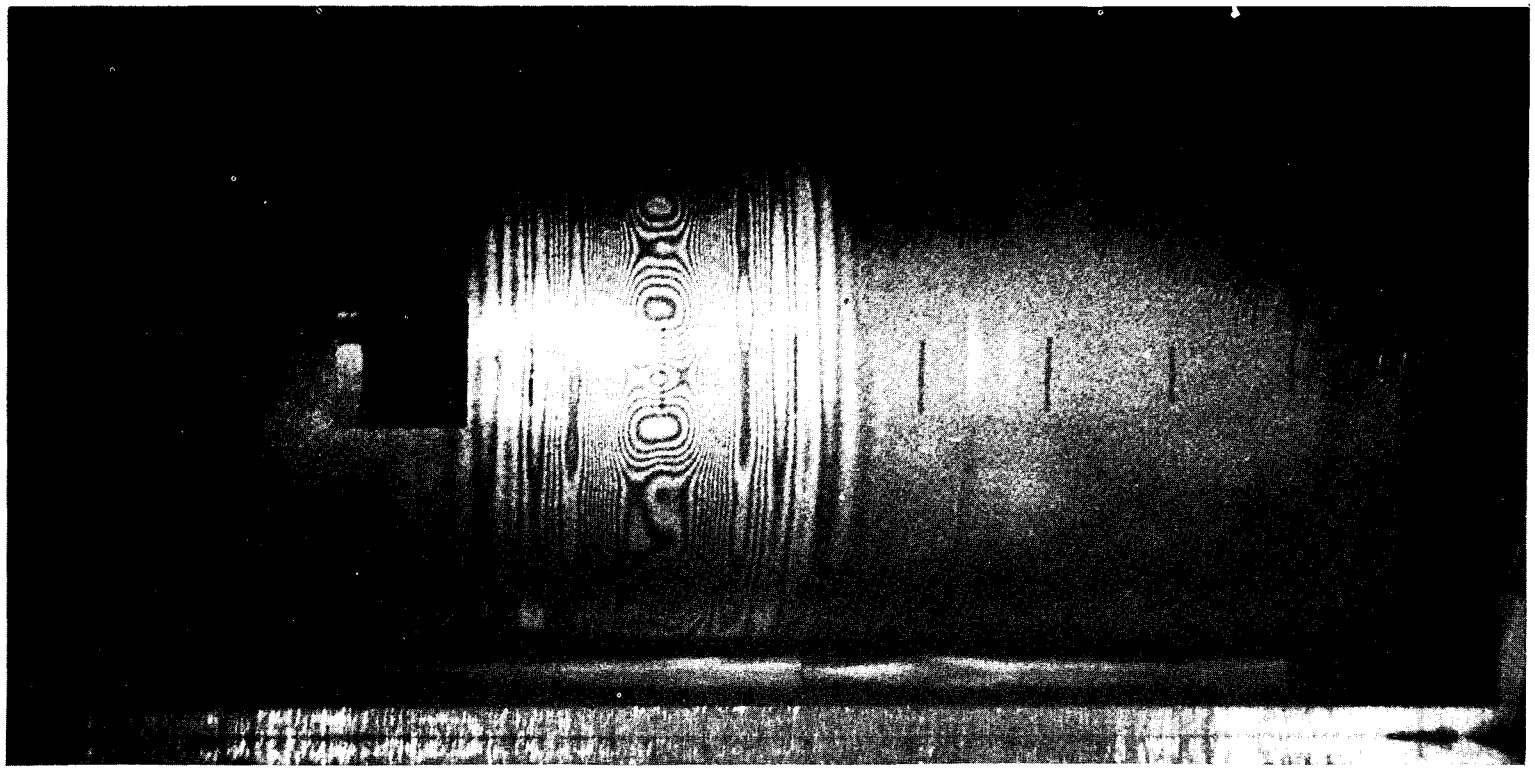

Figure E.9: Wave propagation past a square cut-out. Time t = 31 μsec. (Thin shell, h = .106 wall thickness.)

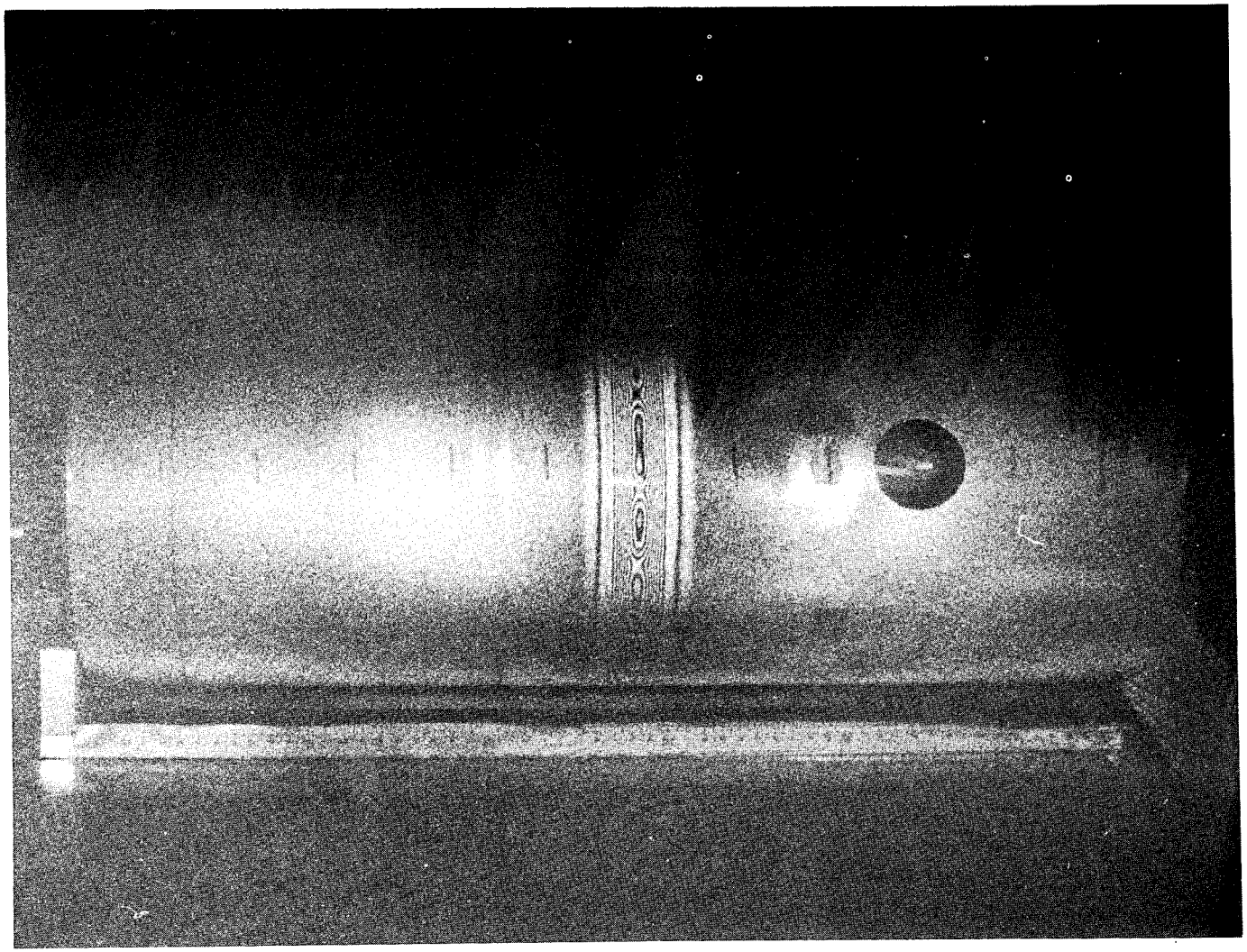

Figure E.10: Wave Interacting with the (Internal) Stiffening Ring (on the left, at x = -4 inches) and the Cut-Out (on the right). Time t = 10 μsec

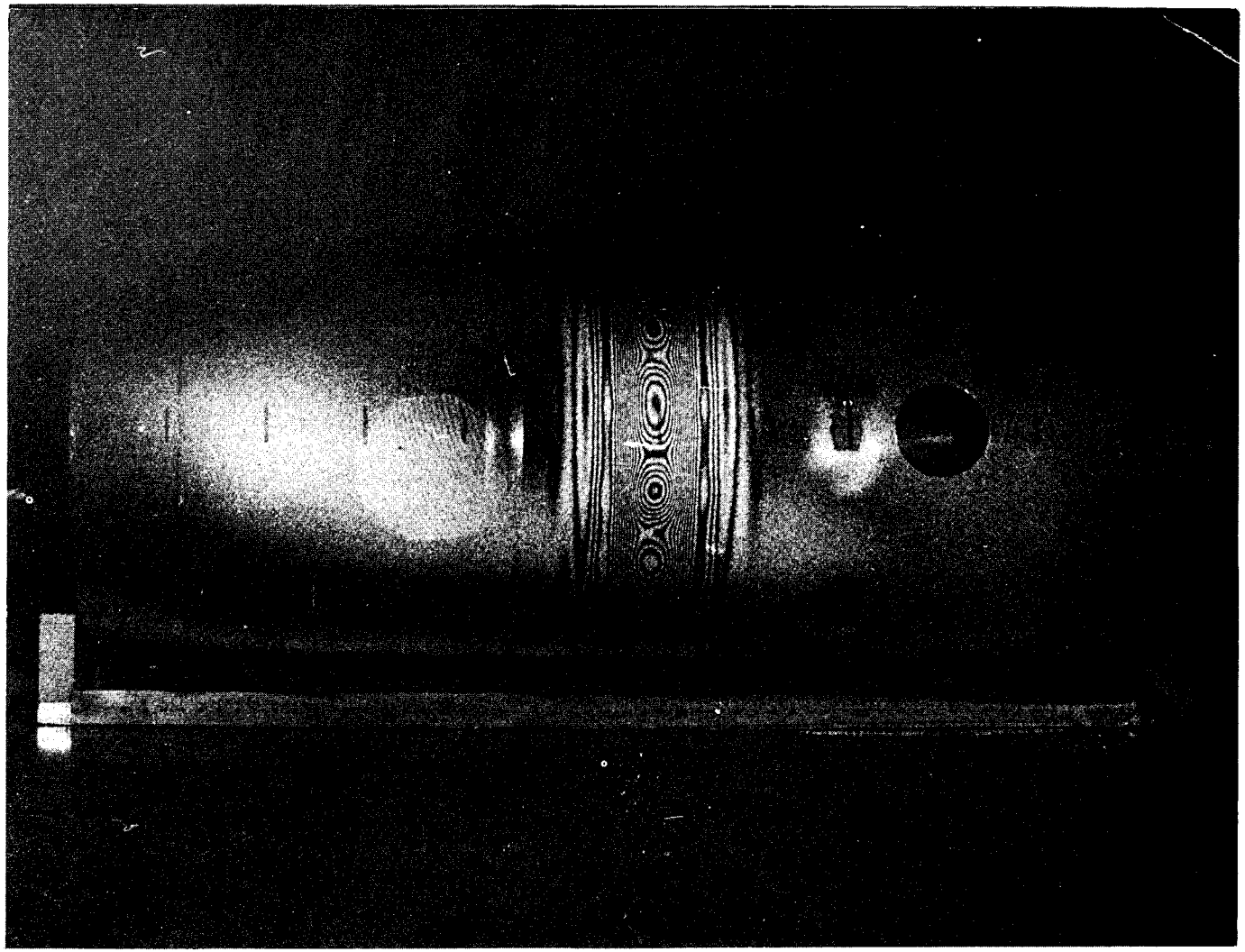

Figure E.11: Wave Interacting with the (Internal) Stiffening Ring (on the left, at x = -4 inches) and the Cut-Out (on the right). Time t = 21 μsec

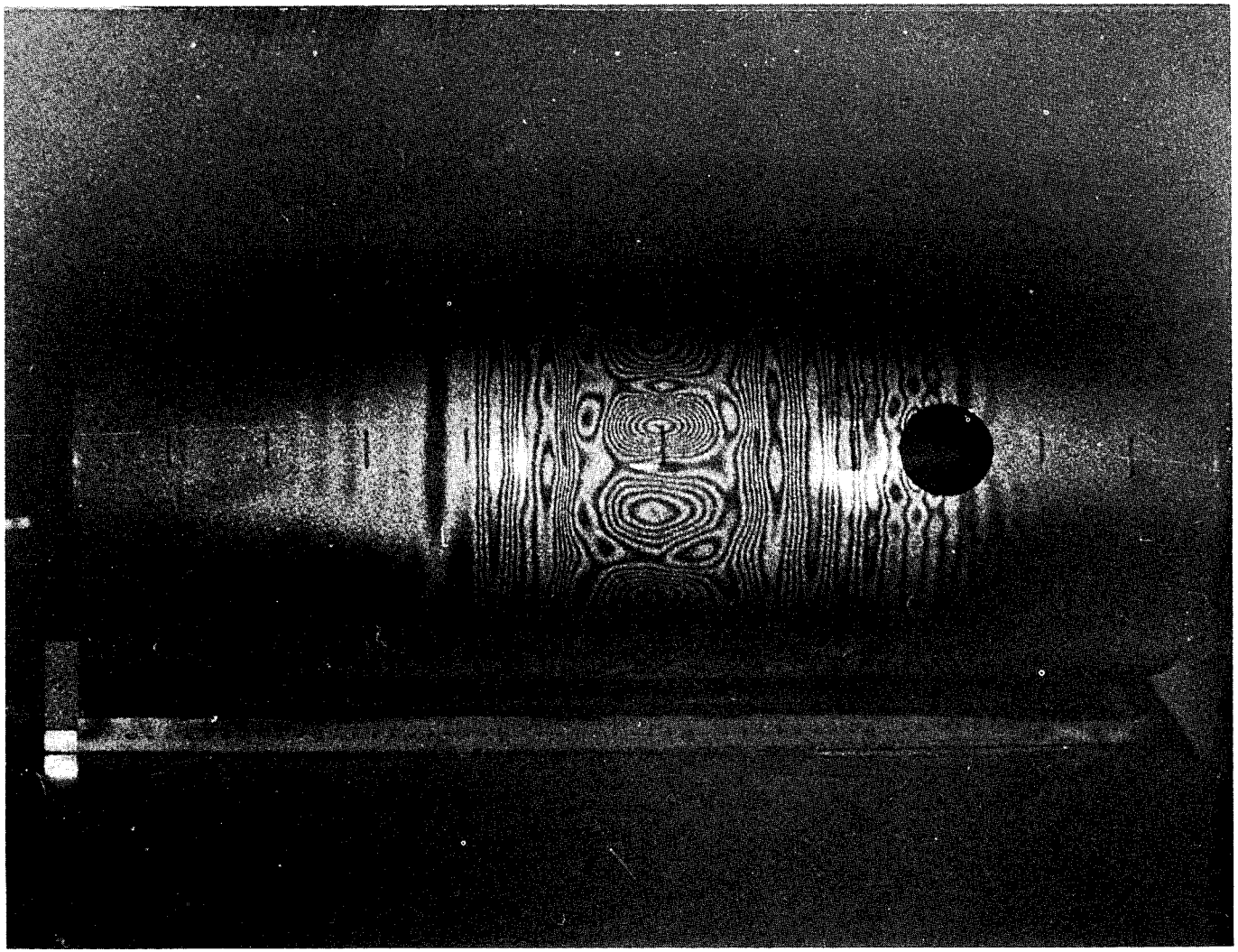

Figure E.12: Wave Interacting with the (Internal) Stiffening Ring (on the left, at x = -4 inches) and the Cut-Out (on the right). Time t = 70 μsec

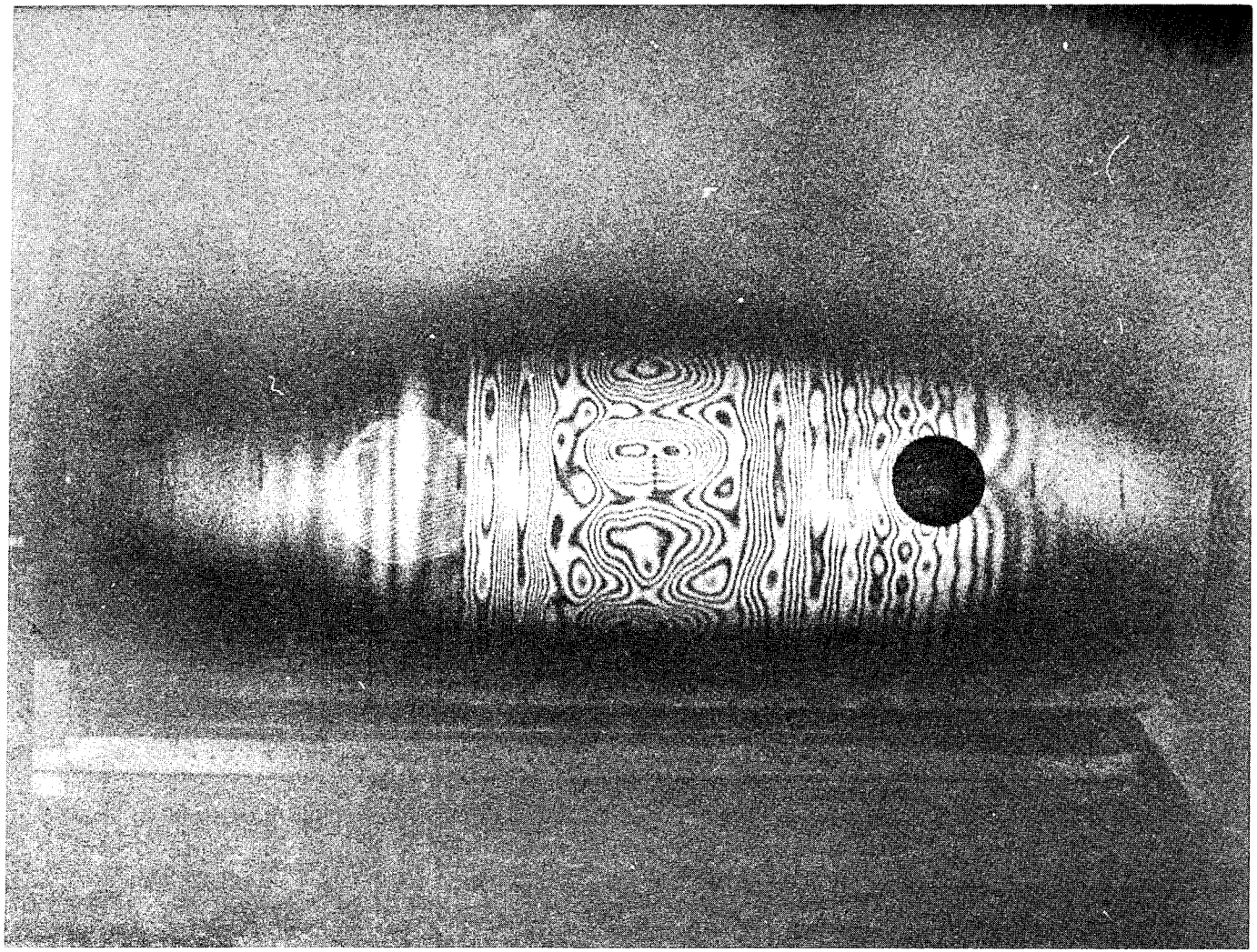

Figure E.13: Wave Interacting with the (Internal) Stiffening Ring (on the left, at x =-4 inches) and the Cut-Out (on the right). Time t = 80 μsec

APPENDIX F

WAVES IN CONICAL SHELLS

(ADDITIONAL INTERFEROGRAMS)

This Appendix is designed to supplement Section 5.0 of the main body of the text.

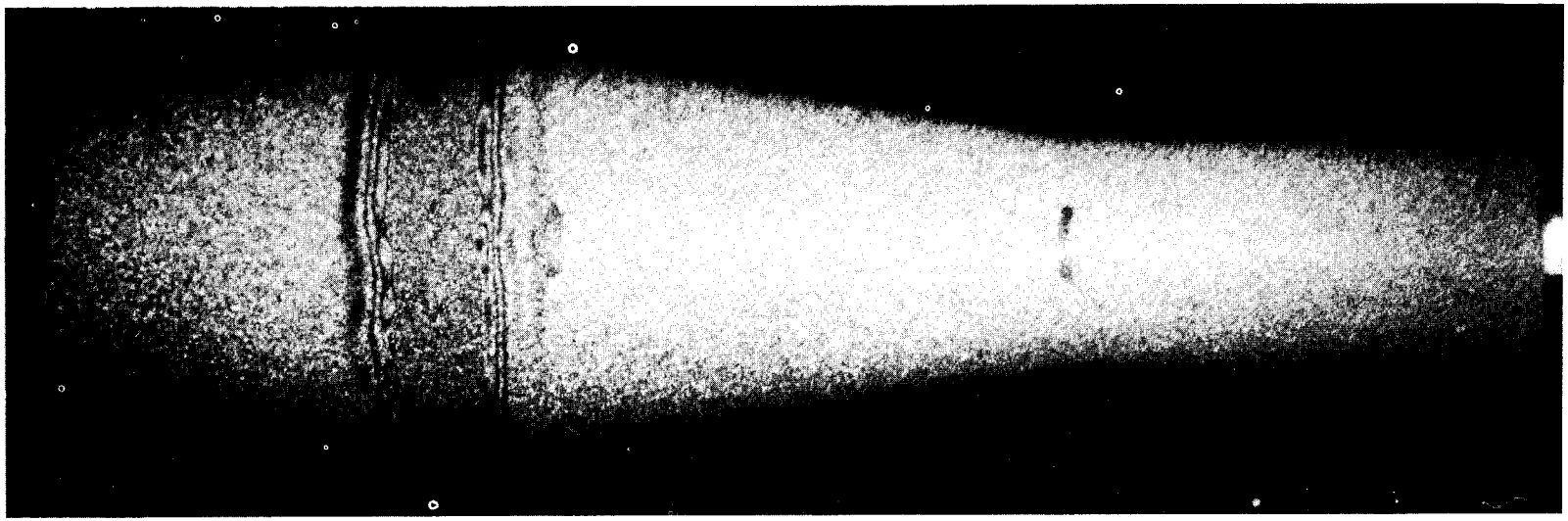

Figure F.1: Wave propagating in a thin-walled cone-cylinder. Time t = 10 μsec.

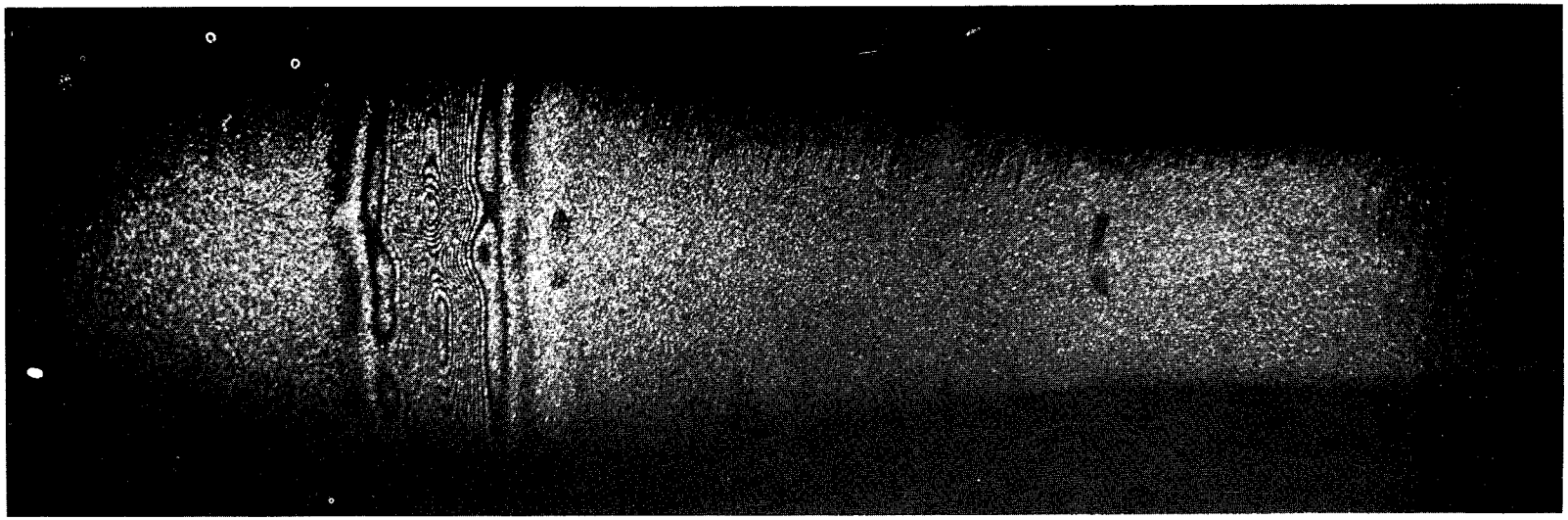

Figure F.2: Wave propagating in a thin-walled cone-cylinder. Time t = 12 μsec.

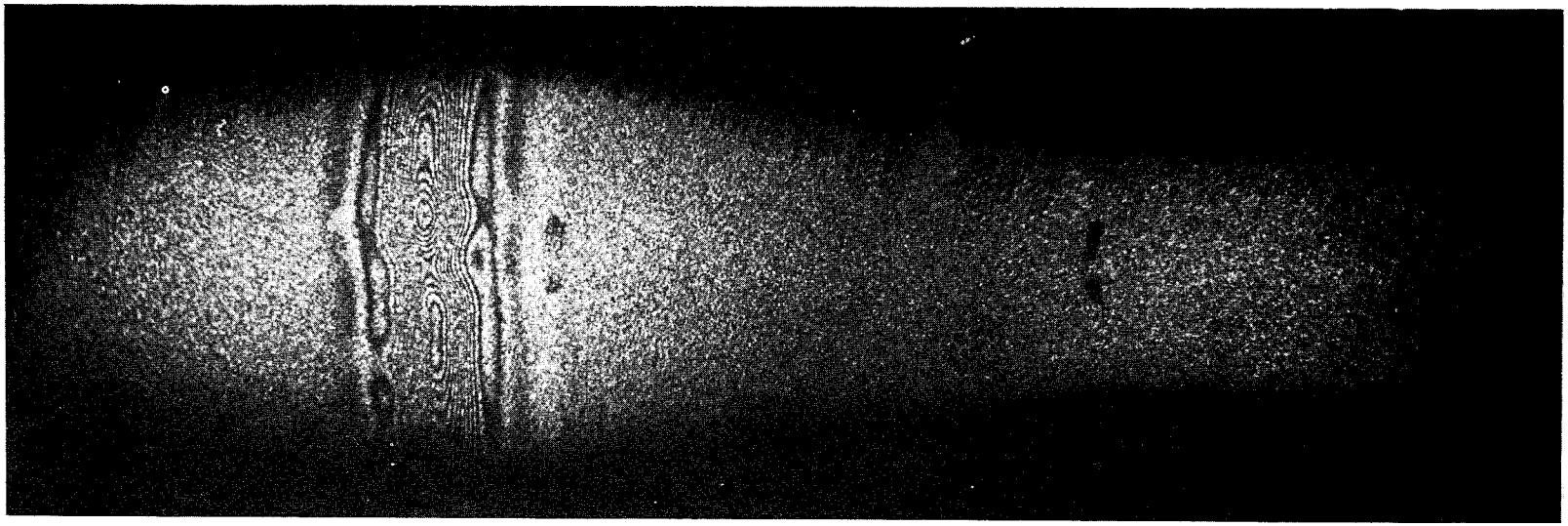

Figure F.3: Wave propagating in a thin-walled cone-cylinder. Time t = 12 μsec.

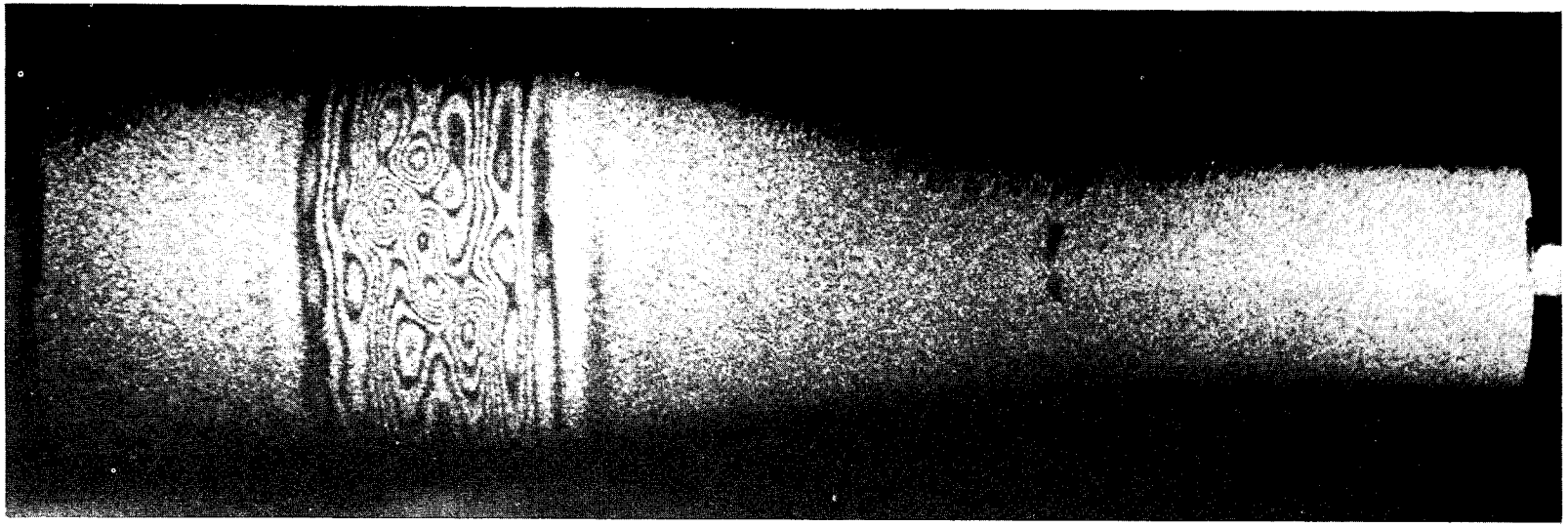

Figure F.4: Wave propagating in a thin-walled cone-cylinder. Time t = 21 μsec.

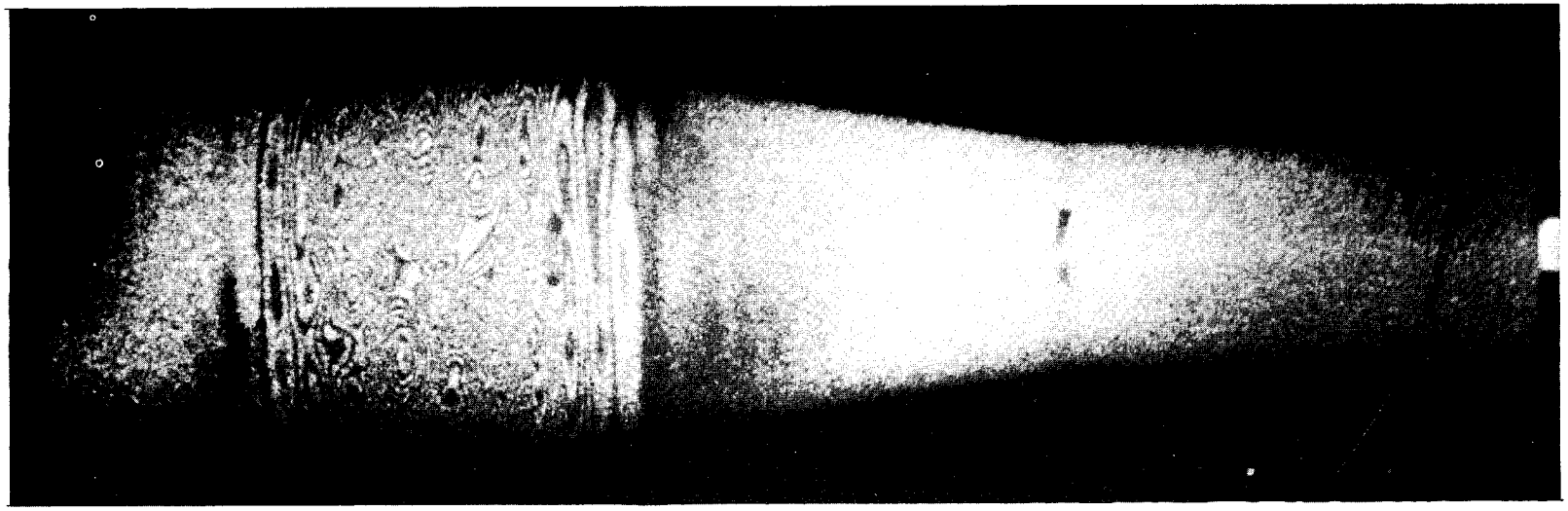

Figure F.5: Wave propagating in a thin-walled cone-cylinder. Time t = 25 μsec.

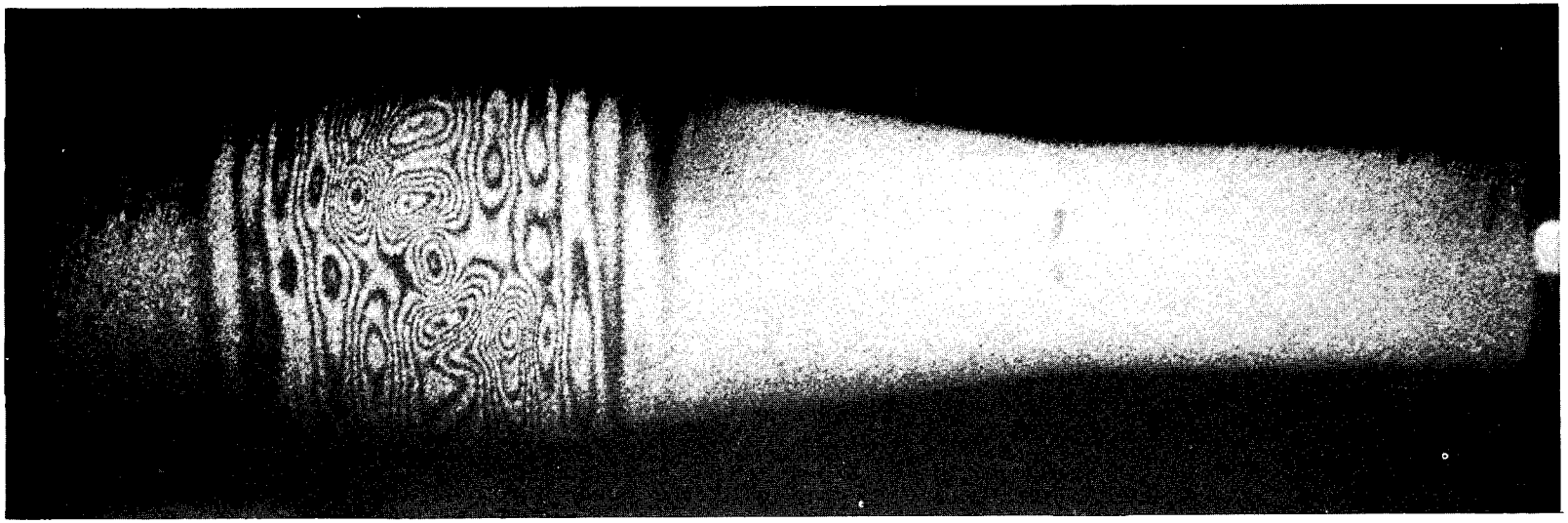

Figure F.6: Wave propagating in a thin-walled cone-cylinder. Time t = 28 μsec.

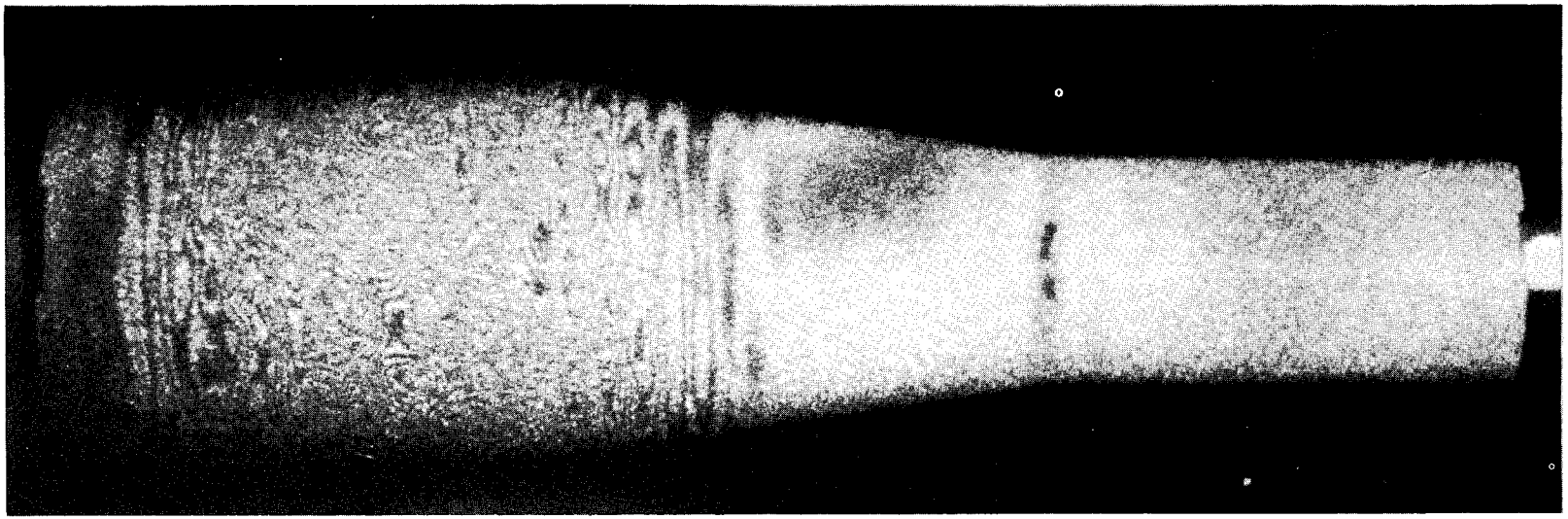

Figure F.7a: Wave propagating in a thin-walled cone-cylinder. Time t = 38 μsec.

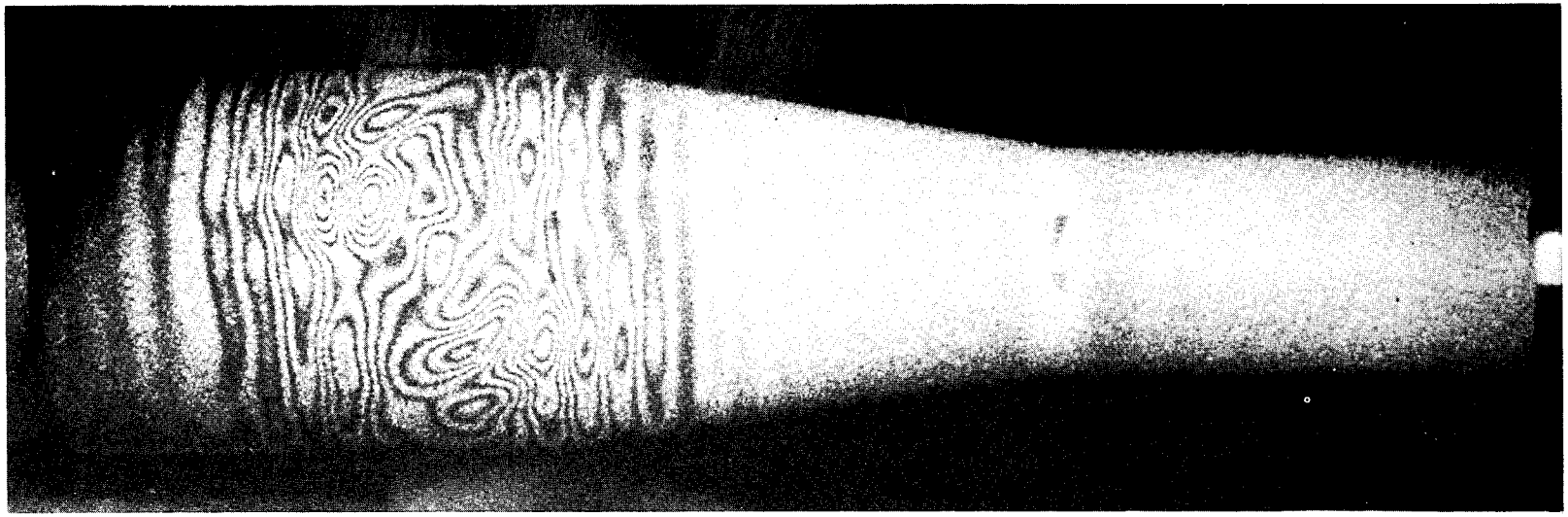

Figure F.7b: Wave propagating in a thin-walled cone-cylinder. Time t = 39 μsec.

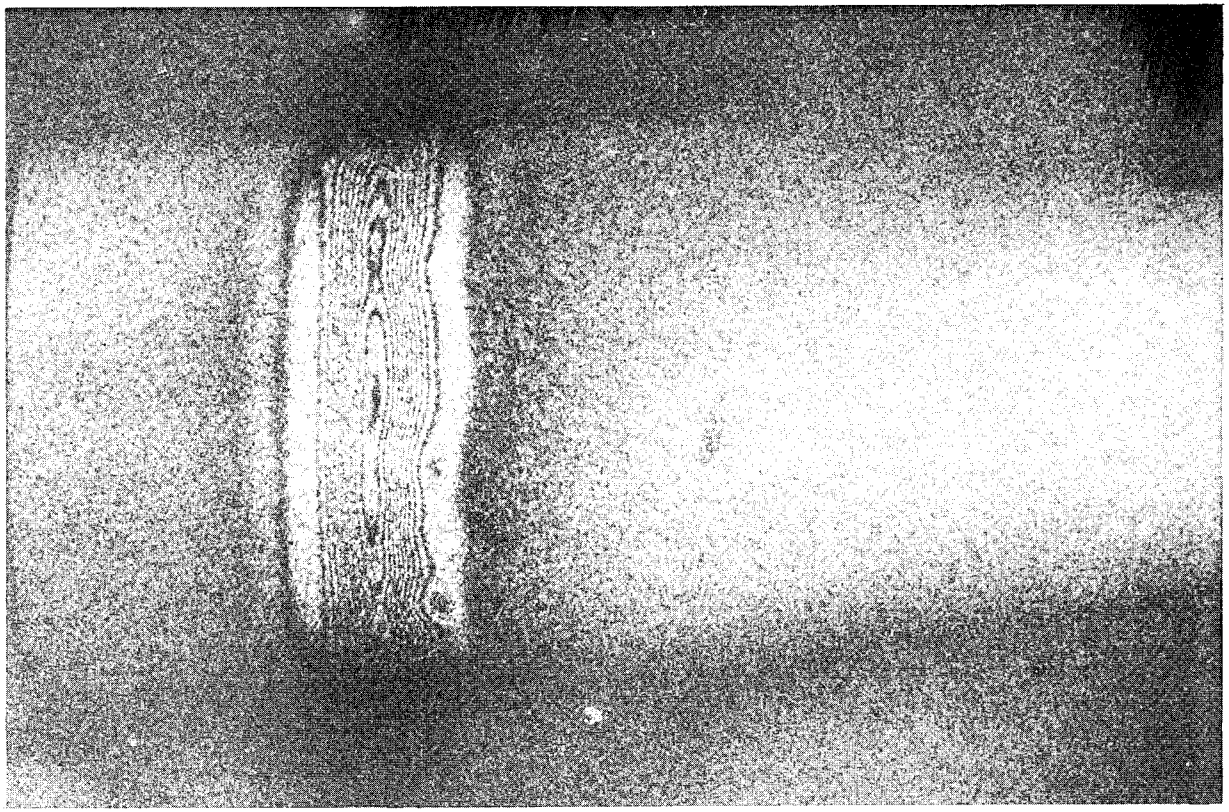

Figure F.8: Wave propagating in thin-walled cone-cylinder. Time t = 10 μsec.

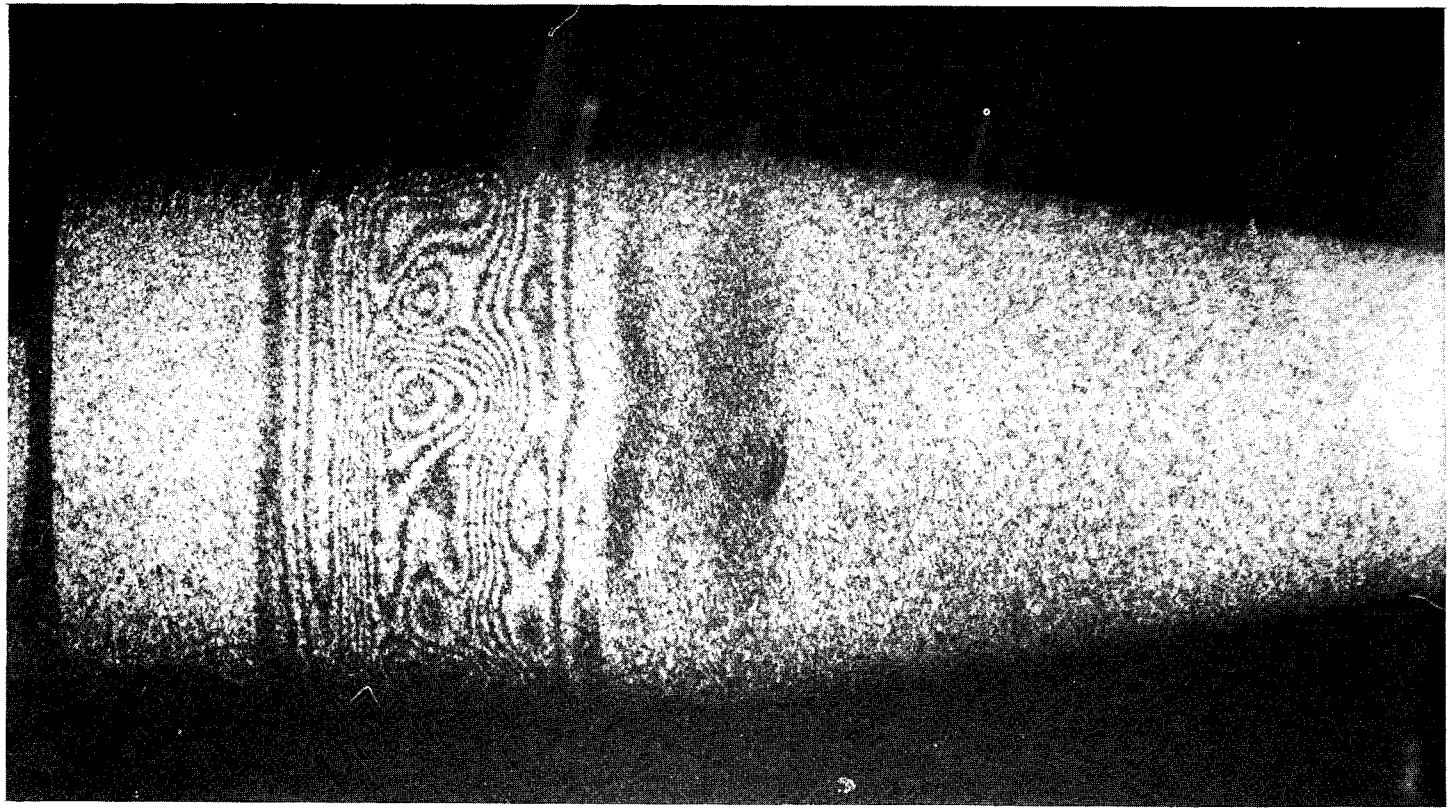

Figure F.9: Wave propagating in thin-walled cone-cylinder. Time t = 20 μsec.

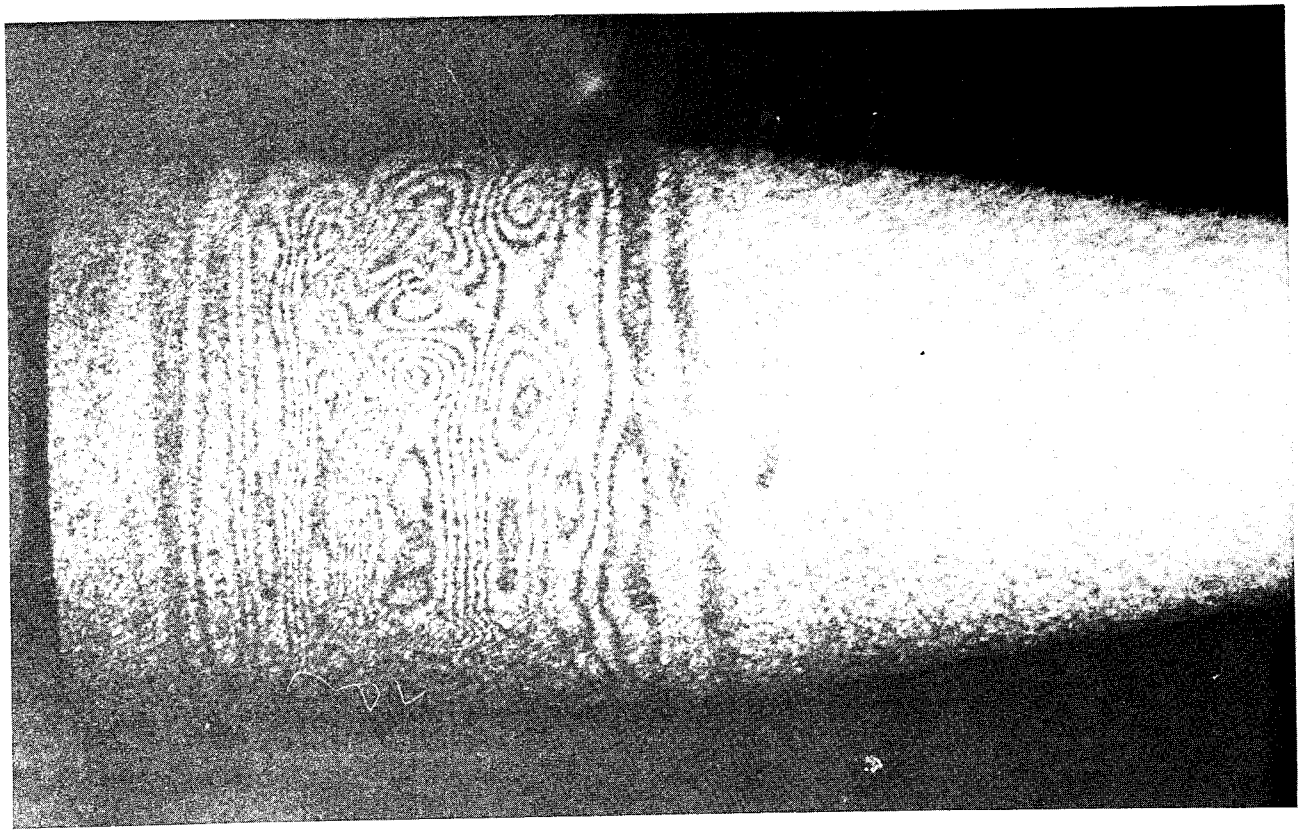

Figure F.10: Wave propagating in thin-walled cone-cylinder. Time t = 30 μsec.

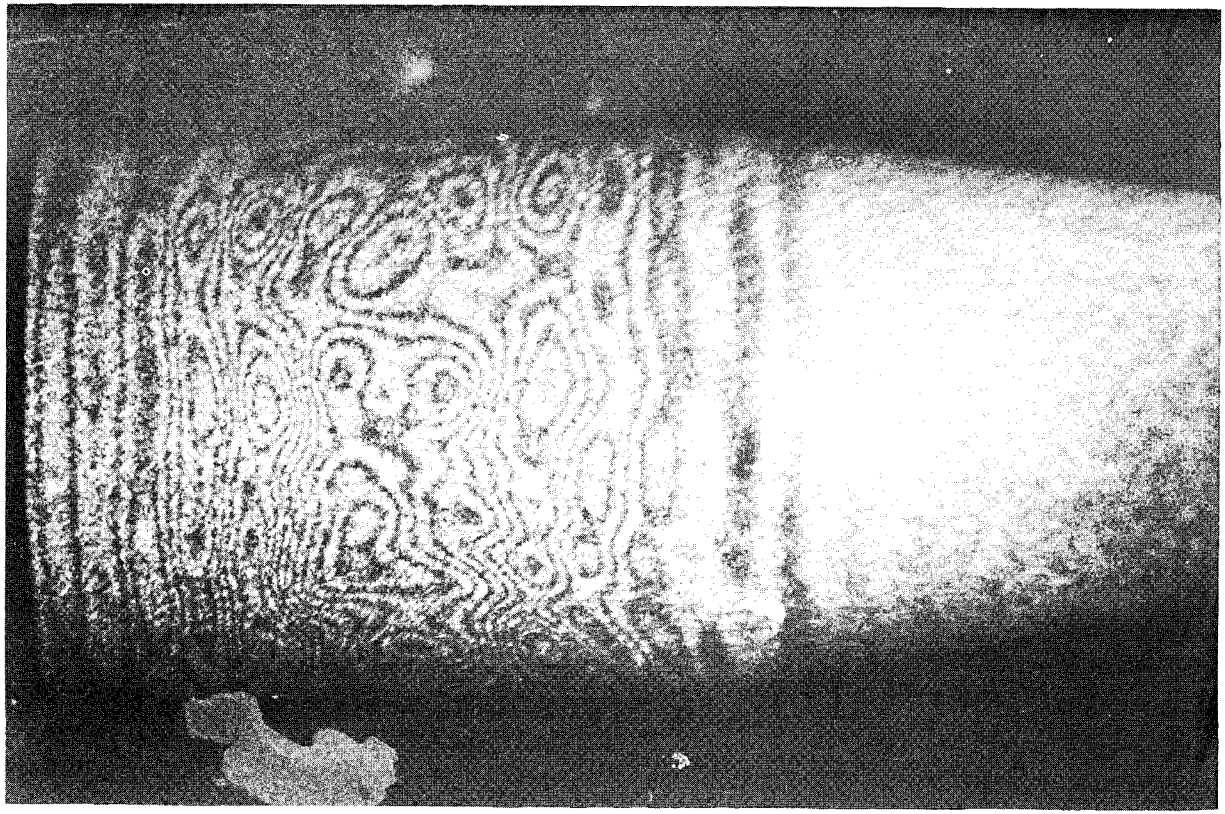

Figure F.11: Wave propagating in thin-walled cone-cylinder. Time t = 39 μsec.

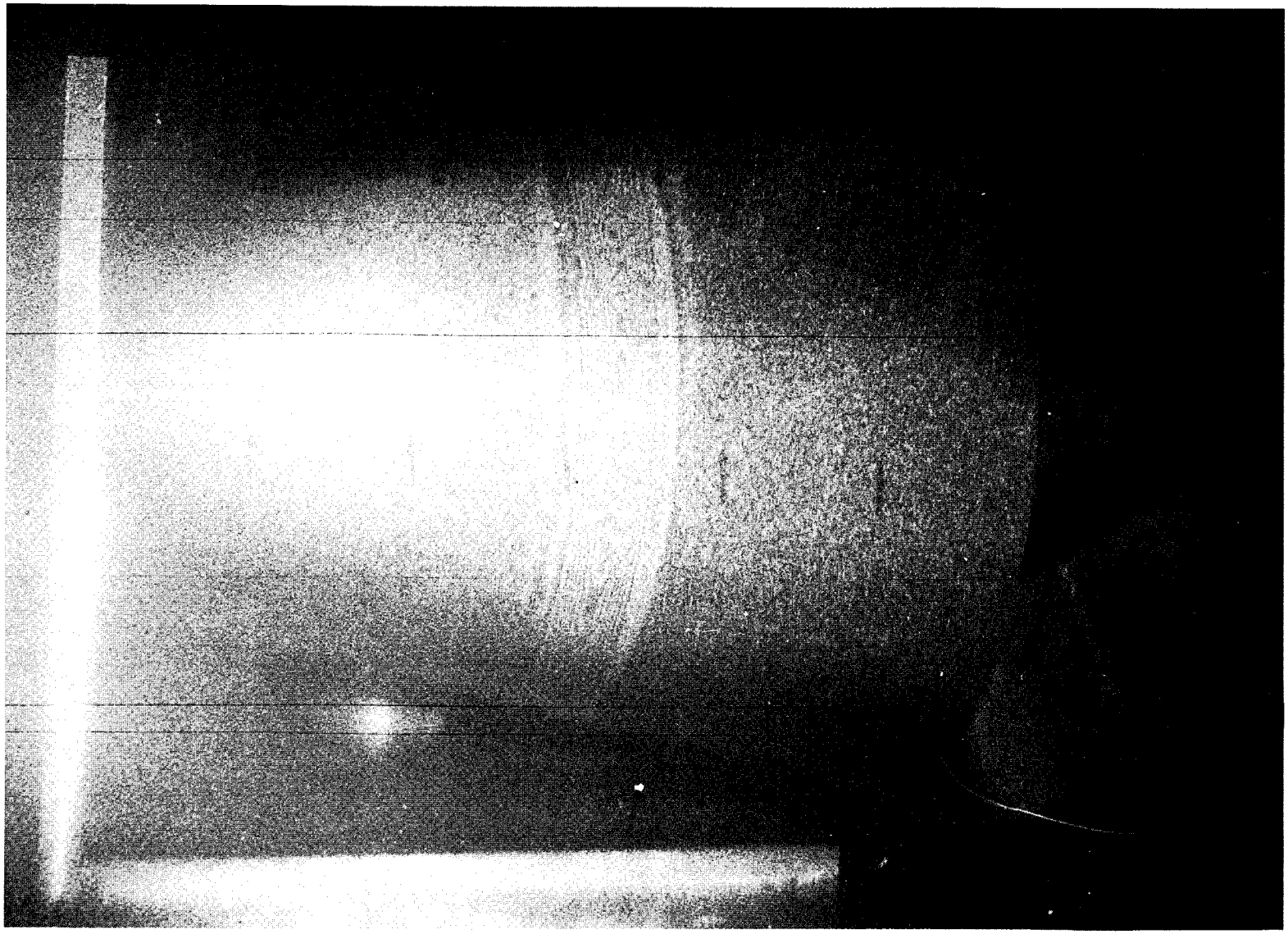

Figure F.12: Wave propagating in a large conical shell. Time t = 10 μsec.

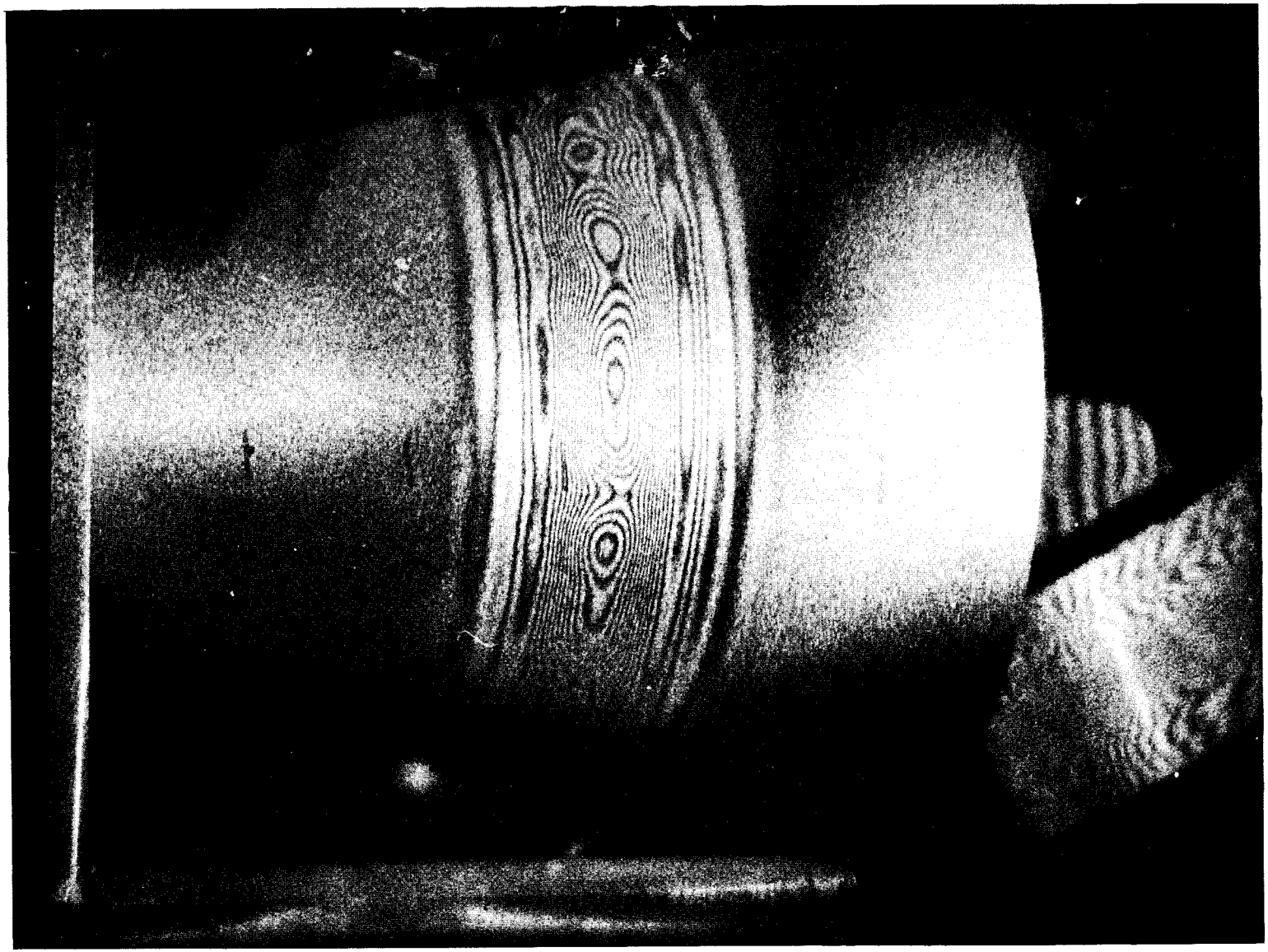

Figure F.13: Wave Propagating in a large conical shell. Time t = 20 μsec.

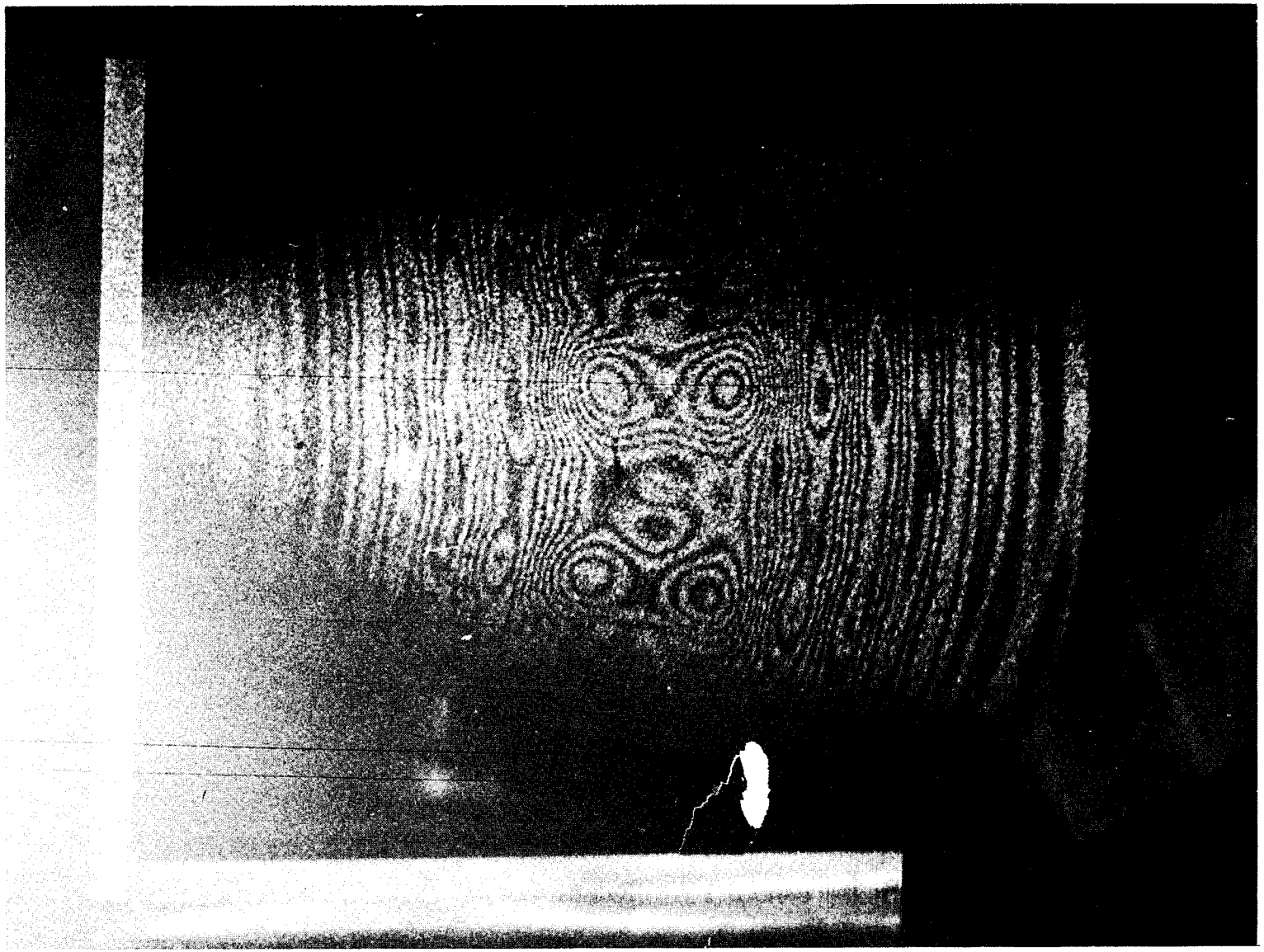

Figure F.14: Wave Propagating in a large conical shell. Time t = 59 μsec.

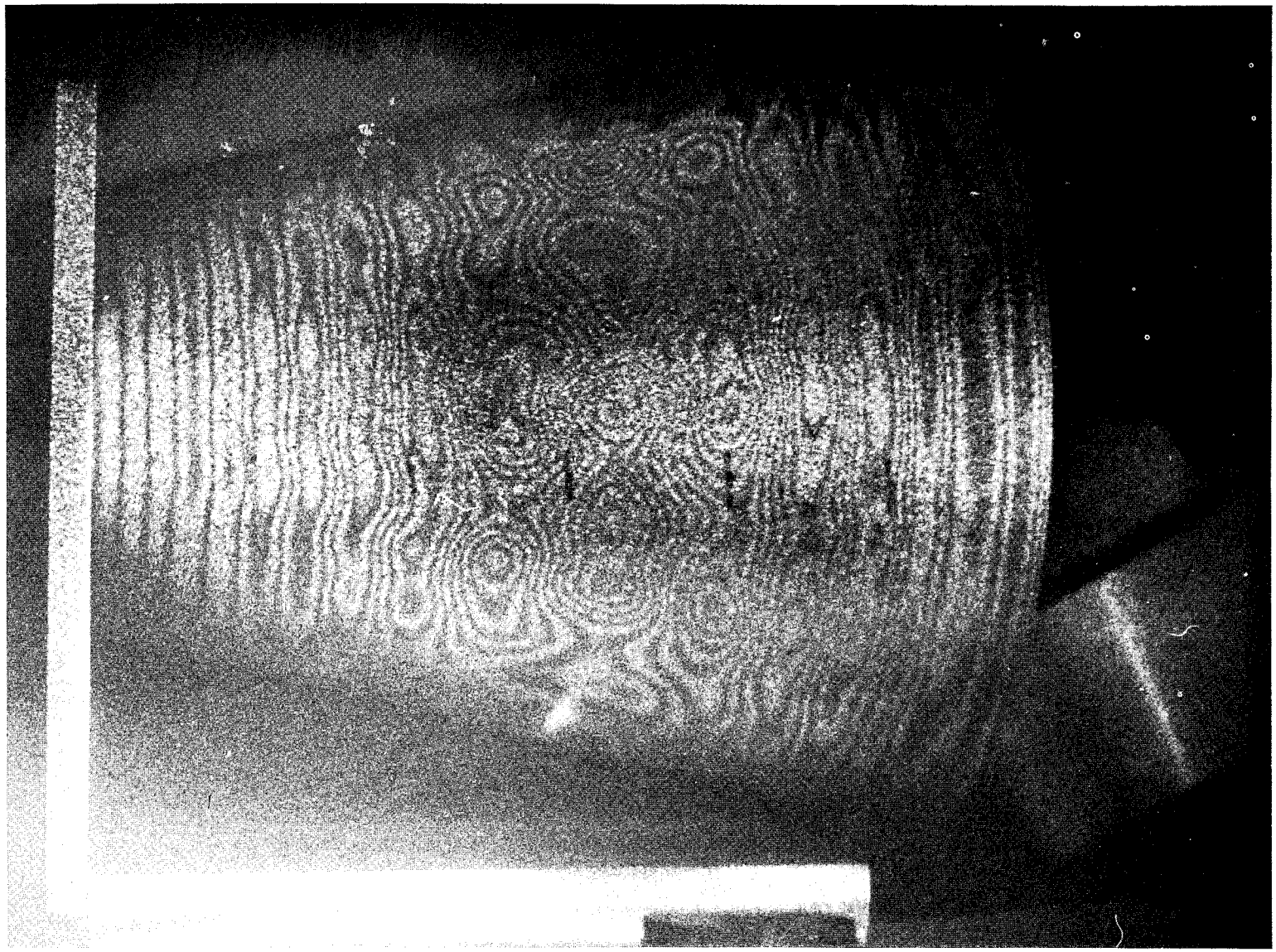

Figure F.15: Wave propagating in a large conical shell. Time t = 81 μsec.

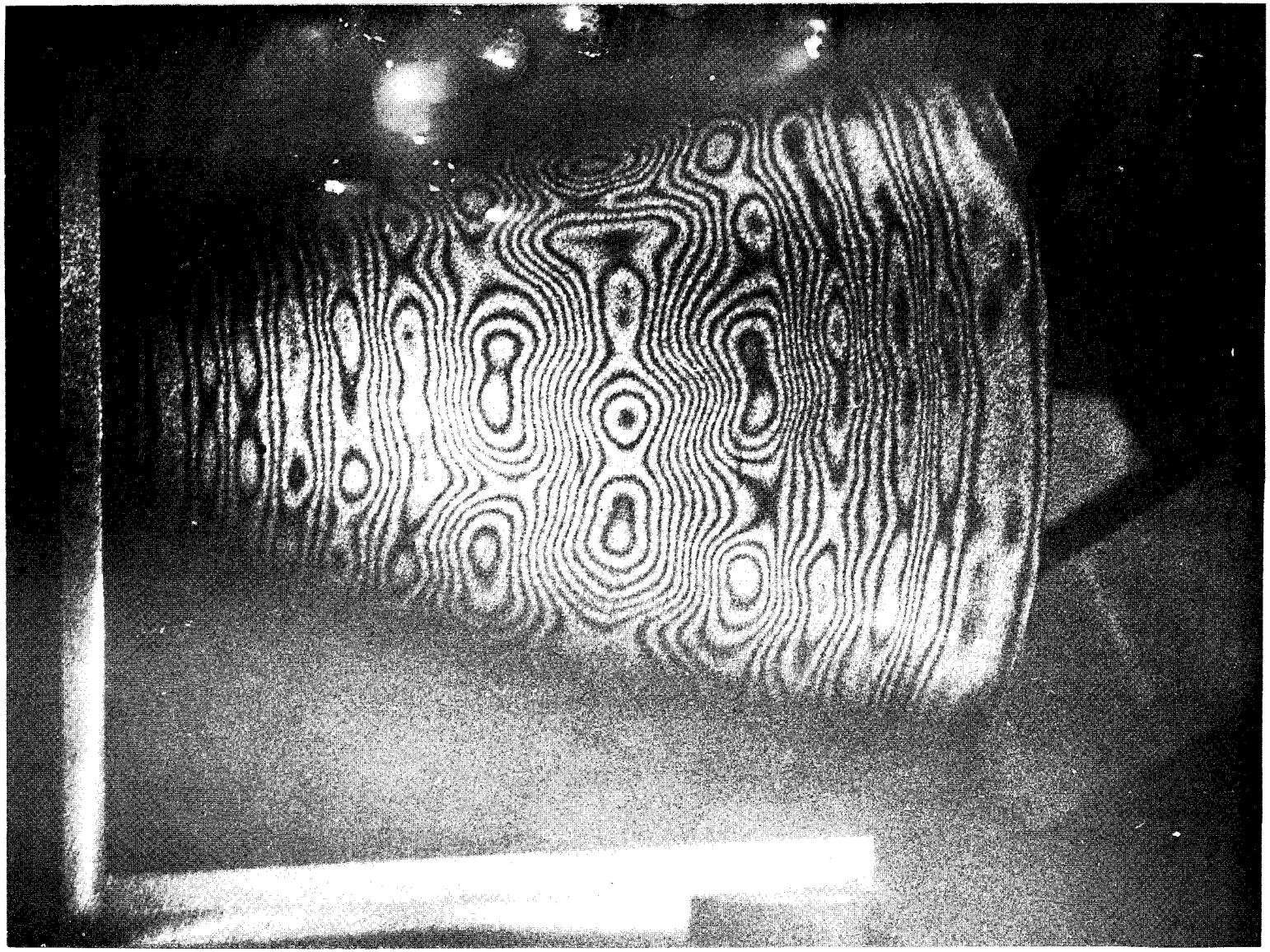

Figure F.16: Wave Propagating in a large conical shell. Time t = 91 μsec.